UNIVERSITY OF MISKOLC
FACULTY OF MECHANICAL ENGINEERING AND INFORMATICS

INVESTIGATION ON DYNAMIC PV ARRAY RECONFIGURATION PERFORMANCE ENHANCEMENT UNDER NON-UNIFORM PARTIAL SHADING CONDITIONS

PhD Dissertation

PREPARED BY:
FATIMAH NADHIM AMEEN

Supervisor
DR. ATTILA TROHÁK
Co-Supervisor
PROF. DR. ABDULRAHMAN I. SIDDIQ
Consultant
DR. RABAB BENOTSMANE

JÓZSEF HATVANY DOCTORAL SCHOOL FOR COMPUTER SCIENCE AND ENGINEERING, FACULTY OF MECHANICAL ENGINEERING AND INFORMATICS

Miskolc
2025

Declaration of Authorship

The author hereby declares that this thesis titled, *'Investigation on Dynamic PV Array Reconfiguration Performance Enhancement under Non-Uniform Partial Shading Conditions'* has not been submitted, either in the same or different form, to this or any other university for obtaining a PhD degree. The author confirms that the submitted work is their own, and where the work of others has been referenced, appropriate credit has been given.

Miskolc, 7th February 2025

Fatimah Nadhim AMEEN

Abstract

The increasing demand for renewable energy has driven extensive research into optimizing photovoltaic (PV) systems to ensure reliable power generation under varying environmental conditions. Partial shading, temperature variations, and electrical mismatch losses significantly affect PV system efficiency, leading to power losses and multiple peaks in the power-voltage curve. To address these challenges, this research introduces a Dynamic Probabilistic Reconfiguration Algorithm (DPRA) integrated into a hierarchical PV array system, enhancing energy extraction through real-time reconfiguration and adaptive control mechanisms.

The proposed system employs a hierarchical switching block (SB) architecture, incorporating microcontrollers, sensors (BH1750, DS18B20), and relays to dynamically adjust PV connections based on shading and temperature variations. A high-temperature isolation mechanism prevents thermal degradation by reducing panel temperatures from 76.45°C to 61.93°C, ensuring system reliability. The study evaluates two hierarchical reconfiguration models using MATLAB-Simulink simulations and experimental validation. Model-A features a simplified design, linking two panels per switching block, while Model-B offers an advanced reconfiguration scheme supporting Series-Parallel (SP), Bridge-Link (BL), and Total Cross-Tied (TCT) topologies.

Results confirm that Model-B significantly improves PV performance, achieving power output gains of up to 81.61% and efficiency improvements of 42.13% under various shading conditions. The HLLBE algorithm dynamically redistributes irradiance across PV layers, improving efficiency by 116.6% compared to fixed TCT configurations. DPRA also reduces computational complexity by 50%, enabling faster optimization and enhanced real-time adaptability.

Comparisons with Sudoku-based, Magic Square, and hybrid PSO-based configurations demonstrate the superiority of the proposed system, with power generation improvements ranging from 21.6% to 39.37% and efficiency gains between 32.39% and 42.52%. Additionally, the probabilistic optimization framework reduces hardware complexity, achieving a 79.17% reduction in switch count compared to Dynamic Electrical Structures (DES).

The proposed DPRA-based hierarchical PV system supports scalability, allowing for seamless integration of additional panels without extensive rewiring, making it suitable for both residential and utility-scale solar applications. Although the initial cost for DPRA implementation is slightly higher ($688) than TCT ($591), the substantial gains in energy output, efficiency, and system longevity make it a cost-effective and scalable solution for improving PV performance. By bridging the gap between theoretical innovation and practical application, this research contributes to advancing PV technology and paves the way for scalable, intelligent systems capable of meeting the growing energy demands of a sustainable future.

Acknowledgements

First and foremost, I would like to express my deepest gratitude to my supervisors, Dr. Attila Trohák, Head of the Institute of Automation and Info-Communication at the University of Miskolc, and my co-supervisor, Prof. Dr. Abdulrahman I. Siddiq from the Department of Electronic and Control Engineering at Northern Technical University, Iraq. Their exceptional supervision, guidance, and unwavering support have been invaluable throughout my doctoral journey. I am deeply grateful for their insights, ideas, and continuous encouragement, which significantly contributed to the development of my research and academic progress. I greatly appreciate their availability, sound advice, and the rigor they maintained while also understanding the challenges I faced during this work.

I would also like to express my sincere gratitude to my consultant, Dr. Rabab Benotsmane, for her valuable contributions and suggestions.

My sincere appreciation goes to my former supervisor, Angéla Váradiné Dr. Szarka, for giving me the opportunity to be accepted and for initiating my PhD journey.

To my husband, Mohammed Alqaradagi, my deepest thanks for his unlimited help, support, and the strength he has given me. His patience and encouragement have been invaluable. I am also deeply grateful to my son, Elias Alqaradagi, who was a constant source of joy and motivation during this journey.

I wish to express my heartfelt thanks and deep gratitude to my parents, whose endless support and belief in me made this journey possible. My sincere thanks also extend to my brothers, sisters, and entire family for their constant encouragement and strength during this process.

To my friends and those I have not mentioned due to space constraints, please know that your support and contributions are deeply appreciated.

I am also grateful to the governments of Hungary and Iraq for enabling me to achieve my dreams.

Lastly, and most importantly, I give my deepest thanks to the Almighty for granting me the strength and perseverance to complete this journey.

Contents

List of Figures

List of Tables

Abbreviations

PV	Photovoltaic
PS	Partial Shading
P-V	Power-Voltage
BL	Bridge-Linked
HC	Honeycomb
SP	Series-Parallel
TCT	Total Cross-Tied
CdTe	Cadmium Telluride
CVP	Concentrated Photovoltaic
I-V	Current-Voltage
I_{sc}	Short-Circuit Current
PCE	Power Conversion Efficiency
Mono-SI	Monocrystalline Silicon
Poly-SI	Polycrystalline Silicon
TFSC	Thin-Film Solar Cells
ANN	Artificial Neural Network
ASB	Automatic Switch Block
ATCT	Algorithm-Based Total-Cross-Tied
BESS	Battery Energy Storage System
CDV	Cross Diagonal View
COA	Coyote Optimization Algorithm
DPRA	Dynamic Probabilistic Reconfiguration Algorithm
EAR	Electrical Array Reconfiguration
FLC	Fuzzy Logic Controller
FRA	Flow Regime Algorithm
FUT	Futoshiki Puzzle Technique
GA	Genetic Algorithm
GMPP	Global Maximum Power Point
HEES	Hybrid Electrical Energy Storage
HLLBE	Highest and Lowest Layer-Based Exchange
IT-2 AFLC	Asymmetrical Interval Type-2 Fuzzy Logic Control
KK	Ken-Ken
LS-TCT	Latin Square Total-Cross-Tied
MAA	Munkres Assignment Algorithm
MAPE	Mean Absolute Percentage Error
MOGEO	Multi-Objective Golden Eagle Optimizer
MOGWO	Multi-Objective Grey Wolf Optimizer
MPP	Maximum Power Point

MPA	Marine Predators Algorithm
MPPT	Maximum Power Point Tracking
MPTT	Maximum Power Transfer Tracking
MS-EC	Magic Square-Enhanced Configuration
MSV	Magic Square View
NB	Naïve Bayes
P&O	Perturb and Observe
PRM-FEC	Physical Relocation of Modules with Fixed Electrical Connection
PVG	Photovoltaic Generator
RM	Reconfiguration Method
RMSE	Root Mean Square Error
SB	Switching Block
SMO	Social Mimic Optimization
SSA	Salp Swarm Algorithm
SS	Skyscraper
WCA	Water Cycle Algorithm
WDO	Wind Driven Optimization
AC	Alternating Current
AM	Air Mass
ARD	Arduino
DC	Direct Current
I2C	Inter-Integrated Circuit
IDE	Integrated Development Environment
ICSP	In-Circuit Serial Programming
LCD	Liquid Crystal Display
LED	Light Emitting Diode
MHz	Megahertz
NC	Normally Closed
NO	Normally Open
PC	Personal Computer
PWM	Pulse Width Modulation
R3	Revision 3
UNO	Arduino UNO Board
USB	Universal Serial Bus
Demux	Demultiplexer
Mux	Multiplexer
PCU	Primary Controller Unit
P-V	Power-Voltage
SCU	Secondary Controller Unit
SISC	Solar Irradiance Sensor Cell
SPDT	Single Pole Double Throw

DR	Dynamic Reconfiguration
IE	Irradiance Equalization
IL	Layer Current
Im	Maximum Current
SBA	Switching Block Array
SW_T	Total Number of Switches
SBs	Switching Blocks
SN	Short–Narrow
LW	Long–Wide
SW	Short–Wide
LN	Long–Narrow
PSC	Partial Shading Conditions
SA	Switch Array
TCP	Temperature Coefficient of Power

Chapter 1. Introduction to PV Panels

1.1 Overview of Photovoltaic Systems

The escalating environmental concerns coupled with the ever-growing global energy demands have spurred a surge in interest towards renewable energy sources, with solar energy emerging as a leading contender [1]. Meanwhile, global climate change movements have galvanized political leaders into action. In response, the United Nations declared 2012 as the International Year of Sustainable Energy for All, establishing three goals to be achieved by 2030: improving energy efficiency, expanding the availability of renewable energy sources, and ensuring access to advanced energy services worldwide [2].

One way of exploiting solar energy is by using photovoltaic (PV) panels, which are designed to convert solar energy into electrical power. This process, known as the photoelectric effect, was first demonstrated by Charles Fritts in 1883 with the creation of the first PV cell, which had a power conversion efficiency (PCE) of only 1%, and he installed the first solar panels on a New York City rooftop in 1884, as shown in Figure 1.1 [3]. PV arrays represent a pivotal technology in this sustainable energy landscape, and with the rising need for clean and sustainable energy, they have garnered popularity and widespread applicability, positioning solar energy as a viable alternative to conventional energy sources [4].

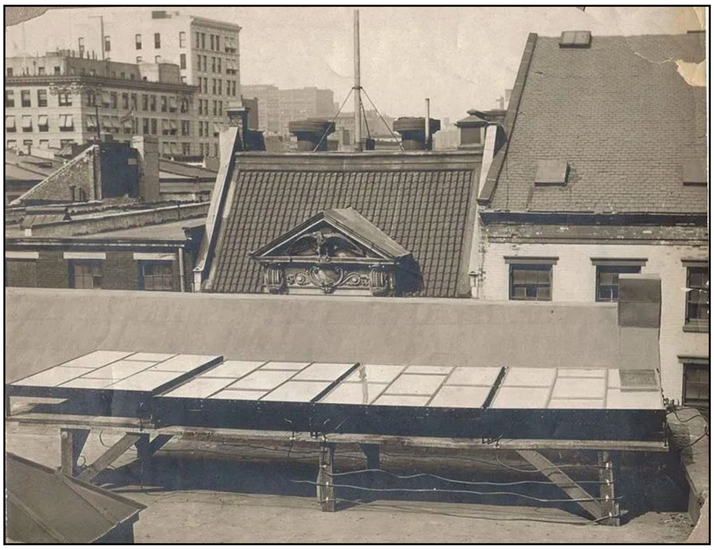

Figure 1.1: Charles Fritts' first solar panels installed on a New York City rooftop in 1884.

1.1.1 Classification and Operation of PV Systems

Photovoltaic systems are categorized into grid-connected and off-grid types. Grid-connected PV systems are attached to the electrical utility grid and utilize grid-tied inverters to convert direct current (DC) power into alternating current (AC) power suitable for the grid. These systems typically lack battery storage, which means they only generate power during daylight hours, but they can feed any surplus electricity back into the grid, making them economical and easy to operate [5],[6]. In contrast, off-grid PV systems incorporate batteries to store electricity for use when there is no sunlight, offering energy independence and making them ideal for remote locations. These systems are more complex and expensive due to the additional components required [7], [8]. Hybrid or grid-tied systems merge the attributes of both, featuring energy storage to supply power during both sunny and cloudy periods while remaining connected to the grid [5],[9]. PV systems are versatile and can be used for various purposes, including charging batteries, refrigeration, powering homes, pumping water, street lighting, hybrid vehicles, swimming pools, heating systems, telecommunications, satellite power, military space operations, and hydrogen production [10],[11]. The design and function of each PV system depend on its type, with grid-tied systems being simpler and less expensive, while off-grid systems provide greater independence but come at a higher cost.

A PV system consists of several solar panels, which are generally formed from a series combination of several solar cells. These cells are made from materials that generate electric current when exposed to light. When sunlight strikes the panel, it energizes electrons in the PV cells, causing them to move and produce electricity. The most used materials for PV devices are semiconductors, typically configured as p-n junctions [12]. Multiple cells are connected to meet the voltage and current demands of a load. Series-connected cells with an anti-parallel bypass diode create a module. Multiple solar panels are often combined to form even larger solar arrays that can generate significant amounts of power [13]. The stages from cell to array are illustrated in Figure 1.2.

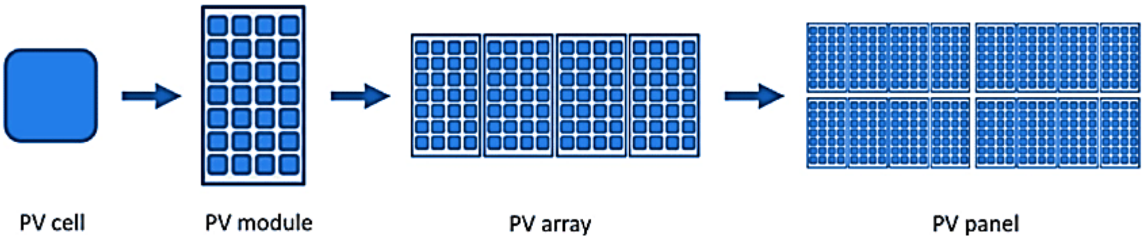

Figure 1.2: PV System from Cell to Array.

1.1.2 Types of Solar Panels

Differentiating between various types of solar panels typically involves distinguishing between single-junction and multi-junction panels, or categorizing them as first, second, or third generations. Single-junction and multi-junction panels vary based on the number of layers exposed to sunlight, while classification by generation focuses on the materials used and the efficiency of the different panel types [14].

A. First Generation Solar Panels [15]

Monocrystalline Solar Panels (Mono-SI) crafted from monocrystalline silicon represent the purest variant. They are distinguishable by their uniform dark appearance and rounded edges. Thanks to the high purity of silicon, these panels boost some of the highest efficiency rates, with recent models surpassing 20%. Monocrystalline panels offer a robust power output, occupy minimal space, and boost impressive longevity. However, their superior quality also translates to a higher price point. Additionally, they exhibit slightly less susceptibility to high temperatures compared to polycrystalline panels. Figure 1.3 illustrates the Monocrystalline panel.

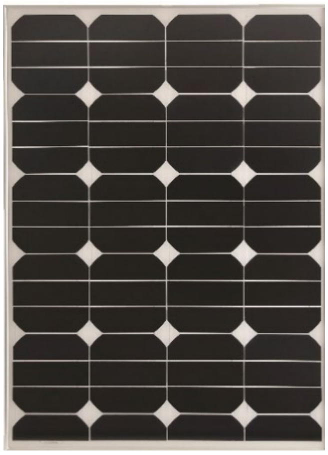

Figure 1.3: Monocrystalline panel.

Polycrystalline Solar Panels (Poly-SI) are easily identifiable by their characteristic square cells, uncut corners, and distinctive blue, speckled appearance. These panels are produced through a process of melting raw silicon, which is both quicker and more cost-effective compared to the manufacturing of monocrystalline panels. As a result, polycrystalline panels are more affordable, yet they tend to have lower efficiency rates, approximately around 15%. They also exhibit reduced spatial efficiency and have a comparatively shorter lifespan, primarily due to their higher sensitivity to temperature increases. Nonetheless, the performance disparities between monocrystalline and polycrystalline solar panels are relatively minor, and the selection between the two typically hinges on specific individual requirements. Monocrystalline panels, while slightly more space-efficient, come at a marginally increased cost, yet the power output of both panel types is generally equivalent. Figure 1.4 illustrates the polycrystalline panel.

Figure 1.4: Polycrystalline panel.

B. Second Generation Solar Panels [16]

Thin-Film Solar Cells (TFSC) present an economical alternative, leveraging the cost benefits of scaled production and reduced material requirements. These panels are fabricated by depositing one or more layers of photovoltaic substances, such as silicon, cadmium, or copper, onto a base material. Their ease of production and the lesser quantity of raw materials needed contribute to their affordability relative to other types. The inherent flexibility of thin-film panels not only broadens the scope for unconventional applications but also imparts a higher tolerance to thermal stress. The primary limitation, however, is their extensive spatial footprint, which typically renders them impractical for residential settings. Additionally, they are generally accompanied by shorter warranty periods due to their decreased longevity compared to monocrystalline and polycrystalline solar panels. Despite these drawbacks, thin-film solar panels are an attractive choice in scenarios where space constraints are minimal. Figure 1.5 illustrates the Thin-Film Solar Cells.

Figure 1.5: Thin-Film Solar Cells.

C. Third Generation Solar Panels

Cadmium Telluride (CdTe) photovoltaic cells represent a significant advancement in solar technology, offering a cost-effective alternative with a rapid energy payback period of less than one year. Among various solar technologies, CdTe cells are distinguished by their minimal water usage during production, aligning with sustainability goals by reducing the overall carbon footprint. However, the application of CdTe solar cells is met with challenges, particularly in Europe, due to the inherent toxicity of Cadmium Telluride when ingested or inhaled. Addressing these environmental and health concerns is paramount for broader acceptance and utilization of this promising solar energy technology. Figure 1.6 illustrates the Cadmium Telluride photovoltaic cells [14],[17].

Figure 1.6: Cadmium Telluride photovoltaic cells.

Concentrated PV Cell (CVP and HCVP) represent the pinnacle of photovoltaic efficiency, boosting an impressive rate of up to 41%, the highest among all solar panel technologies. These multi-junction cells harness the power of sunlight through the use of curved mirrors, lenses, and occasionally cooling systems to concentrate solar radiation, significantly enhancing their performance. The efficacy of CPV cells is contingent upon their orientation; they must be precisely aligned with the sun to achieve optimal efficiency. This is facilitated by an integrated solar tracker that ensures the panels maintain the perfect angle relative to the sun's position. Figure 1.7 illustrates the concentrated PV cells [16].

Figure 1.7: The Concentrated PV cells.

Table 1.1 provides a clear overview of different solar panel technologies, including their efficiency, advantages, and disadvantages [18].

Table 1.1: Overview of Solar Panel Technologies.

Solar Cell Type	**Efficiency Rate**	**Advantages**	**Disadvantages**
Monocrystalline Solar Panels (Mono-SI)	~20%	High efficiency; space-efficient; long lifespan.	Higher cost; performance can decrease in high temperatures.
Polycrystalline Solar Panels (p-Si)	~15%	Lower cost; less waste in manufacturing.	Lower efficiency; requires more space.
Thin-Film: Amorphous Silicon Solar Panels (A-SI)	~7-10%	Lightweight; flexible; aesthetically versatile.	Lower efficiency; shorter lifespan; requires more space
Concentrated PV Cell (CVP)	~41%	High efficiency in sunny areas; scalable.	Requires direct sunlight; high initial cost; large footprint.

1.1.3 Modeling of PV Cells

For modeling PV cells, the one, two, and three-diode models are the most used mathematical representations that detail the electrical conduct of a module [19]. Among these models, the one-diode model is preferred owing to its simplicity, ease of design, and the limited number of parameters involved. Figure 1.8 shows the equivalent circuit diagram of the one-diode PV model, in which the current I generated by the module is a function of the photogenerated current I_L, which is influenced by irradiance, temperature, and the number of PV cells connected in series. In a similar manner, the two-diode and three-diode models comprise two and three diodes, respectively. The current generated by the PV models can be estimated by applying Kirchhoff's Current Law to the equivalent circuit. The electrical behaviors are described by the following equation [20]:

$$I = I_L - I_D - I_{sh} \qquad (1)$$

$$I = I_L - I_0\left[exp\left(\frac{V + IR_s}{nV_T}\right) - 1\right] - \left(\frac{V + IR_s}{R_{sh}}\right) \qquad (2)$$

$$V_T = \frac{kT_c}{q} \qquad (3)$$

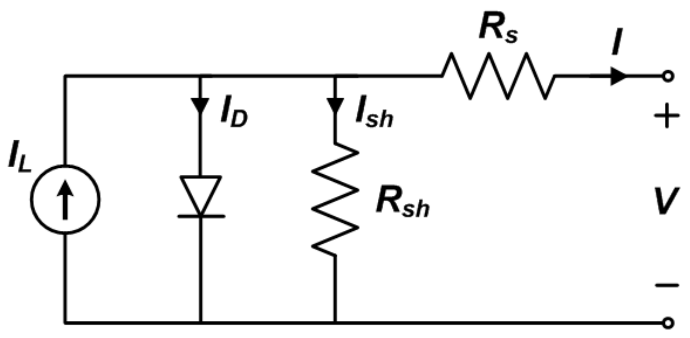

Figure 1.8: A PV cell is represented by a single diode.

where the parameters represent:

- I_L: Light-generated current in the cell (A)
- I_0: Diode reverse saturation current (A)
- R_s: Series resistance (Ω)
- R_{sh}: Shunt resistance (Ω)
- n: Diode ideality factor (unitless)
- V_T: Thermal voltage, calculated as $\frac{kT_c}{q}$, where:
    - k: Boltzmann's constant (1.38×10−231.38×10^{-23} J/K)
    - T: Temperature (K)
    - q: Elementary charge (1.6×10−191.6×10^{-19} C)

1.1.4 Challenges and Technological Advancements

Despite the importance of PV arrays in solar energy generation, their efficiency faces a formidable challenge in the form of partial shading (PS). This phenomenon, caused by factors such as passing clouds or nearby structures, ice, and snow disrupts uniform sunlight exposure across the array, leading to disparate power outputs among PV modules [21]. An example of this is illustrated in Figure 1.9.

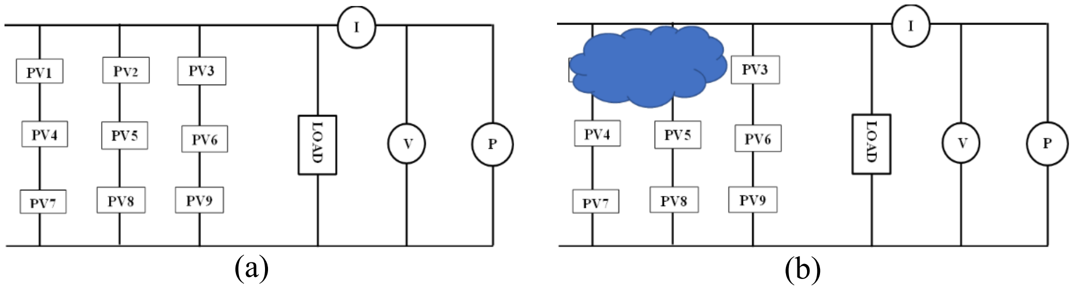

Figure 1.9: Example of a PV Panel in Full Sunlight (a) and Partial Shade (b).

These discrepancies result in a substantial reduction in overall energy harvest and highlight the limitations of traditional fixed-configuration PV systems. Additionally, PS causes some PV modules to receive less irradiance than others, altering their electrical characteristics. This variation among PV modules can significantly reduce the overall output power of the entire PV array and lead to the formation of localized hot spots [22], and some of the examples are shown in Figure 1.10 [23]. These hotspots affect the life of PV panels and may also cause permanent damage if they remain for a longer time [24].

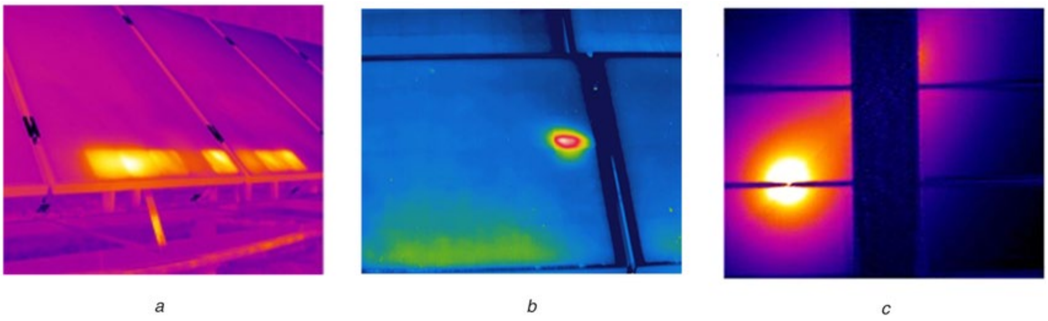

Figure 1.10: Hotspot in solar PV panels: (a) partial shadow, (b) damage cells, and (c) damaged gridline.

Bypass diodes play a critical role in protecting each PV module within an array. Typically connected across each module, these diodes prevent potential damage caused by shading or other operational issues. Bypass and blocking diodes used in the PV array under partial shading conditions are presented in Figure 1.11.

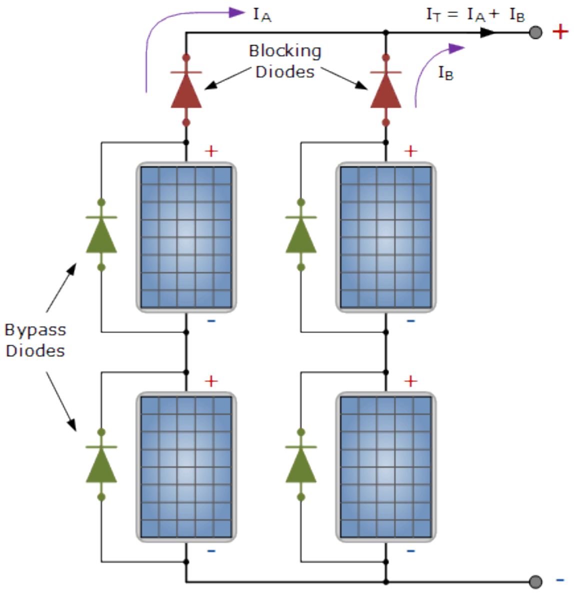

Figure 1.11: PV array with bypass and blocking diodes.

However, the implementation of bypass diodes introduces a phenomenon where multiple peaks appear in the Power-Voltage (P-V) characteristics of the PV array, as shown in Figure 1.12. This effect can impact the overall performance and efficiency of the system [25].

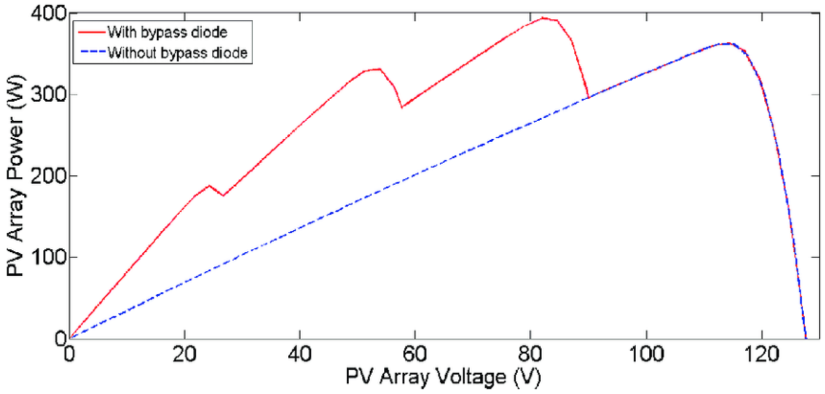

Figure 1.12: P-V characteristic curve with and without bypass diode.

The power loss caused by partial shading is not only related to the shading conditions but also to the interconnection mode of a PV array [26]. Common configurations include series-parallel (SP), total-cross-tied (TCT), bridge-linked (BL) and, honeycomb (HC) [27], as illustrated in Figure 1.13. In the SP configuration, modules are connected in series to increase voltage and in parallel to boost current, making it cost-effective and simple but less efficient under poor conditions [28]. The TCT configuration arranges modules with parallel rows tied to neighboring cells, ensuring consistent voltage and reducing the need for bypass diodes, which is beneficial for large-scale production [29]. The BL configuration features a bridge-rectifier style with multiple series connected in parallel and ties between the series, offering better performance in shaded conditions despite its complexity and higher switching device requirements [28],[30]. The HC configuration uses a hexagonal pattern resembling a honeycomb, with fewer series connections than SP, helping to reduce mismatching power losses [29].

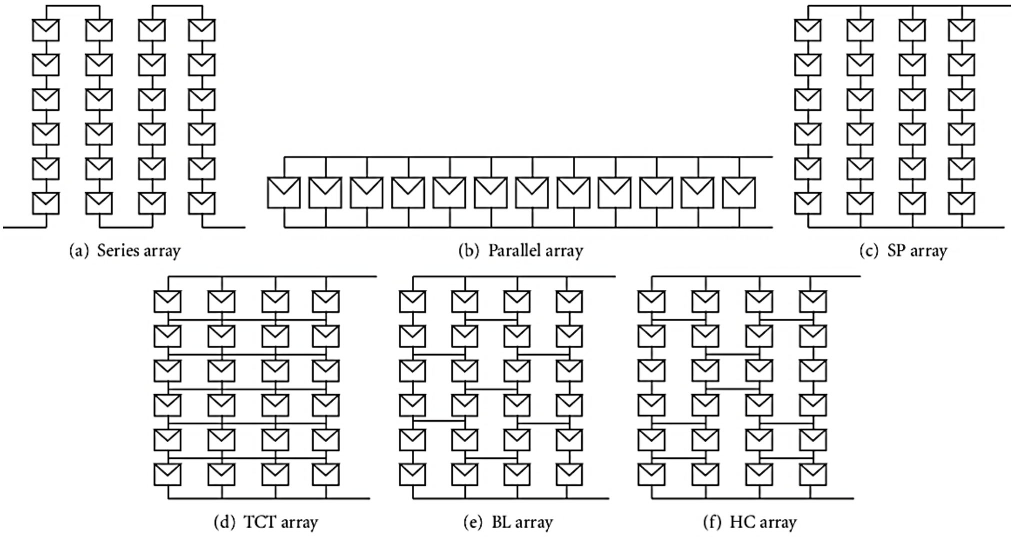

Figure 1.13: PV Array Configurations [30].

It has been found that the TCT topology can minimize mismatch losses and increase reliability better than other configurations [31][32]. However, despite reducing the mismatch loss to a certain extent, these interconnection schemes still fail to maximize the output power [33].

In order to compensate the power loss more effectively, PV array reconfiguration has been proposed. It reconfigures the interconnection of PV modules within the PV array according to the actual shadow conditions, so as to increase the maximum power to a higher level and minimize the influence of mismatch. PV array reconfiguration techniques can be classified as static and dynamic techniques [34],[35]. In static techniques, the physical location of the PV modules is changed according to some arrangements to distribute partial shading effects over the array. Compared with dynamic reconfiguration techniques, static reconfiguration techniques can save a large number of switches. However, they cannot adaptively find the optimal interconnection scheme under changes in the irradiance conditions, since the interconnection scheme is fixed. On the other hand, the more popular alternative are the dynamic reconfiguration techniques, in which the physical location of the modules in the PV array remains unchanged, and shade dispersion is achieved by dynamically changing the electrical interconnections of the PV modules.

Dynamic reconfiguration requires algorithms, controllers, switching matrix, and sensors that increase the complexity in the case of a large-scale PV system and the optimal solution may not be obtained within an acceptable time [36]. Therefore, heuristic algorithms have been applied to PV array reconfiguration. These reconfiguration techniques establish appropriate mathematical models for irradiance equalization, they can flexibly balance the irradiance of PV modules, but their large computational burdens are high and can increase as the PV array scales up [33].

1.2 Research Objectives

1. Develop a Hierarchical PV Array Structure: Design and implement a novel hierarchical photovoltaic (PV) array structure that integrates automatic switching capabilities to address performance losses due to partial shading.
2. Create and Implement a Reconfiguration Algorithm: Develop a custom reconfiguration algorithm capable of dynamically adjusting the electrical connections between individual PV panels to optimize energy harvesting efficiency under varying shading conditions.
3. Conduct Simulation Studies: Model the electrical behavior of the hierarchical PV array using simulation tools to assess its performance across different shading scenarios. Evaluate the effectiveness of the reconfiguration algorithm in maximizing energy production and minimizing energy loss through simulation results.
4. Validation through Experimental Studies: Perform experimental validation of simulation results by measuring key performance metrics such as power production and system response time to shading changes. This will involve setting up the hierarchical

photovoltaic array in a controlled environment and systematically introducing shading conditions to monitor and record the system's adaptive behavior.

5. Monitor Environmental Conditions: Integrate a network of sensors to monitor key environmental conditions, including solar irradiance levels and PV cell temperature. This will ensure accurate data collection and support the evaluation of the reconfiguration algorithm's performance.
6. Optimize Design and Operational Strategies: Refine the hierarchical PV array design and its operational strategies to enhance reliability, complexity, scalability, maximize power output, and cost-effectiveness, aiming for improved efficiency in real-world solar energy systems.

1.3 Thesis Outline

This thesis is organized as follows: Chapter 1 provides an introduction to the research, outlining the objectives and significance of photovoltaic (PV) technology in renewable energy, with a focus on challenges like partial shading and temperature effects. Chapter 2 reviews PV array reconfiguration techniques, categorizing and examining fixed, dynamic, and adaptive reconfiguration methods used to mitigate shading impacts. Chapter 3 covers the design and implementation of the proposed PV system, including the integration of switching blocks, Solar Irradiance Sensor Cells (SISCs), temperature sensors, and optimization algorithms. Chapter 4 introduces the highest and lowest layer-based exchange (HLLBE) algorithm for improving energy output under partial shading, with results from experimental and simulation analysis. Chapter 5 presents a scalable hierarchical model for PV array reconfiguration that uses real-time irradiance data to adjust system configurations dynamically. Chapter 6 details the development of a scalable dynamic reconfiguration system with hierarchical switching blocks, enhancing maximum power point tracking through real-time data application. Chapter 7 introduces the dynamic probabilistic reconfiguration algorithm (DPRA) to improve PV system performance under shading and temperature variations with minimal switching, supported by experimental and simulation validation. Finally, Chapter 8 summarizes the research contributions, including advancements in scalable dynamic reconfiguration models and algorithms for improving PV system efficiency and adaptability.

Chapter 2. Literature Review on PV Array Reconfiguration Techniques

2.1 Introduction

Photovoltaic arrays are essential in harnessing solar energy, but their efficiency can be significantly hindered by shading conditions. Various techniques have been developed to address this issue, aiming to optimize power output and enhance overall system performance. This literature review explores the different reconfiguration techniques employed to improve PV array efficiency under partial shading conditions. The review is organized into three main categories: fixed/static reconfiguration, dynamic reconfiguration, and adaptive reconfiguration. Each category is examined for its methodologies, advantages, and limitations, with a focus on how these approaches can address the challenges posed by shading.

2.2 Overview of Reconfiguration Techniques

Enhancing power output from a PV array under PS conditions can be achieved by adjusting the array's configuration through either electrical or physical changes [37]. Reconfiguration strategies are categorized into two main types: electrical array reconfiguration and special, known as fixed or static, array reconfiguration. Electrical array reconfiguration (EAR) schemes address energy losses caused by shading by using switches to modify the electrical connections between PV modules, thereby altering the array's layout [38]. This method encompasses Adaptive and Dynamic array Reconfigurations [39]. Figure 2.1 shows the PV array reconfiguration categories [40].

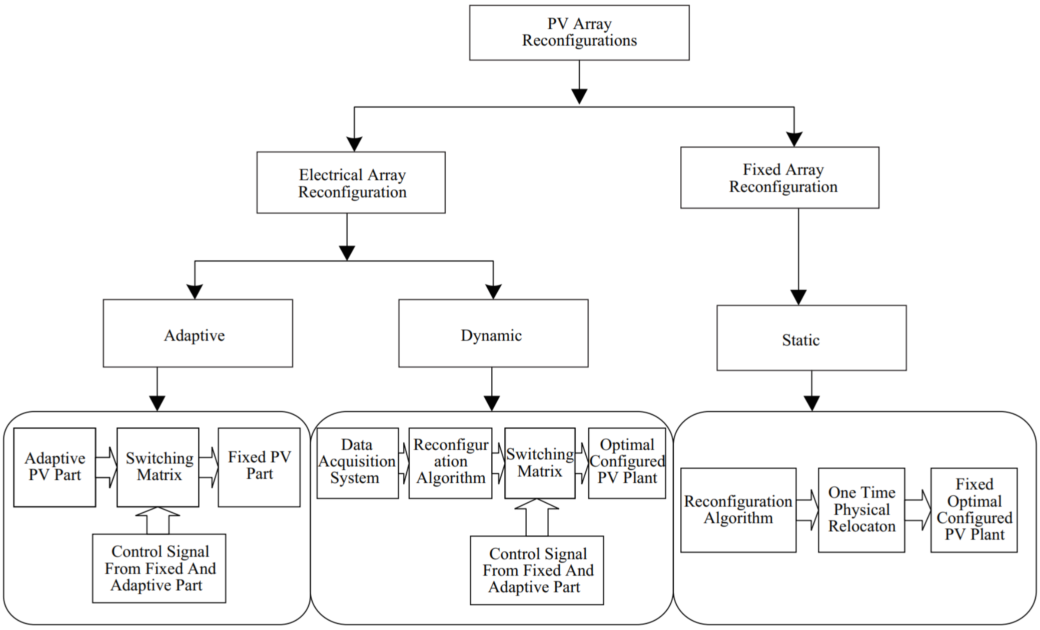

Figure 2.1: Categories of PV Array Reconfiguration.

2.2.1 Fixed/ Static Array Reconfiguration

This approach involves rearranging the physical placements of the PV modules within the array while keeping the electrical connections fixed. Static techniques do not require additional sensors or switching devices, thus simplifying the controller's design. However, because the interconnection scheme is fixed, these methods cannot dynamically adjust to optimize performance in response to changing irradiance conditions. Several static reconfiguration methods have been developed, each offering a unique set of benefits and drawbacks.

A. TCT configuration

In [41], a novel TCT configuration was proposed by modifying the SP arrangement. Each row of junctions is connected with cross ties, with modules in a row connected in parallel and those in a column connected in series. A comprehensive study in [42] analyzed various configurations, including series, parallel, SP, BL, HC, and TCT, under twenty different shading patterns. The results indicated that while TCT generally outperformed other configurations, its performance varied depending on the shading pattern. Specifically, BL and HC configurations outperformed TCT in certain scenarios, and SP was occasionally the most effective for mitigating PS effects.

B. Static Reconfiguration Strategy

A static reconfiguration strategy discussed in [43] involved redistributing shading effects across a 5×5 PV array, resulting in a power output increase from 192.6 W to 245.7 W under one shading pattern, and from 266.4 W to 280.2 W under another, improving the utilization factor from 0.76 to 0.96 and from 0.92 to 0.97, respectively. This approach effectively mitigated mismatch losses and improved power output, although its scalability for larger arrays requires further investigation. In [40] reviewed static reconfiguration techniques such as Sudoku, Optimal Sudoku, Magic Square, Zigzag, and Skyscraper, noting that the Skyscraper method showed superior performance by reducing shading impacts and improving efficiency, although specific quantitative improvements were not detailed.

C. Sudoku and Optimal Sudoku technique

The Optimal Sudoku reconfiguration technique, presented in [44], involved a 9×9 TCT array. MATLAB-Simulink simulations demonstrated a 13.9% increase in maximum power output compared to standard Sudoku patterns, alongside improved efficiency and reduced mismatch losses. The optimal Sudoku configuration achieved an average Global Maximum Power Point (GMPP) increase of 7.03% over TCT and 5.2% over standard Sudoku configurations in [45], highlighting its effectiveness in mitigating shading effects. The physical location of the modules was changed using the Sudoku reconfiguration technique, without affecting the electrical connections between them. Figure 2.2 (c) shows the reconfiguration of the PV array for the Sudoku configuration [46].

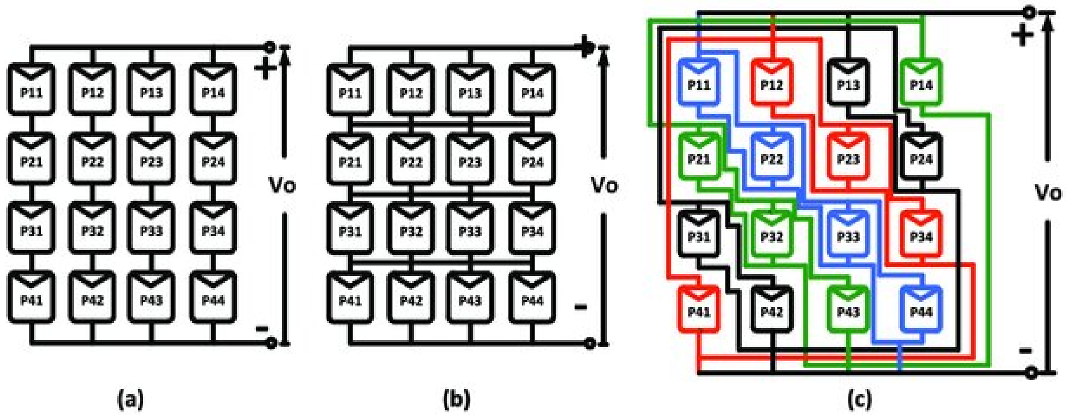

Figure 2.2: Configurations of a 4×4 PV Array: (a) SP, (b) TCT, (c) Sudoku Puzzle Pattern.

D. Latin Square TCT (LS-TCT) Configuration

The LS-TCT configuration presented in [47] used an LS puzzle to optimize PV module placement, achieving up to 27.11% better power efficiency and reducing power losses by up to 1787 W compared to traditional methods, though it involved complex modeling.

E. Magic Square Configuration

The Magic Square View (MSV) configuration, as detailed in [48], arranges PV modules using a Magic Square pattern and achieves a maximum power output of 4146.01 W. This represents a 25.04% increase over the TCT configuration's output of 3099.98 W, and a 6.38% improvement compared to the Sudoku method's output of 3890.47 W, thus demonstrating the MSV's effectiveness in enhancing power generation under shading conditions. Further advancements were seen with the Magic Square-Enhanced Configuration (MS-EC), discussed in [49], which showed a notable power output improvement ranging from 27.72% to 31.13% over the traditional TCT configuration under various shading scenarios. The MS-EC approach consistently outperformed other reconfiguration methods, such as Futoshiki and Physical Relocation of Modules with Fixed Electrical Connection (PRM-FEC), underscoring its superior performance in optimizing PV array efficiency and mitigating shading effects.

F. Zig-Zag Scheme

The Zig-Zag scheme, introduced in [50], improved the global maximum power point from 362.9 W to 466 W under specific shading conditions, reduced power loss from 45.67% to 30.23%, and lowered mismatch loss from 20.43% to 5.0%, with the fill factor increasing from 38.98% to 59.91%. This method showed substantial performance improvements across various shading scenarios, though scalability for large-scale systems requires further investigation.

G. Ken-Ken (KK) and Skyscraper (SS) Configurations

Evaluated Ken-Ken (KK) and Skyscraper (SS) configurations for a 4×4 array in [51], finding that both methods delivered up to 46.9% higher GMPP compared to TCT under vertical shading and improved mismatch loss and fill factor under horizontal shading, though real-world testing is still needed. The KK puzzle-based reconfiguration method in [52] achieved a 10.85% performance enhancement over TCT and other configurations, simplifying complexity and improving dependability. Additional SS configuration in [53] enhanced global maximum power output by 3.5% to 44.5% compared to traditional methods and improved efficiency, despite challenges with method complexity and slower response time.

H. Knight Configuration

In [46], a new PV array configuration based on Knight's chess movement was proposed to mitigate PS effects. This method, which is applicable to both squared and non-squared arrays, redistributes the PV modules to evenly spread shading. The proposed configuration achieved significantly lower mismatch losses (20%) and higher power outputs (up to 2802.4 W) compared to the traditional TCT and Sudoku layouts, which showed mismatch losses of 34% and 47%, respectively. This innovative approach enhances efficiency and reduces power losses under various shading conditions. For more Knight's tour technique was proposed for optimizing PV array performance under PS conditions are presented in [54]. This method, inspired by the chess knight movement, rearranges PV modules to evenly distribute shading and enhance power output. When applied to square and rectangular PV arrays, Knight's tour outperformed traditional configurations such as TCT and Sudoku in various shading scenarios. It achieved higher global maximum power points and efficiency, with values of up to 109.8 I_mV_m and efficiency reaching 9.81%, while also showing lower mismatch losses (as low as 1.88%). The results suggest that Knight's tour method is a promising approach for improving the PV array performance in real-world applications.

I. Futoshiki puzzle technique

In [55], a novel static reconfiguration method for PV arrays based on the Futoshiki puzzle technique is presented. This approach involves rearranging the physical positions of PV modules within a grid without altering the electrical connections, using a puzzle format where each row and column must contain unique numbers from 1 to m. By redistributing the PV modules, the Futoshiki technique effectively disperses shading across the entire array, mitigating power losses and maintaining consistent voltage and current outputs. Implemented in a 5 × 5 PV array configuration, as shown in Figure 2.3 (b), the Futoshiki technique demonstrated superior performance over traditional TCT setups, significantly reducing mismatch losses under PS conditions. This method highlights the potential of using puzzle-based reconfiguration strategies to enhance the efficiency and reliability of PV systems under varying irradiance levels.

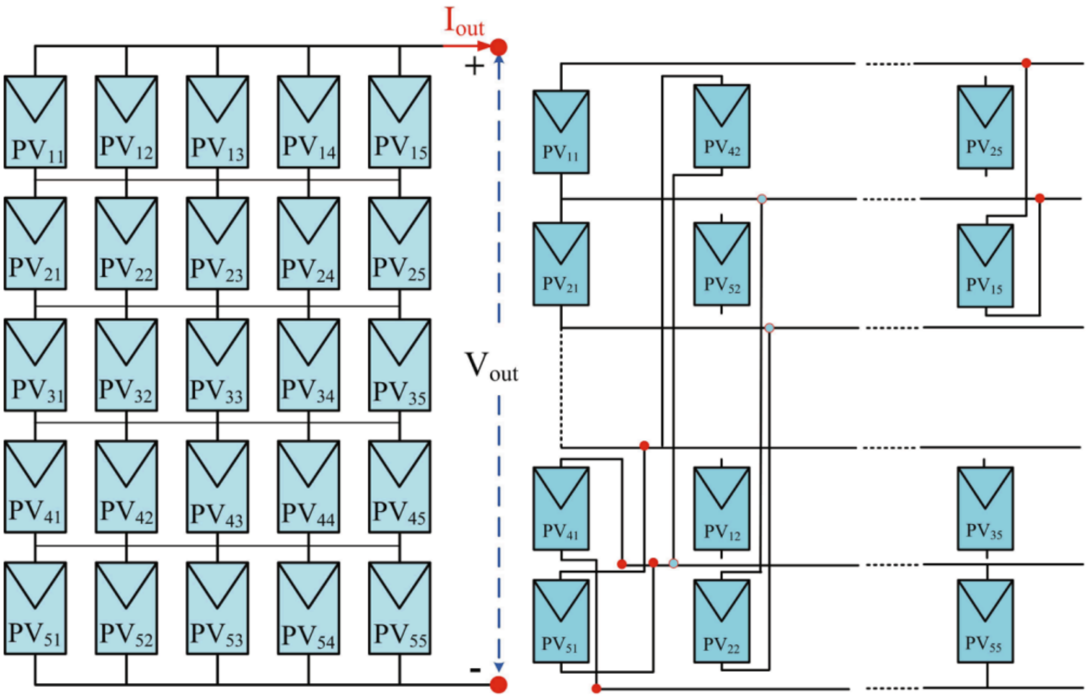

(a) (b)

Figure 2.3: (a) TCT configuration, (b) Futoshiki-based reconfigured pattern [40].

J. Other Techniques

In [56], a mathematical model based on the Eight Queens Problem was proposed to optimize the reconfiguration process of PV arrays by minimizing the number of state switches. This model significantly reduces the frequency of switching operations, which is critical for decreasing switching losses and extending the lifespan of switches. By efficiently solving the switching matrix and employing an optimized solution algorithm, this approach enhances both the reliability and efficiency of the PV system's reconfiguration. The reduction in the number of switches not only lowers operational costs but also improves overall system performance, highlighting the effectiveness of mathematical optimization in PV array management.

2.2.2 Electrical Array Reconfiguration

Electric array reconfiguration is a method used to restore the energy production in PV plants affected by PS by altering the layout through switches [38]. They can be divided into dynamic and adaptive array reconfigurations [39].

2.2.1.1 Dynamic Reconfiguration Techniques

This approach involves adjusting the electrical connections between PV modules to optimize performance without changing their physical layout. These techniques aim to handle changes in shading and irradiance conditions more effectively, significantly enhancing power output. However, they introduce complexity through the need for sophisticated algorithms, controllers, and switching systems. Several dynamic methods have been proposed to improve the handling of PS in PV array modules.

A. Switching Mechanisms

Switching mechanisms involve using switches to dynamically reconfigure PV arrays, thereby improving performance under PS. A notable study introduced an Automatic Switch Block (ASB) system that dynamically adjusts PV connections using relays, enhancing maximum power point tracking (MPPT) by up to 30% compared to traditional configurations [57]. Additionally, the L-shaped propagated array configuration presented in [58] offers superior performance in managing complex shading conditions. In [59], switching mechanisms integrated into the array configuration significantly increased power output from 2.646 W to 5.59 W under PS, compared to 3.71 W achieved by bypass diodes alone. An automatic dynamic reconfiguration system with modular Automatic Switching Blocks (ASB) also demonstrated stable output voltage within 5% of the maximum value across various shading conditions, though it introduced voltage and power losses due to diodes [60].Furthermore, the study in [61] introduced a novel dynamic reconfiguration strategy using direct power evaluation and a switching matrix optimized with the "Eight Queens Problem," which reduces switching operations to one-third compared to traditional methods, thereby lowering power loss. Figure 2.4 illustrates how a switching matrix modifies the connections between PV modules to disperse shade. The effectiveness of switch-based reconfiguration is further highlighted in [62], which reported an 11.82% to 73.56% increase in power output across different shading scenarios.

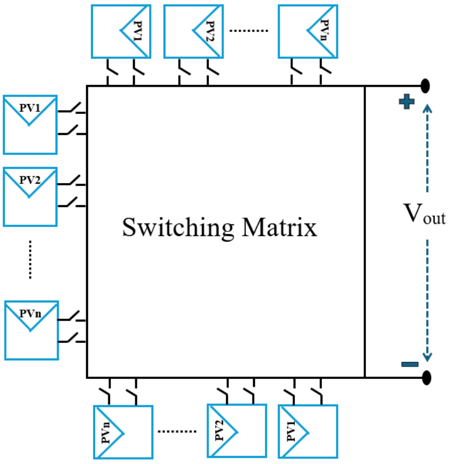

Figure 2.4: PV Array Configured with a Switching Matrix.

B. Heuristic Algorithms

Heuristic algorithms are employed to optimize PV array configurations by leveraging algorithms inspired by natural phenomena or computational models. In [63], a Genetic Algorithm (GA) optimizes PV array connections, increasing power output by up to 34.96% over TCT and 15.18% over Sudoku under PS, despite challenges with computational complexity and shading sensitivity. Similarly, [64] uses a GA for PV array reconfiguration with auxiliary modules, reducing connector switches by 35% and boosting power output by up to 56% under PS compared to TCT, Sudoku, and Step-Wise configurations, with superior performance in diagonal and triangular shadow patterns. The Salp Swarm Algorithm (SSA) has been used for maximum power point tracking in PV systems, achieving around 99% average efficiency and outperforming traditional methods such as hill-climbing (HC) [65]. Another study highlighted the Wind Driven Optimization (WDO) algorithm's superior performance with a tracking efficiency of 99.44% and a low root mean square error (RMSE) of 6.9 compared to other optimization techniques [66]. A Multi-Objective Grey Wolf Optimizer (MOGWO) approach solved multi-peak issues in power-voltage characteristics and achieved power enhancements ranging from 9.4% to 18.8% compared to TCT configurations [67]. The chimp optimization algorithm is applied in [68] for a hybrid MPPT technique, which reported a steady-state MPPT efficiency of 99.54% under non-uniform irradiance conditions, while [69] explores Flow Regime Algorithm (FRA), Social Mimic Optimization (SMO), and Rao Optimization also showed significant improvements, with up to 28.333% increase in power output compared to TCT. Additionally, a PV generator (PVG) rated at 1,621 kW, evaluated in [70], utilized a DC-DC boost converter for MPPT and achieved approximately 99% efficiency, demonstrating its effectiveness in diverse conditions. In [71], the Water Cycle Algorithm (WCA) is proposed to reduce power losses due to PS and minimize the irradiance level mismatch index by producing an optimal PV array reconfiguration. This approach is noted for its faster execution time compared to TCT for addressing similar issues.

C. Reconfiguration Algorithms

Reconfiguration algorithms focus on dynamically adjusting PV array configurations to maximize power output under varying shading conditions. For instance, a novel approach based on direct power evaluation achieved up to 33.4% higher power output compared to traditional irradiance equalization methods [72]. Another study employing a TCT configuration and an Incremental Conductance (INC) algorithm increased power output from 2482 watts to 3102 watts [73]. Enhanced dynamic array reconfiguration (DAR) utilizing current injection (CI) improved power outputs by 20.8% under various shading scenarios [74]. The Maximum–Minimum Tier Equalization Swapping (MMTES) algorithm demonstrated significant performance gains over TCT, improving efficiency and reducing mismatch losses [75]. Additionally, the dynamic reconfiguration method proposed in [76] achieved a percentage power loss (PPL) of 33.2% and mismatch loss of 23.64%, compared to 39.8% and 41.7% for TCT and Sudoku, respectively. Other methods include the optical dielectric circuit in [77], which boosts PV array efficiency under PS by 25.26%, compared to traditional configurations. This system isolates specific modules and optimizes power voltage, providing a scalable and cost-effective solution. The Pelican Optimization Algorithm (POA) achieved up to a 30% reduction in switch actions while maintaining or improving power output [78]. A novel method with a snake-like arrangement increased energy output compared to conventional configurations, though it involved higher initial costs [79]. Finally, highlighted a method that reduces the number of switches and sensors using GA and a switching matrix, optimizing system efficiency [80].

D. Hybrid Approaches

Hybrid Approaches integrate multiple techniques to enhance PV system performance. Integrating PV array reconfiguration with a Battery Energy Storage System (BESS) and using the Multi-Objective Golden Eagle Optimizer (MOGEO) achieves up to a 10.07% increase in PV station profit and a 67.69% reduction in power deviation [81]. The integration of simulated annealing and genetic algorithms achieved up to 22.04% improvement in maximum power point (MPP) compared to SP and Cross Diagonal View (CDV) methods [82]. A fuzzy logic controller (FLC) improved power output by 44% compared to traditional methods under quasi-equalization shading patterns [83]. The TCT-Switch Capacitor (TCT-SC) approach also exemplifies a hybrid strategy by combining TCT with a switch capacitor to balance charge across modules, achieving up to 17.33% more power and 97% conversion efficiency, with a generation of 17.08kW in 9x9 arrays [84]. Additionally, a novel MPPT algorithm detects the boost converter's conduction mode and adjusts the perturb and observe (P&O) method, accordingly, significantly improving efficiency and accuracy [85]. An optocoupler-based circuit enhances PV efficiency by identifying and isolating power from bypassed modules, achieving 14.8% to 66.2% more power than traditional methods, with experimental gains of 28.7% and 48.8% [86].

E. Neural Network Approaches

Neural network approaches utilize machine learning for optimizing PV array reconfiguration. One study demonstrated an up to an 11% power improvement through optimized reconfiguration using neural networks [87]. Another study presents an artificial neural networks (ANN)-based system that achieves 95% average test accuracy, outperforming k-nearest neighbors (K-NN), support vector machines, and Naïve Bayes (NB) in accuracy, precision, recall, and f-measure [88]. This system also reduces the mean absolute percentage error (MAPE) but does not consider cost. Future research should focus on integrating cost-efficiency into the optimization process.

2.2.1.2 Adaptive Reconfiguration Techniques

Adaptive techniques involve dividing the array into two sections: fixed and adaptive [89]. As shown in Figure 2.5, these techniques aim to optimize power output, particularly under conditions like PS. The adaptive section can be dynamically reconfigured using a switching matrix and controller to balance row irradiation. This approach reduces the number of required switching devices and sensors. Several methods have been proposed to enhance the management of PS in PV array modules.

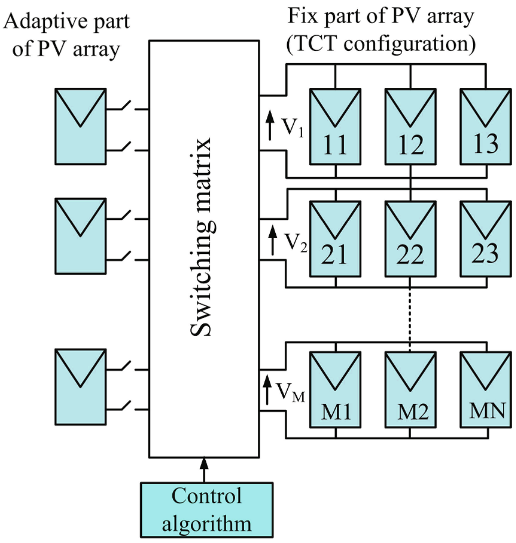

Figure 2.5 : Depicts the execution of the adaptive array reconfiguration [89].

A. Algorithmic Optimization

Algorithmic optimization techniques for PV arrays leverage advanced computational methods to enhance performance. For instance, the TCT layout combined with the Munkres Assignment Algorithm (MAA) significantly boosts power and voltage output, improving from 298.08 W to 474.8 W and 26.7 V to 77.56 V, respectively [90]. The Coyote Optimization Algorithm (COA) has shown superior results in maximizing global power, achieving up to a 26.58% increase in power output under various shading conditions [91]. Genetic algorithms also enhance performance by optimizing configurations with minimal sensors and reducing energy loss, achieving rate improvements from 6.49% to 71.03% across different shading scenarios [92]. Similarly, the Marine Predators Algorithm (MPA) improves power output by 28.6%, 2.7%, and 5.7% for various array configurations [93]. However, these methods are sometimes constrained by fixed switching strategies, necessitating further refinement of dynamic switching operations. Future work should focus on enhancing algorithm flexibility and adapting to real-time conditions.

B. Control Strategies

Control strategies for PV arrays utilize advanced techniques to maximize energy efficiency. The Incremental Conductance MPPT combined with a switch matrix achieves a substantial power increase from 2482 Watts to 3102 Watts post-reconfiguration [94]. Asymmetrical Interval Type-2 Fuzzy Logic Control (IT-2 AFLC) surpasses traditional methods, achieving up to 1028 W under PS with improved efficiency and reduced mismatch losses [95]. The Adaptive Neuro-Fuzzy Inference System (ANFIS) also demonstrates effectiveness in Maximum Power Point Tracking, with varied outputs across different configurations, although it becomes complex for larger arrays [96]. While these methods offer significant performance improvements, they often require complex implementation and tuning. Future research should aim to simplify control strategies and improve real-time adaptability.

C. Hybrid Methods

Hybrid methods integrate various approaches to enhance PV array performance. The combination of Hybrid Electrical Energy Storage (HEES) extended Maximum Power Transfer Tracking (MPTT), and dynamic reconfiguration boosts efficiency by 17.1% to 53.3% compared to baseline systems [97]. Similarly, optimizing reconfiguration with battery backup has shown significant reductions in power loss, ranging from 9.32% to 42.30%, and improved efficiency [98]. These methods, though effective, involve increased system complexity and costs. Future work should explore more cost-effective and simplified hybrid solutions.

D. Dynamic Reconfiguration

Dynamic reconfiguration techniques adapt PV arrays to changing irradiance conditions to optimize power output. A dynamic reconfiguration algorithm, simulated with MATLAB/Simulink, improved power output by 4.7% to 6.1% across various shading scenarios [99]. A module-level reconfiguration method demonstrated a 17.68% efficiency increase, achieving power output improvements from 188.3 W to 221.6 W without measuring irradiance profiles [100]. Additionally, a partial reconfiguration approach can enhance power output by up to 45% compared to static systems, achieving comparable results to full reconfiguration with reduced losses [101]. The main challenge is real-time implementation complexity. Future research should focus on refining reconfiguration algorithms for better efficiency and real-world applicability.

E. Neural Networks

Neural network-based approaches for PV array optimization involve using advanced learning algorithms to improve power production. A neural network method achieved a 12% average power gain and a 16.02% increase in Maximum Power Point after reconfiguring to TCT [102]. While this approach provides high classification accuracy and significant power gains, it may become complex and less effective with larger arrays. Future work should focus on enhancing network adaptability and scalability.

F. Innovative Topologies

Innovative topologies utilize novel circuit designs and configurations to enhance the performance of PV arrays, particularly under PS. For example, a new system employing undercurrent and overvoltage relays effectively increases output power by optimizing current flow in shaded panels [103]. The reconfiguration method (RM) demonstrated superior performance, achieving peak powers of 5.04 kW and 5.21 kW for different PV technologies [104]. The Algorithm-based Total-Cross-Tied (ATCT) method was introduced to enhance PV module performance under PS, achieving up to a 42.6 W power increase in 4×4 arrays and up to 13.27% improvement in performance ratio [105]. These innovative methods effectively boost power output and performance compared to conventional and novel TCT configurations. Future research should focus on simplifying these topologies and exploring their scalability in larger PV systems.

2.2 Problem Statement

The efficiency of solar PV systems is frequently compromised by PS, which significantly reduces energy output. Shading effects can originate from various sources, such as clouds, nearby buildings, trees, or even dirt accumulation on the panels. Traditional PV array configurations—whether static, dynamic, or adaptive—struggle to fully mitigate these losses due to inherent limitations in each approach.

Therefore, static reconfiguration techniques involve arranging PV modules in a fixed electrical layout to distribute shading impacts more evenly across the array. Configurations such as TCT [41], Sudoku [44], and Magic Square [48] have been explored. While these methods can enhance power output by redistributing the impact of shading, they are constrained by their inability to adapt to real-time changes in shading patterns.

In contrast, dynamic reconfiguration techniques address some of these issues by utilizing switches and controllers to alter the electrical connections of the PV modules in response to shading. Methods like the ASB system [57] dynamically adjust connections to optimize power output. Additionally, heuristic algorithms such as GA [63] and the SSA [65] are employed to maximize energy capture. Despite their benefits, these solutions often involve high implementation costs, complex system designs, significant computational demands, and challenges in real-time operation due to the need for sophisticated control algorithms and additional hardware, especially as the PV array scales up. These challenges hinder their practical application.

Moreover, adaptive reconfiguration strategies attempt to bridge the gap by integrating aspects of both static and dynamic techniques [89]. These strategies dynamically adjust part of the array while keeping the rest static, aiming to optimize energy output under varying conditions. However, adaptive systems still face challenges such as high costs, increased complexity, and difficulties in scaling up for larger arrays.

Despite advancements in these areas, the challenge of efficiently managing PS remains significant. The complexity and cost associated with dynamic and adaptive methods, coupled with the static methods' inability to adapt in real-time, continue to limit the widespread adoption and efficiency of PV systems. Additionally, the integration of advanced algorithms and switching mechanisms requires careful consideration of operational reliability and cost-effectiveness.

These ongoing challenges highlight the need for innovative, cost-effective, and scalable reconfiguration strategies that can dynamically adapt to changing environmental conditions while maintaining or enhancing system efficiency. Addressing these issues is crucial for maximizing energy yield, improving efficiency, reducing complexity and cost, ensuring seamless scalability, and enhancing the reliability of solar PV systems, particularly as they become an increasingly integral part of the global energy mix.

2.3 Proposed Scheme

In this work, several innovative reconfiguration schemes for solar PV systems are proposed to enhance efficiency under PS conditions. The first proposed scheme, referred to as Model-A, introduces a hierarchical, controller-based dynamic system featuring switching blocks (SBs) that connect pairs of solar panels through relays. These SBs can switch connections between panels in series or parallel based on real-time shading conditions, allowing for seamless expansion and adaptation without requiring a complete system redesign. Each SB, comprising two relays controlled by a microcontroller, adjusts the connection type according to signals from a solar irradiance sensor cell (SISC). This enables the system to dynamically isolate shaded panels, preventing performance losses and potential damage, with decisions based on a pre-determined threshold value, such as 50% of the maximum generated power.

The second proposed scheme, referred to as Model-B, represents a significant advancement over the initially proposed system. This scheme features a more sophisticated and scalable architecture, employing switching blocks (SBs) organized into link blocks (LBs) to create a hierarchical structure. The controllers in this system manage the connections between panels and enable adaptation to shading conditions by utilizing real-time data from solar radiation sensors. The design of Model-B allows for straightforward scalability and flexibility, accommodating both symmetric and asymmetric configurations. This adaptability facilitates the integration of additional panels in various configurations, thereby enhancing the system's versatility. Furthermore, Model-B can emulate traditional configurations such as SP, BL, and TCT, in addition to replicating the Model-A configuration from the first proposal. This proposal seamlessly integrates conventional configurations with the newly developed dynamic configuration, providing a robust solution capable of easily adapting to diverse shading conditions. The flexibility and scalability of Model-B make it a highly effective system for optimizing PV array performance under varying environmental conditions.

The third proposed scheme leverages a dynamic probabilistic reconfiguration algorithm (DPRA) with a hierarchical switching array to optimize PV array performance under PS and temperature fluctuations. Organized into multiple layers of SBs, each uniquely specified according to its hierarchy, the DPRA assigns probability values to these layers, dynamically adjusting PV connections to track the maximum power point (MPP) based on current environmental data. Excluding fully parallel or series connections, DPRA limits configurations to six, simplifying optimization. In two stages, isolating shaded or overheated panels based on solar irradiance and temperature sensor data, then reintegrating them for optimized output—the system effectively maintains high efficiency. Key advantages include efficient MPP tracking, real-time adaptation, scalability, and enhanced reliability. This advanced scheme integrates traditional and dynamic configurations, ensuring optimal PV array efficiency and durability in diverse environmental conditions.

Additionally, the HLLBE (highest and lowest layer-based exchange) algorithm introduced in this section aims to optimize the radiation distribution across PV arrays by dynamically adjusting the positions of the panels according to sensor data. The algorithm employs mathematical equations to calculate the current output for each individual layer. It then reallocates the panels among the layers based on the detected solar radiation levels and the current generated by each PV panel under conditions of partial shading. This approach mitigates the adverse effects that shaded panels can have on the overall system performance by ensuring a more uniform distribution of current generation across the array. Consequently, it enhances energy production, reduces power losses, and facilitates effective system reconfiguration. The HLLBE algorithm provides a robust and practical solution for optimizing the efficiency and adaptability of PV systems, ensuring that they maintain high performance even under variable environmental conditions.

2.4 Summary

In this chapter, I give a general introduction and background on photovoltaic (PV) array reconfiguration techniques under partial shading conditions. I explore various methods employed to optimize PV array efficiency, including fixed/static, dynamic, and adaptive reconfiguration strategies, examining their methodologies, advantages, and limitations. Moreover, I identify the persistent challenges associated with partial shading, such as efficiency losses, complexity, cost, and scalability limitations in existing solutions. In response to these issues, I propose several innovative reconfiguration schemes, including a scalable hierarchical switching block architecture, dynamic probabilistic reconfiguration algorithms, and the HLLBE algorithm. These proposed methods aim to enhance energy yield, improve efficiency, reduce complexity and cost, ensure seamless scalability, and increase the reliability of solar PV systems under partial shading conditions.

Chapter 3. System Design, Research Methodology, and Implementation

3.1 Introduction

This chapter delves into the core components and methodologies employed in this study to optimize solar energy systems under partial shading conditions. It provides a comprehensive overview of the hardware and software elements—including photovoltaic (PV) panels, microcontrollers, and data acquisition systems—that are crucial for monitoring and control of the PV system. The research methodology is divided into practical (experimental) and simulation tracks. The practical aspect focuses on data acquisition, monitoring, and control through tailored algorithms to manage shading patterns. It involves the design and development of a hardware system to acquire, process, and analyze data from the PV array. The software component enables dynamic adjustment of the PV array configuration to mitigate the impact of shading. On the other hand, the computer simulation uses MATLAB Simulink to model and assess the performance of the system under various conditions, especially partial shading. This simulation provides a virtual environment to evaluate the system's behavior and effectiveness in mitigating shading effects. By integrating practical experimentation with computer simulation, this study aims to develop a robust and efficient solution for optimizing solar energy systems, even in challenging environmental conditions.

3.2 System Design

The system design is centered around the integration of hardware and software components to dynamically reconfigure a solar array, as depicted in Figure 3.1. This design focuses on optimizing the performance and efficiency of the PV system by addressing non-uniform partial shading through adaptive mechanisms, thereby maximizing energy production under varying shading conditions. A detailed overview of each component is provided in **Appendix A**.

The integration of components in this system involves the seamless connection of the PV array, microcontrollers, sensors, communication modules, and relays to ensure cohesive and efficient operation. The PV array's output is continuously monitored by microcontrollers, which process data from various sensors, including the solar irradiance sensing cells and voltage/current sensors. This data is utilized to dynamically adjust system performance, optimizing energy production and utilization. ZigBee communication modules enable the wireless transmission of data to a central PC for monitoring and analysis. Additionally, relays are employed to control high-power devices based on commands from the microcontrollers, ensuring precise and safe operation. Software tools play a crucial role in this integrated system. The Arduino Integrated Development Environment (IDE) is used for programming the microcontrollers, allowing for the implementation of complex algorithms and control logic. XCTU software is employed for configuring the ZigBee communication modules, facilitating reliable and efficient wireless communication. These tools ensure precise control and monitoring, contributing to the system's overall efficiency and reliability under varying operational conditions. This integrated approach not only enhances system performance but also provides a scalable solution for advanced PV system management.

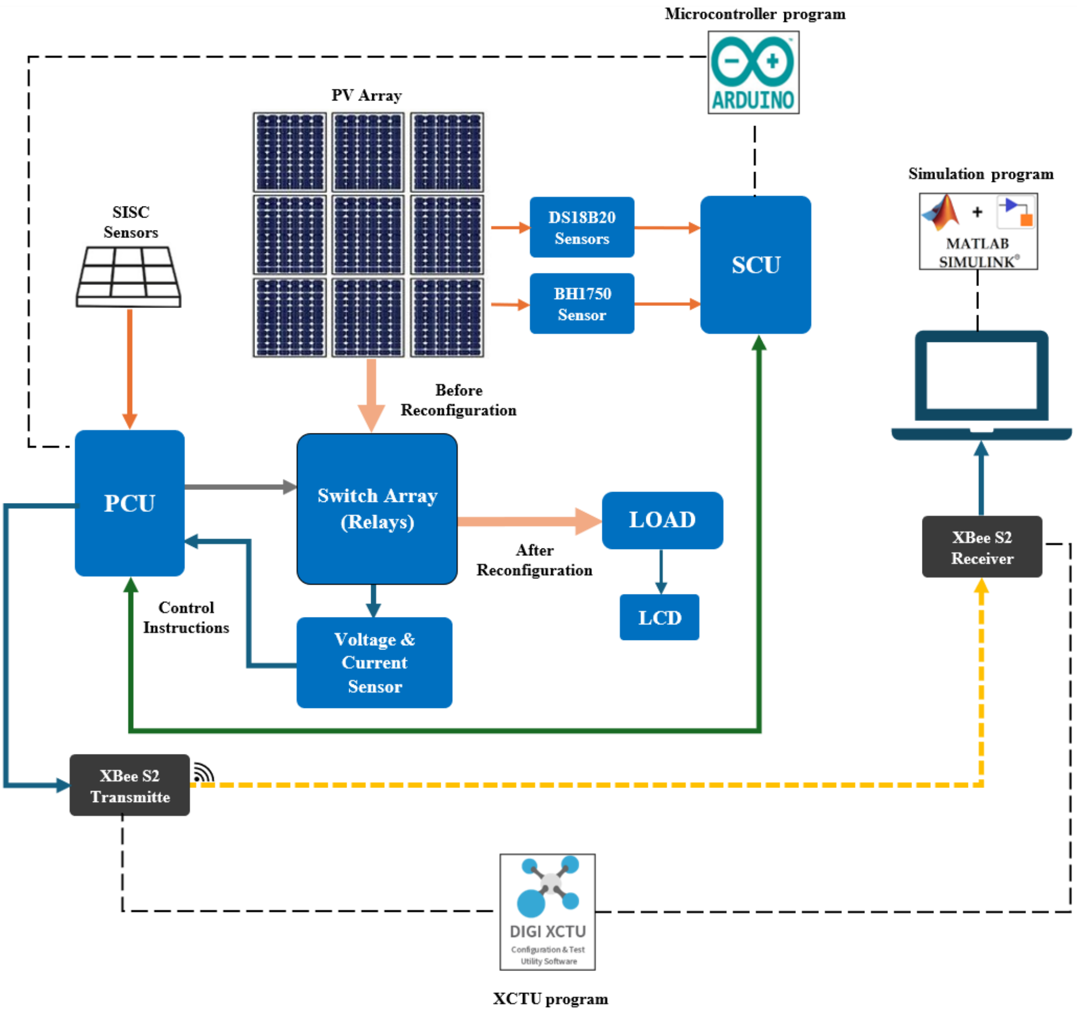

Figure 3.1: The block diagram of the system design.

3.3 Research Methodology

This section outlines the research methodology employed in the design, implementation, and testing the proposed PV system. The methodology was structured to ensure that the same system was implemented and evaluated in both practical and theoretical (simulation) environments, allowing direct and fair comparison of the results and insights.

A. **Computer Simulation:** The theoretical implementation involved simulating the same PV system using MATLAB Simulink. The simulation replicated the design, configuration, and operational strategies used in both the hardware and software components of the practical setup. By modeling the system's behavior under various conditions, the simulation allows for testing different configurations and scenarios, providing insights into the system's potential performance, scalability, and adaptability without the constraints of physical hardware. The simulation also included dynamic adjustments for shading patterns and environmental conditions, ensuring consistency with the practical implementation.

B. Practical Implementation: The practical implementation involved both the hardware and software components of the proposed PV system.

- **Hardware Implementation**: This included the physical construction and testing of the PV system using actual hardware components, such as solar panels, sensors, relays, and microcontrollers. The hardware setup was designed to mirror the system's configuration in the simulation as closely as possible, ensuring consistency across both implementation methods. The practical hardware implementation aimed to evaluate the system's real-world performance, focusing on optimizing power output, managing shading patterns, and maintaining efficiency under varying environmental conditions. Real-time data acquisition and monitoring tools were integrated to track system behavior, enabling analysis of the system's adaptability to changes in solar irradiance and temperature.

- **Software Implementation**: In parallel with the hardware, the practical implementation also involved the development and deployment of software components necessary for the system's operation. This included the programming of microcontrollers, development of control algorithms, and implementation of data monitoring and logging systems. The software was designed to manage the dynamic configuration of the PV array, optimize power output, and ensure real-time response to environmental changes such as shading and temperature fluctuations. The software implementation was closely aligned with the simulation models to ensure that the control logic and data handling processes were consistent between the practical and theoretical setups.

By implementing the proposed system in both practical and simulation environments, the methodology ensures that the insights gained from each approach complement and validate one another, providing a robust foundation for analyzing the system's overall performance.

3.4 Computer Simulation

3.4.1 Introduction

The simulation aims to design and analyze a PV array system to evaluate its performance under varying conditions. Simulations are crucial as they enable testing different configurations and predicting system behavior without incurring the costs and time associated with real-world experiments. These simulations complement physical implementation by identifying potential issues and optimizing designs beforehand, leading to more efficient and reliable systems. MATLAB/Simulink was selected for this study due to its robust modeling and analysis capabilities, providing an accurate platform to simulate complex PV systems and assess their efficiency under different environmental factors.

The primary emphasis of the simulation is on modeling and analyzing the performance of nine PV panels, each replicating real-world characteristics such as power output, efficiency, and responses to varying irradiance and temperature, with specifications detailed in Table A.1. The panels are configured and interconnected to simulate their collective operation, ensuring that the arrangement reflects practical applications. Additionally, the simulation includes an environmental impact analysis, examining how critical factors like solar irradiance (ranging from 200 W/m^2 to 1000 W/m^2) and temperature (ranging from 15°C to 45°C) influence overall system performance. Understanding these effects is vital for optimizing the design.

The system's architecture follows a hierarchical design structure, allowing flexible arrangements of PV panels in groups at different levels, enhancing dependability, adaptability, and scalability. The simulation also incorporates resistive loads to assess system performance under typical operating conditions, laying the foundation for exploring more complex load types in future studies. Conducted using MATLAB R2023b with Simulink on a PC running Windows 11, the simulation ensures real-time capabilities with detailed modeling, supporting accurate and flexible simulations for potential expansions and modifications.

3.4.2 Comparison of Two PV Models

In the simulation of a PV system, two distinct models, Model-A and Model-B, were developed and analyzed. Model-A was both simulated and implemented in real-world conditions, whereas Model-B was only simulated. Despite sharing the same operational principles, both utilizing switching blocks (SBs) for reconfiguration and following hierarchical structures, the primary difference between these models lies in the arrangement of the SBs and solar panels.

Model-A features a configuration where every two solar panels share one SB, as shown in Figure 3.2 (A). Each SB controls its associated solar panels, allowing flexible configurations to optimize power output based on environmental conditions and load requirements. The hierarchical structure of Model-A ensures that the system can be easily scaled and modified.

On the other hand, Model-B introduces a more advanced configuration, where every three solar panels share two SBs. This arrangement offers more complex reconfiguration options compared to Model-A. Specifically, pairs of stages are connected to two SBs, forming a larger unit known as a Link Block (LB). These LBs are further interconnected, creating a comprehensive hierarchical structure, as illustrated in Figure 3.2 (B).

Both models utilize eight SBs and sixteen relays, balancing complexity and component requirements. However, Model-B offers enhanced flexibility and reconfiguration capabilities, enabling more sophisticated operational modes. Model-B can replicate traditional PV configurations such as Series-Parallel (SP), Bridge-Linked (BL), and Total Cross-Tied (TCT) by integrating additional switches between the basic LB modules, as shown in Figure 3.3 This flexibility allows Model-B to seamlessly adapt to different configurations, meeting specific operational requirements with greater efficiency.

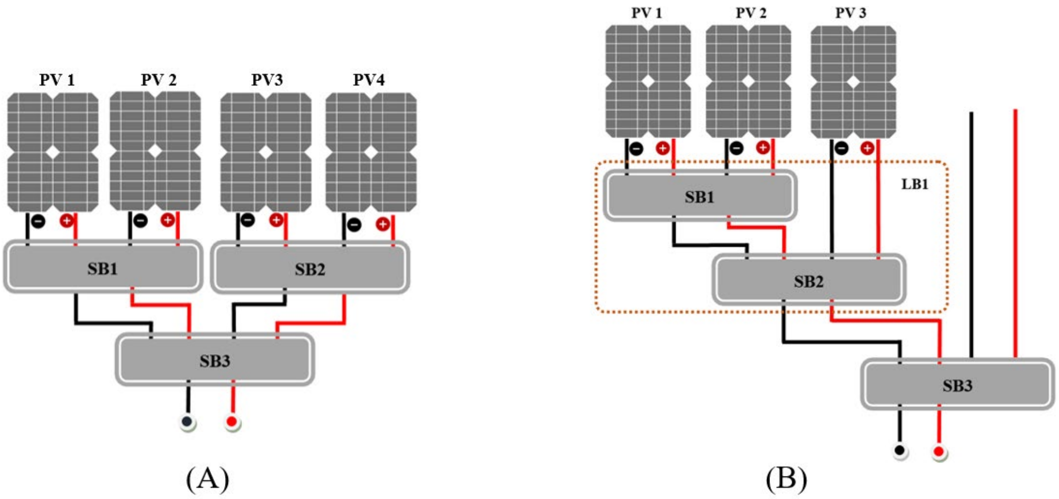

Figure 3.2: SB structures (A) Model-A and (B) Model-B.

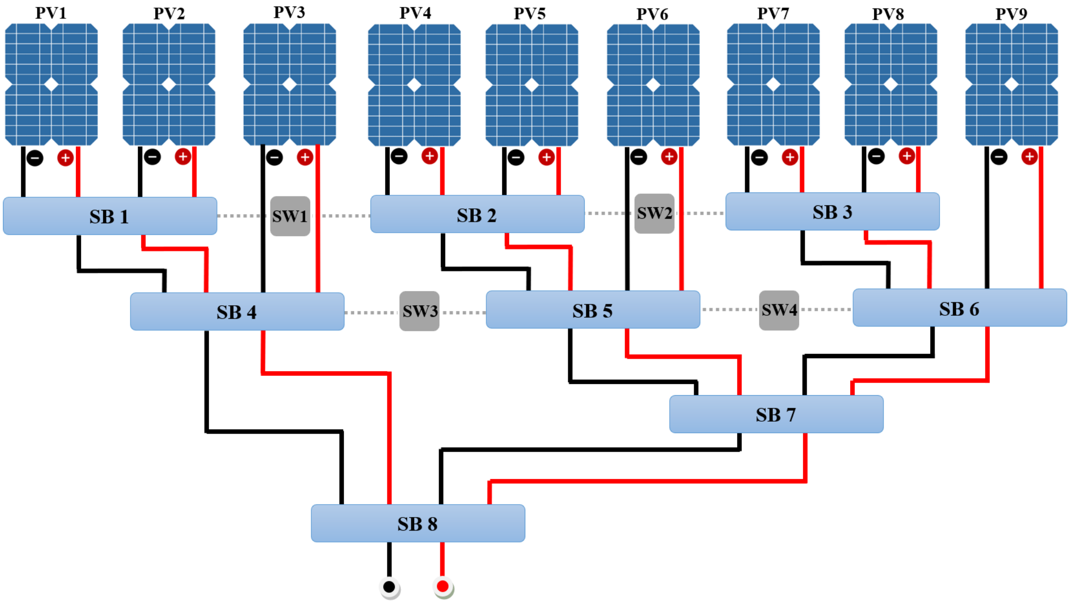

Figure 3.3: Configurable operational modes with switches in Model-B.

The primary advantage of Model-B lies in its ability to dynamically replicate multiple conventional configurations using switch blocks and LB modules. Additionally, Model-B can replicate the operation of Model-A with similar efficiency and accuracy. This versatility enhances the system's flexibility and allows for better utilization of solar panels under varying conditions. The ability to switch between SP, BL, and TCT modes ensures that the system is optimized for maximum power output, reliability, and performance.

In summary, the design and simulation of these two PV system models provide valuable insights into the reconfiguration capabilities and operational efficiencies of hierarchical PV systems. Model-A's practical implementation demonstrates a straightforward and effective design, while Model-B offers advanced reconfiguration options, showcasing its potential for more versatile and efficient PV system operation. The strategic integration of switches in Model-B underscores the importance of flexible design in optimizing solar power systems.

3.4.3 Simulated System Design

The PV array system consists of multiple interconnected components designed to simulate the behavior and performance of nine PV panels using MATLAB/Simulink. The design incorporates several critical subsystems, each meticulously detailed to ensure accurate and efficient simulation of the entire system. These subsystems include the PV panel array, SBs, MPPT, load, and monitoring tools.

A. PV Panel Array Modules (Subsystem)

The PV panel array subsystem is designed to accurately simulate the electrical behavior of solar panels using a single-diode equivalent circuit. This model incorporates essential parameters such as short-circuit current (I_{sc}), open-circuit voltage (V_{oc}), maximum power point, series and parallel resistance, and temperature coefficients, which are crucial for representing the electrical characteristics of each PV panel and the overall array. The subsystem also dynamically adjusts environmental inputs like temperature and irradiance to reflect real-world conditions, as these factors directly influence the panel's output. Specifically, temperature impacts the open-circuit voltage, while irradiance affects the short-circuit current. By integrating these variables, the model effectively captures the nonlinear I-V (current-voltage) and P-V (power-voltage) characteristics of the PV panels, which are essential for accurate performance prediction under varying climatic conditions. This setup enables detailed performance analysis and optimization of the PV array. Figure 3.4 illustrates the module parameters for a single PV panel, whereas Figure 3.5 provides a visual representation of the internal structure of the PV panel subsystem within Simulink.

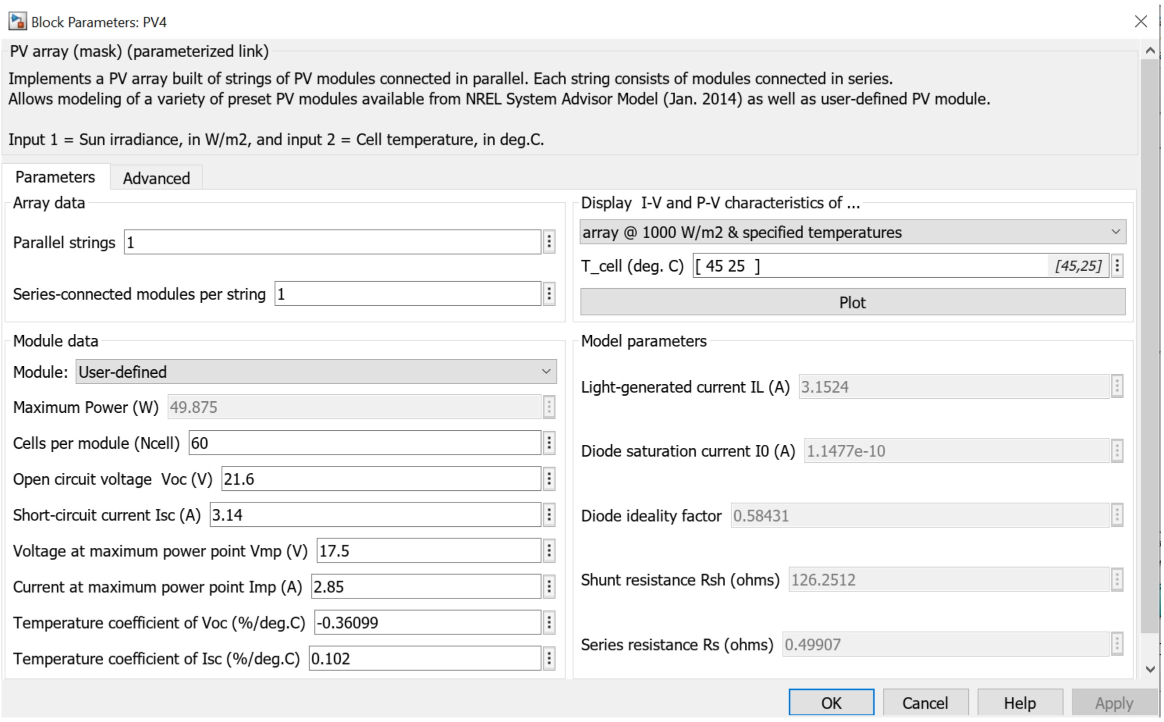

Block Parameters: PV4

PV array (mask) (parameterized link)

Implements a PV array built of strings of PV modules connected in parallel. Each string consists of modules connected in series.
Allows modeling of a variety of preset PV modules available from NREL System Advisor Model (Jan. 2014) as well as user-defined PV module.

Input 1 = Sun irradiance, in W/m2, and input 2 = Cell temperature, in deg.C.

Array data
Parallel strings: 1
Series-connected modules per string: 1

Display I-V and P-V characteristics of ...: array @ 1000 W/m2 & specified temperatures
T_cell (deg. C): [45 25] [45,25]

Module data
Module: User-defined
Maximum Power (W): 49.875
Cells per module (Ncell): 60
Open circuit voltage Voc (V): 21.6
Short-circuit current Isc (A): 3.14
Voltage at maximum power point Vmp (V): 17.5
Current at maximum power point Imp (A): 2.85
Temperature coefficient of Voc (%/deg.C): -0.36099
Temperature coefficient of Isc (%/deg.C): 0.102

Model parameters
Light-generated current IL (A): 3.1524
Diode saturation current I0 (A): 1.1477e-10
Diode ideality factor: 0.58431
Shunt resistance Rsh (ohms): 126.2512
Series resistance Rs (ohms): 0.49907

Figure 3.4: Module parameter for a single PV panel.

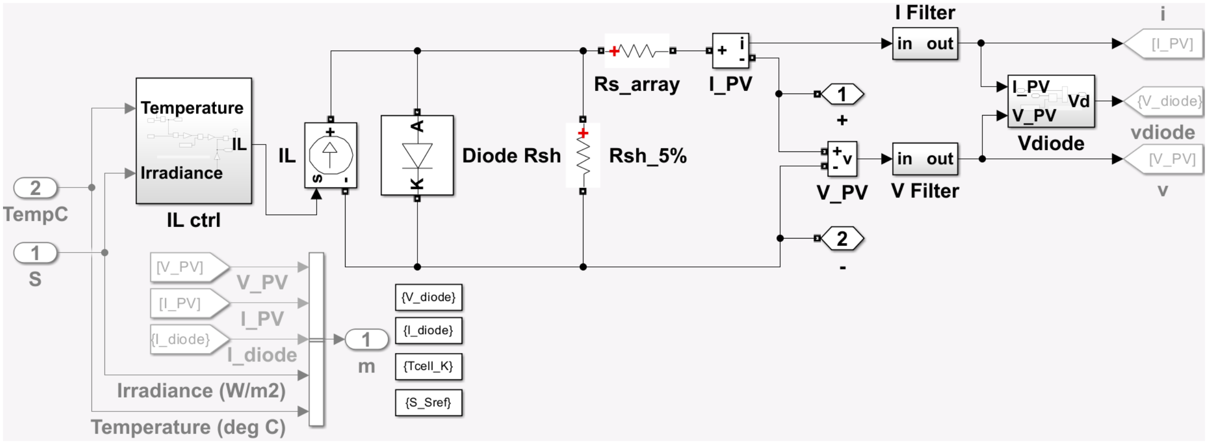

Figure 3.5: The underlying structure of the PV panel subsystem in Simulink.

B. Switching Block (SB) Subsystem Design

The SB subsystem is designed using ideal switches in MATLAB/Simulink to replicate the behavior of real-word relays, aligning with practical implementations. Ideal switches are fundamental components used in models that require switching actions, such as control systems, power electronics, and PV arrays. Figure 3.6 shows the internal structure of the ideal switch model in Simulink.

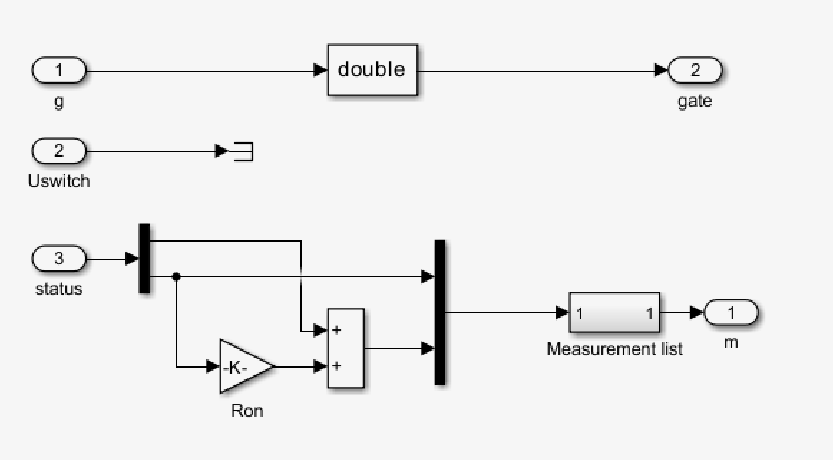

Figure 3.6: Internal components of the ideal switch Simulink model.

To simulate the switching block, two ideal switches were configured to form a Single Pole Double Throw (SPDT) relay. These switches are controlled by logic signals, allowing for dynamic switching actions within the system. Figure 3.7 illustrates the SPDT relay configuration using ideal switches.

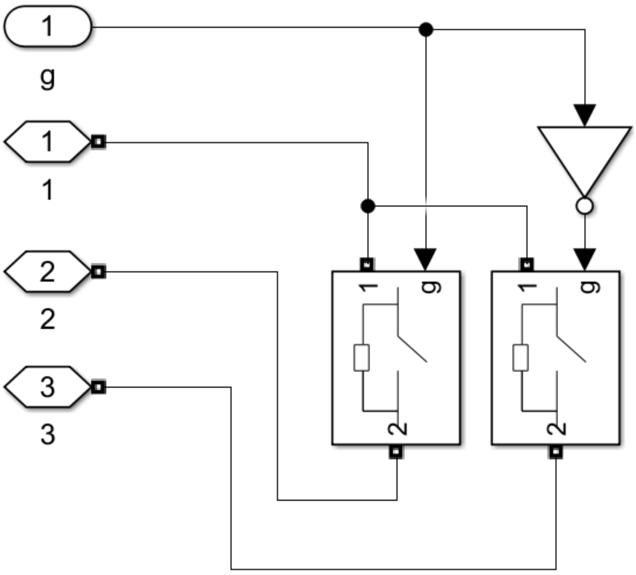

Figure 3.7: Logic-controlled SPDT relay design using ideal switches.

This design approach ensures that the switching mechanism closely mirrors the behavior of a physical relay, providing accurate simulation results. The SPDT relay type was chosen for its ability to switch between two circuits, offering versatile control within the system. The ideal switches in the model are triggered by operational logic signals, which dictate the switching actions based on the system's requirements. This setup facilitates the integration of switching blocks into the larger PV system, enabling dynamic control and reconfiguration of connections as needed. Figure 3.8 depicts the arrangement and control logic of the SPDT relay in the system.

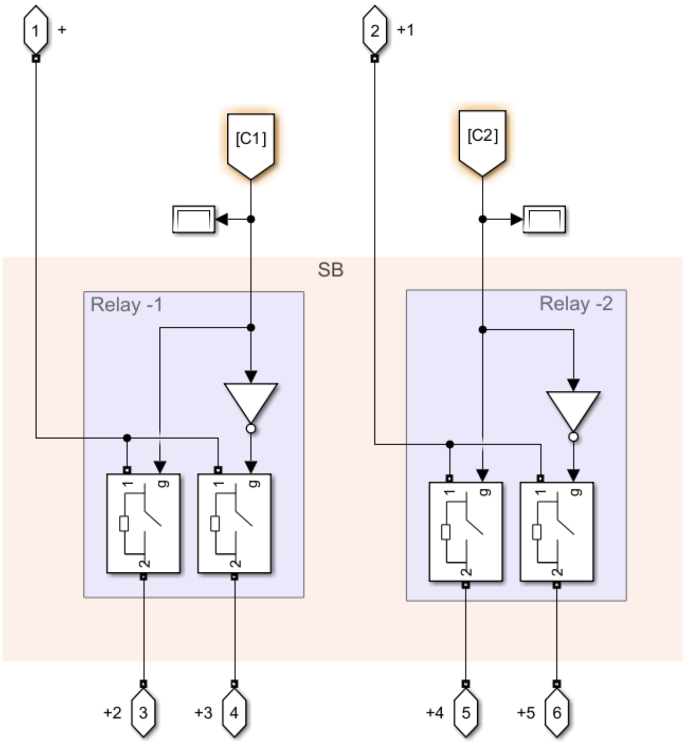

Figure 3.8: The ideal switch arrangement for SPDT relay in SB.

C. Load Subsystem Design

The load subsystem simulates the electrical load in a PV system, modeling energy consumption by various devices connected to the PV array. It uses dynamically adjustable resistors controlled by logic gate signals via ideal switches. Figure 3.9 shows the schematic of this setup, including the switches and logic gates.

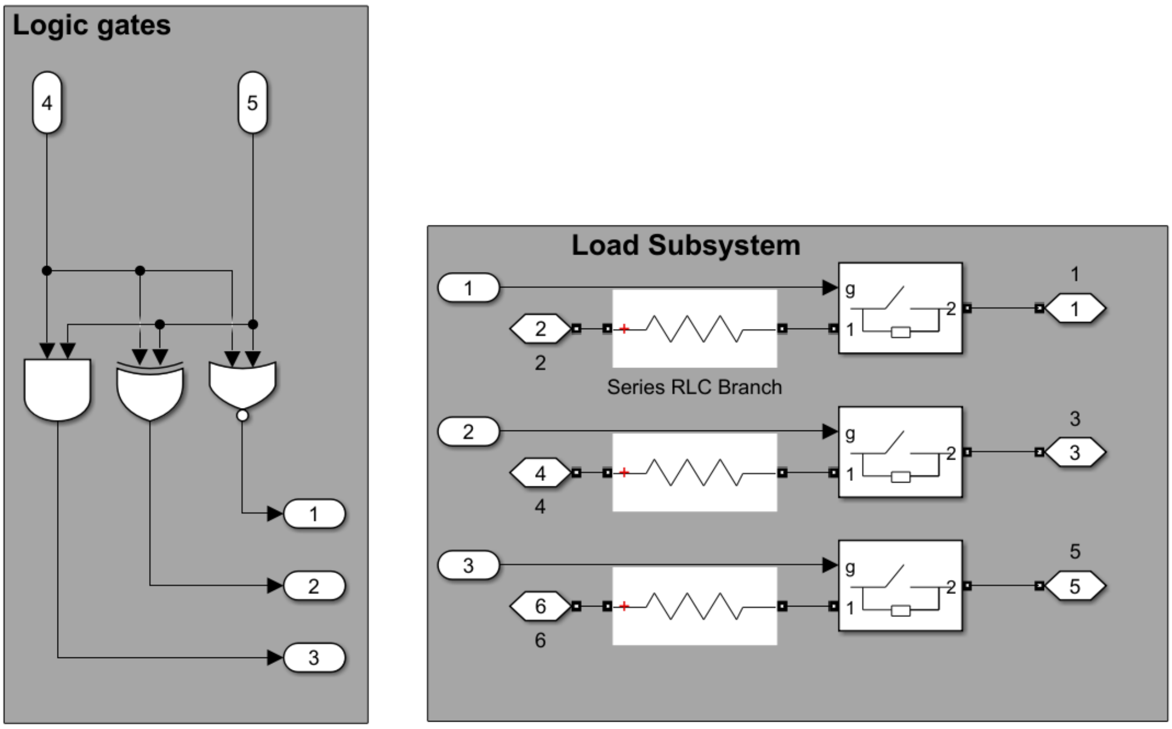

Figure 3.9: Schematic representation of load subsystem.

This design allows the load subsystem to mimic real-world energy consumption patterns, adjusting resistance based on PV output. This approach ensures realistic simulation of operating conditions, enabling accurate evaluation of system performance and efficiency.

D. Monitoring Tools Subsystem

The monitoring tools subsystem is designed to provide real-time data and insights into the performance of the PV system. It includes various sensors and data acquisition components that measure and record key parameters such as voltage, current, and power output. These components are integrated with a user-friendly interface for real-time monitoring and detailed analysis. Voltage and current sensors are strategically placed throughout the system, particularly at the output of each SB, using high-precision sensors to capture comprehensive data. Power calculations are performed using a product block that multiplies voltage and current measurements, delivering real-time power data. Figure 3.10 illustrates the structure of the monitoring tools subsystem.

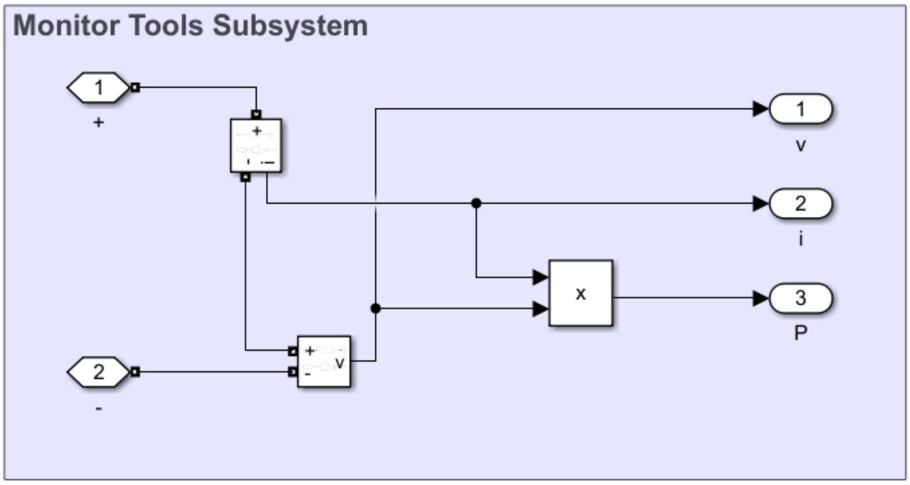

Figure 3.10: Structure of the monitoring tools subsystem.

3.4.4 Designing Simulation Environments for the Proposed System

This section explores two distinct simulation approaches for the proposed PV system. The first approach focuses on a simulation environment utilizing MATLAB Function Blocks within Simulink without involving any hardware integration. The second approach discusses a hybrid simulation environment integrating Simulink with Arduino for real-time control and monitoring.

The key objective of both approaches is to model and simulate the PV system's operation while emphasizing accuracy, operational efficiency, and flexibility. The first approach, centered on MATLAB Function Blocks, allows for detailed analysis of the system's behavior through custom algorithms and control strategies, optimizing performance in a purely software-based setup. The second approach leverages real-time hardware integration, enabling dynamic testing and validation under varying conditions, which enhances the system's performance and adaptability.

3.4.4.1 Simulation with Simulink Function Blocks

The design and implementation of a PV system simulation environment using MATLAB/Simulink is centered on MATLAB Function Blocks for real-time control and data processing. This setup facilitates dynamic analysis of the PV system's behavior under varying conditions, enabling performance optimization and adaptability. By leveraging customized algorithms and control strategies, the environment enhances flexibility and improves system performance across diverse scenarios.

A. System Architecture Overview

The proposed system architecture comprises several key components, each fulfilling a specific role in the data processing pipeline. The primary components include constant blocks to simulate input values, a multiplexer (Mux) block to aggregate these inputs, a MATLAB Function Block for core processing, a demultiplexer (Demux) block to distribute the processed outputs, and display blocks for visualization. This modular architecture ensures clarity, scalability, and ease of maintenance, allowing for easy adjustments and updates as system requirements evolve. Figure 3.11 demonstrates the integration of the MATLAB Function Block with the Mux and Demux blocks, depicting how input values are combined, processed, and distributed as control signals.

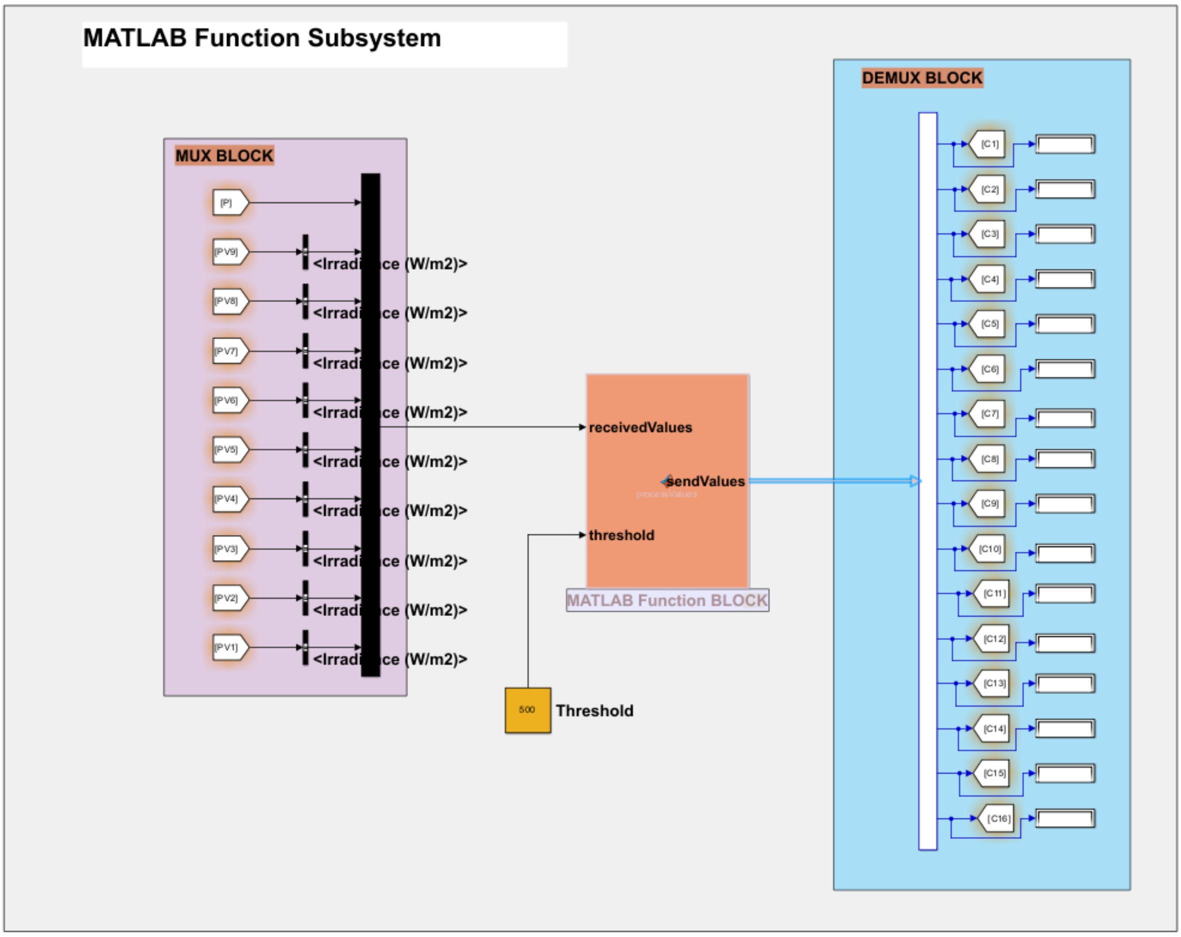

Figure 3.11: Integration subsystem of MATLAB function block with Mux and Demux blocks.

B. MATLAB Function Block as the Core Component

Within the Simulink model, the MATLAB Function Block serves as the core component, executing the primary processing logic essential for system control. This block processes incoming sensor data by applying a threshold-based control algorithm, where an additional constant block defines the threshold value, set to 500. The MATLAB Function Block determines appropriate control actions based on the level of solar irradiance detected by the sensors. Specifically, the block evaluates each input value against the defined threshold, adjusting the system's output accordingly to optimize performance.

For instance, if the irradiance value exceeds the threshold, the function block can alter control signals to modify power output settings or change panel configurations, ensuring the PV system operates efficiently under varying conditions. The MATLAB Function Block is meticulously scripted to evaluate the first nine input values, setting corresponding output values based on the threshold checks. Additionally, the block handles special conditions for certain inputs, incorporating additional logic to meet specific output requirements. This includes a dummy power calculation, which exemplifies the system's capacity to perform complex computations. By integrating these features, the MATLAB Function Block not only manages real-time data processing but also provides a flexible and robust framework for implementing sophisticated control strategies within the simulation environment. Figure 3.12 presents a flowchart detailing the step-by-step data processing and control logic within the MATLAB Function Block. The figure is referenced to better understand how each component functions sequentially from input initialization to output generation. The code implementation is available upon request.

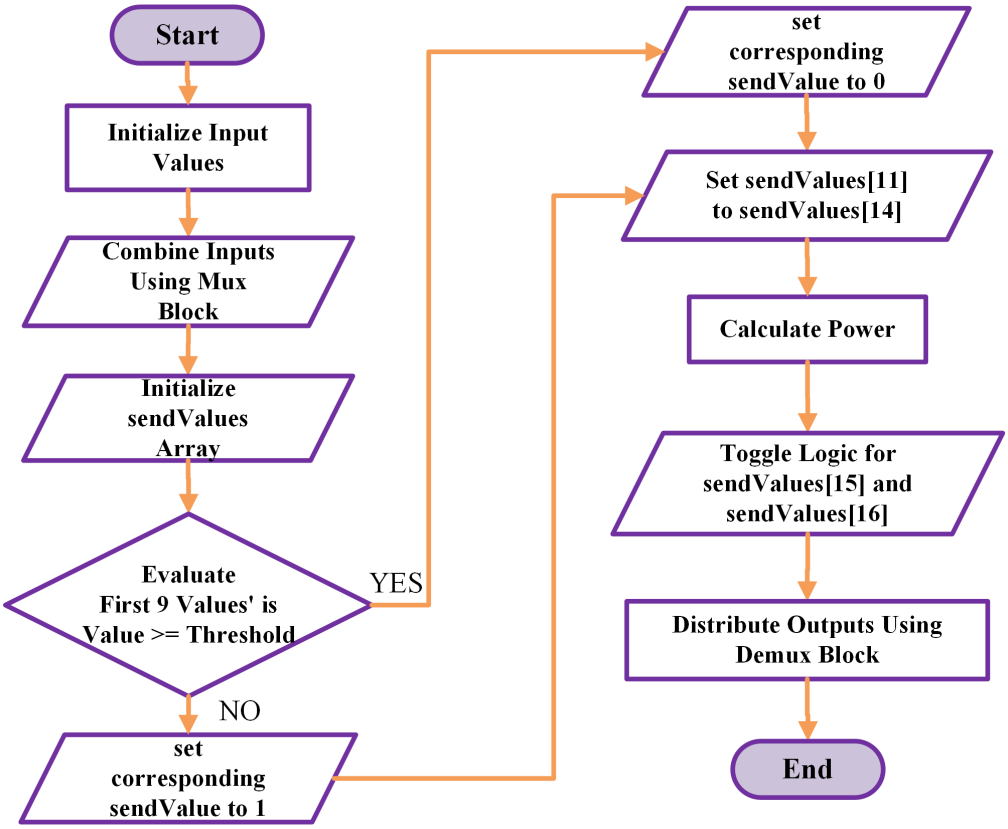

Figure 3.12: Flowchart of MATLAB Simulink function block for control of the proposed system.

C. Input and Output Management using Mux and Demux Blocks

To efficiently manage multiple input values, the outputs of the constant blocks are aggregated using a Mux block. The Mux block combines the individual constant outputs into a single array, facilitating streamlined data handling and input feeding into the MATLAB Function Block. After processing, the output array from the MATLAB Function Block is fed into a Demux block. The Demux block separates the aggregated output into sixteen individual signals, each representing a specific control signal or status indicator.

To provide real-time feedback and monitoring, sixteen display blocks are used to visualize the output signals. Each display block is connected to the output of the Demux block, allowing for clear observation of the system’s responses and control signals. Figure 3.11 illustrates this integration and how each block interacts within the system.

D. Flowchart of the Simulation Process

The flowchart begins with initializing input values from nine PV panels and a set threshold value. These inputs are combined using a Mux block for efficient handling. The central processing occurs in a MATLAB Function Block, which initializes an array (sendValues), evaluates each PV panel output against the threshold, and sets corresponding values based on the comparison. Special conditions are checked for specific sendValues, and a power calculation is performed to implement a toggle logic for the final values. Outputs are then distributed using a Demux block and visualized through display blocks. The process concludes with an end marker, ensuring a structured and systematic flow from input initialization to output visualization. Figure B.1 illustrates the structure of the MATLAB Function Block for real-time simulation control of the proposed system Model- A.

3.4.4.2 Hybrid Simulation with Simulink and Arduino

A hybrid MATLAB-Simulink simulation environment with an Arduino microcontroller is designed and implemented to simulate and control a PV system. This setup combines Simulink's simulation capabilities with the microcontroller's real-time data processing and control functions. It enables accurate testing and demonstration of system performance under various conditions while allowing real-time adjustments based on actual data inputs. This approach enhances simulation accuracy and control flexibility, making it a powerful tool for developing and optimizing PV systems.

A. Interface Program Using MATLAB-Simulink

This interface enables users to input data from various sensors, such as solar irradiance, voltage, and current, and initiate the processing of this data according to predefined algorithms. The processed data generates control signals that are sent back to adjust the system’s operation in real-time. The interface is composed of several key components. The Input and Bus Selector allows for the selection of specific sensor data, such as irradiance, from multiple inputs, offering flexibility to reconfigure for different simulation requirements. Once the data is selected, it is combined into a single stream using a Mux block and scaled by the Gain block to match the microcontroller’s 0-5 V analog input range.

The scaled data is then converted into an 8-bit unsigned integer format to facilitate efficient serial communication. To ensure stable signal processing, the Zero-Order Hold block maintains the most recent data value between sampling intervals, after which the data is cast to a single-precision floating point and packed into a byte array for transmission. Serial communication is managed via the COM7 port configured at a baud rate of 115200, enabling high-speed data exchange between Simulink and the microcontroller. The processed data is sent from Simulink to the microcontroller, where it is analyzed and sent back, maintaining real-time bidirectional communication. On receiving the processed data, it is converted back to double-precision format and separated into individual signals for further use in the simulation. The processed values are displayed within Simulink, allowing users to monitor the system's performance in real-time.

Figure 3.13 illustrates the Simulink and Microcontroller Data Exchange Subsystem via Serial Port, while Figure B.2 demonstrates the integration of Microcontroller with Simulink for real-time simulation control of the proposed system model-B.

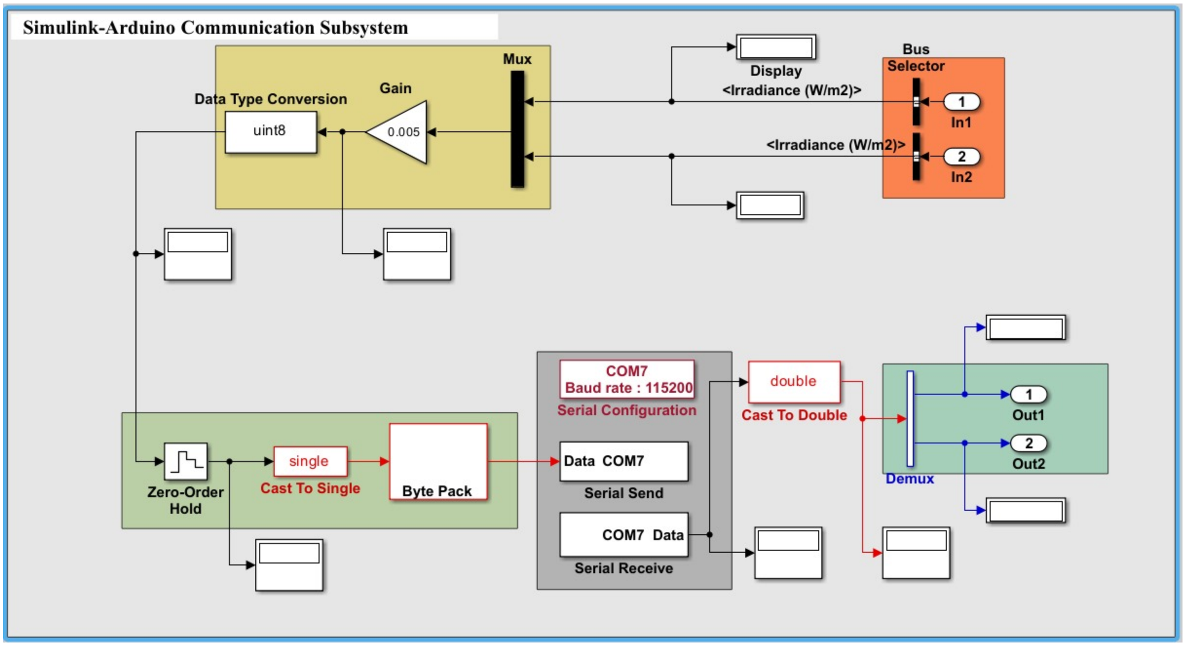

Figure 3.13: Simulink and Arduino data exchange subsystem via serial port.

B. Microcontroller Program

The microcontroller's primary function is to wait for commands from the PC, process the received data, and deliver the results back to the PC. The flowchart for the microcontroller program is presented in Figure 3.14. The microcontroller operates as follows: Once powered on, the microcontroller initializes by configuring its settings and verifying that it is ready for communication. After completing the configuration, the microcontroller continuously checks if a command has been received from the PC. Upon receiving a command, the microcontroller begins processing incoming sensor data. The received data, typically in byte arrays, is converted into float values using a union structure for precise interpretation.

The microcontroller processes 10 received sensor values and compares them against a predefined threshold. For the first nine values, the output is set to 0 if the reading exceeds the threshold; otherwise, the output is set to 1. Additional logic is implemented to handle specific conditions, such as toggling outputs based on a power calculation. If no command is received, the microcontroller loops back to recheck for commands, ensuring continuous monitoring. This logic allows the microcontroller to perform dynamic control operations based on real-time conditions, providing flexibility and accuracy in system performance. The code operation is available upon request.

This integrated approach provides a flexible, dynamic environment for simulating and controlling a PV system, enabling comprehensive testing and optimization of various configurations.

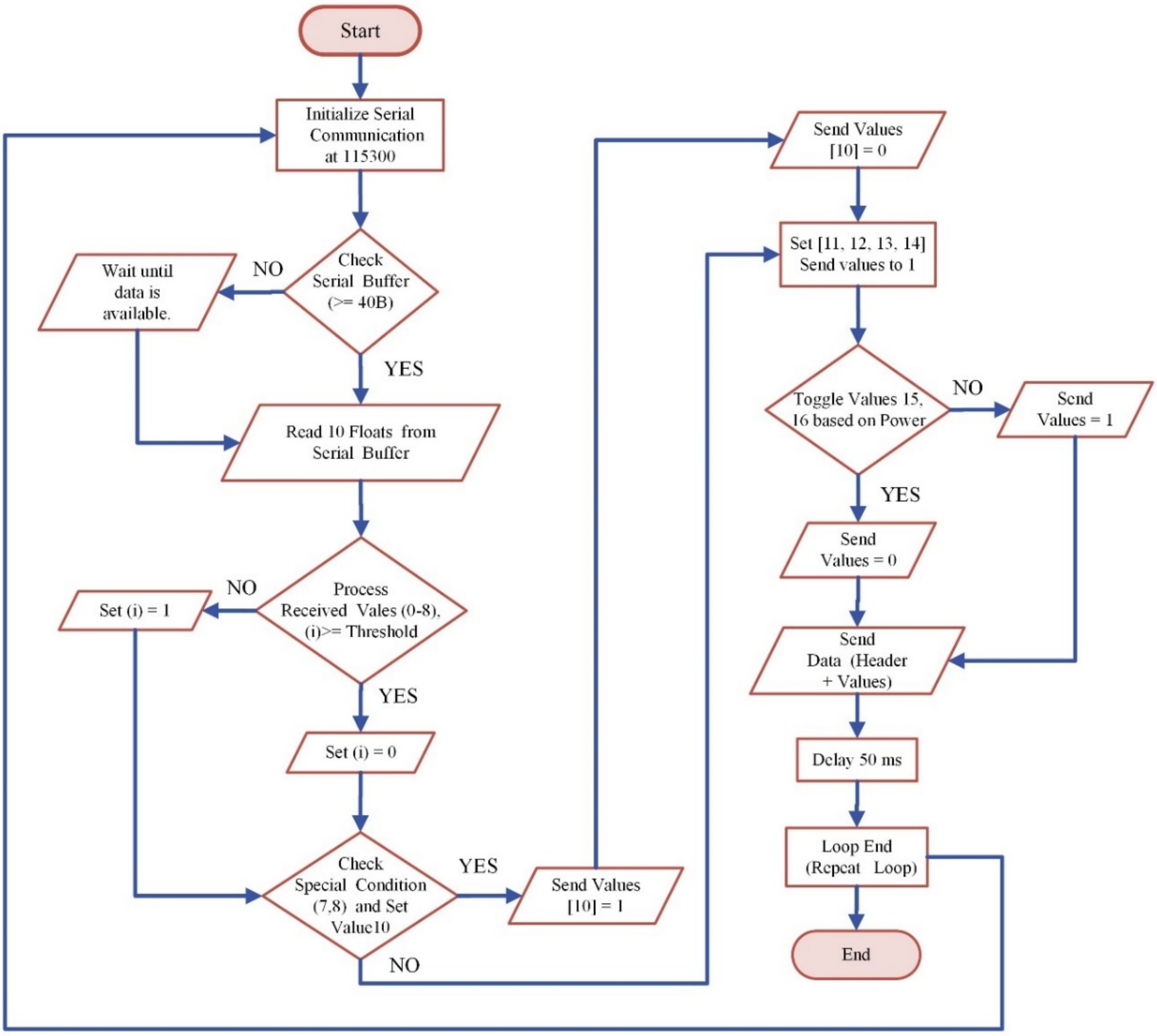

Figure 3.14: Flowchart of Arduino integration with Simulink for control of the proposed system.

3.5 Practical Implementation (Experimental Part)

This section details the practical implementation of the proposed system, including the design and construction of the hardware components.

3.5.1 System Architecture and Configuration

The system architecture centers around the implementation of a dynamic PV array, integrated with Arduino microcontrollers and a suite of sensors, including a solar irradiance sensor cell (SISC), voltage sensor, current sensor, light intensity sensor, and temperature monitoring sensors.

The system employs two interconnected controllers to facilitate real-time data acquisition and analysis. The Arduino Mega, acting as the Primary Controller Unit (PCU), manages the primary operational tasks by interfacing with key sensors to monitor solar irradiance, electrical parameters, and energy flow. By leveraging SISC sensors, the PCU accurately assesses solar irradiance levels while continuously tracking the voltage and current of the PV array. In parallel, the Arduino Uno serves as the Secondary Controller Unit (SCU), dedicated to environmental monitoring. The SCU, integrated with BH1750 and DS18B20 sensors, provides additional insights on light intensity and temperature, ensuring the system remains balanced and protected from potential thermal issues.

A critical component of the system is the switch array, which reconfigures the PV panel connections, switching between series and parallel arrangements to maintain optimal performance under partial shading conditions. This intelligent setup ensures that the PV array operates efficiently, adapting to environmental changes and preserving the system's integrity.

The operational procedure commences with the SISC sensor capturing real-time solar irradiation data, processed by the PCU to assess the PV array's exposure to sunlight. Voltage and current sensors transmit electrical readings to the PCU, enabling the detection of power generation fluctuations. The BH1750 sensor and DS18B20 sensors overseen by the SCU provide additional environmental data, ensuring the PV array consistently operates at optimal efficiency levels, adapting to varying environmental conditions. Figure 3.15 illustrates the system basic architecture.

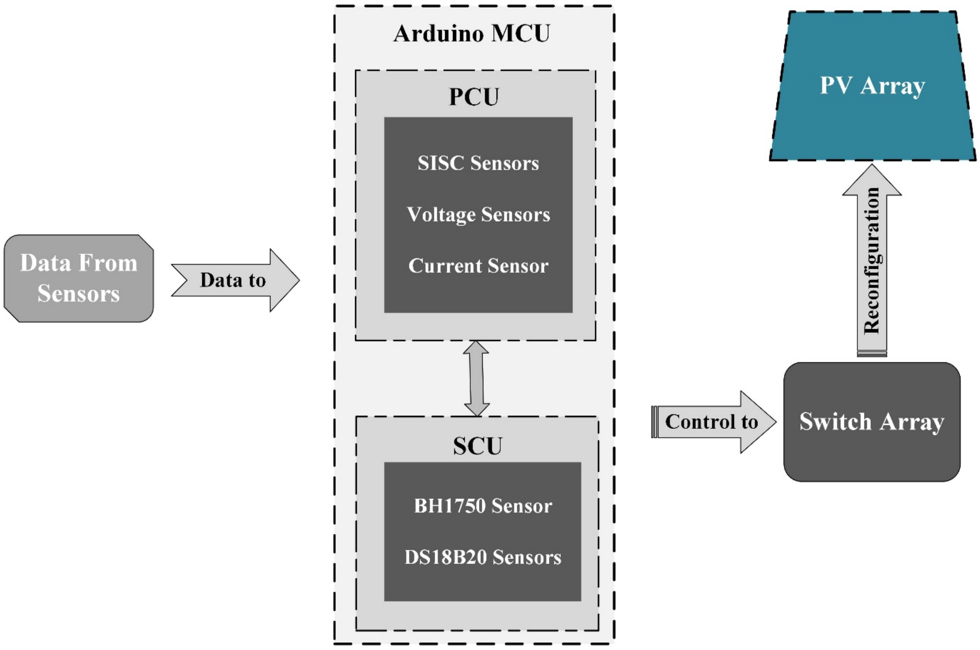

Figure 3.15: The system architecture design and configuration.

3.5.2 Hardware Implementation

The physical infrastructure of the project comprises essential components, including solar panels, switches, and a variety of sensors, which collectively form the foundational framework. This section outlines the methodology for implementing these components to assemble a complete system. It also details the distribution and integration of the sensors to ensure the acquisition of accurate and comprehensive data.

3.5.2.1 PV Array Configuration

The PV array consists of nine solar panels arranged in a 3x3 matrix. Each panel incorporates bypass diodes to mitigate power losses from shading or cell malfunctions. These diodes provide an alternative current path, bypassing affected cells. Additionally, blocking diodes prevent reverse current flow between panels, ensuring system integrity. While these diodes enhance performance, they introduce a voltage drop of approximately 0.7V per series-connected panel. The system employs a flexible panel interconnection design, adjustable through a switch array, to optimize performance under various conditions. This configuration enhances system adaptability and reliability. Figure 3.16 illustrates the structure of the PV array.

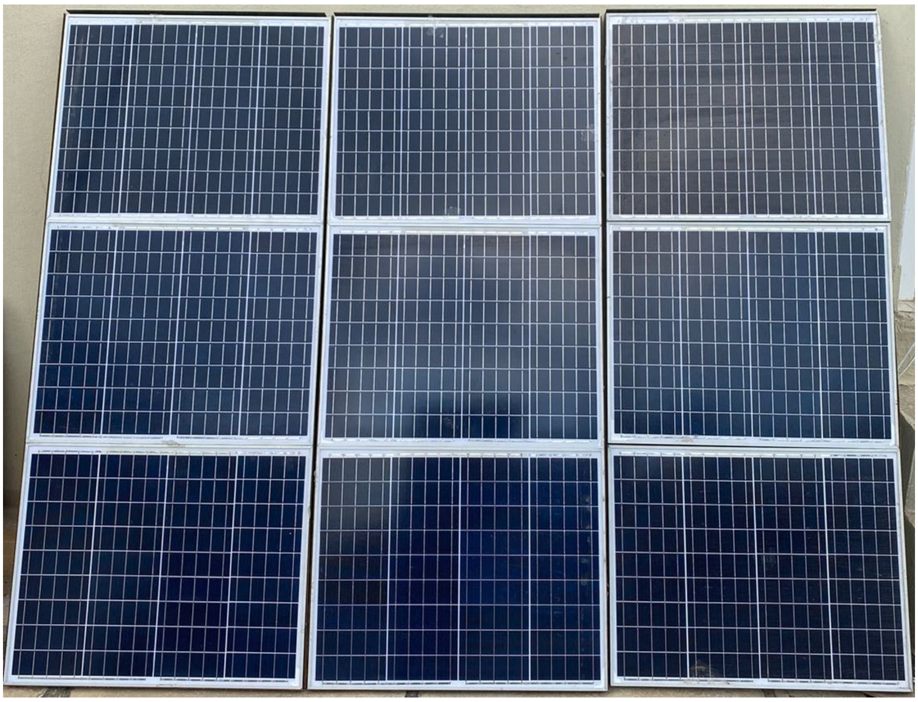

Figure 3.16: Illustrates the structure of the PV array.

3.5.2.2 Implementation of Switch Array

The switch array is a critical component in the PV array system, engineered to optimize the electrical connections between PV panels based on real-time environmental conditions. The system is structured hierarchically, with multiple layers of SBs that manage these connections through relays. **Model-A** is implemented in this system to enhance its functionality by dynamically adjusting the configuration of PV panels to maximize energy output.

A. Hierarchical Structure

The hierarchical structure of the switch array is organized into three primary layers, as illustrated in Figure 3.17. The **First Layer** consists of five Switching Blocks (SB1, SB2, SB3, SB4, and SB5), each equipped with two relays. These blocks are directly connected to the PV panels and are responsible for managing the initial electrical connections. This layer contains a total of 10 relays and is crucial for configuring the array to adapt to immediate shading conditions. The **Second Layer** includes two Switching Blocks (SB6 and SB7), each with two relays, contributing to a total of four relays in this layer. These blocks refine and manage the connections established by the primary layer, enabling the system to adjust to more complex shading patterns and environmental changes. The **Third Layer**, also known as the Load Block (SB8), consists of a single Switching Block containing two relays. This block integrates the outputs from the secondary layer and directs the final electrical output to the system's load, ensuring cohesive and efficient operation.

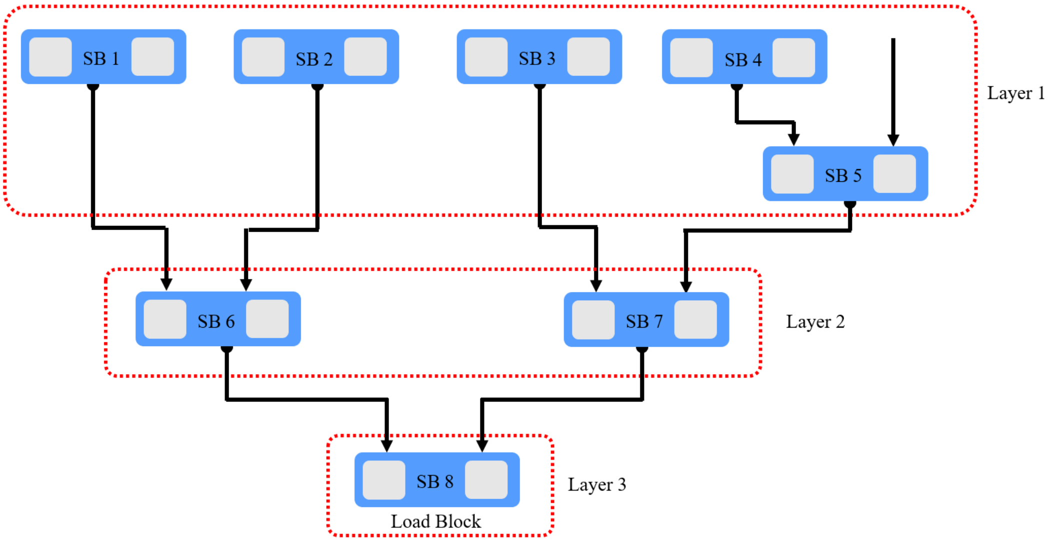

Figure 3.17 The hierarchical structure of SBs in switch array.

B. Relay Configuration

The relay configuration within the switch array is pivotal for dynamically managing the connections between PV panels. Each SB is equipped with two relays, totaling 16 relays across the system. These relays determine whether panels are connected in parallel or series and manage communication between them. The relays are directly connected to the panels and controlled by a microcontroller that processes real-time environmental data. This control mechanism allows for dynamic adjustments to optimize efficiency under varying conditions.

In this configuration, SB1 contains Relay 1 and Relay 2, SB2 contains Relay 3 and Relay 4, and so forth, up to SB8, which contains Relay 15 and Relay 16. PV1 is connected to Relay 1, PV2 to Relay 2, and both relays are grouped within SB1. The same logic applies across the system for PV1 to PV9. The detailed configuration of an individual SB, including its relay setup, is depicted in Figure 3.18.

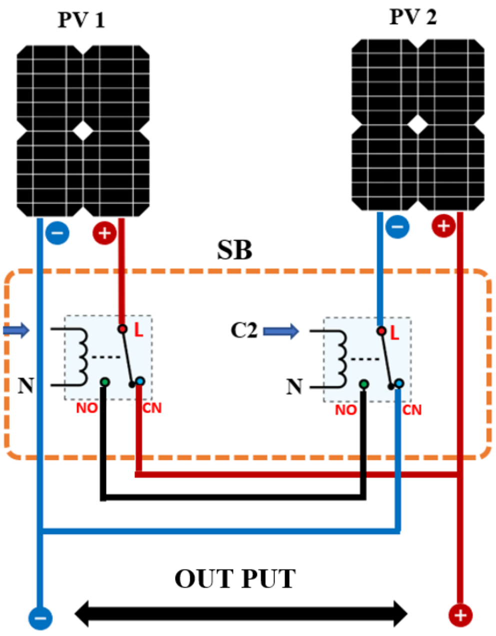

Figure 3.18: The Design of a switching block incorporating two relays in its structure.

The interconnected SBs refine these connections at higher layers. SB1 and SB2 feed into SB6 through Relays 11 and 12, while SB3 and SB5 feed into SB7 via Relays 13 and 14. The final output is managed by SB8, which combines SB6 and SB7, ensuring that the optimized configuration is delivered to the load. Figure 3.19 shows the proposed Model-A system architecture, illustrating the distribution of SBs and relays within each layer. This modular and hierarchical design allows for quick adaptation to changing conditions, enabling consistent, efficient power output across the entire system.

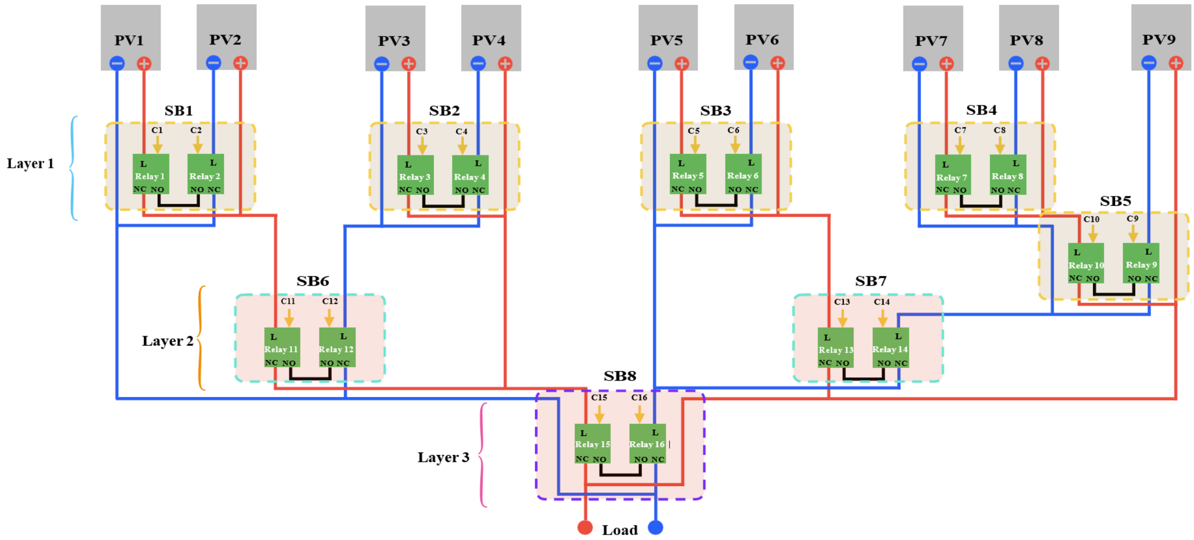

Figure 3.19: Proposed Model-A system architecture.

C. Interconnection

The interconnection of the SBs across the hierarchical layers forms a flexible and adaptable network within the switch array. This interconnection is designed to facilitate seamless communication between the layers, enabling the system to respond quickly and effectively to changes in shading or other environmental factors. The modular design of the interconnection also allows for the easy integration of additional PV modules or SBs without requiring extensive rewiring or significant alterations to the existing system. This flexibility enhances the scalability of the system and ensures consistent power output across a wide range of operational scenarios. The overall architecture of the switch array, including the relay system and hierarchical structure, is illustrated in Figure 3.20.

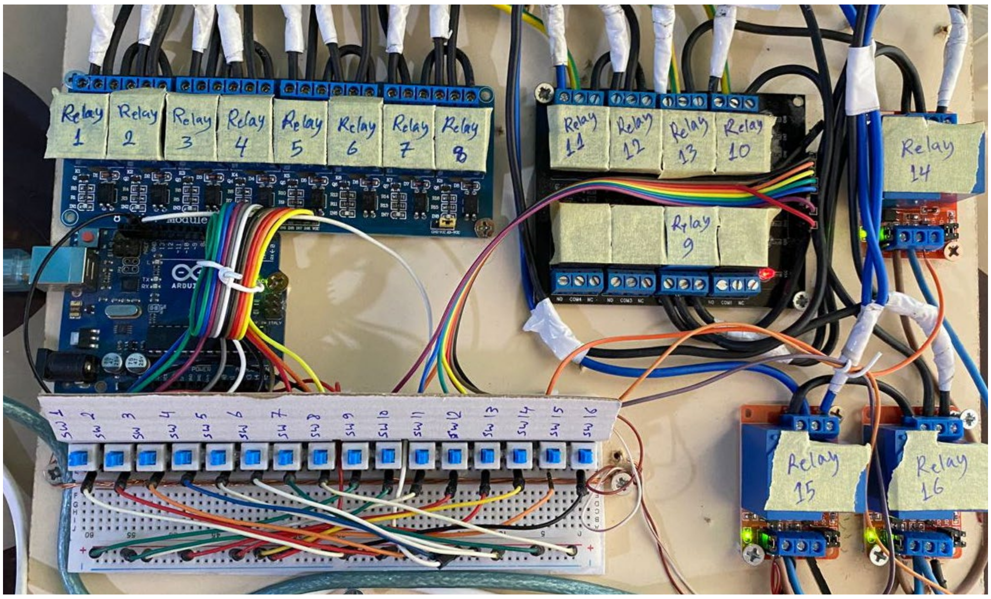

Figure 3.20: The architecture of Switching Array.

3.5.2.3 Sensor Integration

To monitor system performance and environmental conditions, a comprehensive suite of sensors is integrated:

A. Solar Irradiance Sensor Cells:

Placed adjacent to each PV panel, these sensors accurately measure solar radiation intensity. The SISC sensors are critical components in the dynamic reconfiguration of solar panels, ensuring that the system operates efficiently under varying solar conditions.

The KS-M5555 solar panel is utilized as the SISC in the system, with its characteristics detailed in Table A.2. Operating at a nominal voltage of 5 V, the sensor is designed to provide precise measurements of solar radiation. To ensure the highest accuracy, each SISC sensor is meticulously calibrated to correspond with the position and shading conditions of its paired PV panel.

In the system, a total of nine SISC sensors are deployed, with each sensor strategically positioned next to one of the nine main solar panels. This placement ensures that each sensor experiences the same shading conditions as its corresponding PV panel, thereby enhancing the reliability of the solar radiation data collected.

The basic electronic circuitry of the SISC sensor, as shown in Figure 3.21, includes a resistor connected in parallel with the sensor, which is essential for proper functioning and accurate measurement.

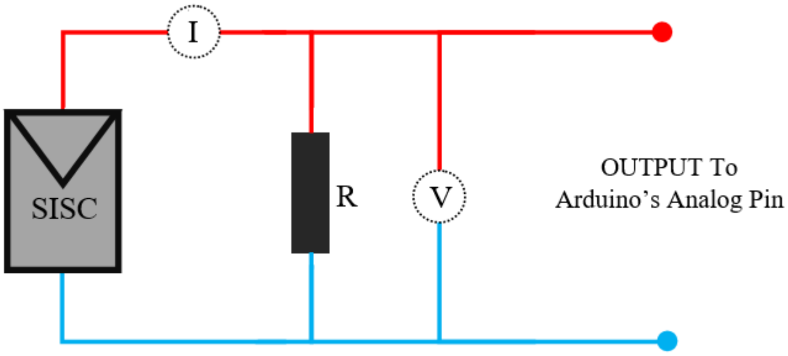

Figure 3.21: The SISC electronic circuit.

Figure 3.22 illustrates the exact placement of the SISC sensors in relation to the main solar panels, highlighting the importance of precise positioning in achieving consistent and accurate data collection for solar energy applications.

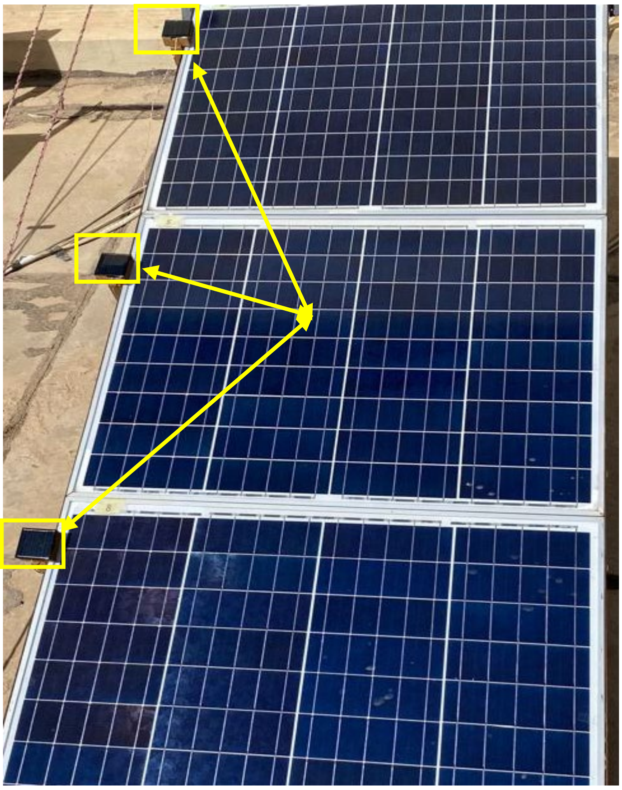

Figure 3.22: The SISC sensors are next to the main solar panels.

B. Voltage and Current Sensors

To accurately monitor the electrical parameters within the PV system, voltage and current sensors are strategically integrated into the hierarchical switch array. These sensors are crucial for power output calculations, fault detection, and overall system efficiency.

1. Voltage Sensors

Placed at the first layer (Layer 1) of the switch array, these sensors measure the voltage across each PV panel. Specifically, four voltage sensors are connected to each Switching Block (SB) in this layer, interfacing directly with the PV panels. The four sensors used for SB1, SB2, SB3, and SB5, as illustrated in Figure 3.23, are vital for ensuring precise voltage measurement. Since the microcontroller's analog inputs operate at 5V, these sensors are essential for scaling down the voltage levels, which typically range from 40 to 60 volts, to make them compatible with the microcontroller's input requirements.

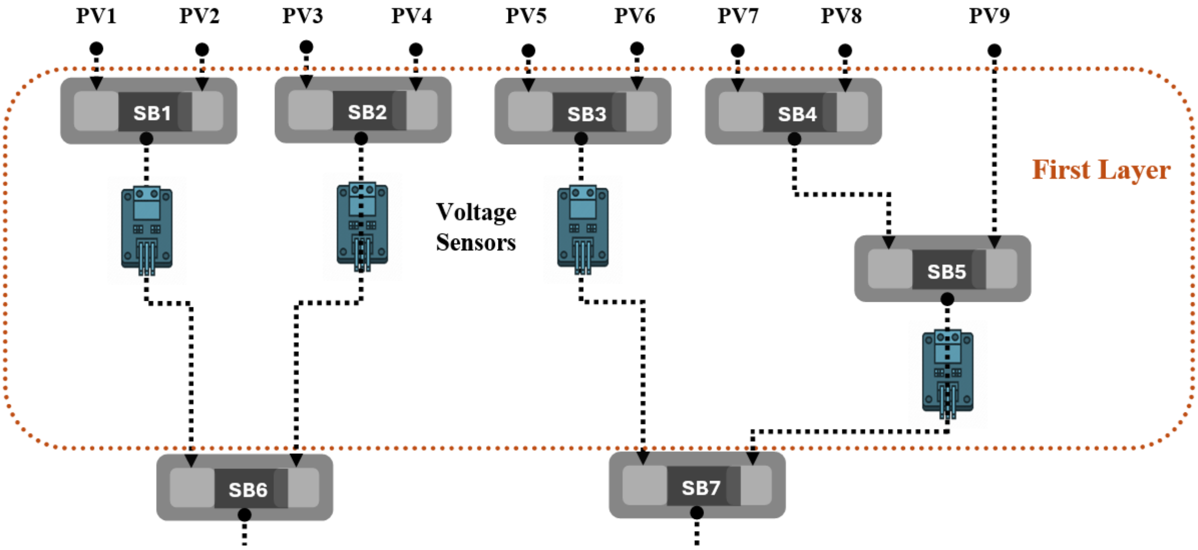

Figure 3.23: The voltage sensors integrated with SBs in the first layer of the switch array.

2. Voltage Divider Voltage Sensor

Integrated at the final switching block (SB8) in Layer 3, this sensor is designed to convert high voltage levels to a lower voltage range compatible with the microcontroller. The voltage divider voltage sensor in SB8 functions as the load SB and is capable of accepting input voltages ranging from 0 to 155 volts, converting them to output voltages between 0 and 5 volts. This conversion process ensures that the microcontroller can accurately measure the system's total voltage without being exposed to potentially damaging high voltage levels. The sensor's electronic circuit includes a Zener diode, providing over-voltage protection by clamping any spikes that exceed the microcontroller's maximum input voltage of 5 volts, thereby ensuring the safety and integrity of the microcontroller. Figure 3.24 illustrates the straightforward electronic circuit design of the voltage sensor.

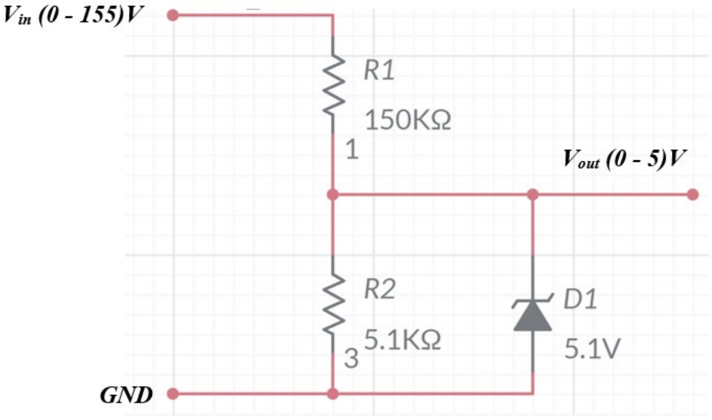

Figure 3.24: The simple electronic circuit design for the voltage divider voltage sensor.

3. Current Sensor

Located at the output of the final switching block (SB8) in Layer 3, the current sensor measures the total current flowing through the system. This sensor is strategically positioned to accurately measure currents up to 30 amps, which is suitable for the expected range of currents in the system. By placing the current sensor at the final level, the design and wiring complexity are significantly reduced, simplifying the overall system while ensuring accurate current measurements. The streamlined design at this level contributes to the system's efficiency and effectiveness.

The implementation of the voltage and current sensors within the switch array is depicted in Figure 3.25. This configuration strategically places the sensors to minimize circuit complexity and reduce the number of sensors required relative to the number of PV panels. At the primary level, four voltage sensors are utilized, complemented by a current sensor and an additional voltage sensor at the third level. This approach effectively reduces the total number of sensors needed, thereby lowering both costs and circuit complexity. Traditionally, equipping each panel with individual voltage and current sensors would require a total of nine sensors and 18 analog inputs for the microcontroller, significantly increasing both financial expenditure and system complexity. Additionally, this conventional method could necessitate a higher number of controllers. The described implementation offers a cost-effective and streamlined solution without compromising the system's operational efficiency.

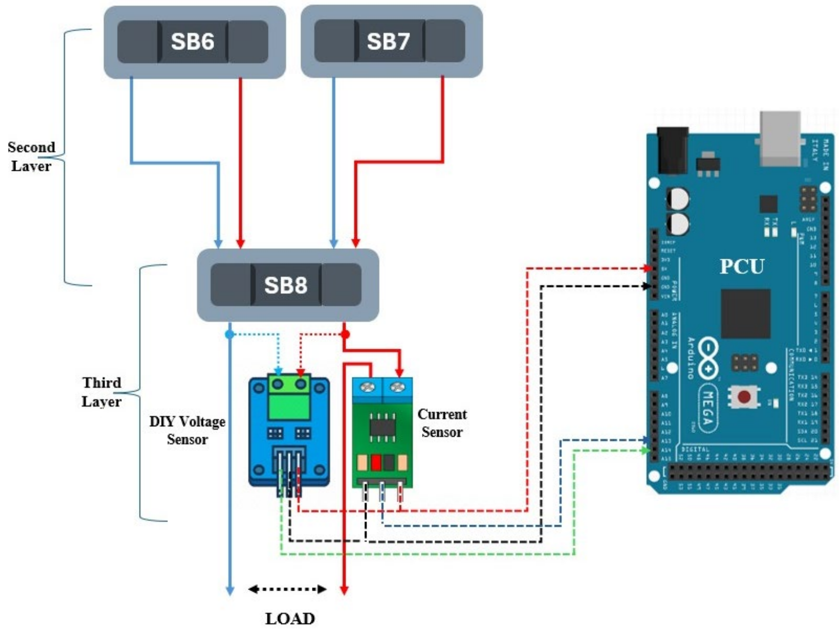

Figure 3.25: The design of the electronic circuit location for the voltage and current sensors within the switch array.

C. Light Intensity Sensor (BH1750)

The BH1750 sensor measures ambient light levels to estimate shadow effects and optimize panel placement for maximum sunlight exposure. It also compares solar radiation readings with SISC sensors to verify data accuracy. The sensor detects sudden light intensity changes, indicating potential issues like dirt accumulation or shading, enabling timely maintenance and cleaning for optimal PV array performance. If equipped with a tracking mechanism, the sensor data can dynamically adjust panel angles to maximize energy capture throughout the day. To assess ambient light conditions and their impact on system performance, a BH1750 light intensity sensor is integrated adjacent to the solar panels, as shown in Figure 3.26.

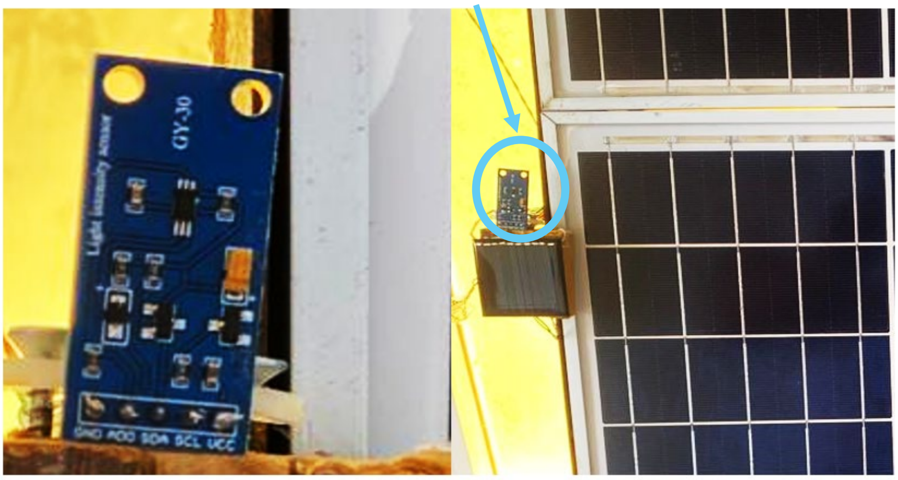

Figure 3.26: The light intensity sensor (BH1750) positioned adjacent to the PV panel.

D. Temperature Sensors (DS18B20)

To monitor PV panel temperatures, prevent overheating, and optimize system efficiency, nine waterproof DS18B20 temperature sensors are strategically placed at the rear center of each panel, as shown in Figure 3.27. These sensors ensure the panels operate within optimal temperature ranges, maximizing efficiency and extending their lifespan. By utilizing the 1-Wire protocol, all sensors are connected to a single microcontroller pin for efficient data management.

Figure 3.27: Placement of DS18B20 temperature sensors at the rear center of PV panels.

Sensor data is collected by microcontrollers, allowing for real-time analysis and control decisions.

3.5.2.4 Microcontroller System Implementation

The microcontroller system is implemented using two Arduino boards: the Arduino Mega as the PCU and the Arduino Uno as the SCU. The SCU, equipped with extensive I/O capabilities, is designed to gather comprehensive data from both light and temperature sensors and relay this information to the PCU. It utilizes digital I/O pins, with pin 2 dedicated to connecting nine DS18B20 temperature sensors, and analog inputs, specifically pins A4 and A5, for interfacing with the BH1750 light intensity sensor. These connections facilitate efficient interaction with the system components. Serial communication via pins TX and RX enables the SCU to exchange data with the PCU and potentially other connected devices, ensuring seamless integration within the overall system. Figure 3.28 provides the electronic circuit connection details for the SCU, including specific wiring instructions, pin configurations, and component placements, ensuring accurate assembly and functionality of the sensors with the controller.

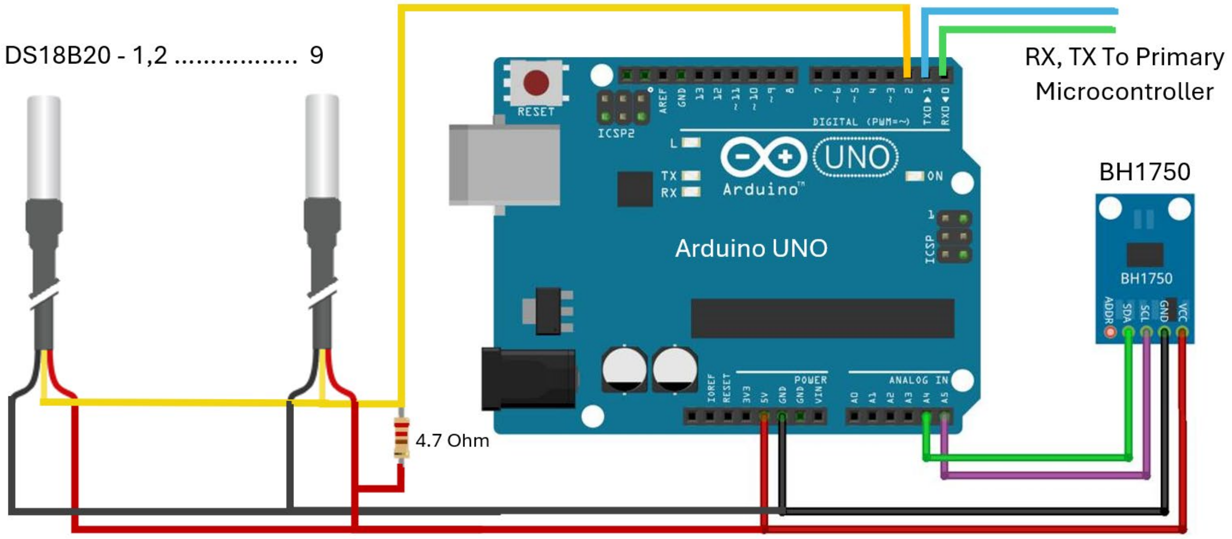

Figure 3.28: The circuit diagram of the SCU integrates the BH1750 light sensor and the DS18B20 temperature sensor.

The Arduino Mega, functioning as the PCU, plays a central role in the dynamic PV array reconfiguration system by managing both data collection and control functions. The PCU collects and interprets data from various sensors directly connected to it, including SISC sensors, as well as voltage and current sensors, utilizing up to 15 analog inputs. Additionally, the PCU integrates light intensity and temperature data from the SCU, transmitted via RX and TX interfaces. Leveraging these inputs, the PCU executes algorithms to generate and dispatch reconfiguration commands to the switch array through 16 digital outputs. Concurrently, the PCU facilitates real-time data transmission to a central computer using an XBee module, enabling continuous monitoring and supervision by system users. The electronic circuit diagram of the PCU provides a comprehensive overview of the integration of all sensors and electrical connections, illustrated in Figure 3.29, including auxiliary devices such as the SCU, the switching array, and the XBee communication module. This underscores the PCU's pivotal role in maintaining system functionality and efficiency.

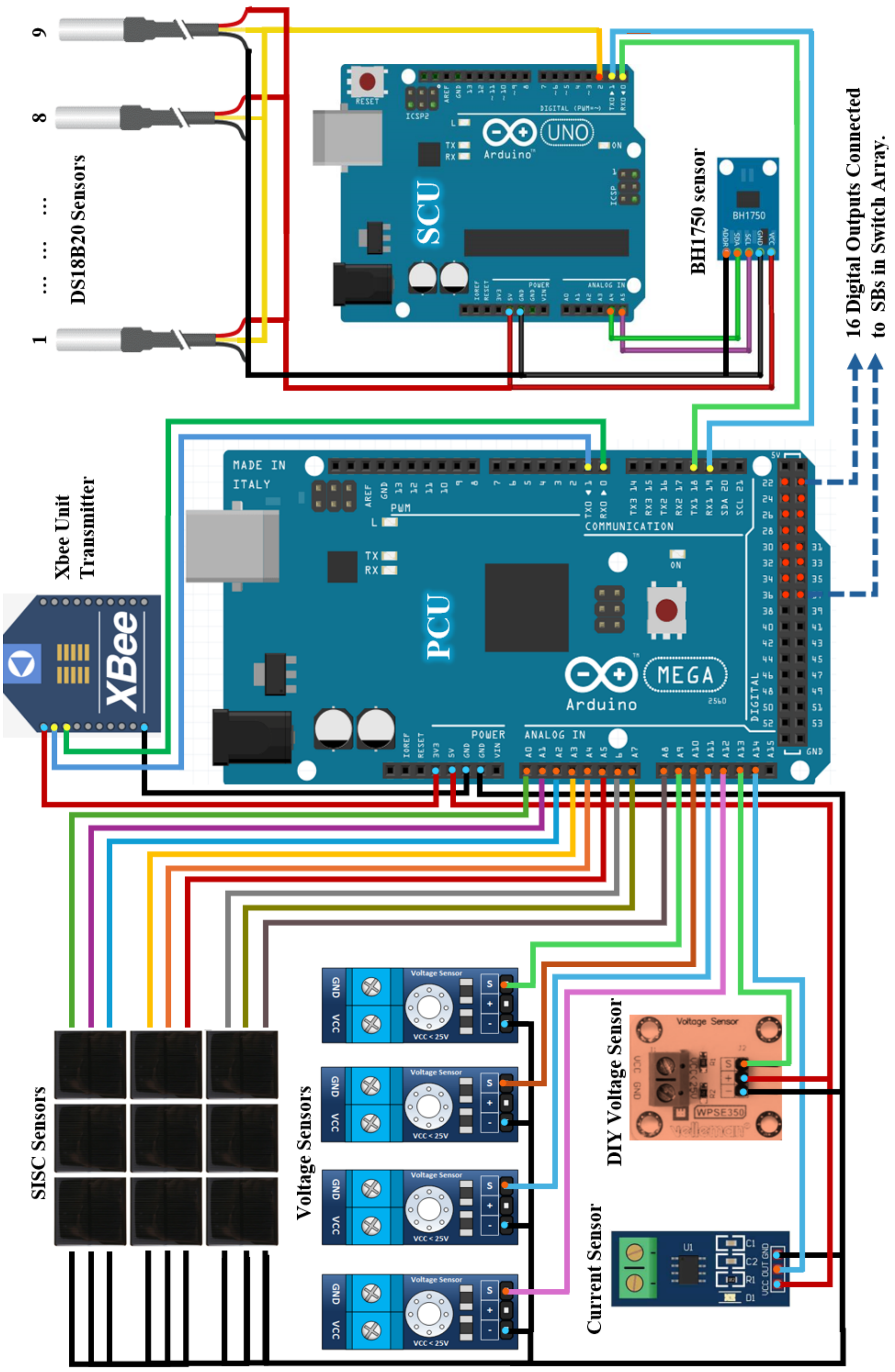

Figure 3.29: The schematic of the PCU's electronic circuit, highlighting the integration of sensors and electrical connections with auxiliary devices like the SCU and the XBee communication module.

3.5.2.5 Implementation of Load Resistance and Digital Voltage/Current Measurement

A. Load Resistance Implementation

The system utilizes stainless steel heating wires as the primary load element due to their high resistance and ability to handle power loads exceeding 500 Watts. With a 1.5 mm diameter, these wires are ideal for varying load conditions and are coiled into a spring-like structure to function as a variable resistor, as depicted in Figure 3.30. The heating wire is divided into several specific points, each corresponding to distinct resistance values—0.7, 3, 6, 10, 13, 15, and 20 Ohms—allowing precise control over the load. The total resistance of the wire is 24 Ohms. This configuration provides the flexibility needed to adjust the resistance according to the system's requirements, making it essential for testing and optimizing the performance of the solar system under different operating conditions. The choice of stainless steel ensures long-term reliability and operational stability, making it an ideal component for this application.

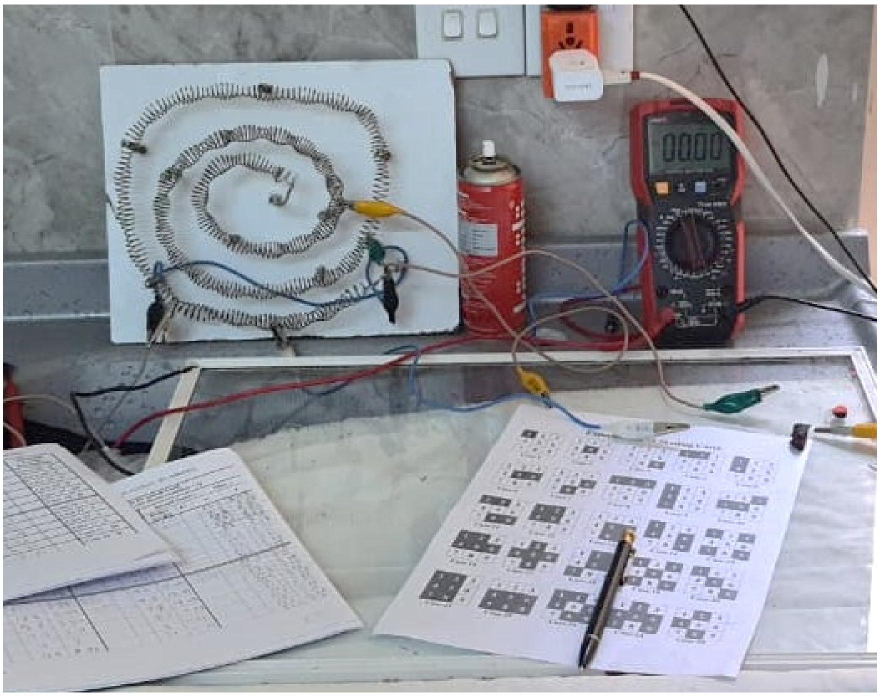

Figure 3.30: Coiled stainless steel heating wire for load resistance.

B. Digital Dual DC 100V 100A Voltmeter Ammeter Implementation

The system incorporates a Digital Dual DC 100V 100A Voltmeter Ammeter to enable real-time monitoring of electrical parameters such as current, voltage, and power. This voltmeter is directly connected to the system load, allowing users to observe and assess fluctuations in these values as they occur. By providing immediate and accurate readings, the voltmeter enhances the ability to monitor and optimize the system's performance effectively.

3.5.3 Software Implementation

This section explains the software components of the proposed system, focusing on the steps for adjusting and calibrating individual parts before integrating them into a comprehensive algorithm. The procedures are divided into stages that occur before full assembly to ensure each component meets performance and compatibility standards. This approach enhances the system's overall reliability and efficiency. The software for the implemented system consists of several parts, as follows:

3.5.3.1 SISC Sensors Calibration

To measure irradiance, a pyranometer is usually preferred for its accuracy and reliability. However, its high cost and limited availability pose significant constraints [106]. To address these issues, the SISC sensor was developed as a cost-effective alternative to replicate pyranometer functionality. Studies have shown that using solar cells as sensors provides an optimal and comparable solution. Solar cells efficiently capture sunlight or electromagnetic radiation, making them suitable for this purpose. The SISC sensor, a small solar cell, is used to measure irradiance in watts per square meter (W/m²), offering a practical solution closely aligned with traditional pyranometers.

Calibration is crucial for accurate measurements and efficient solar energy use. The sensors must be precisely aligned with the main solar panel to ensure consistent exposure to irradiance, reducing variations from different angles. Following alignment, the SISC sensor is calibrated against the main photocell in multiple stages. Various resistance values, including 100, 220, 330, and 470 Ohms, are used during calibration, and a voltage sensor connected to the main board reads these values with a 25-to-5-Volt conversion ratio. Shade conditions are applied intentionally to the SISC sensor and the main panel. By comparing readings under different resistances and shading conditions, optimal resistance values are identified for accurate results. These results are presented in Table 3.1. The microcontroller code for calibration and resistance selection is available upon request.

Table 3.1: Comparison of irradiance readings under varying resistor configurations and shading conditions.

NO.	SISC with 100 Ω Irradiance	SISC with 220 Ω Irradiance	SISC with 330 Ω Irradiance	SISC with 470 Ω Irradiance	Voltage Sensor Connected to main PV Irradiance	Shading percentage
1	781	931	959	1023	797	0 %
2	656	745	720	839	630	20 %
3	453	560	566	620	492	40 %
4	308	375	365	430	327	60 %
5	146	188	199	215	155	80 %
6	0	111	116	115	87	90 %

Using data from a global weather website (https://solcast.com) to measure solar irradiation intensity, the results were calibrated and recorded in Table 4.1 on October 14, 2023. The highest radiation values on that day were observed between 9:00 AM and 1:00 PM, with irradiance peaking at 916 W/m^2 in Kirkuk (35.466633, 44.379889), northern Iraq. Based on these measurements, calibration equations were formulated to achieve results that closely match those observed at this location. These equations aim to estimate irradiance accurately, considering the local climate conditions and available data.

To establish a calibration framework for the measured irradiance values, a mathematical relationship has been developed between the outputs of individual SISC sensors, equipped with various resistors, and the highest irradiance value of 916 W/m², as reported by the reference source. This model will enable the conversion of SISC readings, which may be affected by resistor variations, into values directly comparable to the known reference irradiance of 916 W/m². This approach ensures that the measurements from different sensor configurations can be accurately aligned with the established reference irradiance.

To find the scaling factor for each SISC:

$$Scaling\ Factor\ =\ Reference\ irradiance\ /\ Highest\ Reading \qquad (4)$$

Where Reference irradiance equals to 916 W/m^2

Calculating the scaling factors for each SISC:

- **For SISC with 100 Ω:**
  - Highest Reading = 781 W/m².
  - Scaling Factor = 916 / 781 ≈ 1.173
- **For SISC with 220 Ω:**
  - Highest Reading = 931 W/m².
  - Scaling Factor = 916 / 931 ≈ 0.984
- **For SISC with 330 Ω:**
  - Highest Reading = 959 W/m².
  - Scaling Factor = 916 / 959 ≈ 0.955
- **For SISC with 470 Ω:**
  - Highest Reading = 1023 W/m².
  - Scaling Factor = 916 / 1023 ≈ 0.895
- **For Voltage Sensor Connected to main PV:**
  - Highest Reading = 797 W/m².
  - Scaling Factor = 916 / 797 ≈ 1.149

Leveraging these scaling factors derived from the established relationship, calibration equations can formulate that rectify the measured irradiance values from the SISC sensors to reflect the reference irradiance of 916 W/m²:

- **For SISC with 100 Ω:**
  $$Irradiance100\Omega\ =\ Reading100\Omega\ \times\ Scaling\ Factor100\Omega \qquad (5)$$
- **For SISC with 220 Ω:**
  $$Irradiance220\Omega\ =\ Reading220\Omega\ \times\ Scaling\ Factor220\Omega \qquad (6)$$
- **For SISC with 330 Ω:**
  $$Irradiance330\Omega\ =\ Reading330\Omega\ \times\ Scaling\ Factor330\Omega \qquad (7)$$
- **For SISC with 470 Ω:**
  $$Irradiance470\Omega\ =\ Reading470\Omega\ \times\ Scaling\ Factor470\Omega \qquad (8)$$
- **For Voltage Sensor Connected to main PV:**
  $$IrradiancemainPV\ =\ ReadingmainPV\ \times\ Scaling\ FactormainPV \qquad (9)$$

As depicted in Table 3.2, a series of reference irradiance values were determined for a spectrum of shading conditions, encompassing no shading (0%) to significant shading levels of up to 90%.

Table 3.2: Presents reference irradiance values for various shading conditions, ranging from no shading (0%) to significant shading (90%).

No.	Reference Irradiance	Shading Percentage
1	916	0 %
2	732	20 %
3	549	40 %
4	366	60 %
5	183	80 %
6	91	90 %

The irradiance readings were obtained by applying mathematical equations to data collected from SISC sensors with resistances of 100 Ω, 220 Ω, 330 Ω, and 470 Ω, as well as from a voltage sensor. These results were then compared to the reference irradiance values. Table 3.3 presents the collected data.

Table 3.3: Comparison of irradiance readings from SISC sensors (100 Ω, 220 Ω, 330 Ω, and 470 Ω) and a voltage sensor with reference values.

No	SISC with 100 Ω Irradiance	SISC with 220 Ω Irradiance	SISC with 330 Ω Irradiance	SISC with 470 Ω Irradiance	Voltage Sensor Connected to main PV Irradiance	Reference Irradiance W/m^2	Shading percentage
1	916	916	916	916	916	916	0 %
2	769	733	687	750	729	732	20 %
3	531	551	540	554	542	549	40 %
4	361	369	348	384	355	366	60 %
5	171	185	190	192	180	183	80 %
6	86	104	110	102	97	91	90 %

From the analysis of the data in Table 3.3, it is evident that the readings from the SISC with a 220 Ω resistor are the most consistent with the reference irradiance values. Additionally, these readings closely align with the measurements obtained from the voltage sensor. This suggests that the 220 Ω resistor provides the most accurate representation of the true irradiance among the tested configurations. Therefore, nine SISC sensors with resistances of 220 ohms were utilized to measure the irradiance percentage in the proposed system, incorporating a calibration factor of 0.984 for accuracy. The microcontroller code for the SISC sensor implementation is available upon request.

3.5.3.2 Verification of Relay Functionality in a Switch Array

The relay verification process involves testing relays under various voltage and current conditions to evaluate their response and tolerance. The process begins by applying high, medium, and low voltages and currents to assess the relays' handling of these conditions. Power consumption is calculated, followed by a sequential check where the relays open and close multiple times per minute under different conditions, while current and voltage are monitored continuously.

Additionally, a three-stage experiment is conducted to further test relay performance:

1. **Parallel Configuration**: Solar panels are connected in parallel, increasing the current (17 to 20 Amps) while maintaining constant voltage.
2. **Series Configuration:** Relays are connected in series, resulting in increased voltage (120 to 135 Volts) with a constant current.
3. **Hybrid Configuration**: A combination of parallel and series connections is used, producing current values between 9 to 13 Amps and voltage ranging from 50 to 75 Volts. The relays are instructed to open and close 10 to 15 times per minute.

Each relay operates with a 5V DC coil voltage and a coil current between 70 to 100 mA, consuming approximately 0.35 to 0.5 Watts of power. This results in an energy consumption rate of 21 to 30 Watts per minute when active. Ensuring proper relay functionality within the switch array is essential for maintaining the system's integrity. The verification process also confirms the reliability of the connections between relays. The microcontroller code for automating the relay verification process is available upon request.

3.5.3.3 BH1750 Sensor Calibration

The BH1750 light sensor monitors PV panel performance by measuring ambient light intensity, which is crucial for optimizing solar panel orientation and detecting issues like shading or dirt buildup. The sensor can measure up to 65,535 lux, about half the brightness of direct sunlight, making it suitable for PV applications. To convert lux readings into irradiance (W/m²), a conversion factor is applied. For direct sunlight, the conversion rate is approximately 0.0079 W/m² per lux [107]. Table 3.4 presents the closest values or maximum ranges under different conditions of the brightest sunlight.

To convert the measured light intensity from BH1750 lux (illuminance) readings to irradiance (W/m²), the following equation is applied:

$$Calculated\ Irradiance\ (W/m^2)\ = Illuminance\ (lux) \times 0.0079 \qquad (10)$$

The calibration factor adjusts the BH1750 readings to match reference values, such as sun brightness in lux, and is calculated as follows:

$$Calibration\ Factor = (Sun\ Brightness\ Lux)/(BH1750\ Brightness\ Lux) \qquad (11)$$

The final irradiance value is adjusted using the calibration factor:

$$\mathit{Adjusted\ Irradiance}\ (W/m^2) = \mathit{Calculated\ Irradiance}\ (W/m^2) \times \mathit{Calibration\ Factor} \qquad (12)$$

Table 3.4: Maximum ranges under different conditions of the brightest sunlight.

No.	Case	Illuminance
1	Brightest Sunlight	120000 Lux
2	Normal Bright Sunlight	100000 - 110000 Lux
3	Clear sky with Shade	20000 Lux
4	Overcast Sky	10,000 - 20,000 Lux
5	Heavily Overcast Sky	1,000 - 5,000 Lux
6	Twilight	10 - 100 Lux

By employing this conversion equation, the BH1750 sensor's light intensity values are adjusted to align with the readings from a standard SISC sensor. Table 3.5 illustrates the light intensity values measured by the BH1750 sensor and their corresponding irradiance values after conversion. These are compared to the SISC sensor readings, demonstrating the conversion equation's effectiveness in translating light intensity measurements into accurate irradiance values. The microcontroller code for converting BH1750 readings into irradiance percentages with alerts is available upon request.

Table 3.5: Irradiance of BH1750 sensor compared to SISC sensor.

No.	SISC Sensor		Sun Brightness Lux	BH1750 Sensor		Shading percentage
	Voltage	Irradiance		Lux	Irradiance	
1	4.55	931	120000 - 110000	65500 - 59950	949	0 %
2	3.64	745	90000 - 85000	49000 - 46000	712	20 %
3	2.73	560	65500 - 62000	35500 - 33700	518	40 %
4	1.83	375	42500 - 40000	23000 - 21800	336	60 %
5	0.92	188	23500 - 22000	12800 - 12000	184	80 %
6	0.51	106	16000 - 15000	9000 - 8000	126	90 %

3.5.3.4 DS18B20 Sensor Address Management

To effectively manage nine DS18B20 temperature sensors on a microcontroller, the process begins with scanning the One-Wire bus to detect all connected sensors and retrieve their unique 64-bit addresses. This critical step, typically performed within the setup function, allows the program to uniquely identify and communicate with each sensor individually. Once retrieved, these addresses are stored in an array for later reference, ensuring precise identification and communication on the One-Wire bus.

The code implementation typically includes libraries for One-Wire communication and Dallas Temperature sensors. The setup function scans for sensors, stores their addresses, and optionally prints them for verification. The main loop would then use these addresses to read temperature data from individual sensors. Table 3.6 presents the output data, listing the sensor addresses for all sensors connected to the microcontroller during program execution.

Table 3.6: The DS18B20 sensors' addresses obtained after code execution.

No	DS18B20 Sensors	DS18B20 Addresses
1	Sensor 1	{0x28, 0xFF, 0x1C, 0x1A, 0x64, 0x15, 0x03, 0x9C}
2	Sensor 2	{0x28, 0xFF, 0x3D, 0x4B, 0x64, 0x15, 0x03, 0xF3}
3	Sensor 3	{0x28, 0xFF, 0x4E, 0x5C, 0x64, 0x15, 0x03, 0xE1}
4	Sensor 4	{0x28, 0xFF, 0x5F, 0x6D, 0x64, 0x15, 0x03, 0xF4}
5	Sensor 5	{0x28, 0xFF, 0x6A, 0x7E, 0x64, 0x15, 0x03, 0xD8}
6	Sensor 6	{0x28, 0xFF, 0x7B, 0x8F, 0x64, 0x15, 0x03, 0xC7}
7	Sensor 7	{0x28, 0xFF, 0x8C, 0x9A, 0x64, 0x15, 0x03, 0xAB}
8	Sensor 8	{0x28, 0xFF, 0x9D, 0xAB, 0x64, 0x15, 0x03, 0x9F}
9	Sensor 9	{0x28, 0xFF, 0xAE, 0xBC, 0x64, 0x15, 0x03, 0x8D}

The flowchart of the microcontroller programming for the DS18B20 sensors is shown in Figure B.3, and a summary summary of the DS18B20 sensor management code is available upon request.

3.5.3.5 Microcontroller program implementation

The microcontroller, programmed in Micro C, manages sensor readings and communication between the SCU and PCU. The SCU uses a BH1750 light sensor and nine DS18B20 temperature sensors to monitor and report conditions, triggering alerts for high temperatures, light anomalies, and sensor malfunctions. The PCU processes this data to control the solar system, disconnecting shaded panels, reconfiguring connections, and optimizing performance for maximum efficiency.

3.5.3.5.1 Implementation of SCU Software

The implementation of the SCU involves programming a microcontroller to manage sensor readings, data processing, and communication protocols. The SCU integrates a BH1750 light sensor and nine DS18B20 temperature sensors, with the microcontroller handling data collection, condition monitoring, and communication with the PCU.

The SCU software includes several key features to ensure optimal monitoring and communication. Notifications are sent when panel temperatures exceed set limits, triggering **Temperature Threshold Alerts**. **Light Sensor Anomalies** are detected through the light sensor, generating alerts if reduced values suggest dirt accumulation on the panels. The system also issues **Sensor Malfunction Alerts** to notify users of discrepancies or wire breaks in the temperature sensors. Additionally, **Communication Integrity** is maintained by continuously monitoring the connection between the SCU and PCU, with alerts issued for any loss of communication.

The microcontroller operation begins with an initialization phase, ensuring all sensors and serial communications are correctly set up. During this phase, the connection to each temperature sensor is validated, and any issues are flagged for user attention before data collection begins. The system then enters the main loop, where light intensity readings are continuously monitored to detect decreases or imbalances that might indicate issues such as dirt accumulation on the panels. Simultaneously, temperature readings are checked for disconnections or high temperatures that may require intervention. The SCU transmits all relevant sensor data to the PCU at regular intervals, ensuring real-time monitoring and response. Figure B.4 provides a flowchart of the SCU's operational workflow, outlining initialization, monitoring, alerting, and data transmission processes. The microcontroller code, including alert mechanisms, is available upon request.

3.5.3.5.2 Implementation of PCU Software

The PCU software processes sensor data to analyze shading conditions and optimize solar system performance. The controller algorithm uses data from various sensors to make decisions based on the shading affecting the solar panels. It implements several procedures to control the solar system effectively, including:

A. First Procedure (Shading Threshold)

The PCU algorithm starts by continuously monitoring the shading levels of all solar panels using the SISC sensors attached to each panel. When the algorithm detects that any panel has surpassed the shading threshold, which is set at 50%, it promptly disconnects the affected panel from the system. This proactive measure helps to prevent a decline in overall system efficiency. After the disconnection, the PCU recalculates the system's energy output, ensuring that optimal energy generation is maintained despite the reduced generating capacity. Figure 3.31 shows a flowchart that illustrates the process implemented by the PCU algorithm for handling shading thresholds

Relay operation and condition within an SB follows a specific protocol. Default State (No Shadows), in the default state, when there are no shadows on either solar panel, both relays in each switching block remain in their closed position (normally closed). This configuration connects the solar panels in parallel, which results in doubling the current while keeping the voltage constant. For instance, if (V_1) and (V_2) are the output voltages of the two solar panels, then ($V_1 = V_2$). Shadowed State (Both Panels), Shade detection triggers a reconfiguration strategy. When shadows fall on both panels, the relays switch to the normally open position, connecting the panels in series. This increases the overall output voltage, which helps maintain the output current. For instance, if (I_1) and (I_2) are the output currents of the two solar panels, then ($I_1 = I_2$). Partial Shading (One Panel), partial shading on a single panel necessitates further adaptation. In situations where one solar panel is shaded and consequently produces a lower output voltage than the other, the relay associated with the shaded panel switches to its normally open position, disconnecting the shaded panel. This prevents the shaded panel from adversely affecting the overall system performance. Table 3.7 details the behavior of the SB under different conditions, indicated by the control functions (C_i).

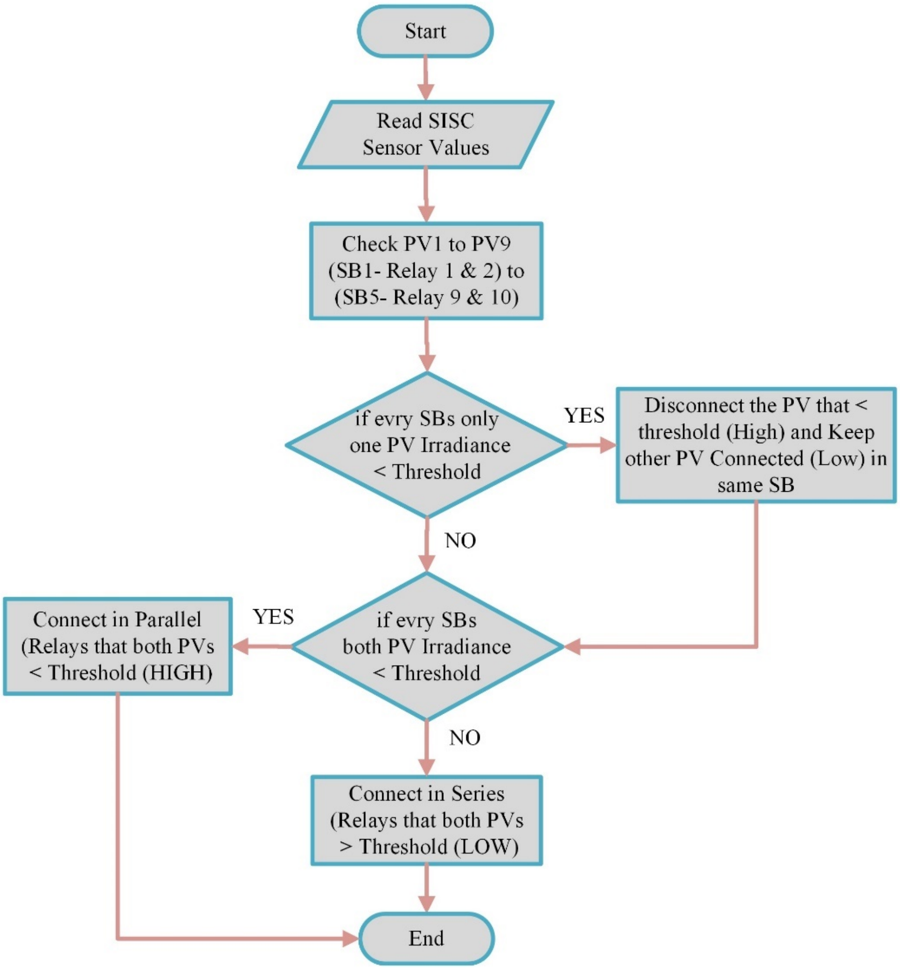

Figure 3.31: Shading threshold process flowchart.

Table 3.7: details the behaviour of the switching block (SB).

Shading Status		**C1**	**C2**	**Output Voltage**	**Output Current**
PV1	**PV2**				
NO Shading	NO shading	0	0	$V_1 // V_2$	$I_1 + I_2$
NO Shading	Shading	0	1	V_1	I_1
Shading	NO Shading	1	0	V_2	I_2
Shading	Shading	1	1	$V_1 + V_2$	$I_1 // I_2$

where ($i \in \{1, 2\}$). Here, ($C_i = 0$) means the relay is normally closed, and ($C_i = 1$) means the relay is normally open. The switching mechanism is governed by control functions (C_i), which are implemented by a PCU. The PCU dynamically adjusts the relay states based on the shading conditions to optimize the performance of the solar panels. These control functions ensure that the system adapts to varying environmental conditions, maintaining optimal voltage and current outputs.

B. Second Procedure (Layer Probabilities)

This procedure is activated when the output power remains unchanged or shows minimal variation after implementing the first procedure. The algorithm then applies a probabilistic approach to reconfigure the system. Each layer within the system is assigned a probability value, either 0 or 1. A probability of 0 indicates that all relays in the layer are in a parallel configuration, meaning the relays remain in their normally closed position. Conversely, a probability of 1 signifies that all relays in the layer are in a series configuration, meaning the relays switch to their normally open position. Given that the proposed system consists of three layers, this results in eight possible combinations of probabilities (2^3). However, two of these combinations, where all layers are either fully in parallel or fully in series, are excluded, leaving six valid configurations. Table 3.8 outlines the specific assignment of probabilities to each layer of the system. Figure 3.32 shows a flowchart that illustrates the process implemented by the PCU algorithm for managing layer probabilities.

Table 3.8: The probability distribution across the system's layers.

No.	Layer 1 Connections Type	Layer 2 Connections Type	Layer 3 Connections Type	Control Function Code
1	*Series*	*Series*	*Series*	000
2	*Parallel*	*Series*	*Series*	100
3	*Series*	*Parallel*	*Series*	010
4	*Parallel*	*Parallel*	*Series*	110
5	*Series*	*Series*	*Parallel*	001
6	*Parallel*	*Series*	*Parallel*	101
7	*Series*	*Parallel*	*Parallel*	011
8	*Parallel*	*Parallel*	*Parallel*	111

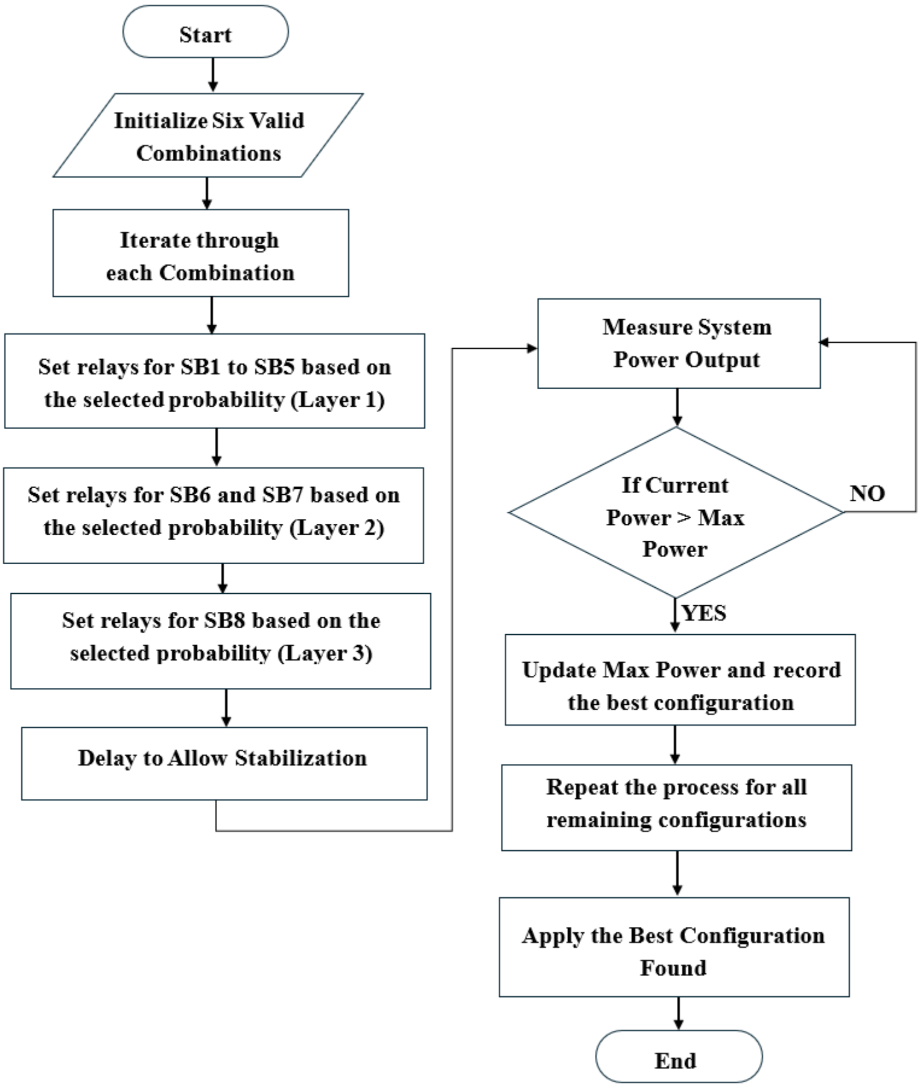

Figure 3.32: Layer probabilities process flowchart.

C. Third procedure (SBs Probabilities)

This procedure involves algorithmic optimization for maximizing output power and minimizing shadow losses by expanding the probabilities base and tracking the MPPT. Specifically, the algorithm assigns probabilities to each SB in the system to optimize their collective performance. Given that the system includes eight SBs, this results in a total of 256(2^8) probability combinations, presenting a significant computational and practical challenge.

To manage the complexity, the problem was strategically addressed by simplifying the probability array, thereby reducing the number of considered probabilities through a targeted reorganization of the probability array. In the first layer of the switch array, probabilities were consolidated into two groups: one combining SB1 and SB2, and another combining SB3, SB4, and SB5. This grouping reduces the dimensionality of the probability space, making the number of combinations more manageable while retaining essential system performance data. In the second layer, the Switching Blocks are further divided by assigning individual probabilities to

SB6 and SB7, while SB8 is assigned a probability in the third layer. This refined model concentrates on the most impactful variables by reducing the number of SBs from 8 to 5, effectively decreasing the total number of distinct probability states from 256 to 32 (2^5). In this configuration, scenarios where all switch blocks are either fully in parallel or fully in series are excluded, resulting in 30 valid probability configurations. This streamlined approach effectively narrows the probability space. Additionally, it enables precise MPPT tracking, ensuring the system operates at maximum efficiency even in the presence of shadows and other environmental factors. Table 3.9 presents the probability distributions assigned to each SB within the proposed system during Procedure Three. Figure 3.33 shows a flowchart that illustrates the process implemented in the third procedure (SBs Probabilities).

Table 3.9: The probability distribution across the system's SBs for procedure three.

No.	**SB1, SB2 Probabilities**	**SB3, SB4, SB5 Probabilities**	**SB6 Probabilities**	**SB7 Probabilities**	**SB8 Probabilities**	**Control Function Code**
1	*Series*	*Series*	*Series*	*Series*	*Series / Parallel*	*0000X*
2	*Parallel*	*Series*	*Series*	*Series*	*Series / Parallel*	*1000X*
3	*Series*	*Parallel*	*Series*	*Series*	*Series / Parallel*	*0100X*
4	*Parallel*	*Parallel*	*Series*	*Series*	*Series / Parallel*	*1100X*
5	*Series*	*Series*	*Parallel*	*Series*	*Series / Parallel*	*0010X*
6	*Parallel*	*Series*	*Parallel*	*Series*	*Series / Parallel*	*1010X*
7	*Series*	*Parallel*	*Parallel*	*Series*	*Series / Parallel*	*0110X*
8	*Parallel*	*Parallel*	*Parallel*	*Series*	*Series / Parallel*	*1110X*
9	*Series*	*Series*	*Series*	*Parallel*	*Series / Parallel*	*0001X*
10	*Parallel*	*Series*	*Series*	*Parallel*	*Series / Parallel*	*1001X*
11	*Series*	*Parallel*	*Series*	*Parallel*	*Series / Parallel*	*0101X*
12	*Parallel*	*Parallel*	*Series*	*Parallel*	*Series / Parallel*	*1101X*
13	*Series*	*Series*	*Parallel*	*Parallel*	*Series / Parallel*	*0011X*
14	*Parallel*	*Series*	*Parallel*	*Parallel*	*Series / Parallel*	*1011X*
15	*Series*	*Parallel*	*Parallel*	*Parallel*	*Series / Parallel*	*0111X*
16	*Parallel*	*Parallel*	*Parallel*	*Parallel*	*Series / Parallel*	*1111X*

The "X" in the control function code indicates that the last bit can be either 0 or 1, representing "Series" or "Parallel" for the combination of SB8.

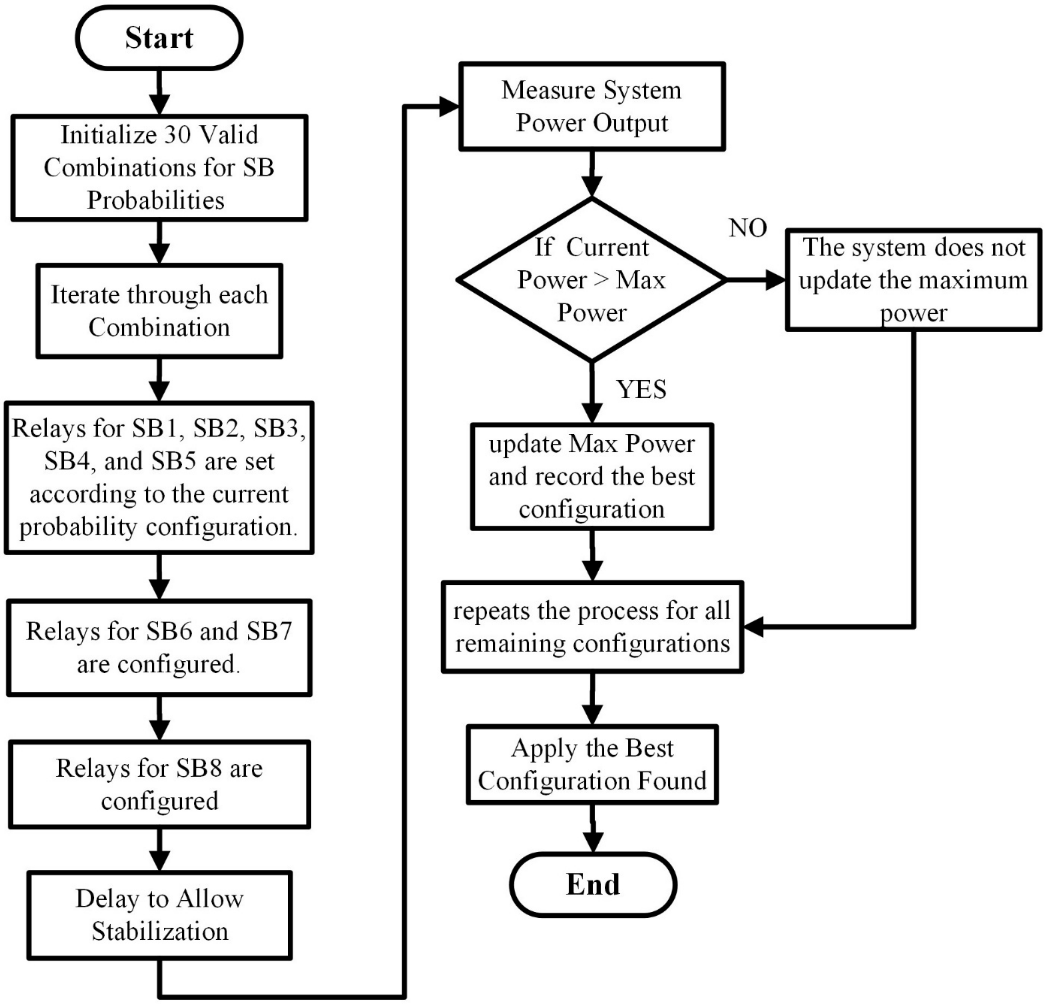

Figure 3.33: Flowchart of the SBs probabilities optimization process.

3.5.3.5.2.1 The high-temperature PV panel isolation mechanism is a critical system designed to protect solar panels from thermal damage and maintain overall system stability. This mechanism is implemented through the algorithm in the second and third procedures, where panels that are more than 50% shaded remain within the system matrix and are not separated. Partially shaded panels tend to overheat, becoming thermal loads. To mitigate this, the isolation mechanism works by disconnecting solar panels that exceed their permissible temperature range. Temperature sensors continuously monitor the PV panels' temperature; if it rises above the set threshold, the sensors send alerts to the CPU via the SCU. In response, the PCU algorithm initiates the process of isolating the affected panel. Figure 3.34 shows a flowchart that illustrates the process implemented by the PCU algorithm for isolating high-temperature PV panels

The procedure for isolating any affected panel within the system involves a series of status checks for the SB to which the panel is directly connected. Specifically, this includes verifying the status of the relay inside the SB that connects to the affected panel. For instance, in the case of PV2, which is connected to relay 2 within SB1, where relay 1 is also located, the isolation protocol follows the steps outlined below:

1. Isolation Procedure for a Single Affected PV Panel:

This procedure is implemented when only one relay within the SB is affected. Under normal operating conditions, both relays (relay 1 and relay 2) are in the normally closed position (0), meaning the panels remain connected to the system. In this configuration, the connection between the two relays is parallel. When the main controller detects a high-temperature alert from PV2, it instructs relay 2 to switch to the open position (1), thereby disconnecting PV2 from the system while keeping relay 1 in the closed position (0). If, however, both relays are found in the open position (1), indicating that the panels are connected in series, the controller issues a command to switch relay 1 to the closed position (0) while maintaining relay 2 in the open position (1), which effectively disconnects PV2.

2. Isolation Procedure of two panels

This procedure is implemented when two relays within the same SB are affected. In situations where both relays in the same SB are compromised—such as when PV1 is also exposed to a temperature rise alongside PV2 in SB1—the algorithm escalates to the secondary layer of SBs. In this scenario, SB6, to which SB1 is linked via relay 11, is involved. SB2 is similarly connected via relay 12. The algorithm first checks the state of SB6: if both relays are in the closed position (0), the controller commands relay 11 to switch to the open position (1), while relay 12 remains closed (0), effectively disconnecting SB1—and consequently PV1 and PV2—from the system. Conversely, if both relays are in the open position (1), the controller instructs relay 12 to switch to the closed position (0), leaving relay 11 open (1), thereby isolating both PV1 and PV2.

3. Isolation Procedure of multiple panels

This procedure is implemented when a group of relays across multiple SBs is affected. If a temperature rise affects PV panels 1 through 4, the algorithm further escalates to the tertiary layer of SBs, specifically targeting SB8. In this case, relay 15 is used to disconnect both SB1 and SB2 from the system, thereby isolating PV panels 1 to 4. This process mirrors the method applied in SB6, ensuring a systematic approach to isolating affected components while maintaining overall system integrity.

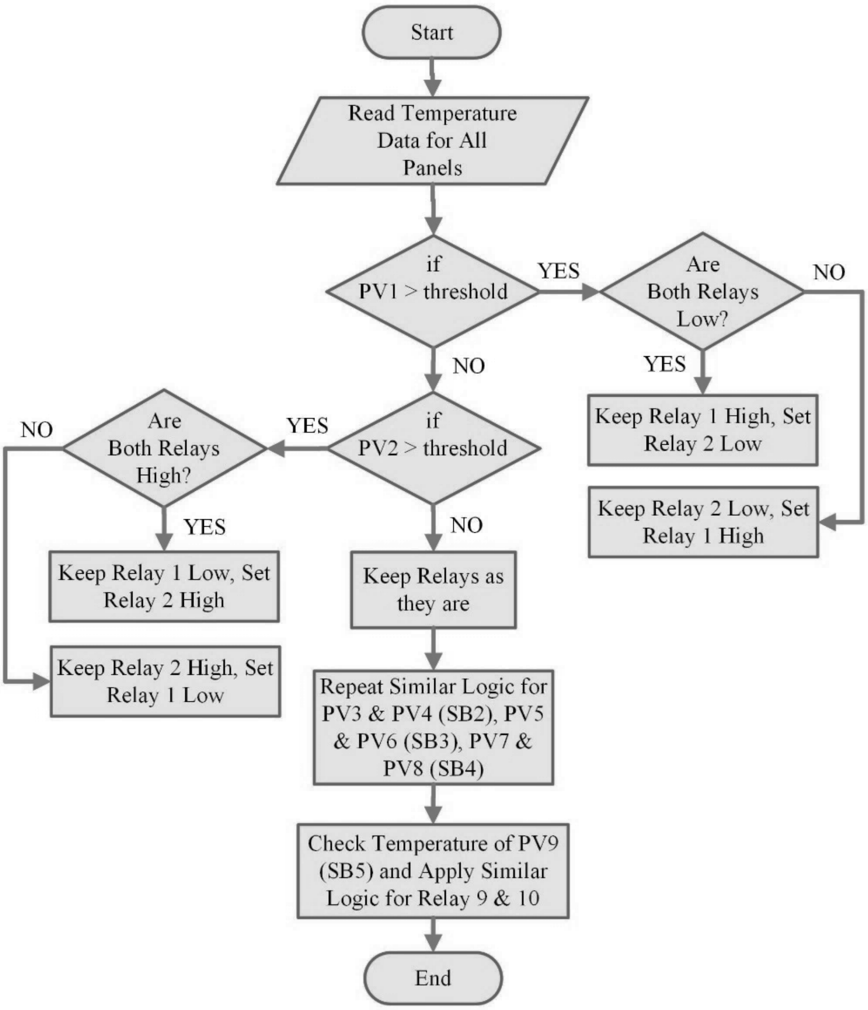

Figure 3.34: High-temperature PV panel isolation flowchart.

3.5.3.5.2.2 Multiple voltage and current sensors exist in its hierarchical structure. In the initial phase, the voltage of the PV panels is measured by four voltage sensors embedded within the SBs of the first layer, managed by the PCU algorithms. These sensors are crucial for determining the panels' voltage output, providing essential data for estimating the overall system voltage and, consequently, the level of incident solar irradiation. Additionally, the algorithm employs a custom-designed voltage sensor at the third layer, paired with a current sensor, to accurately measure the system's final total voltage and current, ensuring precise and comprehensive performance monitoring. This sensor data plays a pivotal role when integrated into the broader system operations.

1. Comparative Analysis with SISC Sensors

The voltage values obtained from these sensors are utilized for comparative analysis with data from the SISC sensors. This comparison is essential since the SISC sensors detect reductions in solar irradiation caused by shadows on one or more PV panels. Concurrently, the voltage sensors measure the corresponding voltage drop attributed to the shadow. The system is designed to ensure that the results from the SISC sensors and the voltage sensors align closely, with a permissible error margin of no more than 5%.

2. Individual PV Panel Voltage Measurement

The system implements a systematic approach for measuring the voltage of any specific PV panel by controlling its associated SB. Each panel’s voltage measurement involves selectively activating relays within the SB to isolate the desired panel. For instance, to determine the voltage output of PV panel 3, the algorithm operates via SB2. The algorithm sends a control instruction (0) to relay 3 (associated with PV panel 3 in SB2) and simultaneously sends a control instruction (1) to relay 4 (associated with PV panel 4 in SB2). As a result, the output of SB2 exclusively reflects the voltage of PV panel 3.

Next, control instruction (0) is issued to relay 12, which is connected to SB2, while instruction (1) is sent to relay 11, connected to SB1, both of which are located in SB6. The sequence is concluded by sending instruction (0) to relay 15 connected to SB6 and instruction (1) to relay 16, both located in SB8. The systematic relay control process, as depicted in Figure 3.35, ensures isolated and accurate voltage measurement for individual PV panels within the system. This method allows the algorithm to perform an approximate comparison of solar irradiation with the SISC sensor associated with panel 3, leveraging the mathematical models previously introduced (refer to Equation 6). The process facilitates accurate assessment and compensation for variations in solar irradiation that impact the performance of individual PV panels. Table 3.10 provides a comprehensive sequence of the algorithm's instructions for reading the voltage value of each PV panel.

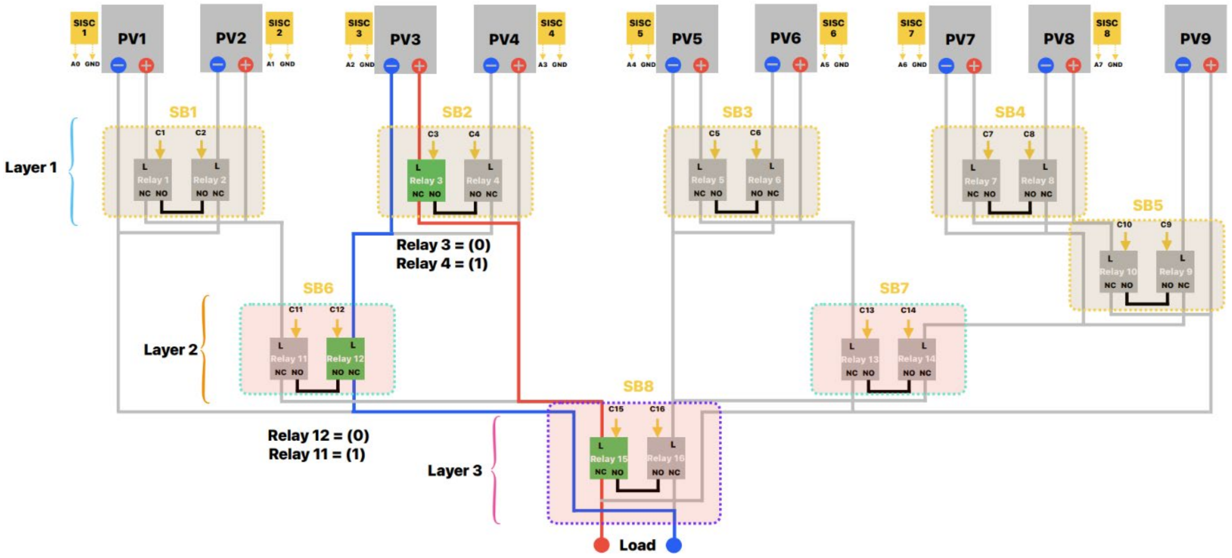

Figure 3.35: A schematic representation of the voltage measurement process for panel 3.

Moreover, these localized measurements contribute to an overarching assessment of system performance.

Table 3.10: The procedure of the algorithm's instructions for measuring the voltage and current of any PV panel within the system involves controlling its associated SB.

No. of PV Panels	**SB1**		**SB2**		**SB3**		**SB4**		**SB5**		**SB6**		**SB7**		**SB8**	
	Relay 1	**Relay 2**	**Relay 3**	**Relay 4**	**Relay 5**	**Relay 6**	**Relay 7**	**Relay 8**	**Relay 9**	**Relay 10**	**Relay 11**	**Relay 12**	**Relay 13**	**Relay 14**	**Relay 15**	**Relay 16**
PV1	0	1	-	-	-	-	-	-	-	-	0	1	-	-	0	1
PV2	1	0	-	-	-	-	-	-	-	-	0	1	-	-	0	1
PV3	-	-	0	1	-	-	-	-	-	-	1	0	-	-	0	1
PV4	-	-	1	0	-	-	-	-	-	-	1	0	-	-	0	1
PV5	-	-	-	-	0	1	-	-	-	-	-	-	0	1	1	0
PV6	-	-	-	-	1	0	-	-	-	-	-	-	0	1	1	0
PV7	-	-	-	-	-	-	0	1	1	0	-	-	1	0	1	0
PV8	-	-	-	-	-	-	1	0	1	0	-	-	1	0	1	0
PV9	-	-	-	-	-	-	-	-	0	1	-	-	1	0	1	0

3. Hierarchical Voltage Computation

The system's overall voltage estimation is derived from sensor readings taken from the first-level SBs. The calculation methodology depends on the configuration of connections between hierarchical switch blocks. Upon acquiring voltage values from these blocks, the algorithm determines the system's total voltage based on the interconnection type (series or parallel) among the blocks.

Specifically, SB1 and SB2 from the first layer are connected to SB6 in the second layer, while SB3 and SB5 are connected to SB7. The algorithm analyzes the connection between SB6 and SB7 to compute the voltage at this intermediate layer. Since SB6 and SB7 are further connected to the final block (SB8), the algorithm computes the system's overall voltage by evaluating the configuration within SB8. Table B.1 provides a comprehensive overview of the computation methodology, detailing the specific equations and logic employed by the algorithm to calculate the voltage values for each SB.

4. System Power Measurement on Load SB

The implemented voltage sensor and current sensor are strategically positioned at SB8, which serves as the final output stage in the hierarchical switch block architecture. SB8 functions as the central node in this configuration, where power from the various panels is aggregated and prepared for output to the load. As the concluding stage in the hierarchical system, SB8 gathers and analyses the combined electrical output from all panels, ensuring stable and optimized power delivery throughout the PV system.

3.5.3.6 XBee and Real-Time Data Display

In the PCU software implementation, the XBee module is integrated to facilitate wireless communication for real-time monitoring of critical system parameters, with the data displayed on the Arduino IDE serial monitor. The `sendDataToComputer()` function handles both the data transmission and display by collecting and formatting measurements such as voltage, current, power, temperatures of individual PV panels, and solar irradiance. These values are gathered from various sensors and transmitted in a structured, labeled format using the serial interface, enabling seamless data communication via the XBee module while displaying the results in real time on the Arduino IDE. The software's modular approach allows for monitoring of system performance. This implementation supports reliable remote monitoring and can be easily scaled for larger systems or extended with additional sensors, enhancing the overall functionality of the PCU.

Together, these processes form a comprehensive and layered approach to monitoring, controlling, and optimizing the PV system, from individual panel measurements to system-wide performance analysis.

3.6 Summary

This chapter introduces the design, research methodology, and implementation of a system aimed at optimizing solar energy systems under partial shading conditions. Moreover, I argue that integrating hardware and software components — including photovoltaic (PV) panels, microcontrollers, and sensors — can effectively address the challenges posed by partial shading through dynamic reconfiguration and control.

In this research, I have developed the system in three key areas: the integration of hardware and software components for dynamic PV array reconfiguration, the use of both practical experimentation and computer simulation to evaluate system performance, and the implementation of hierarchical switching block architectures (Model-A and Model-B) for flexible system adaptation. Moreover, I presented a comprehensive approach that includes both MATLAB/Simulink simulations and real-world hardware implementations to validate the system's effectiveness under various shading scenarios.

To facilitate the optimization of PV system performance under partial shading conditions, the proposed system employs dynamic reconfiguration strategies, real-time data acquisition, and control algorithms. The expected benefits of this system are improved energy harvesting efficiency, enhanced adaptability to changing environmental conditions, reduced mismatch losses, and increased overall reliability and performance of PV arrays.

Thesis I *[1][3][4]*

I have introduced a comprehensive system design and research methodology to enable dynamic PV array reconfiguration under partial shading conditions. This approach involved developing and comparing two conceptual frameworks: Model-A and Model-B. Model-A, simulated and practically implemented, connected every two solar panels with a single switching block, simplifying the hierarchical structure. Model-B offered a more advanced configuration by linking every three panels through two SBs within a link block, thereby enabling greater flexibility and the option to replicate various conventional PV arrangements such as SP, BL, and TCT.

I have integrated and calibrated essential components—microcontrollers, sensors, and relays—ensuring accurate data acquisition and reliable PV panel reconfiguration. In addition, I have introduced a hybrid simulation environment that combines MATLAB-Simulink with a microcontroller, confirming the practical feasibility and responsiveness of the chosen strategies. These efforts have laid a solid foundation for subsequent optimization and testing phases, ultimately enhancing the system's adaptability and overall performance under non-uniform irradiance conditions.

Chapter 4. Enhancing Photovoltaic Array Performance under Partial Shading through Dynamic Reconfiguration and Layer Equalization Algorithm

The content of this chapter has been published in the following paper:

- Ameen, F., Trohák, A., Siddiq, A., & Benotsmane, R. (2024, May). Enhancing Photovoltaic Array Performance under Partial Shading through Dynamic Reconfiguration and Layer Equalization Algorithm. In 2024 25th International Carpathian Control Conference (ICCC) (pp. 1-6). IEEE.

The current study concentrates on enhancing photovoltaic (PV) array performance under partial shading (PS) conditions. The Highest and Lowest Layer-Based Exchange (HLLBE) algorithm is proposed to address the challenges of uneven irradiance and optimize power output. The included experiment presents the findings that the proposed approach effectively improves system efficiency under diverse shading scenarios. Thus, the suggested algorithm, supported by the current chapter, provides scientific proof that the theoretical reconfiguration of PV arrays through MATLAB/Simulink software yields substantial improvements. The chapter demonstrates the algorithm's successful application and validation through simulation.

4.1 System Model

A. TCT Arrangement

Various methods exist for connecting PV arrays, including series-parallel, bridge-link, and TCT configurations [108]. The TCT stands out for its superior performance. In DR, irradiance conditions are mathematically modeled to create an initial irradiance matrix. An optimal configuration method for the PV array is then established based on these conditions, resulting in a new optimal irradiance matrix.

The TCT configuration was adopted due to its ability to generate maximum power under most shading patterns [32]. In the TCT, each row is interconnected in a simple parallel manner, and the current produced by a module under a specific irradiance Z is given by the following equation:

$$Irr_{m,n}\,(shaded) = \; K\,Irr_{m,n}(unshaded) \qquad (13)$$

$$K \; = Z_{m,n} \;/\; Z_{un} \qquad (14)$$

where m and n denote the rows and columns of the array, respectively. $Irr_{m,n}$ (shaded) and $Irr_{m,n}$ (unshaded) represents the module current during shaded and unshaded irradiance (1000 W/m^2) conditions, respectively. $Z_{m,n}$ represents the irradiance received by the module and Z_{un} represents the amount of unshaded irradiance.

B. Switching Block Array (SBA)

The SBA is a DR structure that enables flexible and efficient connection of system components, particularly PV panels, without altering the wiring or physical design. It allows real-time reconfiguration and connection changes without system shutdown. However, using the switch matrix may introduce increased signal delay, and the SBA design and manufacturing costs can be high for certain applications. The SBA is an essential component in the reconfiguration of dynamic PV arrays. It allows the array configuration to be changed quickly and easily, providing greater flexibility in power management and improved productivity. The SBA consists of a set of switches connected to PV modules. Figure 4.1 shows the SBA of a PV module using single-pole double-throw switches. Solar irradiance (SI) sensors provide data for the switching matrix to determine the optimal arrangements of PV modules. The algorithm adjusts connections based on shading conditions and redistributes panels across rows. The switching matrix executes actions by disconnecting and reconnecting the PV modules according to the algorithm's plan.

The operation of the switches is controlled by a reconfiguration algorithm. The number of switches required for reconfiguration depends on the number of modules and levels in the array. The equation for calculating the total number of switches (SW_T) in a PV array with dimensions $m \times n$ is expressed as follows:

$$SW_T = m \times n \times 4 \qquad (15)$$

The operational paradigm of the switch system in Figure 4.1 is as follows: When all switches (1, 2, 3, and 4) are in the OFF position, a PV panel is connected to Layer One. For Layer Two, switches 1 and 3 are ON, whereas switches 2 and 4 remain OFF. For Layer Three, all switches are ON, connecting the panel to the third layer. These switches enable swift modifications to the matrix configuration, thereby enhancing system adaptability.

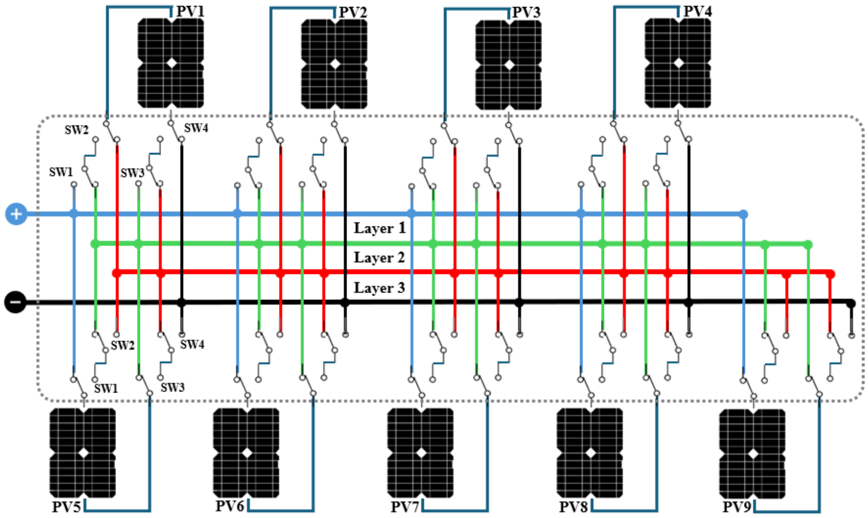

Figure 4.1 :Design of Switching Block Array (SBA).

The SBA design features a significant reduction in the number of switches, surpassing 30% compared to similar systems. This streamlined design reduces complexity, simplifies maintenance, and ensures a high efficiency in switch energy consumption. Furthermore, a decreased number of switches enhances the practicality and effectiveness of the matrix by reducing its overall size.

4.2 Proposed HLLBE Algorithm

Radiation equalization optimizes power generation in solar PV systems by evenly distributing solar radiation among the PV modules. This is accomplished by adjusting the placement of the modules until rows with similar average radiation values are formed, ensuring consistent current generation and increased overall power output. This approach reduces the losses from radiation imbalances and enhances the efficiency.

The proposed HLLBE algorithm was developed to ensure a uniform current across all layers (rows) in the PV array. The restructured SBA achieves this by electrically altering the unit connections within the array, thereby equalizing the radiation levels across all rows. This process is facilitated by sensors mounted on solar panels, which measure the SI levels.

The HLLBE algorithm operates in several stages. Initially, it gathers individual solar radiation readings from each PV panel. It then sorts these readings and identifies their minimum and maximum levels. The algorithm then swaps the elements between the layers based on specific mathematical formulas to maximize the output power. A flowchart of the proposed HLLBE algorithm is shown in Figure 4.2. The HLLBE algorithm guarantees the best switch configuration that balances radiation in each layer (row) of the PV array. The proposed algorithm begins by initializing and collecting the radiation data for each unit in the PV array using SI sensors to determine the radiation location of each solar cell. It then computes the radiation for each layer separately to determine the balance value (M), with the aim of maintaining matrix elements close to this value. Next, the algorithm arranges the matrix elements based on the number of layers or rows, selecting the highest and lowest values and pairing them, with the highest assigned to the lowest for each layer, and distributing the remaining values among the layers. It computes the radiation for each layer and compares it with the balance value, resorting to the values vertically based on probabilities and repeating until each layer's radiation value is close to the balance value. Once balance is achieved between layers, the algorithm sends control commands to the SBA for electrical reconfiguration during PV AR, measures the total current, and compares it with the initial total current before the reconfiguration process begins.

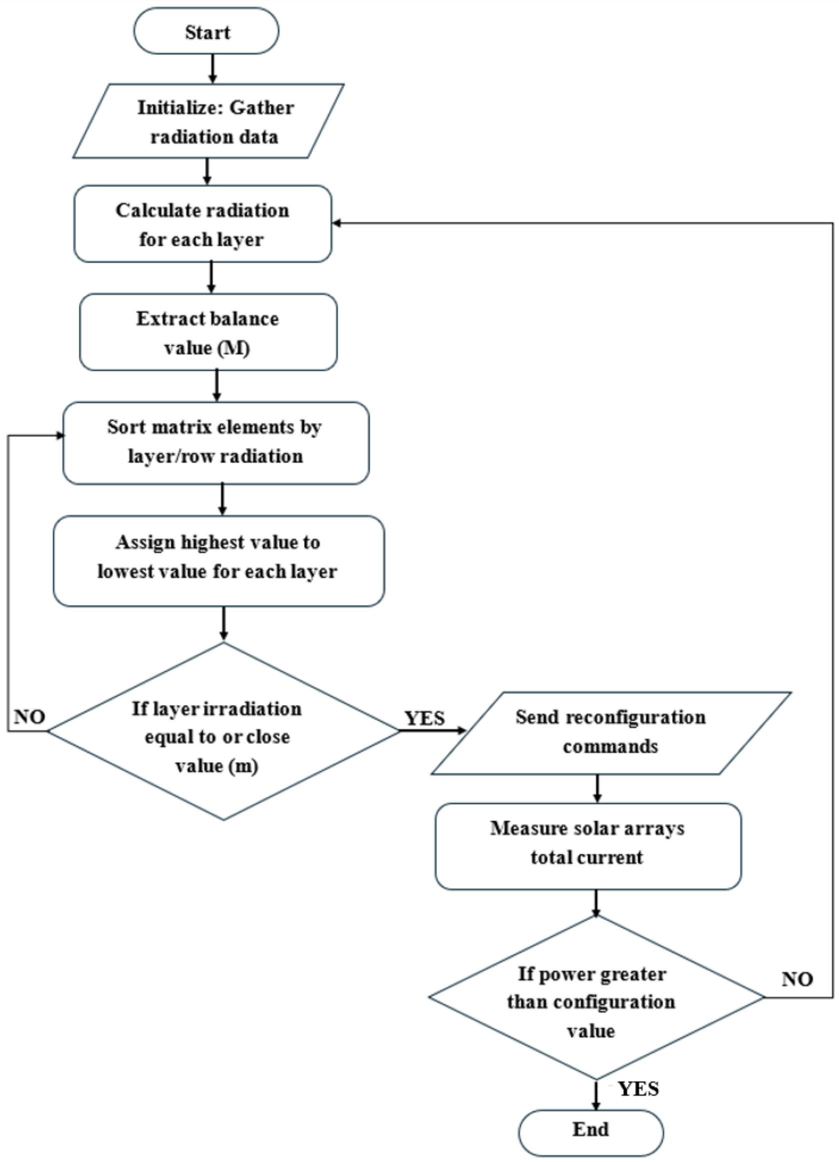

Figure 4.2 :Flowchart of the HLLBE algorithm.

The proposed algorithm simplifies complex optimization techniques using a straightforward sorting and mapping process. This reduces the computational burden, speeds up processing, and improves system functionality. This method is flexible across different array sizes, eliminating the need for specific algorithms for each dimension. It offers versatility, potential cost savings in terms of hardware resources, and easier maintenance and troubleshooting. Overall, the approach streamlines algorithms, making them more comprehensible and adaptable for future enhancement.

4.3 Results and Simulations

Simulations and analysis studies were conducted on a dynamic PV array consisting of nine PV panels (3 × 3). The specifications of the PV panels used as given in Table A.1 A virtual study of the shading patterns on solar modules was conducted in two stages. In the first stage, the shader was divided into three different cases, where the shaders were randomly oriented with irradiance values between 200 W/m^2 and 900 W/m^2. The second stage consisted of six cases, in which a fixed irradiance of 100 W/m^2 was applied in the case of shade, whereas the unshaded units were assumed to receive 1000 W/m^2. This hypothesis seeks to highlight and better understand the effect of different shading modes on the performance of solar modules, and provides a comprehensive overview of how they interact when facing these changing circumstances. The associated mathematical analysis provided an in-depth examination of the effects of changes in shading patterns on the performance of solar systems.

In brief, in the first stage, the effect of random variations in shading intensity on energy extraction efficiency was examined. In contrast, the second stage highlights the effect of static shading with a value of 100 W/m^2 in the shadowed state, which can simulate static shading conditions, such as fixed structures or buildings.

A. Random Intensity Shading

Three test cases are considered. In the First Case, a fixed diagonal shading pattern was assumed, covering all PV modules in the array, as illustrated in Figure 4.3 (a). This shading pattern resulted in multiple peaks in the P-V curves of the PV modules. The layer currents corresponding to the TCT connections are also provided.

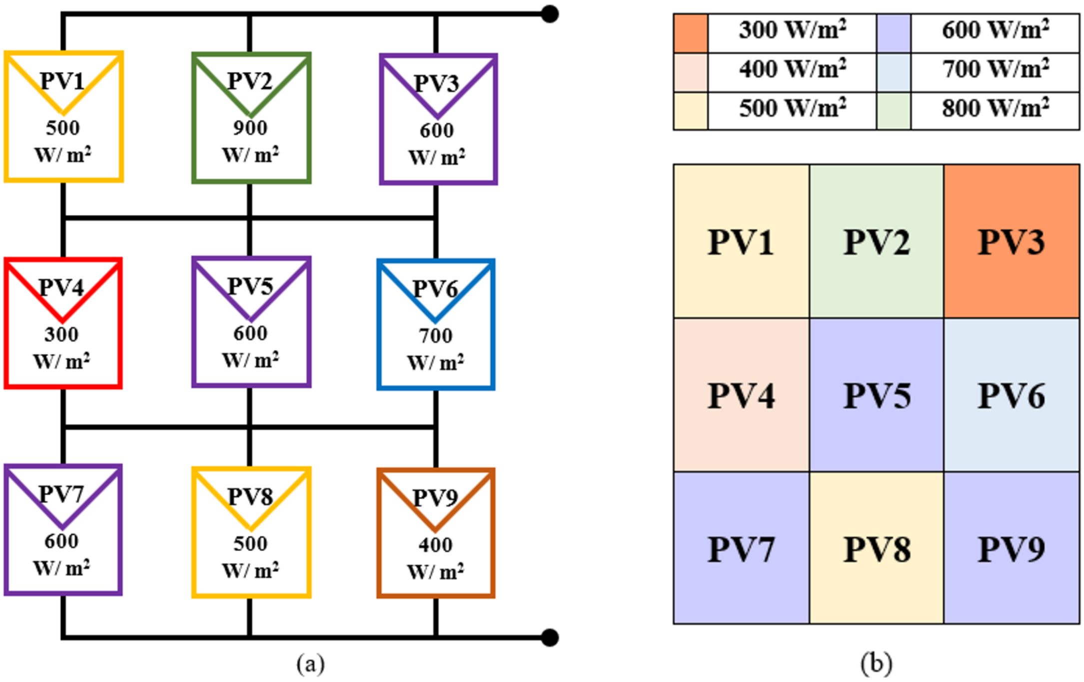

(a) (b)

Figure 4.3 : a) Shading pattern distributions in first case before reconfiguration. b) Shading pattern distributions in the first case after reconfiguration.

The HLLBE algorithm operates as follows:

$$Balance\ value(M) = L1 + L2 + .\, Ln\ /\ m \qquad (16)$$

$$Where\ L = PV1 + PV2 + \cdots .\, PVn \qquad (17)$$

Where L is the layer for one row, and m is no. of rows. PV is the solar panel. According to Equation (16), the M value for the first case was 1700. The layer current (IL) can be obtained using Equation (18).

$$ILn = Ln/1000 \times Im \qquad (18)$$

Where, Im is the maximum current. Therefore, the corresponding layer currents for the TCT connection in the First Cases are given by the following equations.

$$IL1 = 2000/1000 \times Im = 2 \times Im \qquad (19)$$
$$IL2 = 1600/1000 \times Im = 1.6 \times Im \qquad (20)$$
$$IL3 = 1500/1000 \times Im = 1.5 \times Im \qquad (21)$$

Following the reconfiguration shown in Figure 4.3 (b), the modules at positions PV3 and PV4 interchange, and subsequently, the modules at positions PV4 and PV9 also exchange their locations to equalize the irradiance. The current for each layer was provided after this reconfiguration as follows:

$$IL1 = 1700/1000 \times Im = 1.7 \times Im \qquad (22)$$
$$IL2 = 1700/1000 \times Im = 1.7 \times Im \qquad (23)$$
$$IL3 = 1700/1000 \times Im = 1.7 \times Im \qquad (24)$$

With a successful reconfiguration, all tier-irradiance values converged to an identical level, resulting in uniform tier currents. This phenomenon is shown in Figure 4.4, where the previously scattered peaks in the individual tier-current curves coalesced into a single, prominent global peak. This unified peak signifies the balanced state achieved within the PV array in which each tier contributes equally to the overall current output.

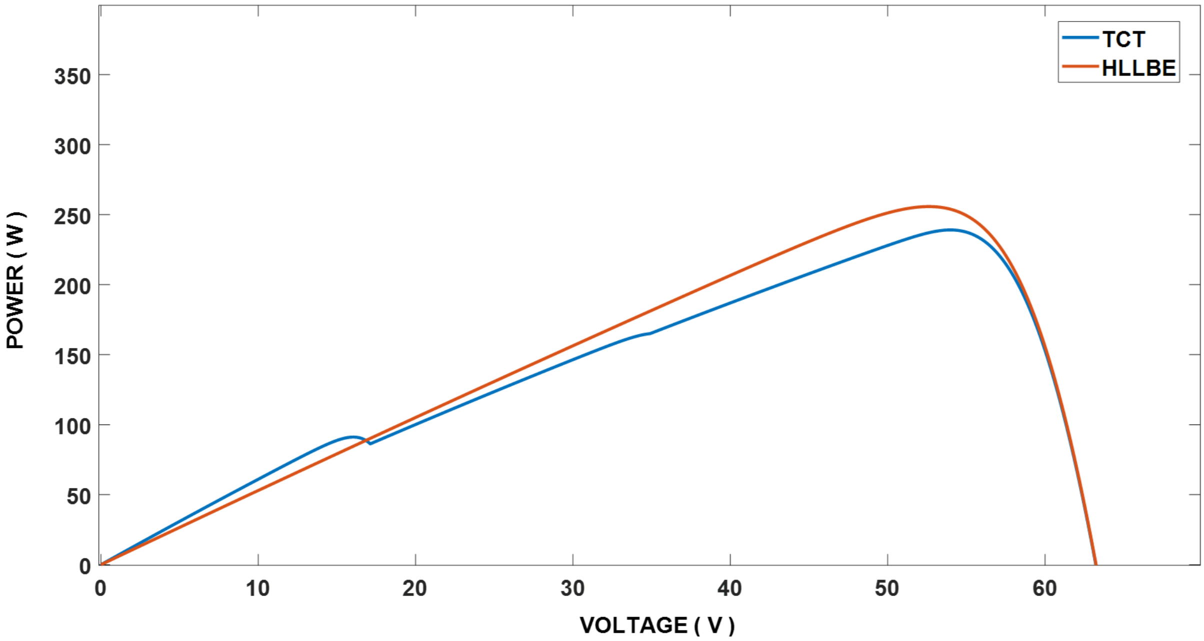

Figure 4.4 :P – V curves for shading patterns in the first case.

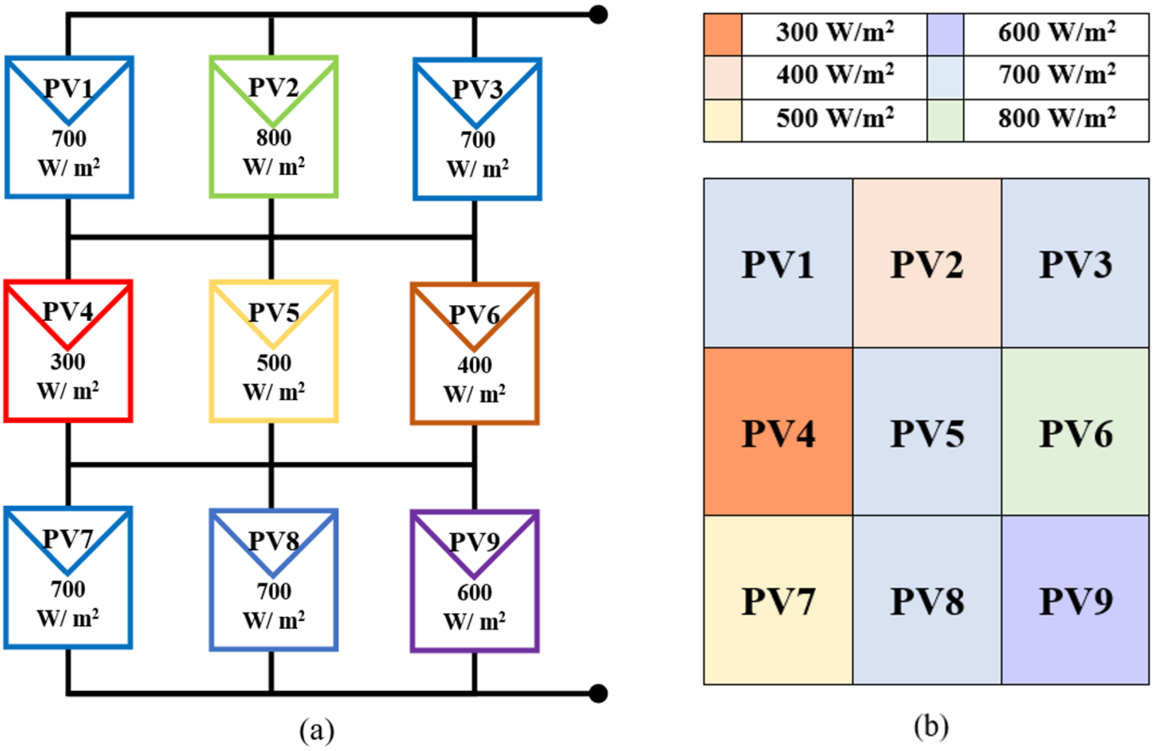

(a) (b)

Figure 4.5: a) Shading pattern distributions in the second case before reconfiguration. b) Shading pattern distributions in the second case after reconfiguration.

In the Second Case, the scenario investigated a PV array subjected to a randomized shading pattern, as illustrated in Figure 4.5 (a). The efficacy of the proposed algorithm is demonstrated by minimizing the number of peaks observed in the P-V characteristic curve. Before reconfiguration, the layer current for the Second Case is expressed as follows:

$$IL1 = 2200/1000 \times Im = 2.2 \times Im \tag{25}$$

$$IL2 = 1200/1000 \times Im = 1.2 \times Im \tag{26}$$

$$IL3 = 2000/1000 \times Im = 2 \times Im \tag{27}$$

After the reconfiguration process, the modules were located at positions PV2 and PV6. Following this, the modules at positions PV5 and PV7 also switch their positions to balance the irradiance, as shown in Figure 4.5 (b). The current for each layer after reconfiguration is expressed as follows:

$$IL1 = 1800/1000 \times Im = 1.8 \times Im \tag{28}$$

$$IL2 = 1800/1000 \times Im = 1.8 \times Im \tag{29}$$

$$IL3 = 1800/1000 \times Im = 1.8 \times Im \tag{30}$$

Figure 4.6 illustrates the elimination of multiple peaks in the power-voltage relationship during the second shading scenario. This occurred after the proposed algorithm effectively balanced the current values across each layer of the PV array.

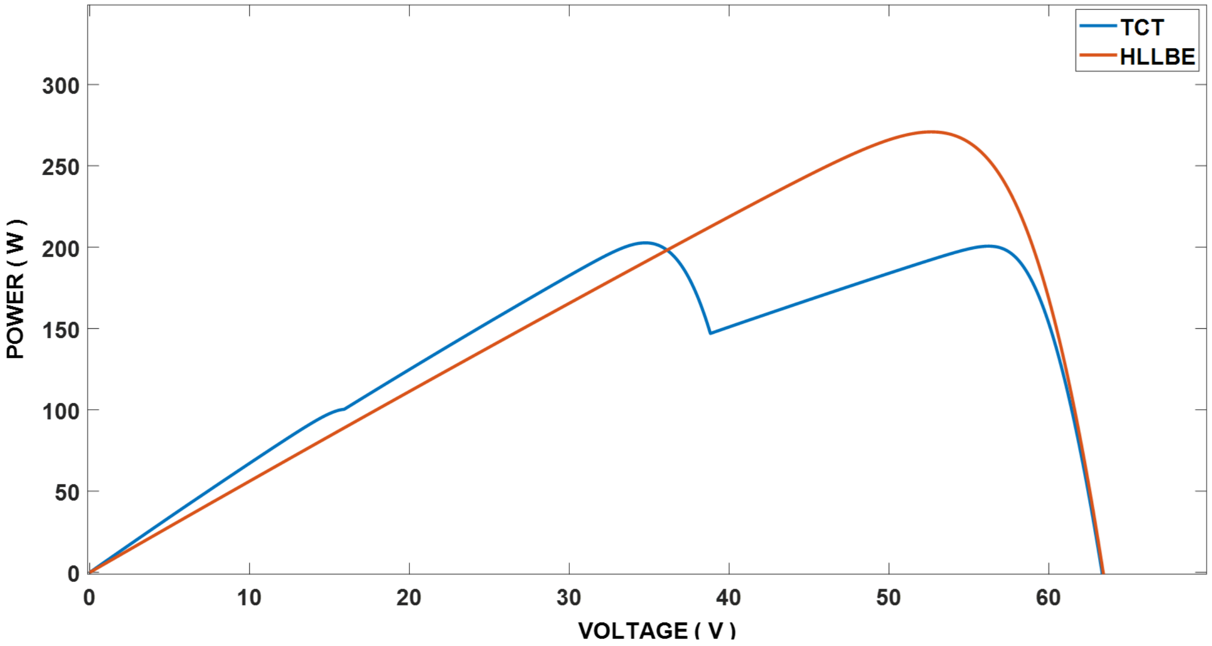

Figure 4.6: P – V curves for shading patterns in the second case.

In the Third Case, the shading patterns were distributed such that every pair of units within a single layer received an equal amount of SI, as illustrated in Figure 4.7 (a). The layer currents for the Third Case were as follows:

$$IL1 = 2000/1000 \times Im = 2 \times Im \qquad (31)$$

$$IL2 = 1200/1000 \times Im = 1.2 \times Im \qquad (32)$$

$$IL3 = 1800/1000 \times Im = 1.8 \times Im \qquad (33)$$

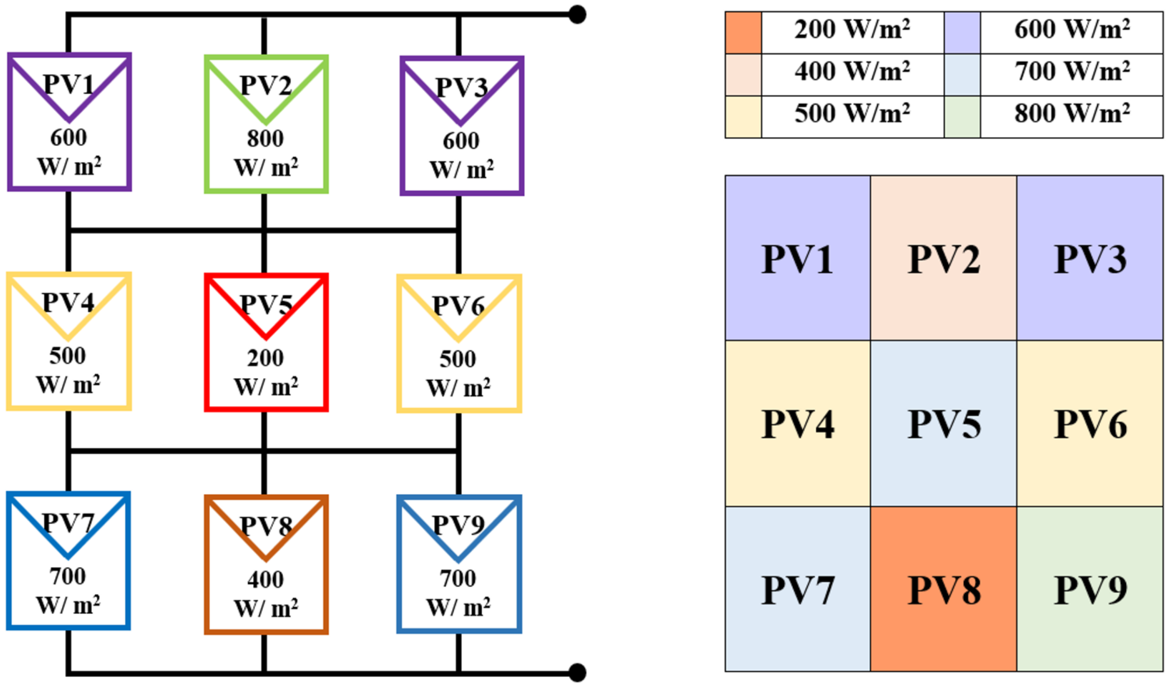

(a) (b)

Figure 4.7: a) Shading pattern distributions in the third case before reconfiguration. b) Shading pattern distributions in the third case after reconfiguration.

During the initial phase of the reconfiguration process, the modules at positions PV2 and PV5 are swapped, followed by a subsequent exchange between the modules at PV2 and PV8. To achieve balanced layer currents, the algorithm subsequently implements a resorting strategy, aiming for a value close to or equal to the M value. This involves swapping the positions of modules PV5 and PV9, as illustrated in Figure 4.7 (b). The current for each layer after reconfiguration is expressed as follows:

$$IL1 = 1600/1000 \times Im = 1.6 \times Im \tag{34}$$

$$IL2 = 1700/1000 \times Im = 1.7 \times Im \tag{35}$$

$$IL3 = 1700/1000 \times Im = 1.7 \times Im \tag{36}$$

Figure 4.8 illustrates the elimination of multiple peaks in the power-voltage relationship during the third shading scenario. This occurred after the proposed algorithm effectively balanced the current values across each layer of the PV array.

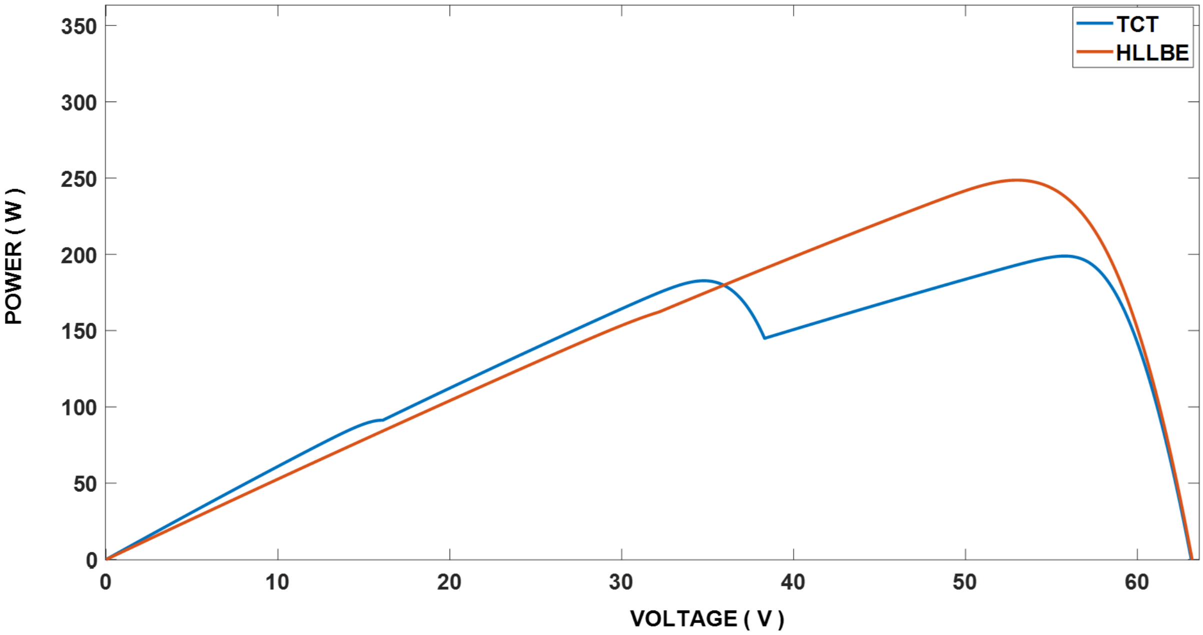

Figure 4.8 : P – V curves for shading patterns in the third case.

This comprehensive study provides a thorough understanding of the behavior of the system under different conditions. The proposed algorithm demonstrated a clear superiority over the conventional TCT configuration under diverse shading conditions. In the three distinct shading scenarios, efficiency improvements achieved by the HLLBE configuration over the TCT configuration were 19%, 21.7%, and 6.8%, respectively. These improvements were achieved due to the enhanced adaptability of the HLLBE approach in mitigating the effects of partial shading. The robust performance across various shading patterns highlights the effectiveness of the proposed system. The detailed results obtained during the implementation of the three shading scenarios are presented in Table 4.1.

Table 4.1: Comparison of current, voltage, power, and efficiency characteristics between TCT and Proposed HLLBE algorithm for the first stage.

Cases	**Configuration Type**	**V_{max} (V)**	**I_{max} (A)**	**P_{max} (W)**	Efficiency(η) = $\frac{P_{\text{shaded}}}{P_{\text{unshaded}}} \times 100\%$	$\eta Improvement = \frac{\eta \text{HLLBE} - \eta \text{TCT}}{\eta \text{TCT}} \times 100\%$
First Case	**TCT**	35.42	4.723	167.3	42	19
	HLLBE	38.78	5.171	200.5	50	
Second Case	**TCT**	37.25	4.967	185	46	21.7
	HLLBE	40.97	5.462	223.8	56	
Third Case	**TCT**	36.39	4.852	176.6	44	6.8
	HLLBE	37.41	4.988	186.6	47	

B. Static Shading

Different static shading patterns have different effects on the output characteristics of PV arrays. This study considered scenarios with fixed shading patterns that affected different numbers of adjacent panels, and each configuration resulted in specific peaks and variations in the PV curves.

In the first case, the analysis of shading patterns on the solar panels and a consistent shading configuration were considered. The first scenario entailed a fixed shading pattern impacting two consecutive PV panels situated in the initial row of the array, as shown in Figure 4.9 (a). This arrangement results in the emergence of distinct peaks in the PV curves of the affected units. The layer currents corresponding to the TCT connection in the initial case were also presented.

$$IL1 = 1200/1000 \times Im = 1.2 \times Im \qquad (37)$$
$$IL2 = 3000/1000 \times Im = 3 \times Im \qquad (38)$$
$$IL3 = 3000/1000 \times Im = 3 \times Im \qquad (39)$$

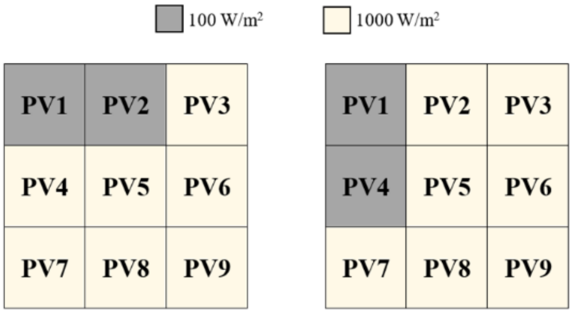

(a) (b)

Figure 4.9: a) Shading patterns of the first case before reconfiguration. b) Shading patterns of the first case after reconfiguration.

Following the reconfiguration, the units positioned at PV2 and PV4 were swapped to achieve IE. As shown in Figure 4.9 (b), the current distribution in each layer was modified after this reconfiguration and aligned with the new arrangement.

$$IL1 = 2200/1000 \times Im = 2.2 \times Im \tag{40}$$
$$IL2 = 2200/1000 \times Im = 2.2 \times Im \tag{41}$$
$$IL3 = 3000/1000 \times Im = 3 \times Im \tag{42}$$

The second case involved a fixed shading pattern that affected the three adjacent PV panels in the first row of the array. As shown in Figure 4.10 (a). The currents within the layers associated with the TCT connection in the second case are outlined.

$$IL1 = 300/1000 \times Im = 0.3 \times Im \tag{43}$$
$$IL2 = 3000/1000 \times Im = 3 \times Im \tag{44}$$
$$IL3 = 3000/1000 \times Im = 3 \times Im \tag{45}$$

After reconfiguration, the panels at positions PV2 and PV4 switch positions, and subsequently, the panels at positions PV3 and PV7 exchange positions to achieve IE. This is illustrated in Figure 4.10 (b). The current distribution for each layer was adjusted according to this reconfiguration as described below.

$$IL1 = 2100/1000 \times Im = 2.1 \times Im \tag{46}$$
$$IL2 = 2100/1000 \times Im = 2.1 \times Im \tag{47}$$
$$IL3 = 2100/1000 \times Im = 2.1 \times Im \tag{48}$$

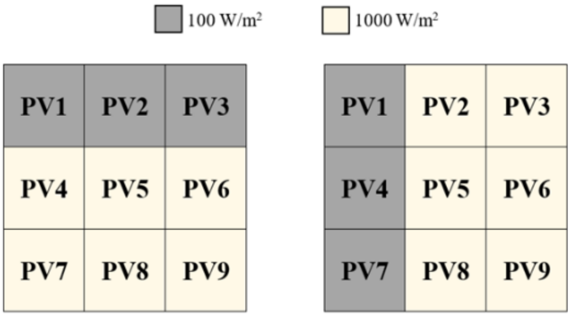

(a) (b)

Figure 4.10: a) Shading patterns of the second case before reconfiguration, b) Shading patterns of the second case after reconfiguration.

The third case featured a constant shading configuration impacting all panels in both the first and second rows of the array, as shown in Figure 4.11 (a). The currents within the layers corresponding to the TCT connection in this instance are detailed as follows.

$$IL1 = 300/1000 \times Im = 0.3 \times Im \tag{49}$$
$$IL2 = 300/1000 \times Im = 0.3 \times Im \tag{50}$$
$$IL3 = 3000/1000 \times Im = 3 \times Im \tag{51}$$

Following the adjustment, panels at PV1 and PV8 interchange locations, and the panels at PV4 and PV9 do the same to attain balance, as shown in Figure 4.11 (b). The current distribution for each layer was subsequently modified under this reconfiguration, as detailed below:

$$IL1 = 1200/1000 \times Im = 1.2 \times Im \tag{52}$$
$$IL2 = 1200/1000 \times Im = 1.2 \times Im \tag{53}$$
$$IL3 = 1200/1000 \times Im = 1.2 \times Im \tag{54}$$

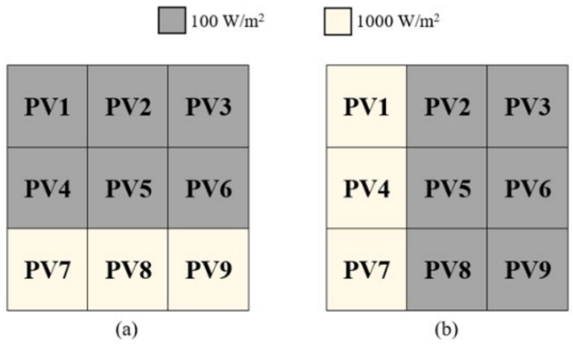

(a) (b)

Figure 4.11 : a) Shading patterns of the fifth case before reconfiguration; b) Shading patterns of the fifth case after reconfiguration.

The proposed algorithmic strategy underwent theoretical validation and empirical Efficiency improvements compared with the existing TCT were significant, with 49%, 45%, and 116.6% across various shading scenarios. These variations highlight the nuanced performance outcomes in different contexts. Consistent and significant improvements were observed across diverse shading patterns, indicating the efficiency of the proposed system. The specific outcomes for the three distinct shading scenarios are summarized in Table 4.2, which provides a detailed overview of the system performance across various test conditions.

Table 4.2 : Comparison of current, voltage, power, and efficiency characteristics between TCT and Proposed HLLBE algorithm for the second stage.

Cases	**Configuration Type**	**V_{max} (V)**	**I_{max} (A)**	**P_{max} (W)**	Efficiency(η) = $\frac{P_{\text{shaded}}}{P_{\text{unshaded}}} \times 100\%$	$\eta Improvement = \frac{\eta\text{HLLBE}-\eta\text{TCT}}{\eta\text{TCT}} \times 100\%$
First Case	**TCT**	39.1	5.213	203.8	51	49
	HLLBE	47.65	6.353	302.7	76	
Second Case	**TCT**	39.1	5.213	203.8	51	45
	HLLBE	41.13	6.284	296.2	74	
Third Case	**TCT**	19.27	2.569	49.49	12	116.6
	HLLBE	27.62	3.683	101.7	26	

4.4 Conclusion

The proposed HLLBE algorithm optimizes the PV array performance under PS conditions by dynamically reconfiguring the connections based on layer equalization. Compared with the fixed TCT configuration, HLLBE achieved an efficiency improvement of up to 116.6% across diverse shading scenarios. Successful reconfiguration eliminated multiple peaks in the power-voltage curves, highlighting the importance of efficient shading management for PV array performance optimization. The HLLBE offers a promising approach for improving the energy extraction efficiency of dynamic solar systems under changing shading conditions.

4.5 Summary

This In this chapter, I propose the HLLBE algorithm to enhance PV array performance under partial shading conditions. The HLLBE algorithm effectively addresses the challenges of uneven irradiance by dynamically reconfiguring PV arrays to equalize irradiance levels across layers, significantly improving power output and efficiency. This optimization is achieved in three ways: implementing the HLLBE algorithm for module rearrangement, utilizing a SBA for flexible reconfiguration without altering physical wiring, and simplifying the computational process through straightforward sorting and mapping adaptable to different array sizes. Validated through simulations in MATLAB/Simulink under various shading scenarios, the HLLBE algorithm demonstrates improved energy harvesting efficiency, enhanced system adaptability to changing shading patterns, reduced computational complexity and hardware requirements, and scalability across different array sizes. Therefore, the HLLBE algorithm offers a practical and effective solution for optimizing energy extraction in dynamic solar systems, ultimately enhancing the reliability and performance of PV arrays under partial shading conditions.

Thesis II ***[2]***

I proposed the Highest and Lowest Layer-Based Exchange (HLLBE) Algorithm, a novel approach for dynamic reconfiguration of PV arrays to tackle partial shading issues. The HLLBE algorithm employs a reconfigurable switch matrix to equalize irradiance levels across PV array layers, optimizing power output while minimizing switching operations. This method significantly reduces multiple peaks in power-voltage curves and enhances system adaptability to varying shade patterns. Simulation results demonstrated that the HLLBE algorithm improved efficiency by up to 116.6% compared to traditional TCT configurations, all while maintaining a streamlined and cost-effective switch design, ultimately enhancing the efficiency and reliability of PV systems.

Chapter 5. A Scalable Hierarchical Dynamic PV Array Reconfiguration under Partial Shading

The content of this chapter has been published in the following paper:

1. Ameen, F., Siddiq, A., Trohák, A., & Benotsmane, R. (2023). A Scalable Hierarchical Dynamic PV Array Reconfiguration under Partial Shading. Energies, 17(1), 181.

The current study focuses on addressing partial shading challenges in PV arrays through a scalable hierarchical system. The proposed model, Model-A, employs a load block integrated with SISCs and is implemented in a nine-panel (3 × 3) PV array simulated within a MATLAB–Simulink environment. By setting a specific threshold value for irradiance, the system dynamically reconfigures to optimize MPPT performance. The experiment tested 18 diverse shading scenarios, showcasing Model-A's scalability, adaptability, and effectiveness under varied conditions. Thus, the findings in this chapter provide scientific proof that this theoretical reconfiguration approach is effective in enhancing energy output, validating its practical application through simulation.

5.1 Proposed Reconfiguration Scheme

A controller-based dynamic system was developed, featuring solar panels interconnected in a hierarchical structure. Each pair of solar cell units is linked via relays within a single entity known as the switching block (SB), which dictates the connection type among the panels depending on the diverse shading conditions that can affect the solar panel. The system's design allows for easy and suitable expansion when incorporating additional solar modules, adapting to the shading conditions impacting the solar units. The SBs are arranged in a tiered level, with each level interconnected via additional SBs to form a comprehensive system. At the initial level, every two cells are linked through a single SB directly. The first level SBs are then connected to the second-level blocks, which in turn link to the third level, and so forth until it concludes in an integrated hierarchical structure. The final block, known as the 'load block', completes the system. This results in a hierarchical diagram that facilitates the effortless addition of new blocks, eliminating the need for a complete system redesign or rewiring each time.

The SB, as depicted in Figure 5.1, is composed of two relays, each straightaway connected to a PV panel. This block has the ability to alter the connection type between the two panels, such as parallel or series, based on the shading percentage on the panel. The relay control process is handled by a microcontroller, which receives signals from a unit known as the solar irradiance sensor cell (SISC). This small, 5-volt solar cell is installed adjacent to the primary PV panel to measure solar irradiation levels. It is calibrated with the PV panel to match voltage changes under different shading conditions. Relays are adjusted from the normally closed state to the normally open state based on the solar radiation level reading. In this case, the decision will be based on a pre-determined threshold value, such as 50% of the maximum generated power.

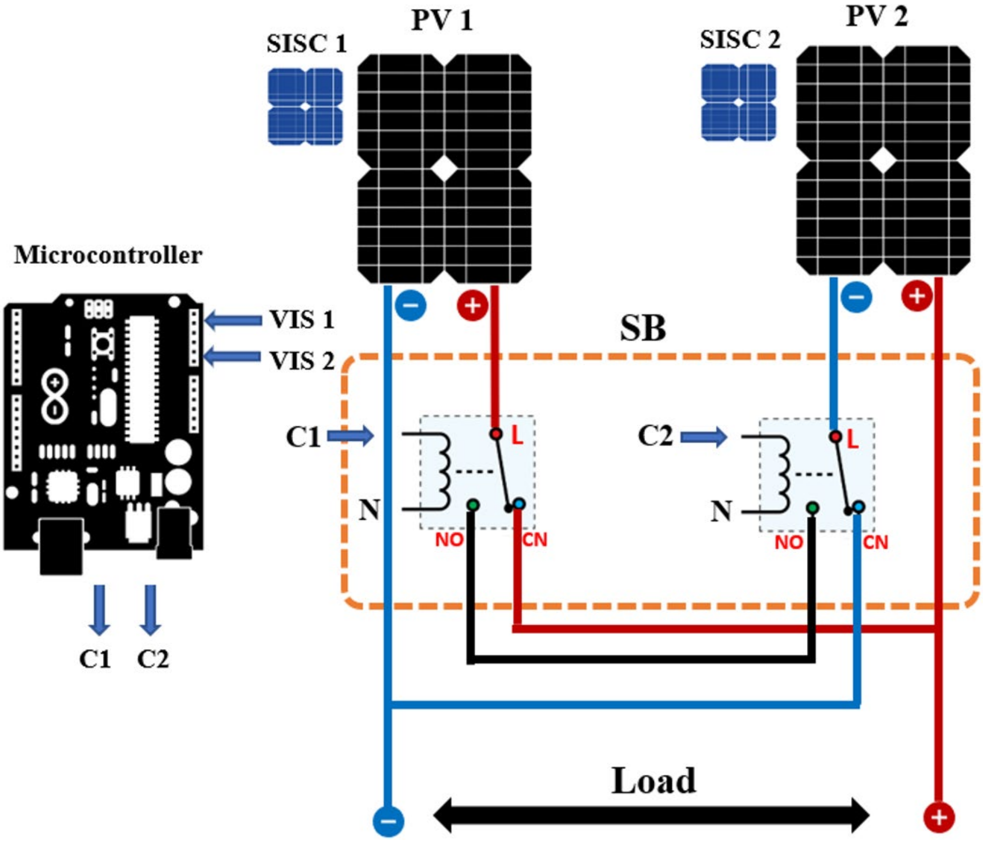

Figure 5.1: Switching Block.

The operation of the proposed system is as follows. Under normal conditions, when both PV panels receive roughly equal solar radiation without any shading, the relays stay in their default state, which are normally closed position. In this state, the two panels are connected in parallel, by way of example V1 equals V2, where V1 and V2 represent the output voltages of the two PV panels. The switching block's output voltage and current are illustrated in Table 5.1.

Table 5.1: The action mechanism of the SB block.

Shading Status		**C 1**	**C2**	**Output Voltage**	**Output Current**
PV1	**PV2**				
NO Shading	NO shading	0	0	V1 // V2	I1 + I2
NO Shading	Shading	0	1	V1	I1
Shading	NO Shading	1	0	V2	I2
Shading	Shading	1	1	V1 + V2	I1 // I2

However, if one of the PV panels is shaded, it will generate a lower output voltage than the other, falling below the threshold value. The relay attached to the shaded solar panel will then switch to the normally open position, disconnecting the shaded panel. Even when a shaded panel is detached from the array, it continues to generate an electrical current, which is drained through the relays. This prevents the shaded panel from acting as an electrical load on the unshaded panel, thereby avoiding voltage surges and power loss across the other panels that could potentially cause damage. Moreover, PS can elevate the temperatures of shaded solar cells, accelerating their aging process. In the event that both PV panels are shaded, their output voltage will drop below the preset threshold.

The relays will then switch to the normally open position, connecting the panels in series. While this increases the overall output voltage, it can help maintain the output current. For instance, I1 equals I2, where I1 and I2 represent the output currents of the two PV panels. Table 5.1 effectively illustrates the behavior of the SB block under various operating conditions.

Where C_i, $i \in \{1,2\}$, stands for the control function executed by the microcontroller. If $C_i = 0$, then the relay is normally closed. If $C_i= 1$, the relay is normally open.

The suggested system incorporates blocking diodes for each solar cell panel to avert reverse currents from flowing into shaded or low-voltage solar cells. However, it causes a voltage drop of approximately 0.7 volts. The PV arrays can be expanded by hierarchically adding SBs, facilitating easy and efficient scalability. To create an array of PV panels, the proposed SB connection system is applied to each pair of PV panels. An array of 9 PV panels was proposed by using eight SB modules to connect each of the nine PV panel pairs at three levels in a hierarchical manner. In the first level, five SBs are used, one block for each pair of solar cells. The SB of the ninth cell is connected to the SB of the seventh and eighth solar cells, as shown in Figure 5.2. The second level consists of two SBs, to which the switch blocks of the first level are connected. The third and final level consists of one switch block, to which the two switch blocks of the second level are connected. This results in an integrated hierarchical structure.

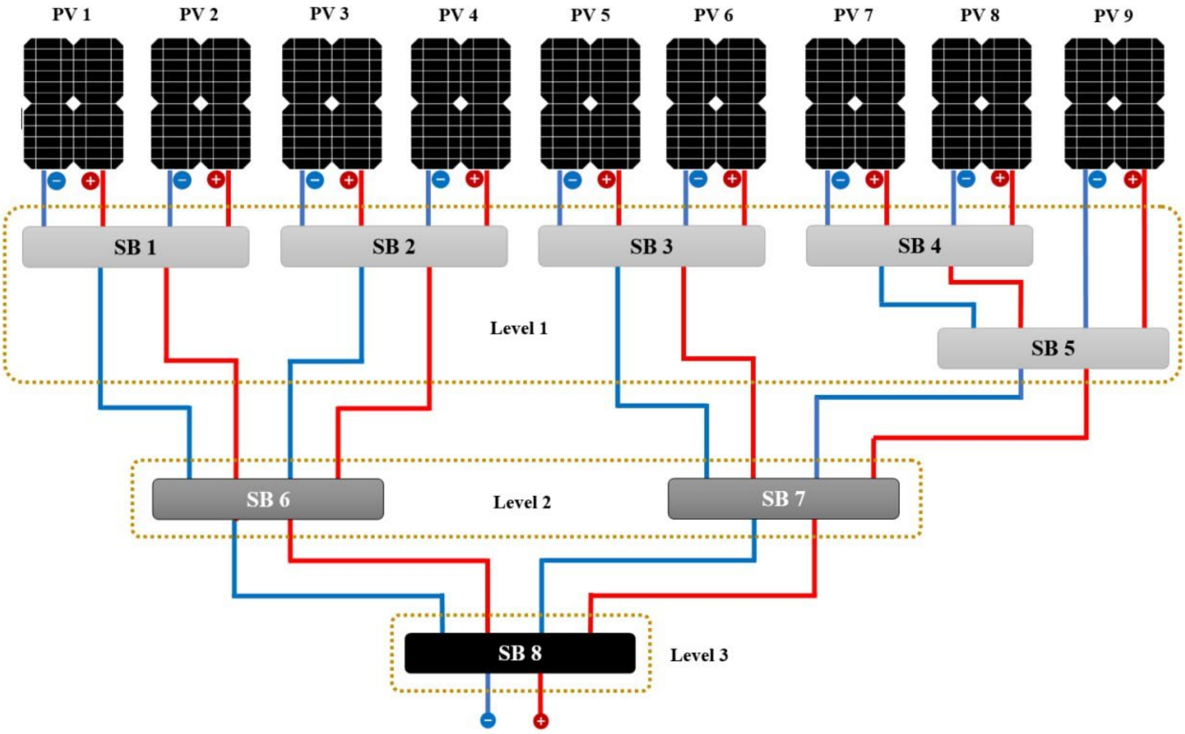

Figure 5.2: Nine PV panels are linked with eight SB modules in the hierarchy structure.

Our proposed system employs a pair of Arduino Uno microcontrollers, each featuring 6 analog inputs and 14 digital outputs. This setup enables us to connect the nine SISC units via the analog inputs and the 16 relays through the digital outputs, as depicted in Figure 5.2.

The following encapsulates a concise overview of the collaborative functionality between the controller and the switching block within the framework of the proposed system. As shown in Figure 5.3, upon initialization, the microcontroller enters a standby mode, awaiting an input signal from the SISC unit. Once the sensor cell unit transmits signals, the microcontroller processes these signals using pre-programmed mathematical calculations. It then compares the processed signal value with a preset threshold value. If the processed signal value exceeds the threshold, the signal is disregarded, and the relay remains in its default state, which is normally closed. Conversely, if the processed signal value falls below the threshold, the microcontroller triggers the relay to switch from its default state to normally open. This switching mechanism alters the connection configuration between the two solar panels from parallel to series, as detailed in Table 5.1. This configuration change is contingent on the signal value being less than the threshold value.

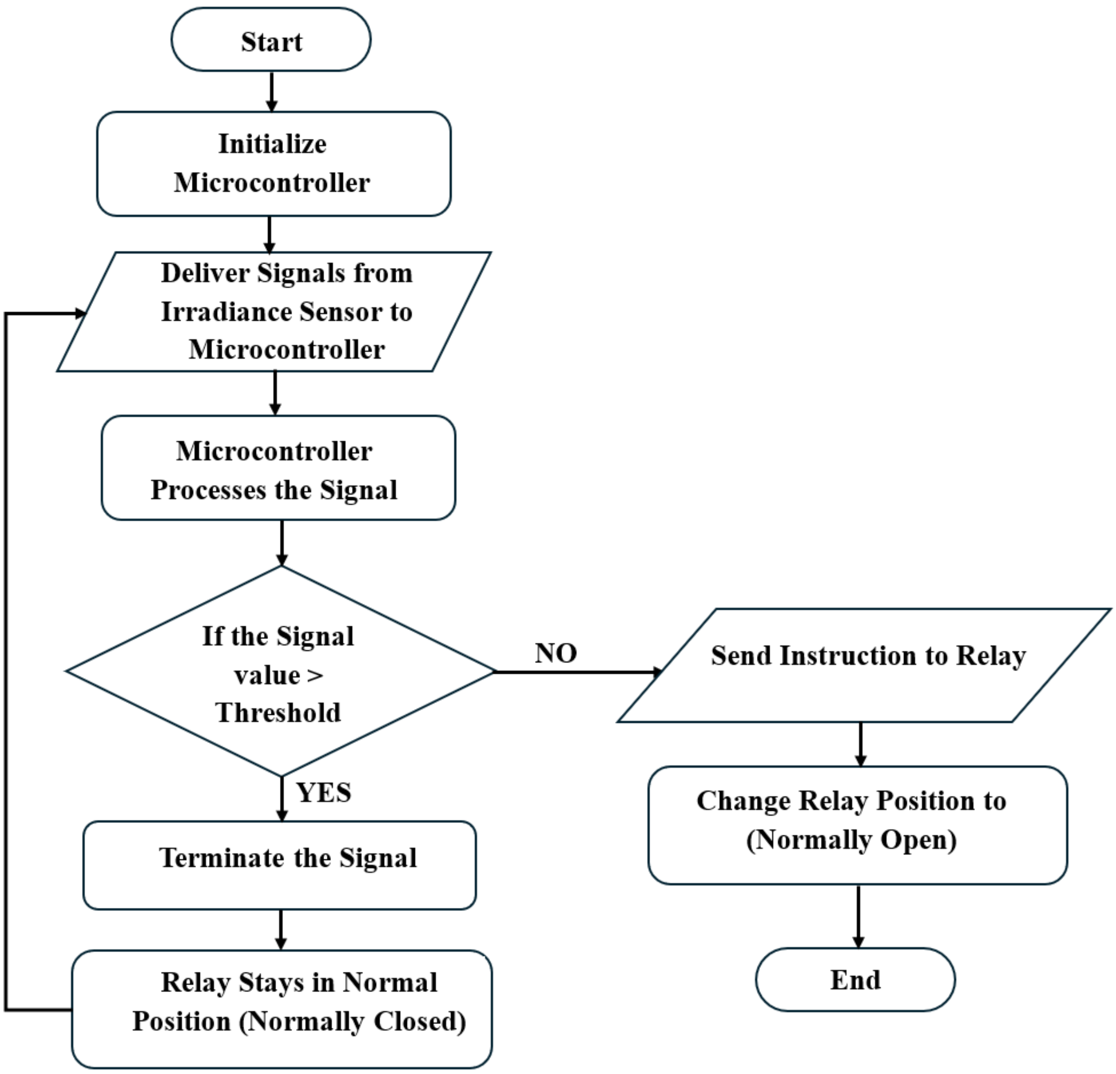

Figure 5.3: Flow chart of the proposed SB system.

- **Solar PV System Modeling**

The study employed MATLAB–Simulink version R2021b for the proposed system modeling and analysis. A detailed model of the system was developed in Simulink, incorporating elements such as photovoltaic panels with nonlinear I–V characteristics, relays represented by SBs, and control algorithms implemented through microcontroller functions. The model sends signals representing solar irradiation to the Arduino, and it receives the processed signals to control the SBs. Figure B.5 illustrates the proposed system in MATLAB–Simulink.

A consistent temperature of 25 °C was established. The attributes of the solar PV system are outlined in Table A.1, and the configuration of the parameters for the solar PV array is depicted in Figure 3.4.

The illustration in Figure 5.4 displays the configuration for the optimal switch, which has a loss in voltage in ON status. The ideal switch acts as a relay and is used in SBs.

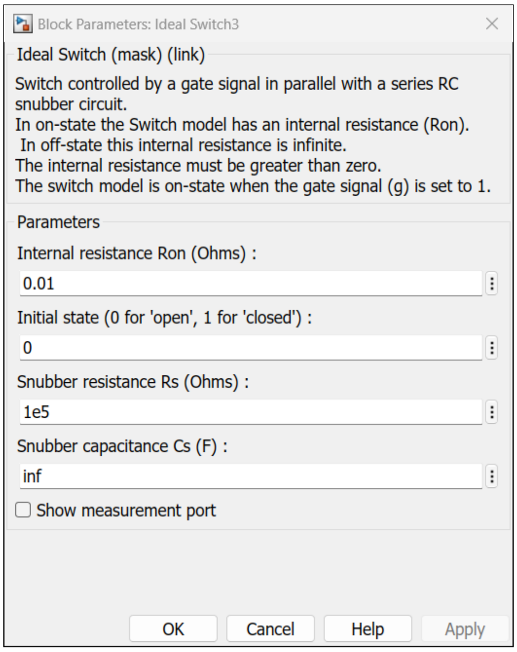

Ideal Switch (mask) (link)

Switch controlled by a gate signal in parallel with a series RC snubber circuit.
In on-state the Switch model has an internal resistance (Ron).
In off-state this internal resistance is infinite.
The internal resistance must be greater than zero.
The switch model is on-state when the gate signal (g) is set to 1.

Parameters

Internal resistance Ron (Ohms) : 0.01

Initial state (0 for 'open', 1 for 'closed') : 0

Snubber resistance Rs (Ohms) : 1e5

Snubber capacitance Cs (F) : inf

☐ Show measurement port

Figure 5.4: Simulink idea switch with loss parameter.

5.2 Simulation Results and Discussion

5.2.1 System Parameter

The proposed SB-based hierarchical scheme was used to control a nine panel PV array (3 × 3) that was built in a MATLAB–Simulink environment using 50 W PV panels and eight SB modules. The details of the PV panel specifications are outlined in Table A.1.

Without sacrificing generality, the nine PV panels are positioned in a singular row, subject to various shading patterns. As outlined in Section 6.1, a PV panel is considered shaded if its output falls below a predetermined threshold; otherwise, it is considered unshaded.

To find the threshold limit, the level of solar irradiance and voltage for the different shading cases were measured for SISC, as shown in Figure 5.5. In mid-October of this year (2023), the irradiance in the Iraq/Kirkuk region was measured to reach 720 W/m^2 during peak hours under non-shading conditions. The coordinates of the location are 35.466633 latitude and 44.379889 longitude. Figure 5.5 illustrates the linear relationship between irradiance and the generated voltage, making the latter a reliable estimate for the imposed irradiance and, hence, the shading level. The details of the SISC specifications are outlined in Table A.2, while the multimeter specifications are presented in Table A.8.

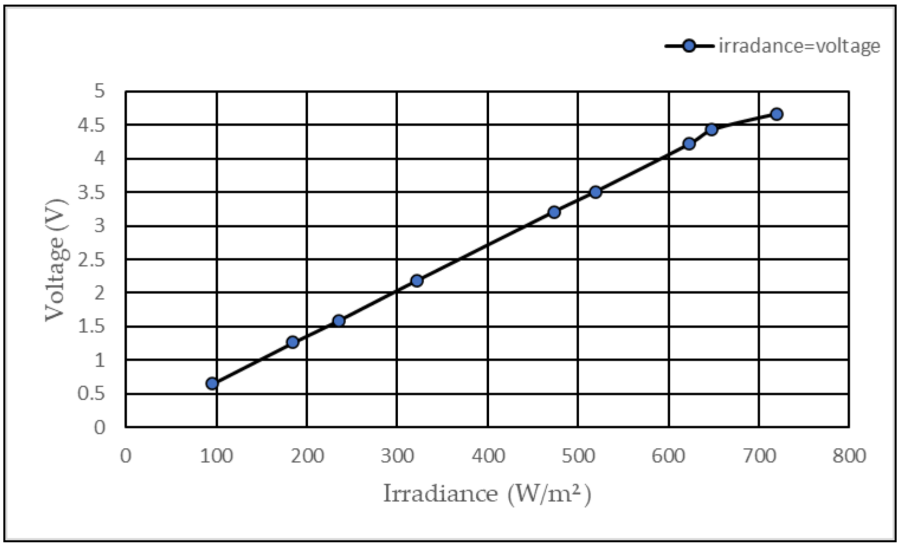

Figure 5.5: Relationship between voltage and solar irradiance.

PS can increase the temperature of shaded PV panels that are in contact with unshaded panels. This can lead to faster cell aging. Therefore, we recommend disconnecting the weak board from the system to prolong its lifespan and efficiency.

Numerous shading cases exist, including standard patterns SP, BL, and TCT. Table 5.2 presents the tested shading cases, utilizing various irradiance values (600, 480, 360, 120, 80, and 720 W/m² for unshaded panels) to monitor MPPT performance.

5.2.2 PS Cases

The experiment conducted tested 18 different shading scenarios, as illustrated in Figure 5.6, and it turned out that for every number of shaded panels, there are numerous equivalent shading patterns. This indicates that regardless of the number of shaded panels, there are several shading patterns that have the same impact on the performance of the matrix. This is due to the symmetrical nature of the PV array design and layout. For example, in the partially shaded (PS) case, where one PV panel is shaded while the other eight remain unshaded, the equivalence holds for all combinations in which one PV panel is shaded, without consideration for the specific location of the shaded panel. This means that the effect on array performance is the same whether the shaded panel is at one end of the array, in the middle, or elsewhere. These point to the fact that the symmetrical design of the PV array leads to identical effects from different shading patterns.

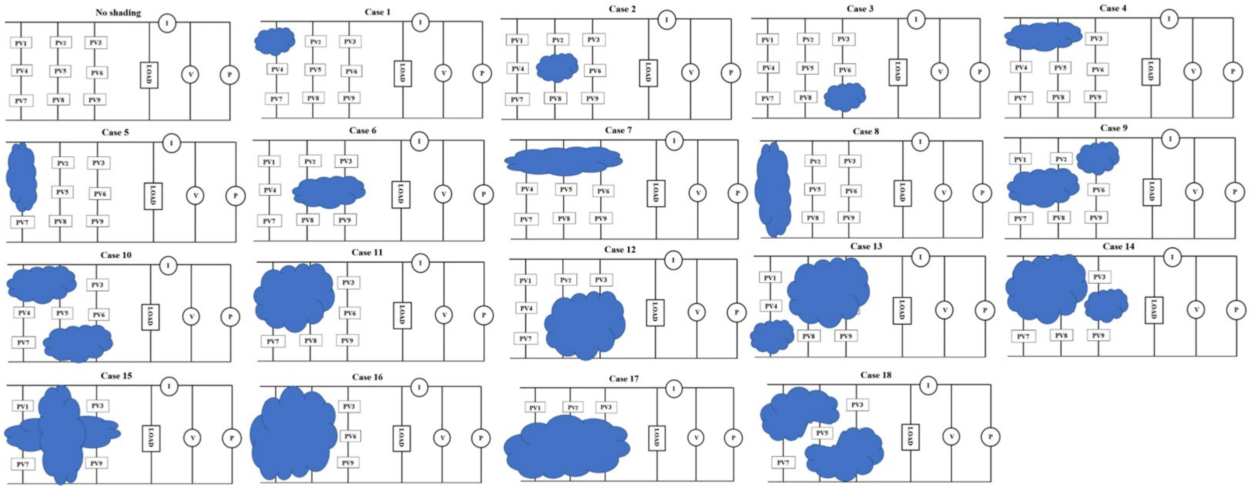

Figure 5.6: Patterns of shading on the solar PV array.

In instances of partial shading, solar radiation decreases from 720 W/m² to 80 W/m² at a temperature of 25 °C, as depicted in Figure 5.7.

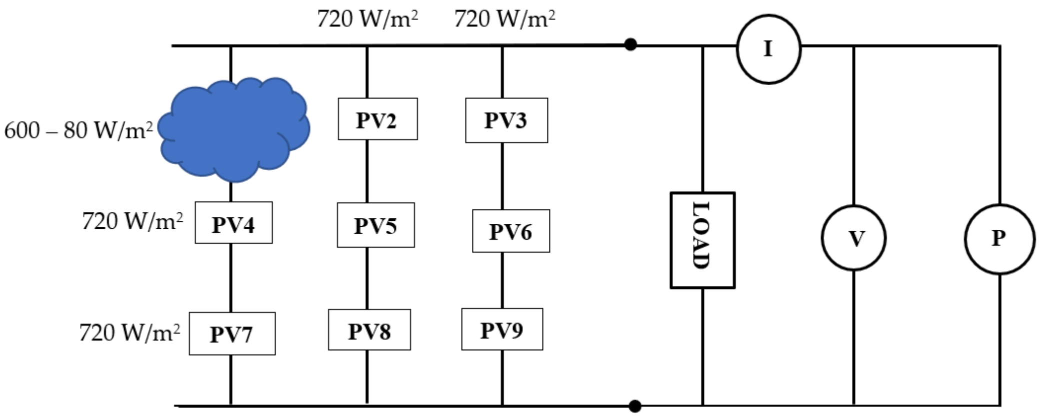

Figure 5.7: Reduced solar irradiance when shading occurs on the PV array.

5.2.3 Results

Table 5.2 presents the maximum power in watts achieved through a comparative analysis of the proposed system with conventional systems, namely SP, BL, and TCT, under the influence of 18 distinct shading scenarios. The discerned outcomes unequivocally establish the superior performance of the proposed system across the majority of shading instances in comparison to the referenced systems.

For example, in **Case 1**, the proposed system achieved **227.4 W**, compared to an average of **208.73 W** for SP, BL, and TCT, demonstrating a **8.94% improvement**. Across all 18 cases, the proposed system achieved an **average improvement of 13.6%** compared to the traditional configurations, confirming its capability to maximize energy harvest under varying shading conditions.

Table 5.2: Cases of PS and the MPPT in the hierarchical nine panel PV array based on SB.

Shading Cases	**MPPT**				**Shading Cases**	**MPPT**			
	SP	**BL**	**TCT**	**SB**		**SP**	**BL**	**TCT**	**SB**
No shading	264.9	264.9	264.9	238.2	Case 10	167.2	121.8	123.8	213.4
Case 1	209.1	195.1	222	227.4	Case 11	122.5	123.8	123.8	124.4
Case 2	209.1	196.1	198.2	227.4	Case 12	122.5	123.8	123.8	124.4
Case 3	209.1	195.1	198.2	227.4	Case 13	120.4	121.1	123.6	146
Case 4	195.7	192.4	188	195.8	Case 14	120.4	121.9	120.3	128
Case 5	187.4	187.5	189	207.8	Case 15	168.8	164.2	164	146
Case 6	195.7	192.4	188	195.8	Case 16	120.9	120.9	120.9	124.5
Case 7	188	188	188	207	Case 17	71.06	71.06	71.06	114.4
Case 8	186.6	186.6	186.6	223.4	Case 18	71.06	71.07	120.9	111.6
Case 9	188	188	172.3	188.3					

No shading irradiance = 720 W/m^2, case1–case18 irradiance = 360 W/m^2.

Figure 5.8 compares the performance of different PV array configurations under varying shading conditions. The proposed SB scheme consistently delivers higher normalized MPPT values even in challenging shading conditions, indicating improved energy harvesting efficiency.

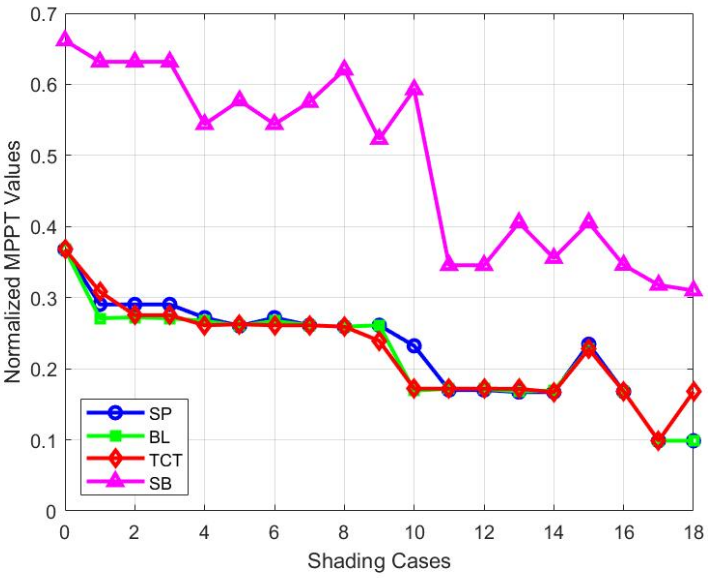

Figure 5.8: Comparison of normalized MPPT values for different configurations.

The equations derived for the proposed system, which theoretically calculate the total output voltage, current, and power for different shading scenarios, are presented in Table 5.3.

Table 5.3: The equations for the total output voltage and current in the SB-based hierarchical configuration for the nine PV arrays.

PS Cases	Shaded PVs	Total Output Voltage (V)	Total Output Current (I)
0	No shading	V1//V2//V3//V4//V5//V6//V7//V8//V9	I1 + I2 + I3 + I4 + I5 + I6 + I7 + I8 + I9
1	PV 1	V2//V3//V4//V5//V6//V7//V8//V9	I2 + I3 + I4 + I5 + I6 + I7 + I8 + I9
2	PV 5	V1//V2//V3//V4//V6//V7//V8//V9	I1 + I2 + I3 + I4 + I6 + I7 + I8 + I9
3	PV 9	V2//V3//V4//V5//V6//V7//V8	I1+ I2 + I3 + I4 + I5 + I6 + I7 + I8
4	PV (1, 2)	(V1 + V2) //V3//V4//V5//V6//V7//V8//V9	I12 + I3 + I4 + I5 + I6 + I7 + I8 + I9
5	PV (1, 4)	V2//V3//V5//V6//V7//V8//V9	I2 + I3 + I5 + I6 + I7 + I8 + I9
6	PV (5, 6)	V1//V2//V3//V4// (V5 + V6) //V7//V8//V9	I1 + I2 + I3 + I4 + I56 + I7 + I8 + I9
7	PV (1, 2, 3)	(V1 +V2) //V4//V5//V6//V7//V8//V9	I12 + I4 + I5 + I6 + I7 + I8 + I9
8	PV (1, 4, 7)	V2//V3//V5//V6//V8//V9	I2 + I3 + I5 + I6 + I8 + I9
9	PV (3, 4, 5)	V1//V2// (V3 + V4) //V6//V7//V8//V9	I1 + I2 + I34 + I6 + I7 + I8 + I9
10	PV (1, 2, 8, 9)	(V1 +V2) //V3//V4//V5//V6//V7	I12 + I3 + I4 + I5 + I6 + I7
11	PV (1, 2, 4, 5)	(V1 +V2) //V3//V6//V7//V8//V9	I12 + I3 + I6 + I7 + I8 + I9
12	PV (5, 6, 8, 9)	V1//V2//V3//V4// (V5 + V6)//V7	I1 + I2 + I3 + I4 + I56 + I7
13	PV (2, 3, 5, 6, 7)	V1//V4// (V5 + V6) //V8//V9	I1 + I4 + I56 + I8 + I9
14	PV (1, 2, 4, 5, 6)	(V1 + V2) //V3// (V5 + V6) //V7//V8//V9	I12 + I3 + I56 +I7 + I8 + I9
15	PV (2, 4, 5, 6, 8)	V1//V3// (V5 + V6) //V7//V9	I1 + I3 + I56 + I7 + I9
16	PV (1, 2, 4, 5, 7, 8)	(V1 + V2) //V3//V6// (V7 + V8)//V9	I12 + I3 + I6 + I78 + I9
17	PV (4, 5, 6, 7, 8, 9)	V1//V2//V3// (V5 + V6)// (V7 + V8)	I1+ I2 + I3 + I56 + I78
18	PV (1, 2, 4, 6, 8, 9)	(V1 + V2) //V3//V5//V7	I12 + I3 + I5 + I7

5.3. Discussion

Simulation results underscore the effectiveness of the proposed method in enhancing energy harvest under varying shading conditions. For simple shading patterns where one or two PV panels were shaded in a nine-panel array (cases 1, 2, and 3), the proposed system achieved an **8.94%–13.25% increase** in energy compared to the average of TCT, SP, and BL configurations. Similarly, for cases 5, 7, and 8, the proposed system demonstrated energy increases ranging from **10.1% to 19.71%**, highlighting its ability to adapt effectively to partial shading scenarios. For cases 4, 6, and 16, the proposed system achieved marginal improvements of approximately **1.96% and 2.97%**, respectively, over traditional methods. In contrast, cases 13 and 14 demonstrated significant improvements of **19.9% and 5.89%**, respectively, indicating the system's robust performance under these conditions. The most notable performance gains were observed in cases 10 and 17, where the proposed system achieved substantial increases of **55.1% and 60.95%**, respectively, showcasing its capability to handle complex shading patterns. Additionally, in case 18, the proposed system outperformed the average of SP, BL, and TCT configurations by **27.28%**, reflecting its strong adaptability to challenging conditions. For cases 9, 11, and 12, the proposed system exhibited comparable performance to the traditional configurations, with minimal differences in energy output, suggesting similar effectiveness in these scenarios. However, in case 15, the average performance of the three traditional configurations surpassed the proposed system by approximately **11.89%**, reflecting a limitation under these specific conditions. Figure B.6 presents a comparative analysis of the energy harvested by the proposed system and the three configurations under various shading patterns. Moreover, the results affirm the effectiveness and high efficiency of the proposed system, attributed to the hierarchical switching blocks that streamline the system, reducing the number of switches, electrical connections, and sensors during the integration of additional solar units for scalability and growth requirements. Moreover, the system's management control operations contribute to safeguarding solar panels against rapid damage, aging, and the direct adverse impact of shaded panels on PV arrays. Finally, the integration of a solar radiation sensor cell into the proposed system enhances its accuracy and reliability. This system is classified as an isolated system, characterized by the absence of a direct physical connection between the microcontroller and the solar panels. One of the key features of such a system is its ability to significantly reduce noise and distortions in the data, thereby achieving near-ideal conditions and preventing signal interference between the primary and secondary circuits. In contrast, similar systems exhibit a direct physical connection between the controller and the solar cell. These types of systems necessitate the addition of numerous electronic components to prevent the occurrence of reverse currents. This can impact the system's operational accuracy and stability, leading to inefficiency. Thus, the proposed system's design offers a distinct advantage in terms of performance and reliability.

5.3.1. Power Generation Performance

The proposed system underwent a comparative analysis concerning its maximum power performance in PS scenarios, juxtaposed with an alternative dynamic system as referenced in [76]. The findings revealed that the proposed system consistently surpassed the dynamic system cited in [76] across all shading instances, alongside its superiority over the Sudoku system. The detailed results of this comparison are elucidated in Table 5.4 for three distinct shading scenarios. The proposed system SB demonstrably outperforms other methods in both power output and efficiency across all three shading scenarios analyzed, as shown in Figures 5.9 and 5.10.

Table 5.4: Comparison table for three different scenarios of partial shading.

Power and Efficiency Formulas	**Types**	**TCT**	**Sudoku [76]**	**Dynamic [76]**	**Proposed SB**
Power (W)	Type 1	153.4	189.4	207.4	213.8
Power (W)	Type 2	144.3	153.3	162.3	182.8
Power (W)	Type 3	162.4	162.3	180.3	197.4
$\eta = \frac{P_{\text{shaded}}}{P_{\text{unshaded}}} \times 100\%$	Type 1	59	72.8	79.8	82.2
$\eta = \frac{P_{\text{shaded}}}{P_{\text{unshaded}}} \times 100\%$	Type 2	55.5	58.96	62.4	70.3
$\eta = \frac{P_{\text{shaded}}}{P_{\text{unshaded}}} \times 100\%$	Type 3	62.4	62.43	69.4	75.9
$Power\ improvement = \frac{P_{SB} - P_{TCT}}{P_{\text{TCT}}} \times 100\%$	Type 1	39.37	12.88	3	-
$Power\ improvement = \frac{P_{SB} - P_{Sud}}{P_{Sud}} \times 100\%$	Type 2	26.6	19.2	12.6	-
$Power\ improvement = \frac{P_{SB} - P_{Dyn}}{P_{Dyn}} \times 100\%$	Type 3	21.6	21.8	9.4	-

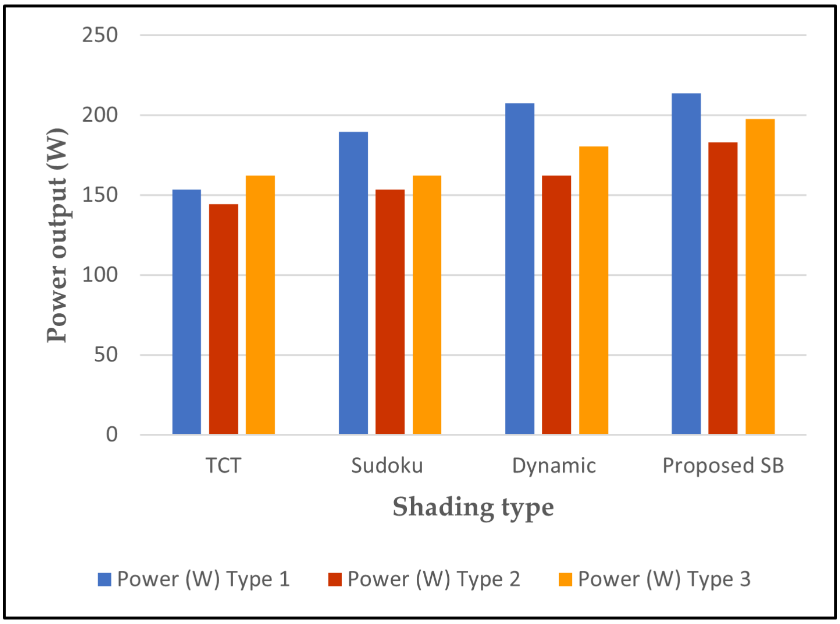

Figure 5.9: Power output for different shading types.

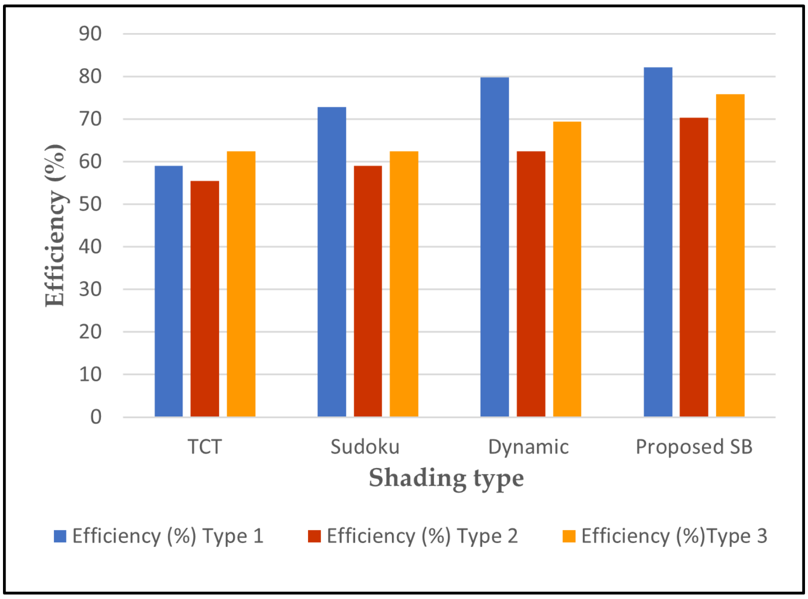

Figure 5.10: Efficiency output for different shading types.

Compared to the traditional TCT system, the proposed SB demonstrates an impressive increase in power generation of 21.6% to 39.37% and an improvement in efficiency ranging from 12.9% to 39.32%. It also outperforms the Sudoku system, showing a superiority of 12.8% to 21.6% in power and 12.6% to 21.63% in efficiency. Even against the dynamic system, the proposed SB maintains a clear lead, offering a 3.1% to 12.6% increase in power and a 3% to 12.6% improvement in efficiency. These consistent and significant gains confirm the effectiveness of the proposed SB in optimizing PV system performance under diverse PS conditions, as shown in Figure 5.11 for power generation and Figure 5.12 for efficiency.

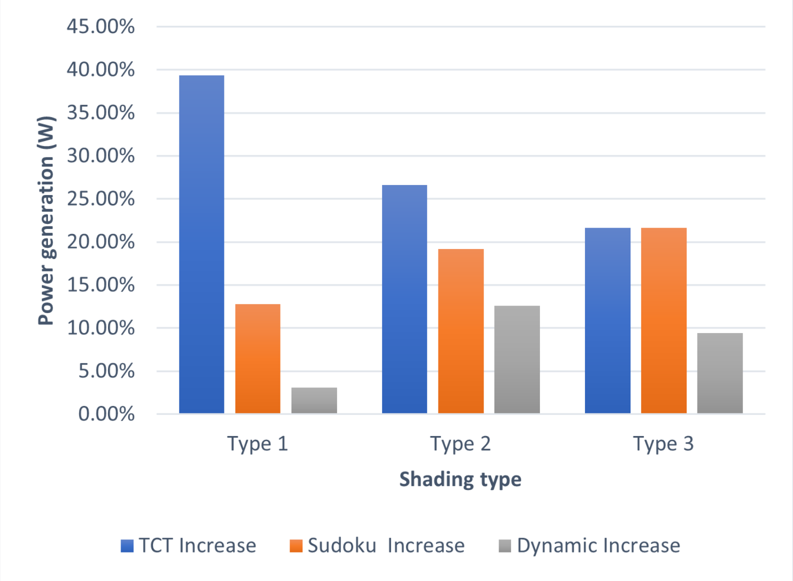

Figure 5.11: Power generation enhancement with the proposed SB compared to TCT, Sudoku, and dynamic systems.

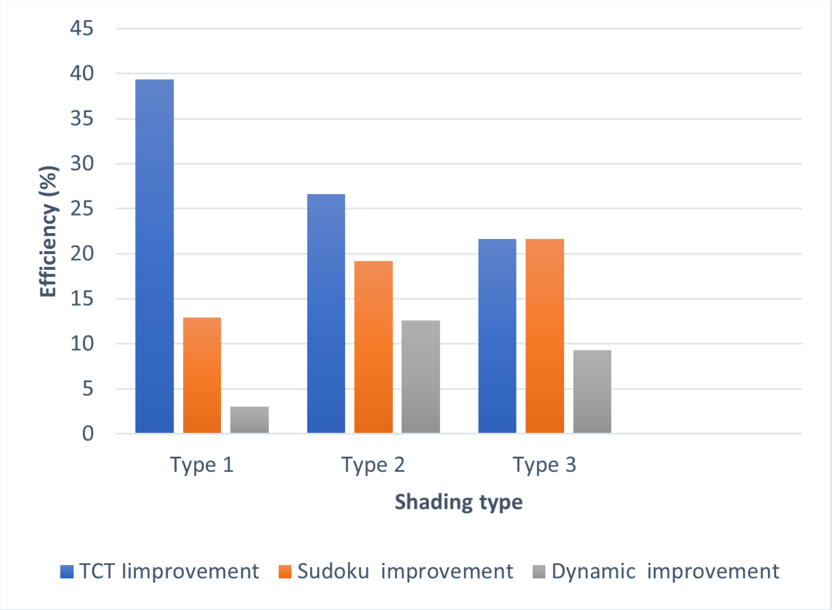

Figure 5.12: Efficiency improvement in PV systems: performance analysis of the proposed SB against various configurations.

Furthermore, to validate the proposed system's efficiency, a comprehensive comparison was conducted with a comparable system from prior research [109]. The results were impressive, with SB significantly surpassing its competitor, particularly relevant for low-power photovoltaic arrays. Table 5.5 provides a detailed breakdown of SB's performance across diverse shading scenarios (short–narrow, long–wide, short–wide, and long–narrow). As Figures 5.13 and 6.14 illustrate, SB demonstrably outperforms other methods in both power output and efficiency across all four scenarios analyzed.

Table 5.5: Comparison table for four different cases of partial shading.

Methods	**Power (W) Case 1 (SN)**	**Power (W) Case 2 (LW)**	**Power (W) Case 3 (SW)**	**Power (W) Case 4 (LN)**	**Efficiency (%) Case 1**	**Efficiency (%) Case 2**	**Efficiency (%) Case 3**	**Efficiency (%) Case 4**
TCT	1.445	1.52	1.184	1.634	41.81	43.98	34.26	47.28
Magic Square configuration [109]	1.53	1.638	1.596	1.887	44.27	47.40	46.18	54.60
Proposed SB	2.031	1.897	1.687	2.027	58.77	54.89	48.81	58.65

Compared to the traditional TCT system, the proposed SB exhibits an impressive 32.39% to 42.52% increase in power generation and a 31.17% to 42.13% improvement in efficiency. It also surpasses the Magic Square system by a 7.53% to 19.61% increase in power generation and a 5.51% to 32.08% improvement in efficiency. These consistent and significant gains confirm the effectiveness of the proposed SB in optimizing PV system performance under diverse PS conditions.

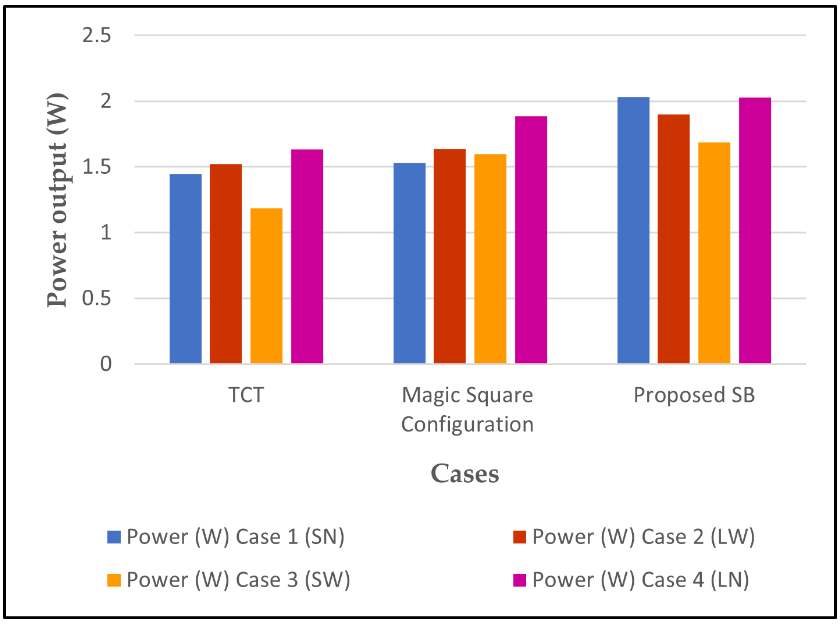

Figure 5.13: Power output for different shading cases.

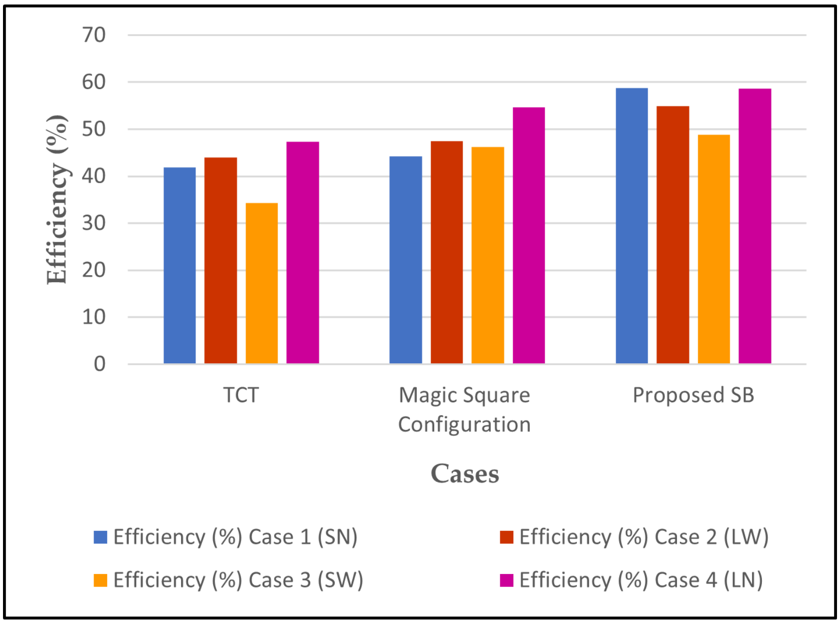

Figure 5.14: Efficiency output for different shading cases.

5.3.2. Scaling

The proposed system utilizes additional units of the same design of two PV arrays without requiring software updates or hardware modifications to the two PV controllers in terms of input and output lines and is easily expanded. In contrast, the dynamic system demands hardware modifications, including an expanded switch matrix ($sw = n \times n \rightarrow (n + 1) \times (n + 1)$), additional output lines for switch control, and increased input lines for additional sensors. Software updates are also necessary for the dynamic system to accommodate the expanded hardware configuration.

5.4 Conclusions

This paper introduces a reconfiguration technique for PV arrays. The technique utilizes a hierarchical structure based on a switching block to optimize the maximum power output under PS conditions. The system, controlled by a microcontroller and equipped with a SISC module, dynamically reconfigures the PV array to maximize power extraction under varying shading conditions. The switching block alters the connection state between the solar panels, switching between parallel and series connections based on a predetermined threshold value. The performance of this technique was evaluated using MATLAB–Simulink, and the results demonstrated that the proposed reconfiguration strategy offers better performance compared to the SP, BL, TCT, Sudoku, the dynamic proposal from reference [76], and Magic Square from reference [125] under similar partial shade conditions. Furthermore, the proposed strategy effectively reduces losses, enhances efficiencies, and improves the overall performance of PV arrays during partial shading. One of the key advantages of the system's hierarchical structure is the ease of array expansion. Additional solar panels can be seamlessly integrated into the PV array without complications in design or the need for re-establishing electrical connections. The results showed the proposed SB consistently outperforms, with increases in power generation (21.6% to 39.37%) and efficiency (21.63% to 39.32%). It also outperforms other systems, including Sudoku and a dynamic proposal, confirming its superiority in optimizing PV system performance. Furthermore, the proposed SB exhibits significant gains when compared to the TCT and Magic Square systems, with a remarkable increase in power generation (32.39% to 42.52%) and efficiency (31.17% to 42.13%). These high-value results underscore the efficiency of the proposed SB in optimizing PV system performance under various PS conditions. In the future, we plan to investigate the impact of different switching block configurations and optimization algorithms on system performance through real-world testing.

5.5 Summary

This chapter introduces a scalable hierarchical dynamic PV array reconfiguration scheme to address challenges posed by partial shading. Dynamic reconfiguration using a hierarchical SB architecture enhances energy output and efficiency in PV systems under varying shading conditions. A controller-based dynamic system is developed, where solar panels are interconnected hierarchically using SBs and SISCs. Each SB comprises relays that adjust the connection type—series or parallel—based on shading conditions detected by SISCs, enabling real-time optimization of MPPT performance. The hierarchical design supports easy PV array expansion without requiring a complete system redesign or rewiring.

The system is implemented in a 3 × 3 PV array within MATLAB–Simulink and evaluated under 18 shading scenarios. The proposed scheme dynamically reconfigures the array based on shading patterns, minimizing mismatch losses and preventing hotspots. Benefits include enhanced energy harvesting efficiency, increased scalability, reduced power losses under partial shading, and improved performance compared to SP, BL, and TCT. The design also ensures ease of maintenance with fewer switches and simplified circuitry.

Thesis III ***[1]***

I developed a scalable hierarchical switching block architecture, Model-A, for dynamic PV array reconfiguration under partial shading. The system integrates SISCs and employs a threshold-based switching mechanism, enabling real-time adjustments of PV module connections to optimize MPPT performance. Simulations conducted in MATLAB–Simulink demonstrated superior results, with the system achieving an average power output improvement of 13.6% compared to SP, BL, and TCT configurations under partial shading conditions. When compared to advanced techniques such as TCT, Sudoku, and other dynamic proposals, the system achieved up to 39.37% improvement in power generation and 39.32% in efficiency. Its hierarchical architecture ensures scalability, adaptability, and enhanced energy harvesting, effectively addressing the challenges of partial shading.

Chapter 6. Scalable Dynamic Photovoltaic Array Reconfiguration Scheme for Mitigating Partial Shading

The content of this chapter has been accepted for publication in the Tikrit Journal of Engineering Sciences (TJES).

The current study concentrates on addressing the challenges posed by partial shading in photovoltaic (PV) arrays through the development of a scalable hierarchical system. The proposed model, Model-B, features switching blocks (SBs) organized in a hierarchical structure and was simulated in various PV configurations, including TCT, BL, and SP setups, using MATLAB-Simulink. Model-B dynamically reconfigures itself based on real-time irradiance data from Solar Irradiance Sensor Cell (SISC) strategically embedded alongside the panels. By setting specific threshold values, the system optimizes the MPPT performance across diverse shading conditions. The study tested multiple shading scenarios, including asymmetric and symmetric expansions, demonstrating the system's adaptability and scalability. Thus, the findings of this chapter scientifically validate the effectiveness of Model-B's dynamic reconfiguration approach in enhancing energy output, confirming its practicality and superiority over conventional methods like TCT, BL, and SP through comprehensive simulation results.

6.1 Proposed System

A sophisticated and adaptable dynamic system was engineered to facilitate the connection of solar panels in a cost-effective and practical manner. The proposed system transcends conventional and intricate methods of PV connections. It employs integrated relays across multiple entities, wherein each pair of phases forms a unit entitled a switching block (SB). Two such units are interconnected within a single block, constituting a group referred to as a link block (LB). These LBs were interconnected via additional SBs, ultimately forming a comprehensive hierarchical structure. The operation of these units is governed by a microcontroller that uses solar radiation data specific to each panel within the PV system. This approach ensures optimal performance and efficiency.

In the proposed system, SBs was stratified based on the number of interconnected solar panels. For instance, in a 3 × 3 solar system, SBs are categorized within LBs, as shown in Figure 6.1, where every trio of the panels is connected. These panels are unified within a single LB, which dictates the connection type between them, either series or parallel, contingent upon the system's requirements, and constitutes the first tier of the system. In the subsequent tier, these blocks are interconnected with other SBs, and this pattern continues up to the final tier, which embodies the ultimate SB at the apex of the hierarchical structure. The final configuration of the proposed 3 × 3 system is shown in Figure 6.2.

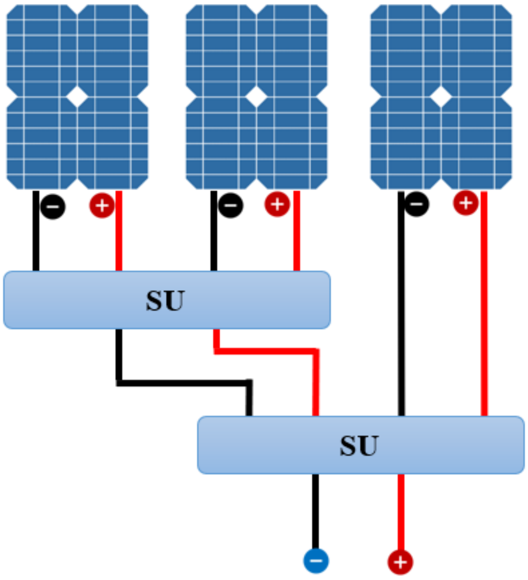

Figure 6.1: Two SBs in One LB.

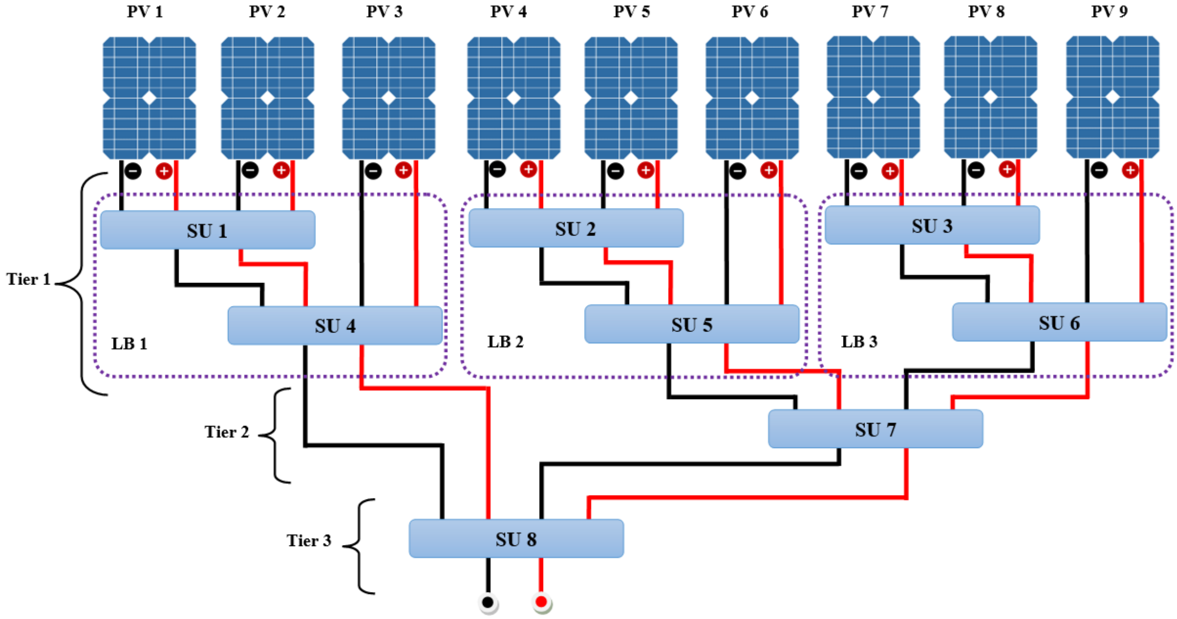

Figure 6.2: Proposed 3 × 3 PV Array.

The SB, as illustrated in Figure 6.3, is composed of a pair of relays directly linked to two solar panels. This configuration enables the merging of two panels, either in a series or parallel arrangement, dictated by the instructions conveyed by the microcontroller. This design ensures precise control over the interconnection of the solar panels, allowing for adaptability in series or parallel configurations based on the operational requirements of the system.

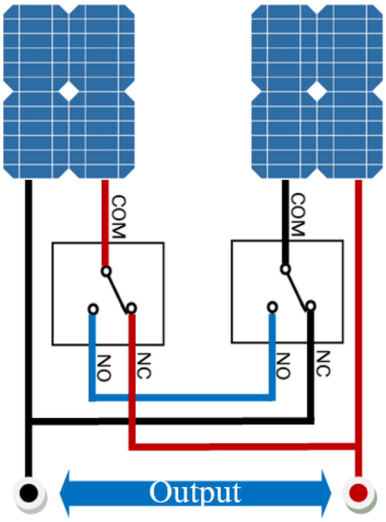

Figure 6.3: Switching Block Linked to Two PV.

The system employs a microcontroller to govern SBs by relying on direct data readings from the panels. This involves assessing the prevailing shading conditions that impact the solar panels within the PV system. Solar irradiation sensors (SISC) were strategically embedded alongside each solar panel within the PV array. These sensors, comprising of small solar cells, were individually assigned to each panel. The calibration of these sensors with the panel was achieved by subjecting them to uniform shading conditions, followed by the calculation of voltage variations for each. Subsequently, by computing the shading ratio, the microcontroller issues specific control commands to SBs. These commands facilitate alterations in the connectivity between the panels, transitioning from series to parallel configurations, or vice versa. In addition, the microcontroller can initiate the disconnection of a panel from the PV array system in response to changing environmental conditions. This dynamic control mechanism ensures optimal performance of a PV system based on real-time data.

The expansion of traditional PV array systems poses a significant challenge, particularly when incorporating additional units of PV panels. Solar panel configurations typically fall into two categories: symmetrical and asymmetrical arrays, each of which has distinct advantages and drawbacks.

In structures with asymmetric configurations, the proposed system stands out for its enhanced flexibility and simplicity when integrating additional PV panels. This was attributed to the hierarchical structure inherent in the proposed system. For instance, when there is a need to add one or more panels to the proposed system, as depicted in Figure 6.2, a new SB is introduced into the system. Placement of the panel can occur within the first, second, or third LB depending on the preference. In cases involving multiple panels, supplementary units can be seamlessly incorporated into other LBs without disrupting the primary electrical connections to the remaining panels and SBs.

In the context of symmetric configurations such as the (4 × 4) system expansion, the proposed system facilitates scalability by increasing the number of LB panels by one and implementing a new fourth LB. This expansion resulted in the integration of seven additional panels into the system. Notably, each set of four solar panels was systematically linked within a dedicated LB, as exemplified by the visual representation provided in Figure 6.4. This demonstrates the adaptability of the proposed system to accommodate specific requirements of identical configurations.

The hierarchical structure of the system plays a crucial role in scalability, making the process of expansion more streamlined and efficient. This allows even more flexibility when it comes to expanding the solar power system, accommodating the addition of more solar panels as needed. This ensured that the system could be scaled up efficiently without disrupting the existing setup or electrical connections.

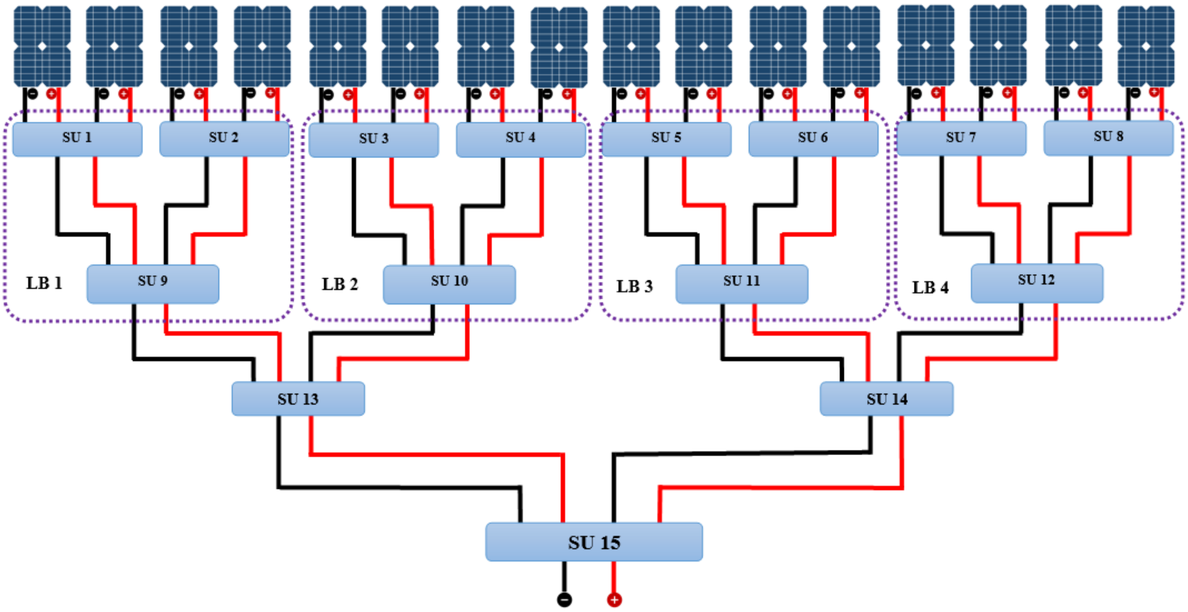

Figure 6.4: New (4 × 4) PV Array for the Proposed System.

The proposed system exhibits the capability to replicate the performance of traditional configurations such as SP, BL, and TCT through the incorporation of switches between the three primary LBs, as illustrated in Figure 6.5. In this configuration, when switches 1, 2, 3, and 4 are in the off position, the system functions in SP mode. However, activating switches 1 and 4, while keeping switches 2 and 3 off, enables the system to operate in the BL mode. Engaging all switches in the on-state configures the system to function in TCT mode. This strategic integration of switches offers operational versatility, allowing the system to adapt seamlessly to various configurations and meet specific operational requirements.

In the dynamic configuration strategy, the connections of the PV modules are dynamically modified by altering the state of the SBs. This section focuses on elucidating the actual switching process in a dynamic configuration. The reconfiguration process inherent in the proposed system is designed to mitigate or eliminate multiple peaks that manifest owing to losses in the overall system capacity when certain units fall under shadow. Consequently, this process diminishes mismatch losses and enhances the fill factor, thereby boosting the system efficiency.

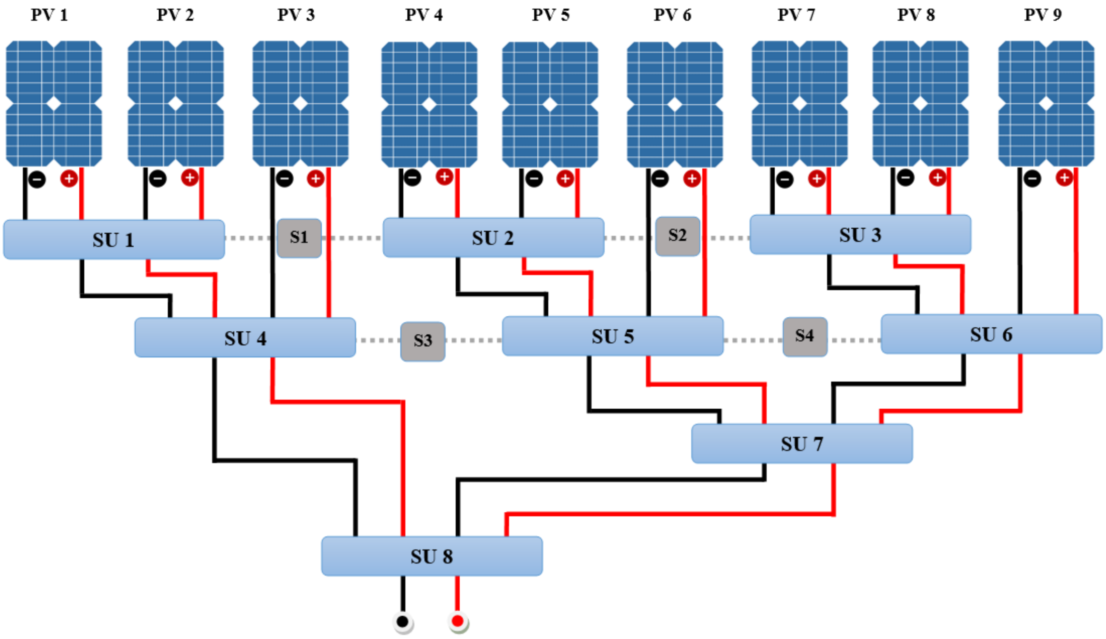

Figure 6.5: Configurable Operational Modes with Switches of the Proposed System.

The proposed algorithm systematically arranges all solar panels within a system based on the solar radiation values. It pairs two solar panels in series or parallel within a single LB, considering the shading conditions affecting the PV array. For instance, in cases where shading occurs on two panels within an LB, the algorithm orchestrates serial interconnections between these panels to double the voltage, while maintaining a constant current. Conversely, if shading is present on only one panel or two panels within different LBs, the algorithm initiates the separation of these panels from the system. This preemptive action is taken to prevent an elevation in the overall system temperature, as a shaded panel may transition to resistance and adversely impact the entire system.

The decision to separate a shaded panel from the system is contingent on the critical limit (threshold) value, a parameter that varies based on the shading state of the panel and its impact on the system. If the shading percentage on the panel exceeds 50%, the algorithm mandates the isolation of the panel to avert damage and mitigate the potential effects on the other panels. Conversely, if the shading percentage is below 50%, the panel can be retained within the system, subject to continuous monitoring to prevent undue temperature rise and associated energy losses.

In the absence of shadows on the panels, interconnections between the panels were maintained in parallel. The processes of parallel or series interconnection as well as the separation of panels occur in the first tier of the system. By contrast, for subsequent tiers, such as the second and third tiers, the algorithm dynamically alters the connection states between the SBs from series to parallel or vice versa within each tier. The algorithm explores various possibilities between series and parallel configurations with the aim of achieving the highest attainable system power.

The proposed system is economical, simple, and practical for several reasons. First, it utilizes a minimal number of switches compared with similar systems, thus contributing to cost efficiency. Additionally, the system has simplicity in its electrical circuit, facilitating ease of maintenance. A noteworthy feature is the cost-effectiveness of the system during operation. Importantly, the proposed system excels in its user-friendly approach to expansion, eliminating the necessity for complete system redesign or rewiring with the addition of new units.

6.2 Simulation and Results

6.2.1 System Parameters

The proposed hierarchical system, which is based on SB, was employed to manage a PV array consisting of nine panels (arranged in a 3 × 3 array). This array was constructed in a SIMULINK/MATLAB setting using PV panels with a capacity of 50 W and eight SB modules. Details of the PV panels used are listed in Table A.1.

6.2.2 Modeling and Simulation of 3 × 3 PV Modules Under PSCs with A Constant Shading Value

This section presents multiple PS scenarios for a 3 × 3 PV array with varying shading configurations applied to different sections of solar panels. Factors such as clouds, nearby structures, vegetation, or uneven terrain can cause partial shading, leading to a decrease in the energy output and potential hotspots on the PV modules. PS can occur owing to factors such as nearby buildings, vegetation, or uneven terrain, leading to reduced energy output and potential hotspots on PV modules. By examining 25 suggested PS cases, including configurations in which four or five panels are shaded, the aim was to assess the array's response under diverse shading conditions. Each shading scenario represents a unique challenge that affects the efficiency and energy production of an array. Through modeling and simulation, we analyzed the effects of shading on array performance by considering factors such as voltage drops, current imbalances, and overall energy yield.

Shading cases were categorized into groups based on the number of shaded panels within the system, as shown in Figure 6.6 (a).

The simulation was conducted under uniform conditions, specifically at 25°C and 1000 W/m^2 without shading. Additionally, simulations were performed under PSCs at 25°C and three different irradiance levels: 750 W/m^2, 500 W/m^2, and 250 W/m^2, as outlined in Table B.2.

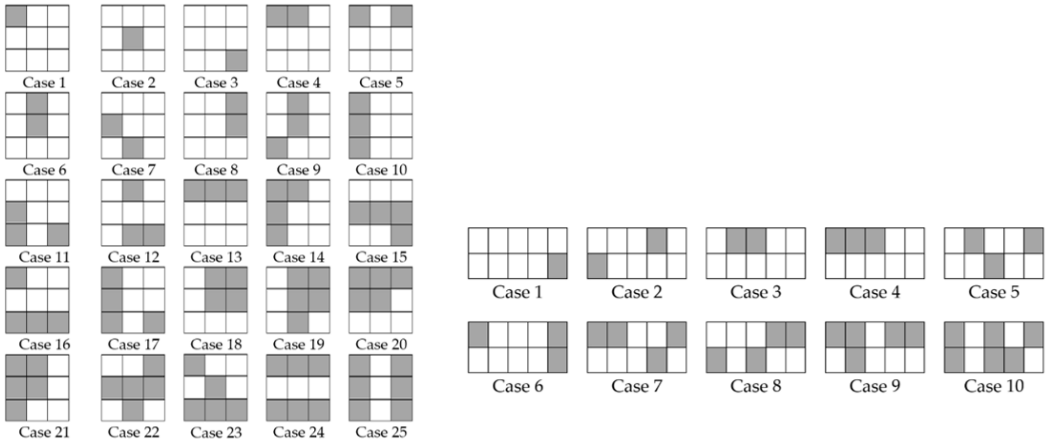

a. 3 × 3 solar PV array.

b. 2 × 5 solar PV array.

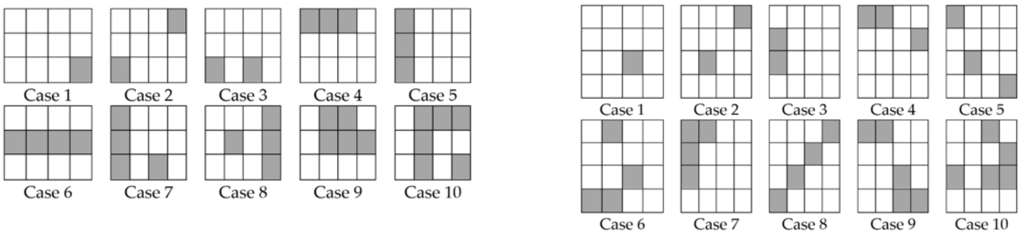

c. 3 × 4 solar PV array.

d. 4 × 4 solar PV array.

☐ 1000 W/m^2

▨ 750 W/m^2, 500 W/m^2, and 250 W/m^2

Figure 6.6 : Shading patterns for different solar PV array configurations.

6.2.3 Asymmetric Simulation and Expansion of System under PSCs with Fixed Shading Values

This section addresses the expansion of the system that involves the integration of additional solar cells into the primary system. The expansion, which is asymmetric, is executed in two stages. During the initial stage, a single solar cell was incorporated, resulting in a system configuration of either 2 × 5 or 5 × 2. In the subsequent stage, an additional three solar cells are integrated, leading to a system configuration of either 3 × 4 or 4 × 3.

6.2.3.1 Stage 1: Single Solar Cell Integration (2 × 5 PV Array)

At this stage, one PV cell was integrated into the system, accompanied by an additional SB. This unit is interconnected with the SB associated with the ninth PV panel, as shown in Figure 6.7.

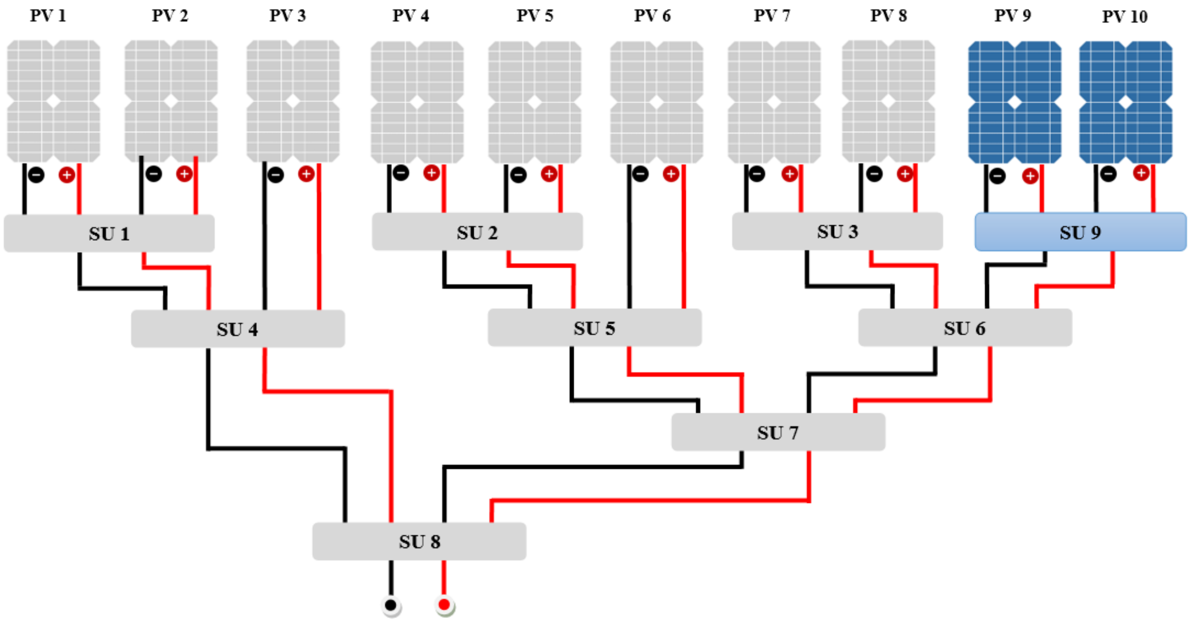

Figure 6.7: Expansion of The Proposed System by Adding One Panel and an SB.

The new expanded system underwent simulations using various traditional configurations. The results demonstrated the superior performance of the proposed system post-expansion, as indicated in Table 6.1. The table delineates the system's efficiency across ten distinct shading scenarios, showcasing its effectiveness under diverse conditions, and Figure 6.6 (b) shows the shading patterns.

Table 6.1: Simulation Results for A 2 × 5 PV Array for 10 PS Cases with Three Different Irradiance Values.

PS Cases	**MPPT at Irradiance 700 W/m^2**				**MPPT at Irradiance 500 W/m^2**				**MPPT at Irradiance 200 W/m^2**			
	SP	**BL**	**TCT**	**SB**	**SP**	**BL**	**TCT**	**SB**	**SP**	**BL**	**TCT**	**SB**
1	431.9	431.9	431.9	435.6	404	404	404	433	358.5	358.5	358.5	427.6
2	392	396.7	425.1	404.5	330.2	334.1	396.7	364.3	241.4	246.2	351.4	290.8
3	392	296.7	391.7	404.5	330.2	334.1	329.3	364.2	241.4	246.2	243.3	290.8
4	347.8	349.5	344.7	399.6	258.2	260.1	257.1	361.4	144.4	147	146.6	290.1
5	347.8	351.3	390	404.5	258.2	262.1	328.1	366.1	144.4	149.5	242.4	292
6	390.1	392.3	390	404.5	328.9	330.8	328.1	366.1	240.8	243.2	242.4	292
7	303.9	305.5	344	350	194.2	196.3	256.6	253.4	133.8	131.8	146.3	194.7
8	303.9	347.9	382.1	383.4	194.2	258.9	321.3	350.6	133.8	146.4	235.2	285.9
9	302.4	305.1	299.3	343	192.8	196.1	192.3	244.5	131.3	123.8	125.1	123.4
10	300.8	302	336.6	342.6	191.5	192.6	249	244.3	126.7	123.2	139.6	123.4

6.2.3.2 Stage 2: Three Additional Solar Cell Integrations (3 × 4 PV Array)

In this stage, the three PV cells were seamlessly incorporated. This is complemented by the addition of three supplementary SBs. This augmentation process involved the introduction of a novel LB within the system architecture, as illustrated in Figure 6.8.

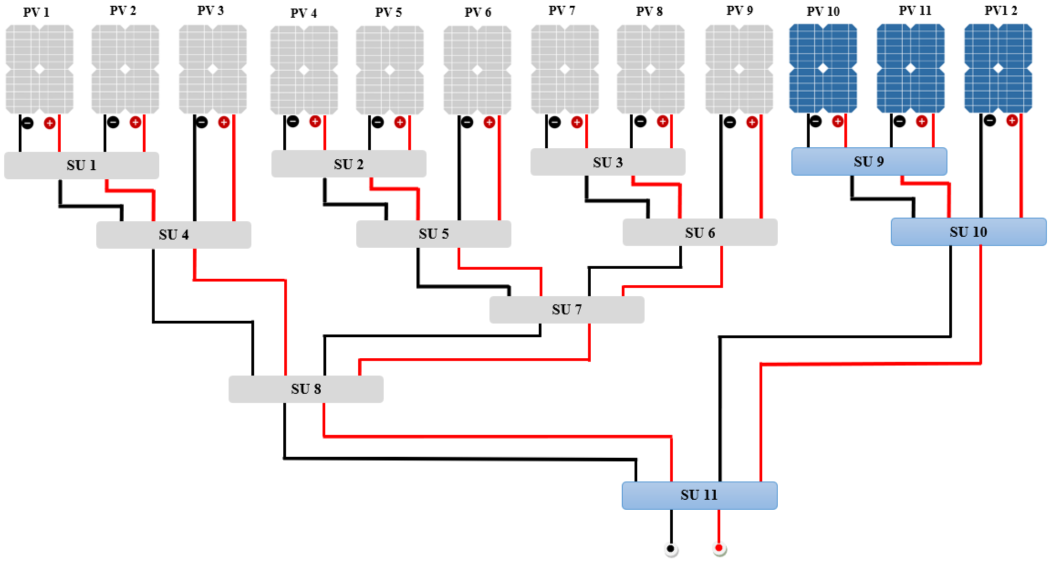

Figure 6.8: Expansion of Proposed System by Adding Three Panels and Three SBs.

The system expansion proceeded smoothly with no need to reconfigure the wiring entirely. Instead, the process involved the addition of PV cell wires and SBs. Subsequently, the expanded system was simulated and compared with traditional configurations. Across ten different shading conditions, the results consistently demonstrate the superior performance of the proposed system, as illustrated in Table 6.2, and Figure 6.6 (c) shows the shading patterns.

Table 6.2: Simulation Results of A 3 × 4 PV Array for 10 PS Cases with Three Different Irradiance Values.

PS Cases	**MPPT at Irradiance 700 W/m^2**				**MPPT at Irradiance 500 W/m^2**				**MPPT at Irradiance 200 W/m^2**			
	SP	**BL**	**TCT**	**SB**	**SP**	**BL**	**TCT**	**SB**	**SP**	**BL**	**TCT**	**SB**
1	529.7	533.5	544.5	554.2	488.5	491.7	529.3	520.6	418.3	420.6	471.6	456.1
2	472.2	482.2	534.4	551.5	377.4	387.3	495.4	507	319.1	297.9	423.4	405.4
3	472.2	479.6	482.7	551.5	377.4	384	387.9	507	319.1	304.2	287.9	405.4
4	406.5	410.8	411.1	388.3	300	295.8	287.9	358.1	300	287.9	287.9	358
5	524.4	524.4	524.4	541.8	484.8	484.8	484.8	496.5	416.6	416.5	416.5	399.5
6	343.3	343.3	343.3	347.8	287.9	287.9	287.9	320.6	287.9	287.9	287.9	324
7	467.7	475.8	479.5	533.3	373.8	380.8	385.2	486.5	305.6	274.3	265.7	394.5
8	467.7	472.5	479.5	482.4	373.8	376.9	385.2	368.6	305.6	246.6	265.7	324.6
9	400.8	403.1	408.9	473.5	290.9	287.7	278.3	339.9	227.9	237.5	232.4	309.3
10	397.9	404.4	408.2	472.2	264.2	273.2	277.8	339.3	110.5	218.8	229.5	173.6

6.2.4 Symmetric Simulation and Expansion of the System Under PSCs with Fixed Shading Values (4 × 4)

In this section, the system underwent an analogous expansion process. A solar cell with a corresponding SB was added to each LB of the primary system along with the inclusion of a new LB, as shown in Figure 6.4. The simulation results show the superior performance of the proposed system compared to traditional configurations across ten distinct shading scenarios, as presented in Table 6.3, and Figure 6.6 (d) shows the shading patterns.

Table 6.3: A 4 x 4 PV Array Simulation Results Under 10 PS Cases with Three Different Irradiance Values.

PS Cases	MPPT at Irradiance 700 W/m^2				MPPT at Irradiance 500 W/m^2				MPPT at Irradiance 200 W/m^2			
	SP	**BL**	**TCT**	**SB**	**SP**	**BL**	**TCT**	**SB**	**SP**	**BL**	**TCT**	**SB**
1	717	733	744.2	754	662.5	678.4	691.4	726.2	582.4	579.3	596.5	629.1
2	643	718.1	730	750	531.2	660.7	678.1	709.7	531.2	565.8	579.2	613.3
3	715	718	730	749.5	659.6	663.1	678.1	709.7	565.7	568.2	579.2	613.3
4	558	565.7	657.8	692.9	504.7	489.7	533.7	563.3	504.7	489.7	468	472.4
5	558	653.4	718.6	738.9	504.7	527.2	668.8	695.5	504.7	462.4	571.3	604.5
6	553	560.6	655.8	690.5	490.2	484.8	531.9	561.5	458.6	468.8	452.1	457.9
7	637	647.6	655.8	690.5	525.9	519.3	531.9	561.5	485	467.9	452.1	457.9
8	487	708.7	708.7	729.3	487.3	656.1	656.1	683	487.3	564.3	564.3	595.5
9	485	555.8	644.6	678.6	470	443.4	514	544.8	442.4	322.3	338.9	359.9
10	548	560	564	595.1	456.1	472.9	469.7	473.2	323.9	451	452.1	457.8

6.2.5 Comparative Study of Asymmetric and Symmetric Expanded PV Systems

An exhaustive comparative analysis was conducted by juxtaposing the proposed expanded system with analogous systems delineated in previous research. The objective of this comparative study was to assess the proficiency and practicality of the proposed system, particularly in scenarios requiring system expansion via the integration of PV panels. This evaluative review serves as a critical tool for ascertaining the relative efficacy of the proposed system compared with other systems.

6.2.5.1 Asymmetric 4 x 3 PV Array

A comparative analysis of the proposed expanded system and a similar existing system was performed in [110]. The evaluation involved conducting simulations using MATLAB for two distinct shading scenarios. The findings demonstrate the notable superiority of the proposed expanded system over the comparative system. These results validate the resilience of the system in handling diverse random shading conditions, its effectiveness in minimizing power loss, and its simplicity in installation and panel integration. A detailed summary of the results is presented in Table 6.4. Notably, the proposed SB system exhibited superior performance in terms of energy generation and efficiency across all shading scenarios, as depicted in Figure 6.9.

The proposed SB method achieves significant efficiency improvements over TCT, Zig-Zag, and hybrid particle swarm optimization (HPSO) for both Pattern 1 and Pattern 2. In Table 6.4 (Pattern 1), the Proposed SB method reaches an efficiency gain of 27.94%, surpassing TCT and Zig-Zag (both 22.08%) by 5.86% points each **(27.94%−22.08%=5.86%)**. It also maintains a slight advantage over HPSO. In Pattern 2, the efficiency gains are even more pronounced, with improvements of 6.04% points over TCT and 2.57% points over Zig-Zag, while still maintaining a slight advantage over HPSO.

Table 6.4: Comparative Analysis of the Performance of the Proposed System with Similar Systems Across Different Shading Scenarios (4 × 3 PV array).

Methods	**Power (W) Pattern 1**	**Power (W) Pattern 2**	**Efficiency (%) Pattern 1**	**Efficiency (%) Pattern 1**
TCT	808.3	1205.0	22.08	21.12
Zig-Zag	808.3	1403.3	22.08	24.59
HPSO	1021.3	1545.5	27.88	27.08
Proposed SB	1023.7	1549.5	27.94	27.16

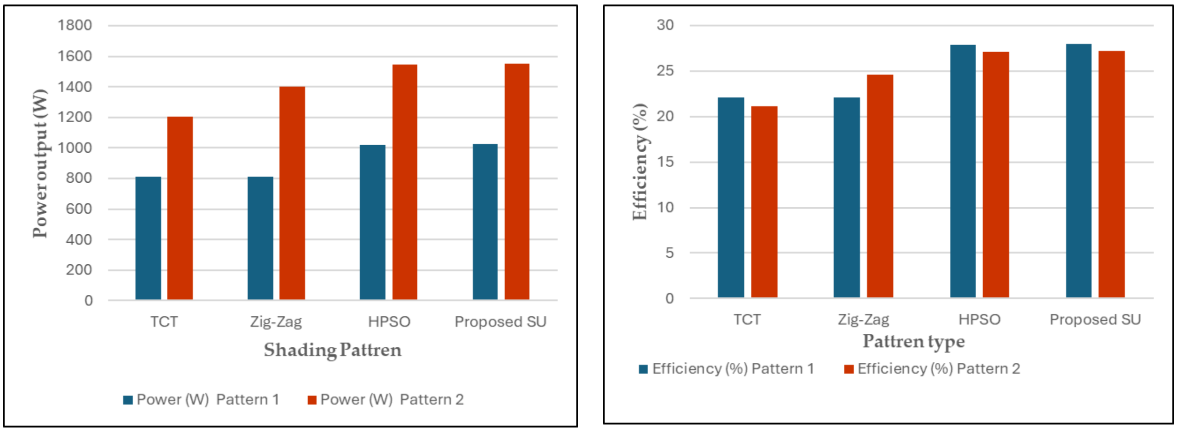

A. Power output for different shading types.

B. Efficiency output for different shading types.

Figure 6.9: Comparative Analysis of Power Output and Efficiency Across Various Shading Types.

6.2.5.2 Symmetric 4 x 4 PV Array

A comprehensive comparative study utilizing MATLAB simulations was conducted to evaluate the performance of the proposed expanded PV system against other similar systems under eight distinct shading scenarios [58]. The proposed system further solidified its position by consistently and significantly outperforming its counterpart in all the simulated shading patterns. These results underscore the remarkable robustness of the system in managing diverse shading conditions, highlighting its exceptional efficiency in minimizing energy losses. The detailed results are presented in Table 6.5. Notably, the proposed SB system exhibited superior performance in terms of energy generation and efficiency across all shading scenarios, as depicted in Figure 6.10 and Figure 6.11.

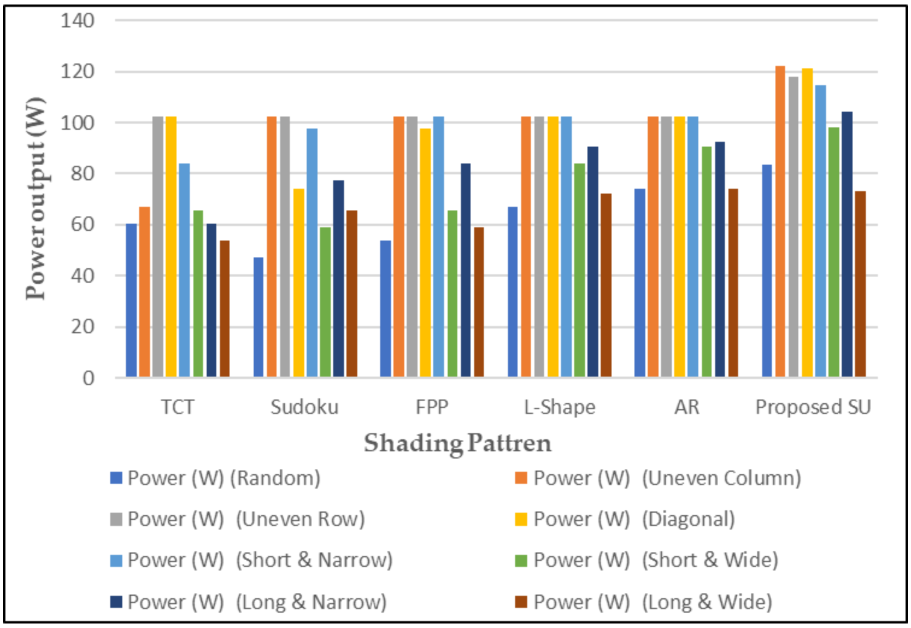

Figure 6.15: Power output for different shading types.

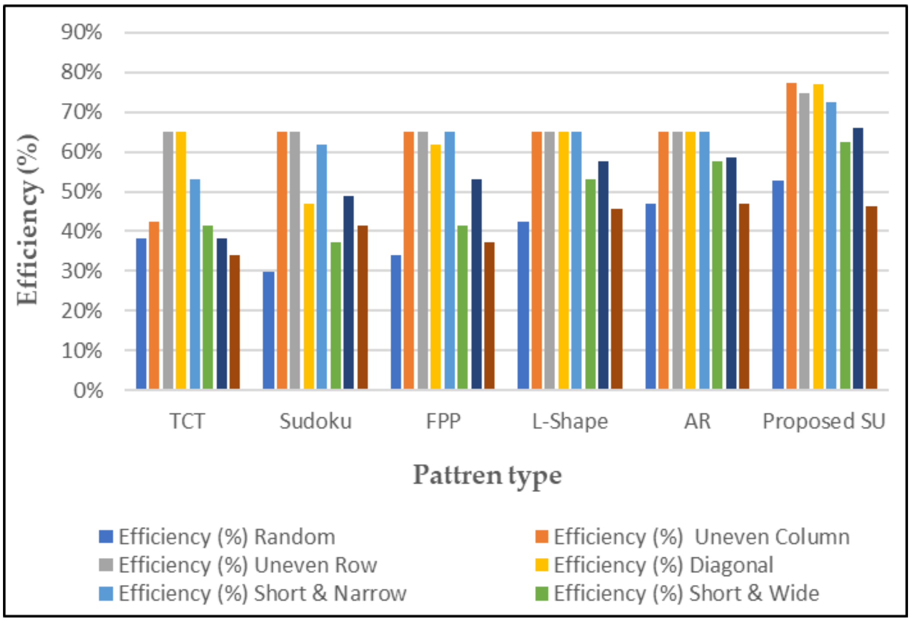

Figure 6. 16: Efficiency output for different shading types.

The proposed SB method consistently outperforms TCT, Sudoku, FPP, L-Shape, and AR across various shading patterns, with efficiency improvements ranging from approximately 12.86% to 81.61% in Pattern 1 (Random), 15.03% to 81.61% in Pattern 2 (Uneven Column), 15.03% to 81.61% in Pattern 3 (Diagonal), 18.24% to 63.99% in Pattern 4 (Short & Narrow), 11.67% to 36.34% in Pattern 5 (Short & Wide), and 8.48% to 72.99% in Patterns 6 and 7 (Long & Narrow, Long & Wide). These results underscore the consistent superiority of the proposed SB method in optimizing the efficiency across diverse shading scenarios.

Table 6.5: Comparative Analysis of the Performance of the Proposed System with Similar Systems Across Different Shading Scenarios (4 × 4 PV Array).

Methods	**Power (W) Pattern 1 (Random)**	**Power (W) Pattern 2 (Uneven Column)**	**Power (W) Pattern 3 (Diagonal)**	**Power (W) Pattern 4 (Short & Narrow)**	**Power (W) Pattern 5 (Short & Wide)**	**Power (W) Pattern 6 (Long & Narrow)**	**Power (W) Pattern 7 (Long & Wide)**
TCT	60.5	67.2	102.5	102.5	84	65.5	60.3
Sudoku	47	102.5	102.5	73.9	97.4	58.8	77.3
FPP	53.9	102.5	102.5	97.4	102.5	65.5	84
L-Shape	67.2	102.5	102.5	102.5	102.5	84	90.7
AR	73.9	102.5	102.5	102.5	102.5	90.7	92.4
Proposed SB	83.42	122.1	117.9	121.4	114.6	98.3	104.2
Methods	**Efficiency (%) (Random)**	**Efficiency (%) (Uneven Column)**	**Efficiency (%) (Diagonal)**	**Efficiency (%) (Short & Narrow)**	**Efficiency (%) (Short & Wide)**	**Efficiency (%) (Long & Narrow)**	**Efficiency (%) (Long & Wide)**
TCT	38.34	42.58	65.02	65.02	53.23	41.53	38.27
Sudoku	29.82	65.02	65.02	46.87	61.76	37.28	49
FPP	34.16	65.02	65.02	61.76	65.02	41.53	53.23
L-Shape	42.58	65.02	65.02	65.02	65.02	53.23	57.51
AR	46.85	65.02	65.02	65.02	65.02	57.51	58.61
Proposed SB	52.87	77.35	74.78	76.88	72.60	62.42	66.16

6.2.6 Comparison of the Number of Connections (Switches)

Analyzing the switch requirements for dynamic PV array reconfiguration across six array sizes (2x2 to 4x4), this study highlights the substantial advantages of the proposed method. The Proposed SB method achieves a significant reduction in switch count compared to existing techniques. Specifically, it **reduces switches by 79.17% c**ompared to the Dynamic Electrical Scheme (DES), **76.56%** compared to the Electrical Array Reconfiguration (EAR), and **11.76%** compared to the Modified Circuit Reconfiguration (MCR) for a 4×4 PV array, demonstrating its superior efficiency in minimizing hardware complexity. The switch reduction equation, expressed as:

$$R_{\text{switch}} = \left(\frac{S_{\text{Reference}} - S_{\text{SB}}}{S_{\text{Reference}}}\right) \times 100 \tag{55}$$

where $S_{Reference}$ represents the switch count in DES, EAR, or MCR, and S_{SB} corresponds to the optimized switch count in the Proposed SB method. This equation quantifies the percentage decrease in switch usage, confirming the Proposed SB's capability to significantly reduce hardware complexity while maintaining system performance. Although DES generally requires the most switches and EAR exhibits a simpler equation, it does not match the efficiency of the proposed method, especially in larger arrays. The MCR offers balance but still exceeds the switch count of the proposed method. Overall, the clear advantage of the proposed method in the switch count across various sizes suggests its promise for more practical and efficient dynamic reconfiguration solutions. Further considerations include evaluating other factors, such as switch complexity and cost, exploring applicability to different circuits, and validating the findings through experimentation. Table 6.6 lists the variations in the number of switches utilized for each dynamic system. There are different types of switches used in electrical circuits: single pole, single throw (SPST), double pole, single throw (DPST), single pole, double throw (SPDT), and single-pole m-throws (mPST).

Table 6.6: Comparison of the Number of Switches Among Dynamic Circuit Reconfiguration Techniques.

Methods	**Switches Equation**	**2 x 2 PV array**	**2 x 3 PV array**	**3 x 3 PV array**	**2 x 5 PV array**	**3 x 4 PV array**	**4 x 4 PV array**
DES [111]	$(2mN_{PV})$ DPST + (N_{PV}) SPST	(16 SPDT + 4 SPST)	(36 SPDT + 6 SPST)	(54 SPDT + 9 SPST)	(100 SPDT + 10 SPST)	(96 SPDT + 12 SPST)	(128 SPDT + 16 SPST)
EAR [111]	$(2N_{PV})$ mPST	16 SPST (8 mPST)	36 SPST (12 mPST)	54 SPST (18 mPST)	60 SPST (20 mPST)	96 SPST (24 mPST)	128 SPST (32 mPST)
MCR [111]	$[2N_{PV} + (m-2)]$ SPST	8 SPST	13 SPST	19 SPST	23 SPST	26 SPST	34 SPST
Proposed SB	$(N_{PV}2) - 2$	6 SPDT	10 SPDT	16 SPDT	18 SPDT	22 SPDT	30 SPDT

6.3 Comparative Analysis of MPPT Techniques Across Different PV Array Configurations

This section compares the performance of MPPT techniques applied to PV array configurations (SP, BL, TCT, and SB) under varying irradiance levels. As shown in Tables B.3–B.5, in a 3 × 3 PV array, the SB method consistently outperforms other techniques, achieving average efficiency improvements of 10.95% at 750 W/m², 20.6% at 500 W/m², and 21.7% at 250 W/m². Across different array configurations and irradiance levels, SB remains superior. For a 3 × 4 PV array, it demonstrates average improvements of 7.82% at 700 W/m², 16.32% at 500 W/m², and 18.67% at 200 W/m². Similarly, in a 4 × 4 PV array, SB achieves 12.1% at 700 W/m², 11.55% at 500 W/m², and 6.34% at 200 W/m². These results highlight the consistent effectiveness of SB in optimizing PV array performance across various conditions, reinforcing its superiority over SP, BL, and TCT techniques.

6.4 Conclusions

This paper introduces a hierarchical PV array reconfiguration method with a switching block to enhance power output under partial shading conditions. MATLAB-Simulink evaluations confirm that the proposed SB method outperforms TCT, Zig-Zag, and HPSO [110], as well as TCT, Sudoku, FPP, L-shape, and AR [58]. The hierarchical structure ensures scalability, making expansion efficient. In a **3 × 3 PV array**, the Proposed SB method consistently achieves higher efficiency compared to conventional configurations, with **average improvement efficiencies of 10.95% at 750 W/m², 20.6% at 500 W/m², and 21.7% at 250 W/m²**. Across different PV array sizes, SB maintains superiority, demonstrating **7.82% to 12.1% improvements at 700 W/m², 11.55% to 16.32% at 500 W/m², and 6.34% to 18.67% at 200 W/m²**. Additionally, it shows **5.86% to 6.04%** efficiency gain improvements over **TCT, Zig-Zag, and HPSO**, and **8.48% to 81.61%** over configurations in [111]. Furthermore, the Proposed SB method significantly reduces the switch count, achieving a **79.17% reduction** compared to **DES**, **76.56%** compared to **EAR**, and **11.76%** compared to **MCR** for a **4 × 4 PV array**, minimizing hardware complexity. Its minimal switches and simple circuitry enhance reliability, reduce maintenance, and improve adaptability under various shading conditions. These findings highlight the SB method's effectiveness in optimizing PV system performance while maintaining a streamlined and efficient design.

6.5 Summary

This chapter introduces a scalable hierarchical SB architecture for dynamic PV array reconfiguration under PS conditions. This hierarchical SB system enhances PV array performance by enabling real-time adjustments to module connections, optimizing energy harvesting efficiency across various scenarios. The research develops a dynamic reconfiguration method employing SBs organized hierarchically. This system supports seamless expansion and adaptability to both symmetric and asymmetric configurations without requiring complete system rewiring. Additionally, an efficient control algorithm utilizing real-time irradiance data from embedded sensors dynamically adjusts the PV array configuration. The proposed SB architecture reduces the number of required switches compared to existing techniques, ensuring scalability and efficiency. Expected benefits include improved energy generation, enhanced system flexibility, minimized power loss under PS conditions, and ease of maintenance due to reduced circuit complexity.

Thesis IV *[3]*

I proposed Model-B, an optimization-driven dynamic PV array reconfiguration system that adapts electrical connections in real time based on irradiance sensor data. The system dynamically switches between series and parallel configurations, maximizing energy output and outperforming traditional methods such as SP, BL, and TCT. Simulations demonstrated scalability with seamless asymmetric and symmetric expansions, achieving an efficiency gain of up to 6.04% over TCT, Zig-Zag, and HPSO, while reducing the switch count by up to 79.17% compared to DES. This approach simplifies connections, reduces complexity, and enhances system robustness under diverse shading conditions.

Chapter 7. Dynamic Probabilistic Reconfiguration for Optimized Photovoltaic Performance under Shading and Temperature Variations

The content of this chapter has been accepted for publication in the International Journal of Intelligent Engineering and Systems (IJIES).

The current study addresses partial shading and temperature variations in photovoltaic (PV) arrays by developing a scalable hierarchical system. The proposed model, featuring switching blocks in a hierarchical structure, was simulated in various PV configurations, including SP, BL, and TCT, using MATLAB-Simulink. A dynamic probabilistic reconfiguration algorithm (DPRA) enables real-time electrical adjustments with minimal switches, guided by Solar Irradiance Sensor Cells (SISCs) and DS18B20 temperature sensors to optimize Maximum Power Point Tracking (MPPT).

Testing across multiple shading scenarios demonstrated the DPRA's scalability and adaptability. Simulation and experimental results showed that the DPRA achieved an average energy improvement of 32% in simulations and 39% in experimental results compared to conventional methods. Thus, this chapter confirms the DPRA's effectiveness as a scalable, cost-effective solution for enhancing PV system efficiency and longevity.

7.1 Artificial Partial Shading Effects on PV Arrays

To assess the effects of partial shading (PS) on a PV array, a shading experiment was conducted. A white raw fabric was employed to simulate real-world shading scenarios, such as those caused by trees, buildings, or clouds. The choice of white raw fabric was intentional due to its neutral light-blocking properties. Each layer of raw fabric reduced sunlight by approximately 10%. Shading levels were systematically increased from 10% to 80% by adding up to eight layers, allowing for precise control and consistent results.

The baseline performance of the PV array was first recorded under full sunlight with no shading. Subsequently, raw fabric layers were gradually added, and the resulting voltage, current, and power outputs were measured and compared to the baseline. A 5% margin of error was incorporated to account for potential inconsistencies in the fabric material and environmental testing conditions.

The shading simulation revealed a strong correlation between the degree of shading and the reduction in energy output. At 50% shading, the PV array's energy production decreased by 45% to 55%, while at 70% shading, the energy output declined by 65% to 75%. These findings highlight the significant impact of shading on PV performance and underscore the importance of strategies aimed at minimizing energy losses under PS conditions. Figure 7.1 shows the use of raw fabric layers to apply different stages of shading on the PV array.

Figure 7.1: Different stages of shading applied using fabric layers.

7.2 Dynamic Probabilistic Reconfiguration Algorithm (DPRA)

The proposed DPRA governs the switching blocks (SBs) within the switch array (SA) through the following processes. For instance, the control of a single SB connected to two PV panels, which is managed through the use of two relays. Under standard operating conditions, both relays within the SB are in their default state, which is the normally closed position. In this configuration, the two PV panels are connected in parallel, ensuring that both contribute to the system's power output. When the DPRA issues a command to change the state of any relay within the SB to the normally open position, the PV panel connected to that relay is effectively isolated from the system, resulting in its disconnection. Consequently, the output of the SB in this scenario will solely reflect the output of the remaining connected PV panels.

On the other hand, if the DPRA modifies the state of both relays to the normally open position, the connection between the two PV panels is altered from a parallel to a series configuration. This change in the electrical connection impacts the overall system performance by adjusting the voltage and current characteristics of the output. Table 7.1 illustrates the various control states executed by the DPRA within a single SB. This table outlines the fundamental principles governing the proposed system's reconfiguration processes for the PV panel array, which are critical to optimizing system performance under varying operational conditions.

Table 7.1: Control States Executed by DPRA for Reconfiguration in a Single SB.

DPRA Commands		SB 1		Connection Type
PV1	PV2	Relay 1	Relay 2	
0	0	NC	NC	Parallel
0	1	NC	NO	PV1 Output
1	0	NO	NC	PV2 Output
1	1	NO	NO	Series

The proposed DPRA begins by measuring and recording solar radiation intensity using SISC sensors, alongside measuring the system's total power output and the temperature levels of the solar panels. Upon acquiring this data, the DPRA initiates the following computational procedures.

In the first procedure, if PS is detected that affects one or more PV panels within the system, the DPRA initially reconfigures the connections between the relays within the SBs that are directly connected to the PV panels. Specifically, this adjustment involves altering the configuration of the relays in the first layer of the SA while maintaining the existing configurations of the relays in the SBs of the subsequent layers. The DPRA changes the connection type of the SBs associated with the affected or partially shaded panels from a parallel to a series configuration. This reconfiguration aims to prevent or mitigate voltage collapse while preserving the current output.

However, if the extent of shading is significant enough to adversely impact the overall power output, the DPRA transitions to the second procedure to further optimize system performance. This second procedure forms the core of the system’s response to PS by employing a probabilistic reconfiguration strategy. This procedure dynamically adjusts the connections within the PV system across multiple layers based on the shading conditions. The system leverages the flexibility offered by configurable SBs, each of which can toggle between series and parallel configurations according to probabilistic control.

7.2.1 Layer Probabilities Approach

In this configuration, the system is divided into three layers, each with a distinct role in managing the connections between PV panels. Each layer is assigned a probability value of 0 or 1. A probability of 0 indicates that all relays within that layer are in parallel configuration (normally closed), while a probability of 1 indicates that all relays within that layer are in series configuration (normally open).

Given that the system contains three layers, the possible combinations of these probabilities result in eight different configurations (2^3). However, fully parallel or fully series configurations are excluded due to their inherent inefficiency under diverse shading conditions, leaving six valid configurations for real-time optimization. The probability configurations are represented by control function codes, as shown in Table 7.2.

Table 7.2: The probability distribution across the system's layers.

No.	Layer 1 Connections Type	Layer 2 Connections Type	Layer 3 Connections Type	Control Function Code
1	*Parallel*	*Series*	*Series*	100
2	*Series*	*Parallel*	*Series*	010
3	*Parallel*	*Parallel*	*Series*	110
4	*Series*	*Series*	*Parallel*	001
5	*Parallel*	*Series*	*Parallel*	101
6	*Series*	*Parallel*	*Parallel*	011

The system cycles through these configurations, analyzing the power output at each stage. By selectively adjusting layer configurations based on shading conditions, the system optimizes the overall power output.

7.2.2 Dynamic Probabilistic Adjustments

During real-time operation, the algorithm continuously monitors changes in solar irradiance across different PV panels. If a configuration is detected that offers only minimal improvement or maintains constant output, the algorithm adjusts the probabilities within each layer to explore alternate configurations. These adjustments are calculated using predefined rules, ensuring that the system remains stable while responding dynamically to changes in environmental conditions. The second procedure is highly adaptive, enabling the PV system to optimize output even in conditions where traditional MPPT techniques would struggle. By allowing for a fine-tuned, layer-based reconfiguration, this procedure serves as the system’s primary method for addressing PS.

7.2.3 High-Temperature PV Panel Isolation Mechanism

The DPRA is particularly effective in managing high-temperature conditions in PV systems due to its real-time monitoring, adaptive reconfiguration, and probabilistic adjustments. By continuously tracking temperature, the DPRA promptly detects overheating and responds by dynamically reconfiguring the electrical connections within the SA. This reconfiguration helps to mitigate hotspots by isolating affected panels or adjusting their connection type, thereby reducing heat generation. Additionally, the DPRA's ability to distribute thermal load evenly across the system prevents further temperature escalation, enhancing the overall reliability and longevity of the PV panels. Through these capabilities, the DPRA ensures that the PV system operates efficiently and safely, even under varying and extreme temperature conditions.

The procedure for isolating any affected panel within the system involves a series of status checks for the SB to which the panel is directly connected. Specifically, this includes verifying the status of the relay inside the SB that connects to the affected panel. For instance, in the case of PV2, which is connected to relay 2 within SB1, where relay 1 is also located, the isolation protocol follows the steps outlined below:

A. Isolation Procedure for a Single Affected PV Panel

This procedure is implemented when only one relay within the SB is affected. Under normal operating conditions, both relays (relay 1 and relay 2) are in the normally closed position (0), meaning the panels remain connected to the system. In this configuration, the connection between the two relays is parallel. When the main controller detects a high-temperature alert from PV2, it instructs relay 2 to switch to the open position (1), thereby disconnecting PV2 from the system while keeping relay 1 in the closed position (0). If, however, both relays are found in the open position (1), indicating that the panels are connected in series, the controller issues a command to switch relay 1 to the closed position (0) while maintaining relay 2 in the open position (1), which effectively disconnects PV2.

B. Isolation Procedure of Two Panels

This procedure is implemented when two relays within the same SB are affected. In situations where both relays in the same SB are compromised—such as when PV1 is also exposed to a temperature rise alongside PV2 in SB1—the algorithm escalates to the secondary layer of SBs. In this scenario, SB6, to which SB1 is linked via relay 11, is involved. SB2 is similarly connected via relay 12. The algorithm first checks the state of SB6: if both relays are in the closed position (0), the controller commands relay 11 to switch to the open position (1), while relay 12 remains closed (0), effectively disconnecting SB1—and consequently PV1 and PV2—from the system. Conversely, if both relays are in the open position (1), the controller instructs relay 12 to switch to the closed position (0), leaving relay 11 open (1), thereby isolating both PV1 and PV2.

C. Isolation Procedure of Multiple Panels

This procedure is implemented when a group of relays across multiple SBs is affected. If a temperature rise affects PV panels 1 through 4, the algorithm further escalates to the tertiary layer of SBs, specifically targeting SB8. In this case, relay 15 is used to disconnect both SB1 and SB2 from the system, thereby isolating PV panels 1 to 4. This process mirrors the method applied in SB6, ensuring a systematic approach to isolating affected components while maintaining overall system integrity.

7.2.4 Individual PV Panel Voltage and Current Measurement Process

The DPRA is designed to optimize the performance of PV panels by dynamically adjusting their configuration based on real-time data. It achieves this by using strategically placed sensors and controlling relays within the SBs of the SA. When the DPRA needs to measure the voltage and current of a specific panel, it selectively activates the relays to disconnect other panels, ensuring that the output reflects only the target panel's electrical parameters. This approach allows the DPRA to accurately monitor the performance of individual panels and compare the SISC sensor data with the power output of the targeted panel, providing insights into how shading and irradiance variations affect each panel's performance. The power output of a PV panel has a quadratic relationship with the irradiance measured by the SISC sensor. This relationship is captured by the formula.

$$P(G) \approx 4.9875 \times 10^{-5} \times G^2 \tag{56}$$

where ***P(G)*** represents the power output of the PV panel, and ***G*** represents the solar irradiance. The coefficient 4.9875×10^{-5} is derived from the panel's characteristics, linking the irradiance to the panel's power output.

If the ambient temperature exceeds 45°C, the power calculation must be adjusted to account for the impact of temperature. The power reduction factor is given by:

$$Power\ reduction\ factor \ = \ 1 \ + \ TCP \ \times \ (T - 25) \tag{57}$$

where ***TCP*** is the temperature coefficient of power, and ***T*** is the ambient temperature. Assuming a standard temperature coefficient of power of −0.4% per °C and considering that the temperature is 45°C (which is 20°C above the standard reference temperature of 25°C), the power output is reduced by a factor of 0.92. Therefore, the new power output at 45°C is expressed as:

$$P_{45^{0}C}(G) = 0.92 \times P(G) \tag{58}$$

This accounts for the temperature effect on the panel’s performance under elevated ambient conditions.

Figure 7.2 shows the relationship between solar irradiance (simplified) and the power output of a PV panel at 45°C ambient temperature. As the irradiance increases, the power output rises, but at a reduced rate due to the higher temperature, demonstrating how high temperatures can negatively affect power generation efficiency.

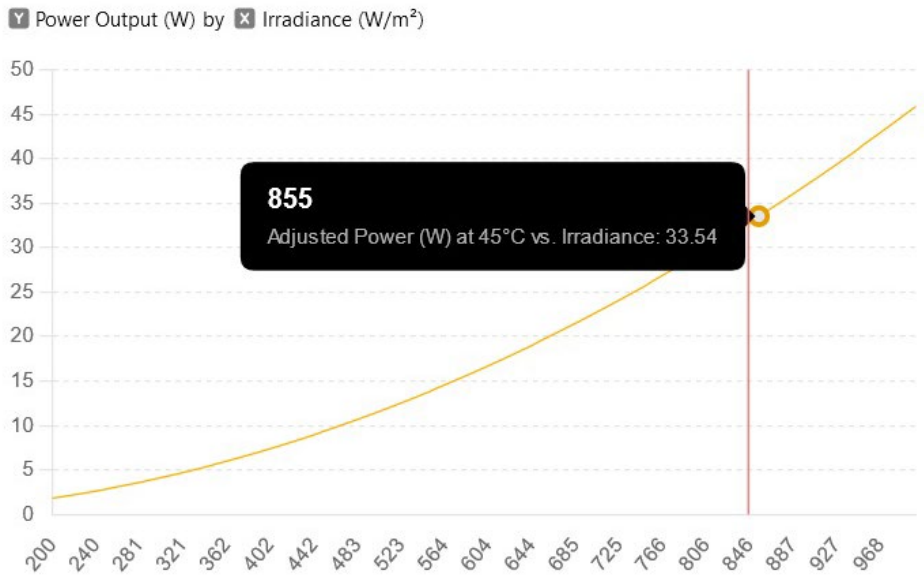

Figure 7.2: The relationship between irradiance and power output at 45°c ambient temperature.

To measure a panel’s voltage, the DPRA selectively activates the relays within the SB to segregate the desired panel. For instance, to determine the voltage output of PV panel 3, the DPRA operates through SB2 by sending a control instruction (0) to relay 3 (connected to PV panel 3) and a control instruction (1) to relay 4 (connected to PV panel 4). This ensures that the output of SB2 exclusively reflects the voltage of PV panel 3.

The process continues with the DPRA issuing a control instruction (0) to relay 12, connected to SB2, while sending instruction (1) to relay 11, connected to SB1—both located in SB6. Finally, the DPRA sends instructions (0) to relay 15 and instruction (1) to relay 16 in SB8. This systematic relay control process, depicted in Figure 4.14, ensures segregated and accurate voltage measurement for individual PV panels within the system. This method allows the DPRA to perform a comparative analysis of solar irradiation data from the SISC sensor associated with panel 3 and the panel's power output, leveraging previously introduced mathematical models. This process facilitates accurate assessment and compensation for variations in solar irradiation that impact the performance of individual PV panels. Table 7.3 provides a comprehensive sequence of the algorithm's instructions for reading the voltage and current values of each PV panel. Complementing this, Figure B.7 offers a schematic representation of the voltage and current measurement process for panel 3, illustrating the specific relay paths that need to be opened and closed until the final block is reached. Figure B.8 represents the DPRA flowchart, highlighting dynamic reconfiguration, temperature isolation, and panel measurement processes for PV optimization.

Table 7.3: The procedure of the algorithm's instructions for measuring the voltage and current of any PV panel within the system involves controlling its associated SB.

PV Panels	**SB1**		**SB2**		**SB3**		**SB4**		**SB5**		**SB6**		**SB7**		**SB8**	
	Relay 1	**Relay 2**	**Relay 3**	**Relay 4**	**Relay 5**	**Relay 6**	**Relay 7**	**Relay 8**	**Relay 9**	**Relay 10**	**Relay 11**	**Relay 12**	**Relay 13**	**Relay 14**	**Relay 15**	**Relay 16**
PV1	0	1	-	-	-	-	-	-	-	-	0	1	-	-	0	1
PV2	1	0	-	-	-	-	-	-	-	-	0	1	-	-	0	1
PV3	-	-	0	1	-	-	-	-	-	-	1	0	-	-	0	1
PV4	-	-	1	0	-	-	-	-	-	-	1	0	-	-	0	1
PV5	-	-	-	-	0	1	-	-	-	-	-	-	0	1	1	0
PV6	-	-	-	-	1	0	-	-	-	-	-	-	0	1	1	0
PV7	-	-	-	-	-	-	0	1	1	0	-	-	1	0	1	0
PV8	-	-	-	-	-	-	1	0	1	0	-	-	1	0	1	0
PV9	-	-	-	-	-	-	-	-	0	1	-	-	1	0	1	0

7.3. Results and Discussion

The performance of the DPRA was evaluated under three different irradiance levels 680 W/m² (20% shading), 425 W/m² (50% shading), and 255 W/m² (70% shading), and compared to traditional PV) configurations: SP, BL, and TCT, across 25 distinct shading patterns. The results demonstrate that the DPRA consistently outperforms traditional methods across varying shading conditions, maintaining higher energy output and optimizing system performance. Below is a detailed discussion of the results, including comparative analysis of simulation and practical data.

7.3.1 Power Output Comparison at 680 W/m², 425 W/m², and 255 W/m²

Table B.6 summarizes the simulation and practical results of power output for different shading cases across three irradiance levels. The DPRA consistently provided higher energy output compared to the traditional methods (SP, BL, and TCT) under all conditions, particularly in severe shading cases.

7.3.2 Analysis of Simulation and Experimental Results

The results demonstrate that the DPRA consistently outperforms conventional configurations like SP, BL, and TCT under various PS conditions. Across all 25 shading cases, DPRA showed significantly higher power outputs, particularly in challenging scenarios with severe shading and lower irradiance levels. The experimental data, while slightly lower than simulation results, confirm the robustness and effectiveness of DPRA in real-world conditions, validating its potential for optimizing PV performance and maximizing energy yield under non-uniform irradiance.

7.3.2.1 Grouped Analysis of Shading Cases

Group 1: Case 0 (No Shading)

In this baseline case, all configurations performed similarly under both simulation and experimental conditions, as expected in the absence of shading. This serves as the reference point for evaluating the impact of shading in subsequent cases.

Group 2: Cases 1, 2, 3 (Mild Shading)

These cases feature mild, uniform shading patterns. DPRA consistently outperformed other configurations across all irradiance levels. For example, under 680 W/m² in Case 1, DPRA achieved 314.6 W in simulations and 298.2 W in experiments, demonstrating better adaptation and optimization compared to other methods.

Group 3: Cases 4, 5, 6, 7 (Moderate Shading)

These cases involve moderate shading, with more complex patterns than the previous group. DPRA showed a significant performance advantage, particularly in Case 5, where it achieved 305.7 W (simulation) and 303.5 W (experimental), highlighting its capability to handle more intricate shading scenarios effectively.

Group 4: Cases 8, 9, 10 (Complex Shading)

These cases present complex shading scenarios with non-uniform distribution across the array. DPRA maintained higher power outputs, especially in Case 8, achieving 286.4 W (simulation) and 269.2 W (experimental) under 680 W/m², whereas other configurations struggled below 250 W.

Group 5: Cases 11, 12, 13, 14, 15 (Severe Shading)

Severe shading cases demonstrated the robustness of DPRA, particularly under lower irradiance levels. For instance, in Case 15 under 255 W/m², DPRA achieved 213.8 W (simulation) and 176.8 W (experimental), significantly outperforming other configurations, which were below 110 W.

Group 6: Cases 16, 17, 18 (Partial Row Shading)

These cases feature partial row shading affecting specific sections of the PV array. DPRA effectively managed these scenarios, achieving up to 278.8 W (simulation) and 255.5 W (experimental) in Case 18 under 680 W/m², outperforming other configurations by a significant margin.

Group 7: Cases 19, 20, 21 (Severe and Uniform Shading)

Uniform severe shading across most of the array tested the resilience of each configuration. In Case 19 under 255 W/m², DPRA recovered more power, achieving 75.8 W (simulation) and 65.4 W (experimental), while other configurations fell below 40 W.

Group 8: Cases 22, 23, 24, 25 (Mixed Shading Patterns)

These cases incorporate a variety of shading patterns, combining mild to severe shading. DPRA adapted well, achieving 249.3 W (simulation) and 235.6 W (experimental) in Case 24 under 680 W/m², consistently outperforming SP and BL configurations.

Overall, DPRA's dynamic reconfiguration approach proves highly effective in optimizing power output under diverse shading scenarios, showcasing its robustness and potential for real-world applications in PV systems.

Figure B.9 (a)-(c) presents the comparison between DPRA and other configurations (TCT, BL, SP) for all shading cases under both simulation and experimental conditions. It clearly illustrates the superior performance of the DPRA configuration across various shading patterns, highlighting its capability to adapt dynamically and recover more power compared to traditional configurations. The visual representation further validates the numerical analysis, demonstrating the effectiveness of DPRA in maximizing energy yield under PS conditions.

7.3.2.2 Power Losses for Different Shading Cases

Shading impacts on PV configurations were analyzed by comparing power losses across different shading cases. DPRA consistently showed the lowest losses. In Shading Case 1, DPRA losses were 8.52% (simulation) and 5.62% (experimental), lower than SP (12.55%, 11.13%), BL (11.03%, 11.16%), and TCT (8.15%, 10.98%). This trend highlights DPRA's effectiveness in reducing power losses under varying shading conditions, as illustrated in Figure 7.3.

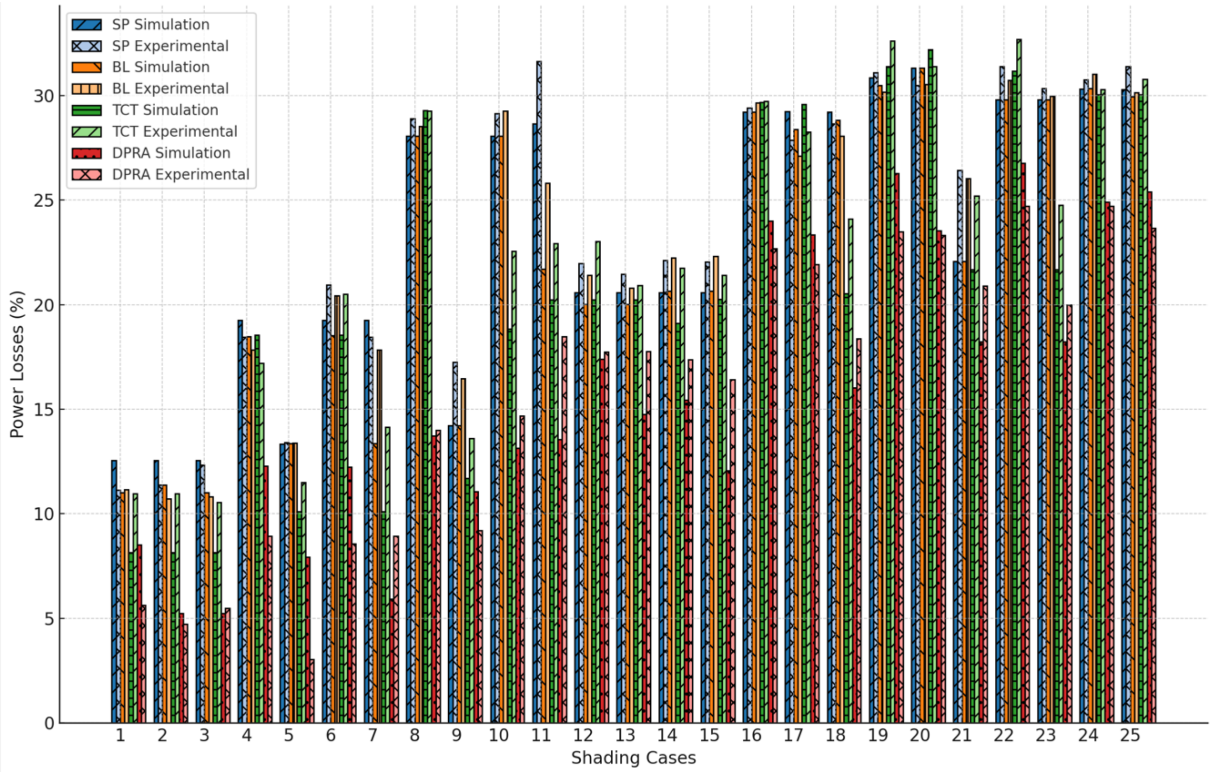

Figure 7.3: Effect of shading cases on power losses for different PV configurations.

7.3.2.3 Efficiency Analysis

The efficiency analysis, as illustrated in the Figure 7.4, highlights the superior performance of the DPRA configuration compared to conventional configurations (SP, BL, TCT) across all irradiance levels (680 W/m², 425 W/m², and 255 W/m²). At 680 W/m², DPRA achieved an average experimental efficiency of 84.2%, showing a minimal deviation of 0.024% from its simulation result of 84.18%. Similarly, at 425 W/m², DPRA exhibited an experimental efficiency of 64.27%, with only a 0.65% reduction from its simulation efficiency of 64.69%. Even under low irradiance conditions (255 W/m²), DPRA maintained its robustness, recording an experimental efficiency of 51.7%, with a minimal deviation of 0.008% from the simulation value of 51.8%. The deviation between simulation and experimental efficiency is calculated using the formula.

$$\text{Deviation}(\%) = \left| \frac{\text{Simulation Efficiency} - \text{Experimental Efficiency}}{\text{Simulation Efficiency}} \right| \times 100 \tag{59}$$

This analysis underscores the reliability and adaptability of DPRA in mitigating shading effects and maximizing efficiency across diverse environmental conditions, outperforming conventional methods.

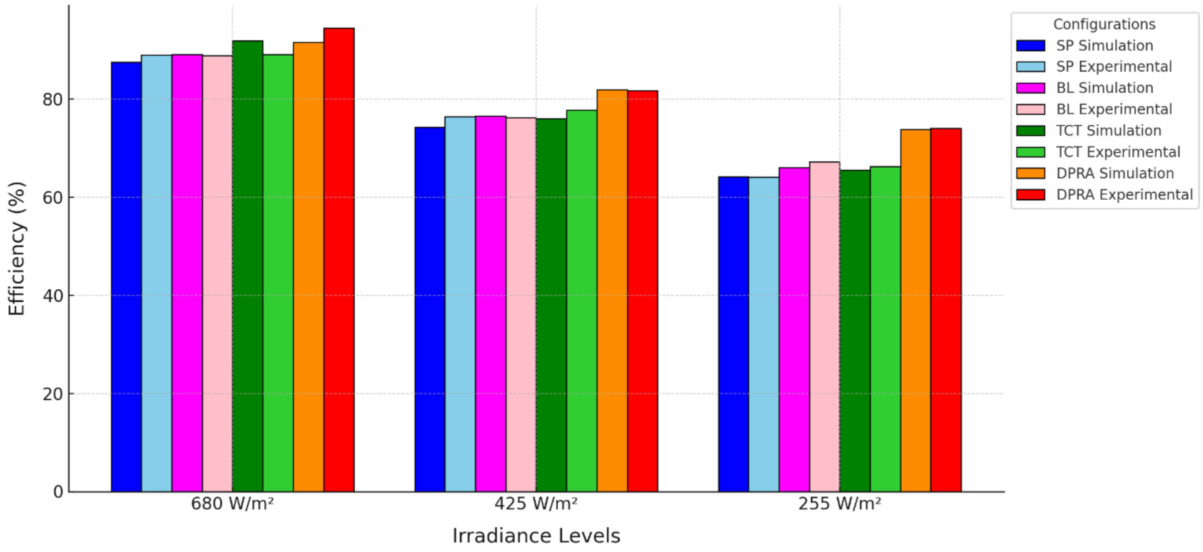

Figure 7.4: Efficiency comparison of SP, BL, TCT, and DPRA configurations under different irradiance levels.

7.3.3 Probability Optimization for Performance and Efficiency

The study highlights a significant optimization in probability combinations for reconfiguring PV arrays, showing that reducing the original six combinations to the best three (001, 010, 100) still yields 100% of the optimal energy output while using only 50% of the combinations. This reduction leads to faster reconfiguration decisions, improving both computational efficiency and system performance, as the DPRA requires fewer iterations to determine the optimal configuration. This enhances the algorithm's ability to quickly adapt to dynamic shading conditions, particularly in larger or highly variable environments. The reduction in probability combinations directly improves time efficiency, crucial in real-time reconfiguration systems where rapid adaptation to changes, such as passing clouds or temporary obstructions, is essential for maintaining energy efficiency. Faster reconfigurations minimize unnecessary adjustments, reducing wear on switching components and contributing to the long-term reliability and durability of the PV system. By streamlining the process, the DPRA becomes more scalable and robust, especially in environments with frequent shading fluctuations.

7.3.4 Temperature and Lifespan Impact on PV Panels

In addition to the shading experiments, the impact of temperature on PV panel performance and lifespan was also investigated. On June 25th, 2024, an experiment was conducted in the Kirkuk region of Iraq to assess how temperature variations affect the operational life of PV panels. This experiment provided crucial data on the relationship between panel temperature, shading, and lifespan, allowing for more accurate predictions of long-term panel degradation.

7.3.4.1 Experimental Setup and Temperature Measurement

The temperature experiment took place between 13:05 PM and 14:35 PM at coordinates 35.466633 latitude and 44.379889 longitude, with ambient temperatures ranging from 43°C to

46°C. DS18B20 temperature sensors were used to monitor the surface temperature of the PV panels, strategically placed at the rear center of the panels where shading effects were most pronounced. Artificial shading was applied to cover 20%, 40%, 60%, or 80% of the incoming solar radiation, leading to a decrease in both voltage and current output. Temperature readings were recorded every 10 minutes to capture detailed variations, and the PV module was manually adjusted every 5 minutes to maintain optimal orientation toward the sun.

7.3.4.2 Temperature's Effect on PV Panel Lifespan

The relationship between temperature and the operational lifespan was modeled using an Arrhenius-type equation (Equation 58), which relates the rate of degradation to temperature. At a reference temperature of 25°C, the operational life of a PV panel is typically estimated to be 25 years. However, as the panel temperature increases, the operational life decreases exponentially, as shown in the equation:

$$Life\ Reduction\ Factor = 2^{\left(\frac{T_{operating} - T_{refrence}}{10}\right)} \qquad (60)$$

Where $T_{operating}$ is the actual operating temperature of the panel and $T_{refrence}$ is the reference temperature, typically 25°C. The operational life is then calculated using (Equation 59).

$$Operational\ Life = \frac{25\ years}{Life\ Reduction\ Factor} \qquad (61)$$

Table 7.4 shows the operational life and temperature of PV panels under varying shading levels, comparing scenarios where the shaded panels were connected to the system versus those where they were disconnected.

Table 7.4: Solar Cell Lifespan and Temperature: Shading Impact Analysis.

Time of Measurement (PM)	Shading Level (%)	Operational Life (Years) - Disconnected	Temperature (°C) - Disconnected	Operational Life (Years) - Connected	Temperature (°C) - Connected
13:05	0	1	76.45		
13:15				1	70.3
13:25	20	2	61.93		
13:35				1.5	64.73
13:45	40	3	56.64		
13:55				2	58.48
14:05	60	4	51.77		
14:15				3	53.59
14:25	80	6	46.58		
14:35				4	49.88

Figure 7.5 illustrates the temporal surface temperature variation during the experiment and the relationship between cell age and temperature across various levels of PS. The results demonstrate that as shading levels and corresponding temperatures increase, the operational

lifespan of the PV panels decreases significantly. Panels left connected under shading conditions experienced higher temperatures and a more rapid decline in operational life compared to disconnected panels.

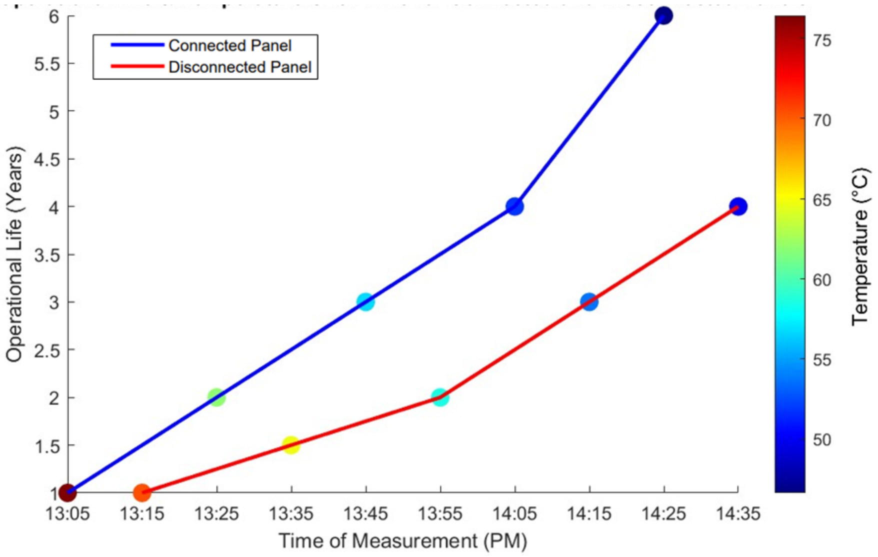

Figure 7.5: Operational life and temperature over time for connected and disconnected shaded panels.

7.3.5 Cost Analysis

The cost analysis in Table 7.5 illustrates that the traditional TCT configuration versus the proposed DPRA configuration reveals a modest increase in expenditure for the latter, with costs totaling $591 for TCT and $688 for DPRA. This $97 increase in the DPRA setup is primarily due to the inclusion of additional components essential for its advanced reconfiguration capabilities. These components include SISCs, relays, microcontrollers, temperature sensors, all of which are not required in the TCT configuration. While the initial investment for the DPRA system is higher, it offers significant advantages in terms of optimizing energy yield and efficiency under PS and temperature variations, thereby justifying the additional cost. This enhanced performance makes the DPRA configuration a cost-effective solution for improving PV system reliability and energy output in diverse environmental conditions.

Table 7.5: Cost Comparison of TCT and DPRA Configurations.

No	**Components and types**	**TCT**	**DPRA**	**Cost in USD**
1	Solar cell 670 × 530 × 25 mm (50 Watts)	✓	✓	450 $
2	Small Solar cell 50 ×50 mm (0.50 Watt)	✗	✓	27.5 $
3	Xbee Module S2C & shield	✓	✓	126.5 $
4	Switch Relays	✗	✓	25 $
5	Arduino Mega	✗	✓	22 $
6	DS18B20 Temperature sensor	✗	✓	22.5 $
7	Voltage Divider Voltage sensor	✓	✓	1 $
8	Current sensor	✓	✓	3.5 $
9	Others	✓	✓	10 $
10	***Total Price***	***591 $***	***688 $***	***688 $***

7.4. Conclusion

This study introduced a DPRA to enhance PV performance under partial shading and temperature variations by dynamically adjusting electrical connections. As shown in Table B.7, the DPRA improved energy output by **8.19% (simulation)** and **9.70% (experiment)** at 680 W/m², **28.58%** and **32.21%** at 425 W/m², and **32% and 39.20%** at 255 W/m², outperforming traditional configurations (SP, BL, and TCT). For instance, as presented in Table B.6, under severe shading (255 W/m², Shading Case 15), the DPRA delivered **213.8 W (simulation)** and **176.8 W (experiment)**, nearly doubling the output of conventional methods. Additionally, at 680 W/m² (Shading Case 1), DPRA reduced power losses to **8.52% (simulation)** and **5.62% (experiment)**, lower than the 8.15%–12.55% losses in SP, BL, and TCT.

The integration of effective isolation mechanisms reduced operating temperatures from **76.45°C to around 61.93°C**, extending the panel lifespan. During testing, cell temperatures approached the manufacturer's maximum of 85°C, underscoring the need for robust isolation to prevent overheating and ensure long-term system durability. The DPRA also reduced computational complexity **by 50%** through probabilistic optimization, enhancing its adaptability without compromising performance.

Although the initial cost for DPRA implementation is slightly **higher ($688)** compared to **TCT ($591)**, the substantial gains in energy output, efficiency, and system longevity make it a cost-effective, robust, and scalable solution for improving PV system performance in diverse environmental conditions.

7.5 Summary

This chapter introduces the DPRA, a scalable hierarchical system designed to optimize PV performance under partial shading and temperature variations. The DPRA offers significant advancements in PV array reconfiguration, enhancing energy output and system efficiency. It employs a hierarchical SA that dynamically adjusts connections using probabilistic methods, guided by data from SISCs and DS18B20 sensors. This minimizes mismatch losses, mitigates thermal degradation, and optimizes MPPT.

Additionally, the DPRA includes an isolation mechanism for high-temperature PV panels, enhancing safety and extending lifespans by disconnecting panels exceeding temperature thresholds. A layer-based probabilistic approach reduces computational complexity by 50%, ensuring efficient system adaptation to environmental changes. The DPRA significantly improved energy output, achieving an average energy improvement **of 32% in simulations** and **39% in experimental conditions** compared to SP, BL, and TCT configurations. It maintains high efficiency under varying irradiance, robust performance against shading and temperature variations, and notable gains in energy output and system longevity with modest implementation costs.

These contributions establish the DPRA as an innovative solution for improving PV system performance. By integrating probabilistic methods and sensor-based controls, it enhances energy efficiency and adaptability, advancing renewable energy systems.

Thesis V *[4]*

I proposed a DPRA to optimize PV system performance under partial shading and temperature variations. The DPRA employs a hierarchical switch array with SISCs and DS18B20 temperature sensors to dynamically adjust electrical connections in real time, minimizing mismatch losses and mitigating thermal degradation. By integrating minimal hardware, the system optimizes voltage and current flow, enhancing energy harvesting efficiency.

Simulation and experimental results demonstrated that the DPRA improved energy output compared to conventional configurations such as SP, BL, and TCT. It achieved an average energy improvement of 32% in simulations and 39% in experimental results. The DPRA offers a scalable, cost-effective solution to enhance PV efficiency, extend panel lifespan, and adapt to diverse environmental conditions.

Chapter 8. Summary

8.1 Contributions

The rapid advancement of PV technology is critical in meeting the global demand for sustainable and renewable energy sources. However, challenges such as partial shading, temperature variations, and system scalability continue to hinder the optimal performance of PV systems. The primary motivation of my doctoral work is to contribute to overcoming these challenges by developing innovative technologies and algorithms that enhance the efficiency, adaptability, and scalability of PV systems under varying environmental conditions. This research presents seven key contributions that collectively advance the field of photovoltaic technology:

Firstly, the development of hierarchical photovoltaic array configurations (Models A and B) introduces a scalable and adaptable structure utilizing Switching Blocks (SBs) and Link Blocks (LBs). This hierarchical design reduces the number of required switches for dynamic reconfiguration, enabling real-time adjustments to optimize performance under partial shading and fluctuating temperatures.

Secondly, the creation of control algorithms using probabilistic methods to facilitate dynamic reconfiguration of PV panels. These algorithms leverage real-time data from Solar Irradiance Sensor Cells (SISCs) to adjust panel configurations probabilistically, ensuring optimal power output despite unpredictable shading patterns and environmental changes.

Thirdly, the integration and calibration of multiple sensors, including SISCs and BH1750 light sensors, enhance real-time system control and monitoring. This integration provides accurate irradiance measurements and dust detection capabilities, reducing operational costs and improving system reliability through precise data acquisition.

Fourthly, the development of an isolation mechanism for high-temperature photovoltaic panels ensures system safety and longevity by automatically disconnecting panels that exceed temperature thresholds. This proactive thermal management prevents overheating and protects the overall system from thermal damage.

Fifthly, the introduction of a method for individual PV panel voltage and current measurement allows for precise performance monitoring and diagnostics. By selectively activating relays within SBs, this method facilitates accurate isolation and measurement of each panel's electrical parameters without additional hardware, enhancing maintenance efficiency and reducing costs.

Sixthly, the optimization of PV array configuration through reduced probabilities streamlines the reconfiguration process by minimizing computational complexity and processing time. By focusing on the most energy-efficient configurations, this strategy improves system responsiveness and reduces wear on physical components, ensuring sustained optimal performance.

Lastly, the development of the Highest and Lowest Layer-Based Exchange (HLLBE) algorithm offers a novel approach for dynamic reconfiguration of PV arrays to address partial shading issues. The HLLBE algorithm uses a reconfigurable switch matrix to equalize irradiance levels across PV array layers, optimizing power output while minimizing switching operations. This approach focuses on maximizing energy efficiency while maintaining cost-effective switch designs, offering a flexible solution to the challenges posed by partial shading.

Through these contributions, my doctoral research addresses critical challenges in photovoltaic technology, providing innovative solutions that enhance efficiency, adaptability, and scalability. The integration of advanced algorithms, sensor technologies, and optimization strategies lays the groundwork for more resilient and efficient PV systems, contributing significantly to the advancement of renewable energy solutions.

8.2 Theses

Thesis I **[1] [3] [4]**

I have introduced a comprehensive system design and research methodology to enable dynamic PV array reconfiguration under partial shading conditions. This approach involved developing and comparing two conceptual frameworks: Model-A and Model-B. Model-A, simulated and practically implemented, connected every two solar panels with a single switching block, simplifying the hierarchical structure. Model-B offered a more advanced configuration by linking every three panels through two SBs within a link block, thereby enabling greater flexibility and the option to replicate various conventional PV arrangements such as SP, BL, and TCT.

I have integrated and calibrated essential components—microcontrollers, sensors, and relays—ensuring accurate data acquisition and reliable PV panel reconfiguration. In addition, I have introduced a hybrid simulation environment that combines MATLAB-Simulink with a microcontroller, confirming the practical feasibility and responsiveness of the chosen strategies. These efforts have laid a solid foundation for subsequent optimization and testing phases, ultimately enhancing the system's adaptability and overall performance under non-uniform irradiance conditions.

Thesis II **[2]**

I proposed the HLLBE Algorithm, a novel approach for dynamic reconfiguration of PV arrays to tackle partial shading issues. The HLLBE algorithm employs a reconfigurable switch matrix to equalize irradiance levels across PV array layers, optimizing power output while minimizing switching operations. This method significantly reduces multiple peaks in power-voltage curves and enhances system adaptability to varying shade patterns. Simulation results demonstrated that the HLLBE algorithm improved efficiency by up to 116.6% compared to *traditional TCT configurations, all while maintaining a streamlined and cost-effective switch design, ultimately enhancing the efficiency and reliability of PV systems.*

Thesis III **[1]**

I developed a scalable hierarchical switching block architecture, Model-A, for dynamic PV array reconfiguration under partial shading. The system integrates SISCs and employs a threshold-based switching mechanism, enabling real-time adjustments of PV module connections to optimize MPPT performance. Simulations conducted in MATLAB–Simulink demonstrated superior results, with the system achieving an average power output improvement of 13.6% compared to SP, BL, and TCT configurations under partial shading conditions. When compared to advanced techniques such as TCT, Sudoku, and other dynamic proposals, the system achieved up to 39.37% improvement in power generation and 39.32% in efficiency. Its hierarchical architecture ensures scalability, adaptability, and enhanced energy harvesting, effectively addressing the challenges of partial shading.

Thesis IV **[3]**

I proposed Model-B, an optimization-driven dynamic PV array reconfiguration system that adapts electrical connections in real time based on irradiance sensor data. The system dynamically switches between series and parallel configurations, maximizing energy output and outperforming traditional methods such as SP, BL, and TCT. Simulations demonstrated scalability with seamless asymmetric and symmetric expansions, achieving an efficiency gain of up to 6.04% over TCT, Zig-Zag, and HPSO, while reducing the switch count by up to 79.17% compared to DES. This approach simplifies connections, reduces complexity, and enhances system robustness under diverse shading conditions.

Thesis V **[4]**

I proposed a DPRA to optimize PV system performance under partial shading and temperature variations. The DPRA employs a hierarchical switch array with SISCs and DS18B20 temperature sensors to dynamically adjust electrical connections in real time, minimizing mismatch losses and mitigating thermal degradation. By integrating minimal hardware, the system optimizes voltage and current flow, enhancing energy harvesting efficiency.

Simulation and experimental results demonstrated that the DPRA improved energy output compared to conventional configurations such as SP, BL, and TCT. It achieved an average energy improvement of 32% in simulations and 39% in experimental results. The DPRA offers a scalable, cost-effective solution to enhance PV efficiency, extend panel lifespan, and adapt to diverse environmental conditions.

Appendix A: System Components

A.1 Hardware Components

A.1.1 PV array

A PV array is designed to convert solar energy into electrical power through interconnected solar panels. Each panel contains solar cells that generate DC electricity when exposed to sunlight. This DC power is then transformed into AC by inverters for use in the electrical grid. The efficiency of the PV array is influenced by factors such as solar irradiance, temperature, shading, and soiling. Optimal performance is achieved with high solar irradiance and cooler temperatures, while shading and soiling can reduce energy production. The angle of sunlight and panel degradation over time also affect the array's output [112]. This system employs HL-Mono 50W modules made from high-efficiency monocrystalline silicon, which perform well even under partial shading. Designed for easy integration into residential and commercial systems, the PV array features dynamic reconfiguration to adapt to changing environmental conditions. Detailed specifications of the PV panels are listed in Table A.1.

Table A.1: Specifications of HL-Mono 50W PV Module at at standard test condition (1000 W/m², 25°C)

Characteristics	**Unit**	**Spec.**
PV Module Type	-	HL-Mono 50W
Size	mm	670*530*25
Working Voltage (*Vmp/V*)	V	17.5
Working current (*Lsc/A*)	A	2.85
Open circuit current (*Vmp/V*)	V	21.6
Short circuit current (*Lsc/A*)	A	23.14
Cell Number	-	9*4 psc
Cell efficiency	%	19
Net weight	kg	3.7
Max. System Voltage	-	DC1000V(*IEC*)

A.1.2 Microcontroller

A microcontroller is a compact computing device housed within a single integrated circuit, encompassing a processor core, memory, and configurable input/output components. Many devices, including widely used platforms like Arduino, are built around microcontrollers [113].

A.1.2.1 Arduino Boards

The Arduino board is an open-source platform that integrates a microcontroller with an Integrated Development Environment (IDE), allowing users to write and upload code via USB. The IDE uses a simplified version of C++ for ease of use, and the board’s standardized form factor organizes its functionalities effectively [114]. Among the numerous Arduino boards available, this study focuses on the UNO (R3) and Mega (R3) models.

A. Arduino UNO(R3)

The Arduino Uno (R3) features the ATmega328P microcontroller and includes 14 digital I/O pins (6 of which support Pulse Width Modulation, or PWM), 6 analog inputs, and a 16 MHz clock speed. It connects via USB for programming and serial communication, has a power jack for external power, an in circuit serial programming (ICSP) header for advanced programming, and a reset button. It is commonly used for educational purposes, basic prototyping, and simple robotics [115]. Figure A.1 depicts the Arduino UNO board.

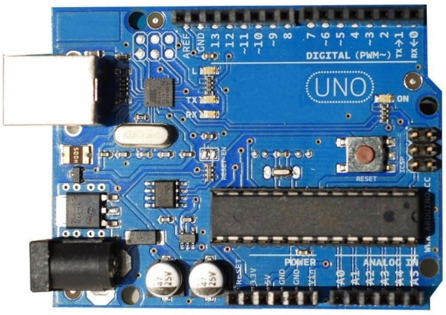

Figure A.1: The Arduino UNO Board.

B. Arduino Mega (R3) Board.

The Arduino Mega (R3), powered by the ATmega2560 microcontroller, offers 54 digital I/O pins (15 with PWM), 16 analog inputs, and 4 UARTs for serial communication. It runs at 16 MHz, with a USB connection, power jack, ICSP header, and reset button. This board is ideal for advanced robotics, 3D printing, data acquisition, and large-scale prototyping. Figure A.2 shows the Mega (R3) board [116].

Figure A.2: Arduino Mega (R3) Board.

A.1.3 Zigbee Wi-Fi

Zigbee is a low-power, low-data-rate wireless protocol operating on the IEEE 802.15.4 standard. It works at 2.4 GHz with a 250-kbps data rate, offering low power consumption and scalability. Zigbee is widely used in smart homes, industrial automation, and sensor networks. It supports a mesh topology, allowing devices to communicate over longer distances by relaying signals through other devices [117].

A.1.3.1 XBee S2

The XBee S2 module, using the ZigBee protocol, supports mesh networking for reliable, low-power wireless connections. Operating at 2.4 GHz with a 250-kbps data rate, it offers a range of 40 meters (indoor) and 120 meters (outdoor). This module is ideal for battery-powered applications that require extended reach and low power consumption [118]. Figure A.3 illustrates the XBee S2.

Figure A.3: The Xbee S2.

A.1.4 KS-M5555 Solar Panel

The KS-M5555 is a monocrystalline silicon solar panel used as a solar irradiance sensor cell (SISC). Known for its high efficiency, it operates at 5V and is encapsulated in durable epoxy resin, making it suitable for small-scale renewable energy systems, industrial applications, and consumer electronics. Figure A.4 shows the KS-M5555, with detailed specifications listed in Table A.2.

Figure A.4: KS-M5555 Module.

Table A.2: Specifications of the SISC module.

Characteristic	**Unit**	**Specification**
PV Module Type		KS-M5555 Monocrystalline silicon
Maximum Power (*Pm*)	W	0.4
Operating Voltage (*Vmp*)	V	5
Operating Current (*Imp*)	mA	80
Power Tolerance	%	±5
Dimensions	mm	55 x 55 x 3
Sealed Technology		Encapsulated with epoxy resin
AM		1.5
Irradiance	W/m^2	1000

A.1.5 Voltage Sensor

The SEN32 REV1.1 (ARD-000774) is a versatile AC/DC voltage sensor for measuring voltages from 0 to 50V, ideal for industrial automation, power systems, and renewable energy. It offers high accuracy (±1% of full-scale range), fast response, and an analog output (0-5V) for easy integration with microcontrollers. The sensor has high input impedance and overvoltage protection up to 60V for safety and durability. Figure A.5 shows the sensor, with specifications listed in Table A.3 [119].

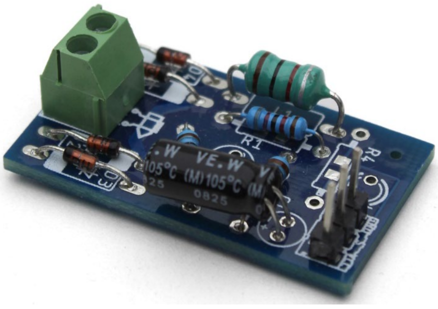

Figure A.5: ARD-000774 Voltage Sensor Unit.

Table A.3: Specifications of the ARD-000774 voltage sensor unit.

Parameter	Specification
Input Voltage Range	0-50V AC/DC
Output Signal	Analog 0 – 5V
Operating Temperature	up to + 60ºC
Measurement Accuracy	±1% of full-scale range
Response Time	< 200ms
Resolution	0.01V (10mV)
Input Impedance	Typically, high (e.g., >1MΩ)

A.1.6 Current Sensor

The ARD-000635 current sensor measures electric current using a hall-effect sensor or similar mechanism. It is known for its precision, reliability, and easy integration with Arduino platforms. Its compact design allows for effortless use in various projects. Figure A.6 shows the sensor, with specifications detailed in Table A.4 [120].

Table A.4: Specifications of the ARD-000635 current sensor unit.

Parameter	Specification
Current sensor chip	ACS712-30A
Measure Current Range	0 - 30A
Supply Voltage	4.5V~5.5V DC
Input current response	5 µs
Minimum isolation voltage	2.1 kVRMS
Output voltage	VCC/2

Figure A.6: ARD-000635 Current sensor unit.

A.1.7 Relay Module

The Relay Module is an electromechanical switch used with microcontrollers like Arduino to control high-voltage devices. It features three high-voltage terminals: Normally Closed (NC), Common (C), and Normally Open (NO), and three low-voltage pins: Ground, Vcc, and Signal. The relay can be programmed to activate based on conditions like temperature or timed intervals, enabling safe control of high-voltage devices via low-voltage systems. Figure A.7 shows the schematic of the relay module [121].

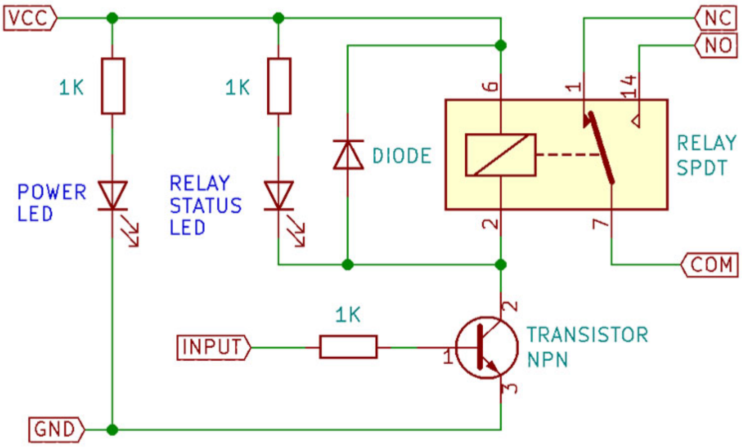

Figure A.7: Basic schematic of the relay module.

A.1.7.1 8CH Relay Module 5V 10A

The 8CH Relay Module 5V is an 8-channel module used to control multiple high-power devices with low-voltage signals, ideal for microcontrollers like Arduino or Raspberry Pi. Each relay handles high-voltage and high-current loads. Operating at 5V, it integrates easily with standard platforms. The module's eight independent channels, each with signal, ground, and Vcc pins, allow control of up to eight devices. Figure A.8 illustrates the module, and specifications are listed in Table A.5 [122].

Table A.5: Specifications of the ARD-002668-8CH Low-Level Relay.

Parameter	Specification
Maximum load	AC 250V/10A, DC 30V/10A
Trigger current	5mA
Working voltage	5V

Figure A.8: 8CH- Relay module 5V 10A.

A.1.7.2 1CH Relay module 5V 30A

The 1-Channel Relay Module 5V 30A is designed for controlling high-power devices using low-voltage signals from microcontrollers like Arduino. It supports a single device or circuit, with seamless 5V compatibility for easy integration with microcontroller systems. With a maximum capacity of 30A, it is ideal for high-demand applications like motors, heating elements, and lighting systems. Figure A.9 shows the module, and detailed specifications are listed in Table A.6 [123].

Figure A.9: 1CH Relay module 5V 30A.

Table A.6: Specifications of the ARD-002663-1CH 5V 30A.

Parameter	Specification
Maximum load	AC 250V/30A, DV 30V/30A
Static current	5mA
Working voltage	5V
Working current	190 mA
Trigger current	2-4 mA

A.1.8 DS18B20 Sensor

The DS18B20 is a highly accurate digital temperature sensor, operating over a range of -55°C to +125°C with ±0.5°C accuracy between -10°C and 85°C. It uses a one-wire bus protocol, requiring just one data line and ground for microcontroller interfacing, like with Arduino. Available in a waterproof version, it's ideal for various environments. The sensor's 64-bit serial code allows multiple sensors on a single data line. Figure A.10 shows the DS18B20 [124].

Figure A.10: The DS18B20 sensors.

A.1.9 BH1750 Sensor

The BH1750 is a digital ambient light sensor that measures illuminance in lux, ranging from 1 lux to 65535 lux, using the I2C protocol for communication with microcontrollers like Arduino. It features a 16-bit analog-to-digital converter and supports various modes, including continuous and one-time measurements. Commonly used in devices like mobile phones for brightness adjustment, it's also applied in automotive systems for controlling headlight intensity. Figure A.11 shows the BH1750 sensor [125].

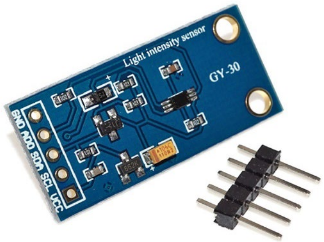

Figure A.11: The BH1750 sensor.

A.1.10 Digital Dual DC 100V 100A Voltmeter Ammeter

The 100V 100A digital voltmeter ammeter is a combined instrument for measuring voltages up to 100V and currents up to 100A, utilizing a precision shunt resistor for large current measurements. The shunt allows the ammeter to measure current indirectly by detecting the voltage drop across it. Commonly used in automotive, industrial, and solar systems, this device provides real-time monitoring of both voltage and current. Figure A.12 shows the wiring diagram. Specifications are detailed in Table A.7 [126].

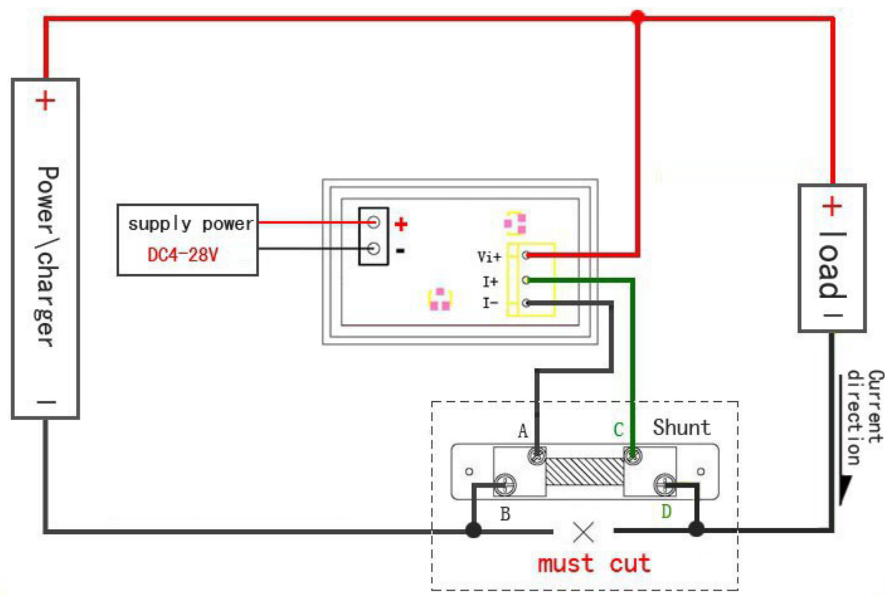

Figure A.12: The Wiring diagram of Digital Dual DC 100V 100A Voltmeter Ammeter.

Table A.7: Specifications of the ARD-070009- 100v 100A voltmeter Ammeter.

Parameter	Specification
Display	0.28"LED, red + red/red+green
Refresh rate	≥300mS/times
Permissible Error	1%(±1)
Power supply	DC 4.5V - 30V
Measure range	DC0-100V
Testing current	DC 0-100A
Operating temperature	-10~+65
Operating humidity	10~80%
Working air pressure	80~106kPa

A.1.11 UT89X Digital Multimeter

The UNI-T UT89X Digital Multimeter, current, resistance, capacitance, frequency, and temperature. It features an LCD display, auto-ranging, data hold, and supports diode and continuity checks. Designed for professionals and enthusiasts, it’s widely used in fields like consumer electronics, automotive, and industrial applications. Table A.8 outlines the detailed specifications of the UT89X [127].

Table A.8: UT89X Digital Multimeter Specifications.

Characteristic	Unit	Range	Uncertainty
DC Voltage	V	600mV/6V/60V/600V/1000V	± (0.5% to 2%)
AC Voltage	V	6V/60V/600V/1000V	± (0.8% to 5%)
DC Current	A	60µA/60mA/600mA/20A	± (0.5% to 9%)
AC Current	A	60mA/600mA/20A	± (1% to 15%)
Resistance	Ω	600Ω/6kΩ/60kΩ/600kΩ/6MΩ/60MΩ	± (0.4% to 10%)
Capacitance	F	100mF	± (2.5% to 60%)

Frequency	Hz	9.999Hz/9.999MHz	± (0.1% to 0.5%)
Duty Cycle	%	0.1%~99.9%	± (2% to 10%)
Temperature	°C	-40°C~1000°C	± (2% to 4%)
Temperature	°F	-40°F~1832°F	± (2% to 8%)

A.2 Software Tools

A.2.1 Simulation Program

Simulation is essential for designing solar array systems, enabling performance testing under various conditions before implementation. MATLAB/Simulink is widely used for these simulations, offering a robust platform for developing control algorithms, analyzing data, and visualizing results [128]. This approach optimizes energy capture and evaluates system responses to shading and environmental changes, enhancing reliability and reducing prototyping costs.

A specialized PV simulation model is developed using a MATLAB®/GUI interface. This model incorporates PV solar cell circuit equations, accounting for real-time solar radiation and temperature changes. It is crucial for designing maximum power point tracking systems. The simulation shows current-voltage (I-V) and power-voltage (P-V) characteristics, illustrating temperature and solar radiation effects.

The HL-Mono 50W PV module is modeled, providing a maximum power output of 50 Watts with 36 monocrystalline silicon cells. Key specifications are listed in Table A.1. The model calculates current (I) using parameters like temperature (T), voltage, open-circuit voltage (Voc), irradiation (G), and short-circuit current (Isc) to analyze power output under varying conditions.

A.2.2 Microcontroller Program

The microcontroller program, developed using the Arduino IDE, is crucial for integrating and processing data from various sensors in the solar array system. The program, or "sketch," begins by including libraries specific to the sensors—temperature, voltage, current, and irradiance. It sets up the Arduino board to read sensor outputs and manage other components. During operation, the sketch periodically collects sensor data, processes it, and transmits it to a connected PC via serial communication at a baud rate of 9600 bits per second. The data packets include readings for temperature, voltage, current, and irradiance. The program also includes error-handling routines to address potential issues with sensors or communication, ensuring consistent performance. Additionally, it can output data to the Arduino IDE's Serial Monitor for real-time monitoring and debugging.

A.2.3 XCTU Program

The XCTU software tool is essential for configuring and managing XBee modules, which play a crucial role in Zigbee wireless communication networks. In this system, two XBee S2 modules are used, with each module assigned a specific role—either Coordinator or Router—via XCTU to ensure proper network hierarchy and data routing. XCTU provides a user-friendly interface that simplifies the setup of these XBee devices, allowing for the configuration of network parameters such as personal area network ID, channel, and network topology to ensure optimal performance. The software enables testing of the Zigbee network by monitoring signal strength and communication reliability, and it includes diagnostic tools to address any connectivity issues. Additionally, XCTU supports data logging to track network performance over time, which helps in fine-tuning settings for robust communication. Figure A.13 shows the interface of XCTU [129].

Name: RT1-R2D2
Function: ZigBee Router API
Port: COM1 - 9600/8/N/1/H - API1
MAC: 0013A20040A198CD

Name: CO-YODA
Function: ZigBee Coordinator API
MAC: 0013A20040A9E78B

Name: RT1-WINDU
Function: ZigBee Router API
MAC: 0013A20040A9527D

Name: RT2-OBI-WAN
Function: ZigBee Router API
MAC: 0013A20040A9E883

Name: RT4-LUKE
Function: ZigBee Router API
MAC: 0013A20040A9E756

Name: BAYMAX
Function: XBee DigiMesh 2.4
Port: COM6 - 9600/8/N/1/H - AT
MAC: 0013A20040D2B039

Radio Configuration [RT1-R2D2 - 0013A20040A198CD]

Product family: XBP24BZ7 **Function set:** ZigBee Router API **Firmware version:** 23A7

Networking
Change networking settings

ID PAN ID C3B0
SC Scan Channels 7FFF Bitfield
SD Scan Duration 3 exponent
ZS ZigBee Stack Profile 0
NJ Node Join Time FF x 1 sec
NW Network Watchdog Timeout 0 x 1 minute
JV Channel Verification Enabled [1]
JN Join Notification Disabled [0]
OP Operating PAN ID C3B0
OI Operating 16-bit PAN ID 5EE9
CH Operating Channel F
NC Number of Re...ing Children C

Addressing
Change addressing settings

SH Serial Number High 13A200

Figure A.13: The XCTU platform application.

Appendix B: Figures and Tables

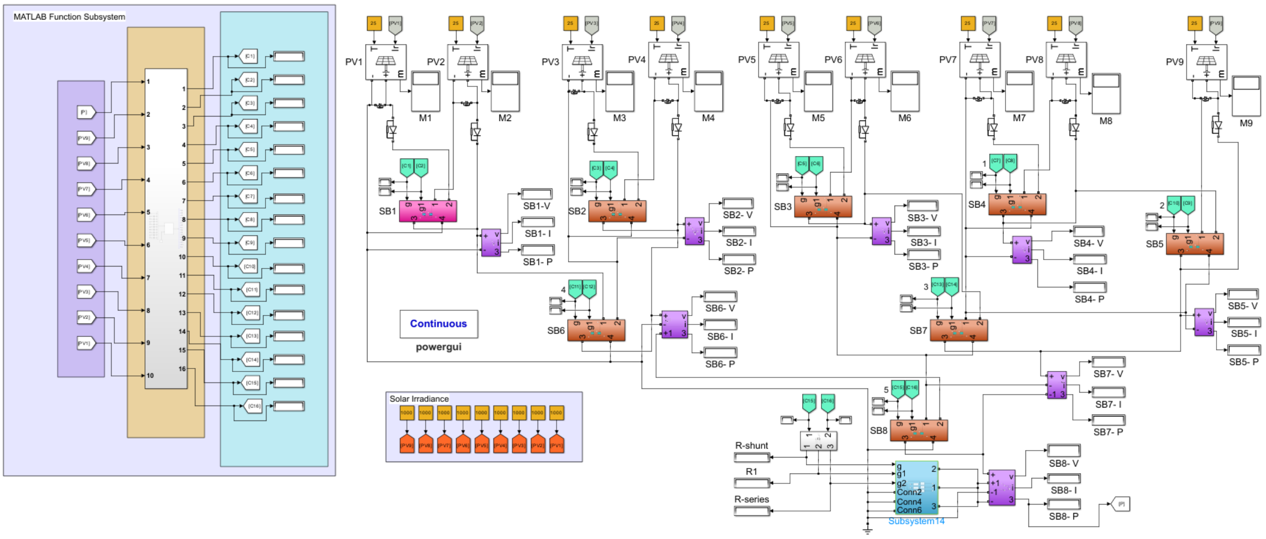

Figure B.1 : The real-time simulation architecture controlled by MATLAB function subsystem for the proposed system Model-A.

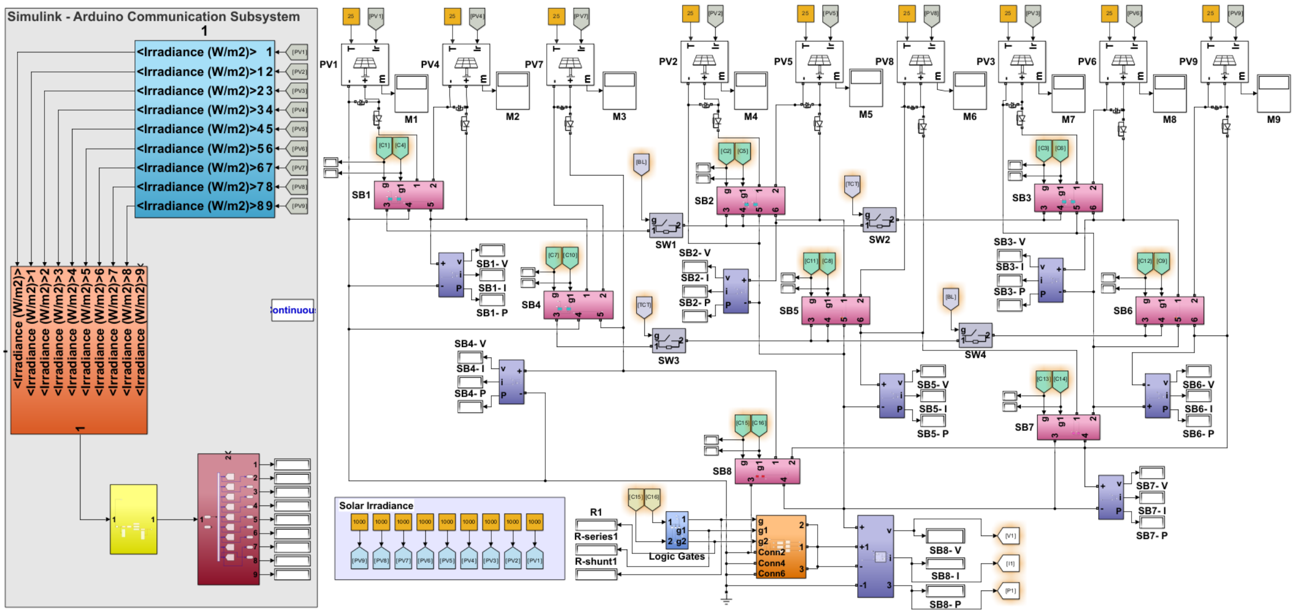

Figure B.2: The real-time simulation architecture combining Simulink and Arduino for the proposed system Model-B.

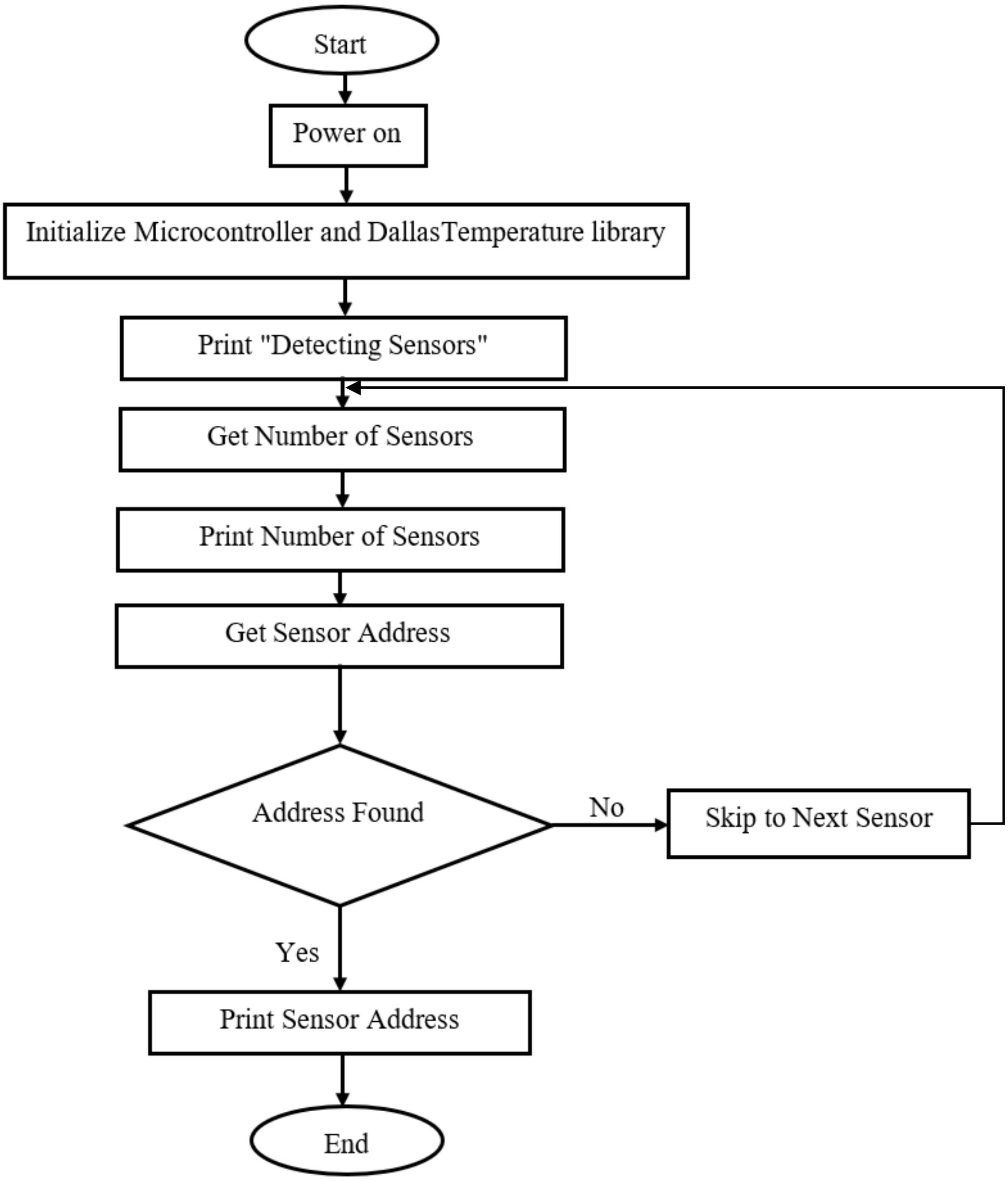

Figure B.3: DS18B20 sensor address management flowchart.

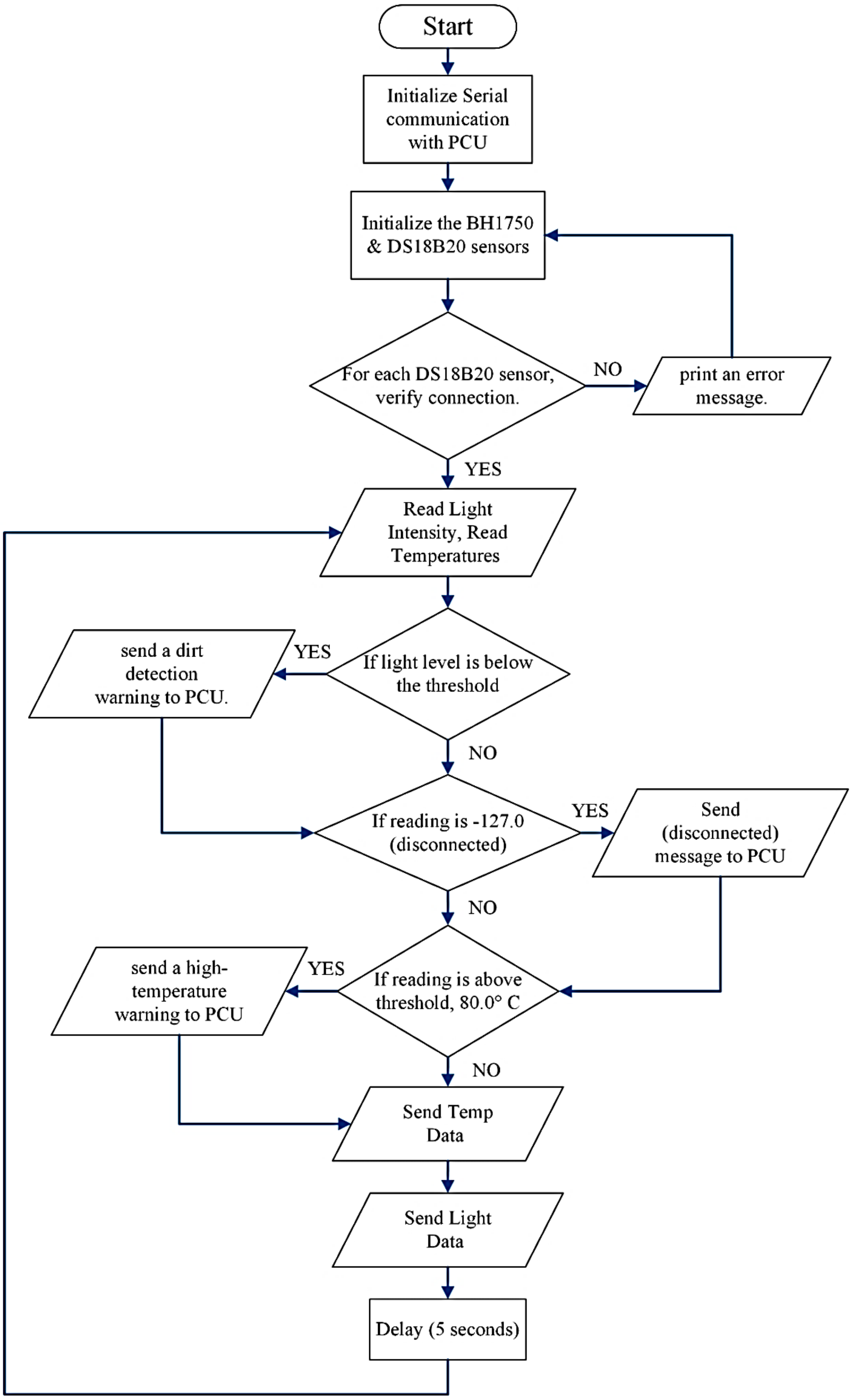

Figure B.4: SCU operational flowchart.

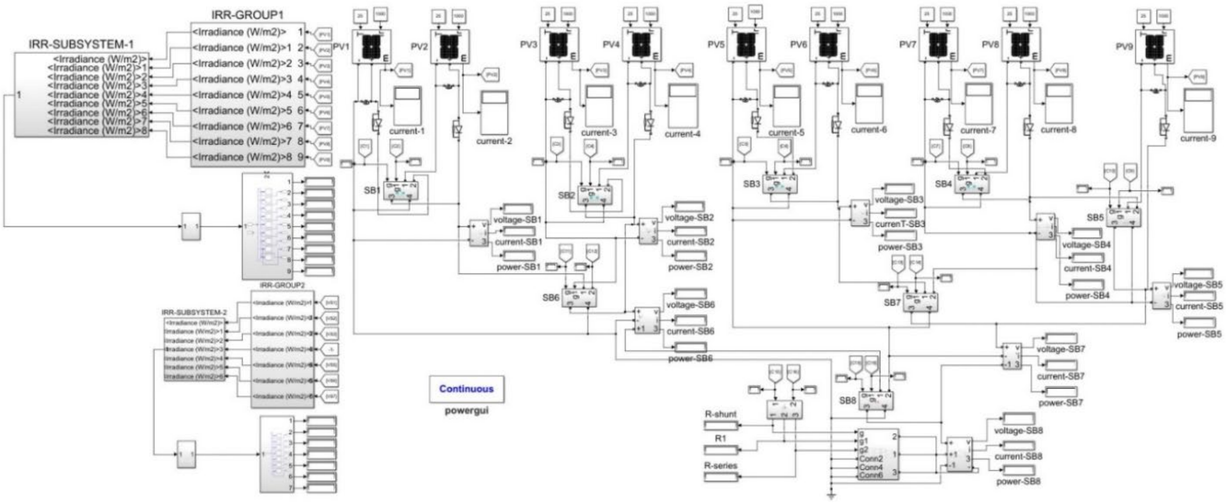

Figure B.5: Proposed system in a MATLAB–Simulink environment.

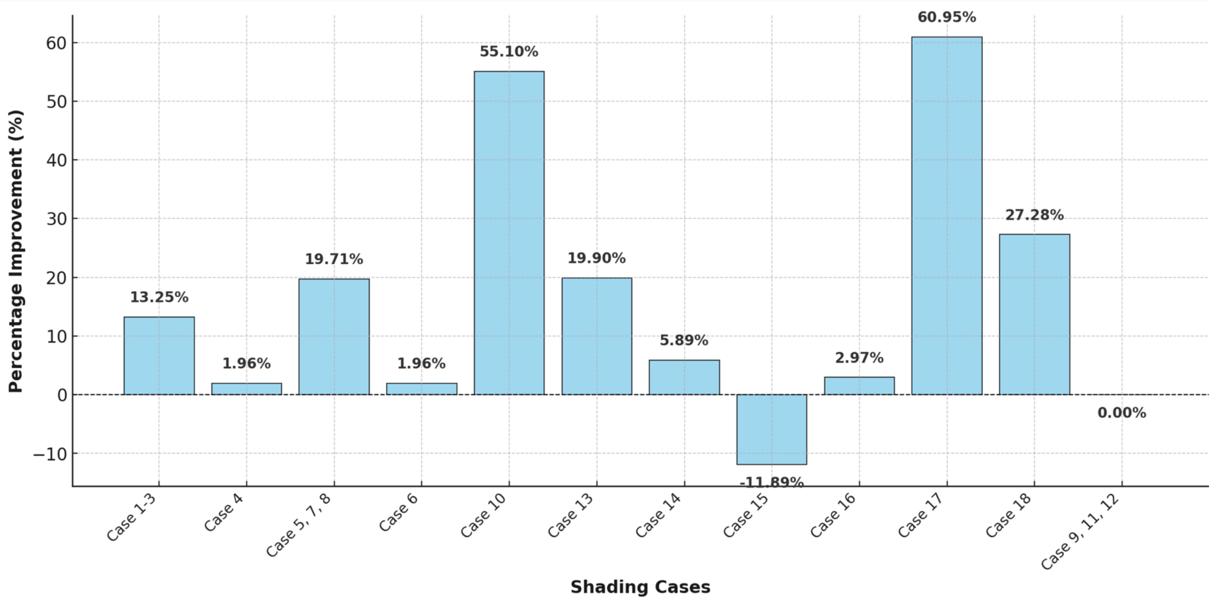

Figure B.6: Energy harvesting improvements across shading cases.

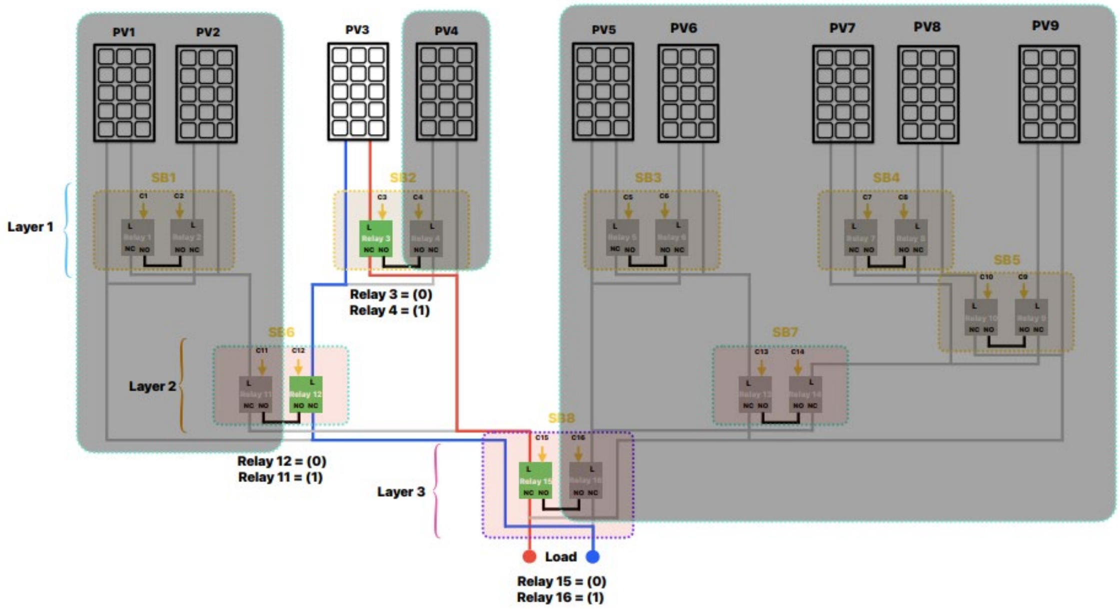

Figure B.7: A schematic representation of the voltage and current measurement process for panel 3.

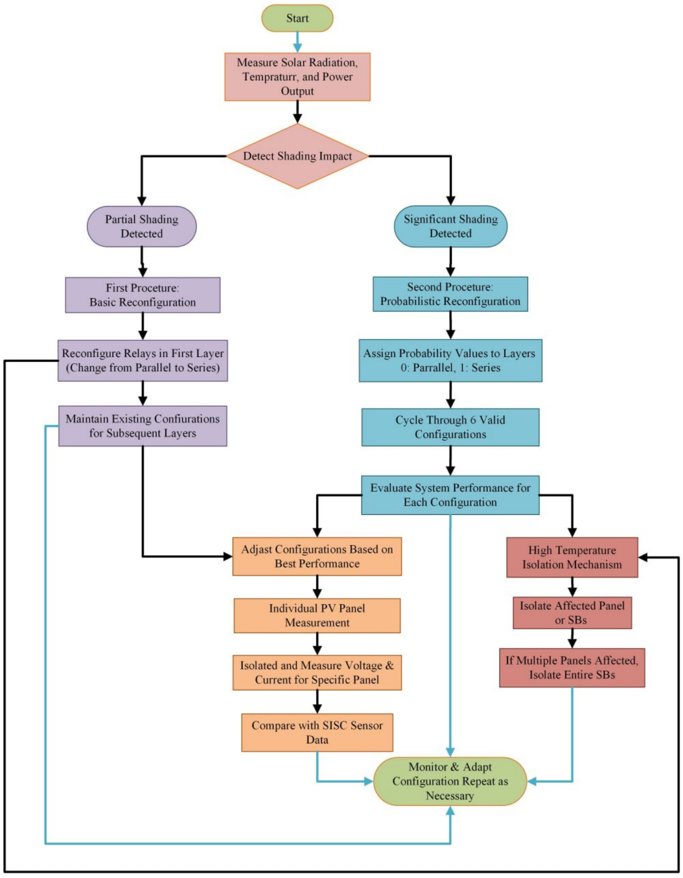

Figure B.8: Flowchart of the DPRA.

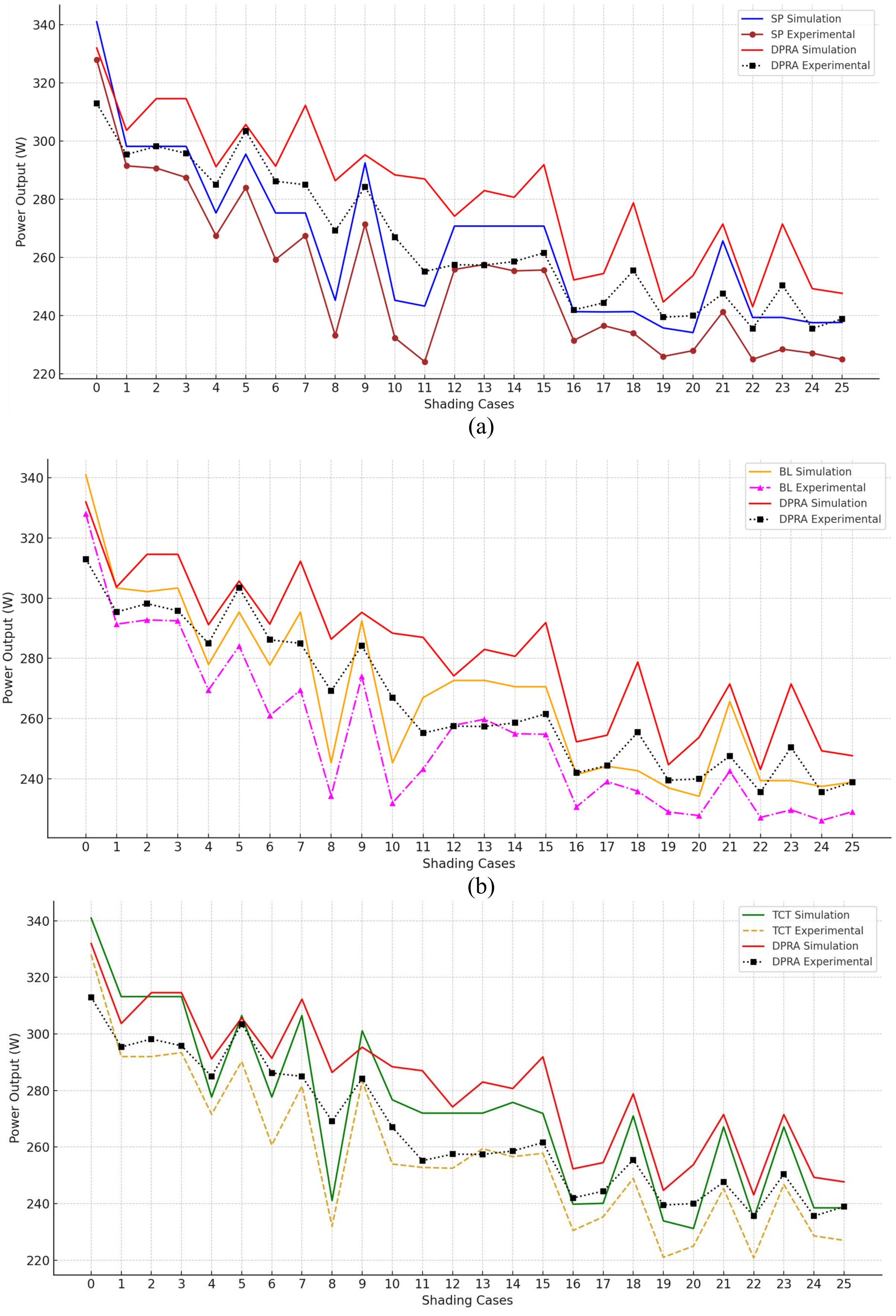

(a)

(b)

(c)

Figure B.9: Comparative analysis of DPRA and conventional PV configurations: (a) SP, (b) BL, (c) TCT under simulation and experimental shading scenarios.

Table B.1: A mathematically comprehensive of the system's total voltage calculation process.

No	**SB1 Values**	**SB2 Values**	**SB3 Values**	**SB5 Values**	**SB6 Values**	**SB7 Values**	**Connection Type of *SBs***	**V_{SB1}, V_{SB2}, V_{SB3}, V_{SB5}, V_{SB6}, V_{SB7} Values Condition**	**Output Voltage**
1	V_{SB1}	V_{SB2}	---	---	---	---	*Series* SB6	$V_{SB1} > V_{SB2}$	$V_{output} = V_{SB1} + V_{SB2}$
2	V_{SB1}	V_{SB2}	---	---	---	---	*Series* SB6	$V_{SB1} < V_{SB2}$	$V_{output} = V_{SB1} + V_{SB2}$
3	V_{SB1}	V_{SB2}	---	---	---	---	*Series* SB6	$V_{SB1} = V_{SB2}$	$V_{output} = V_{SB1} + V_{SB2}$
4	V_{SB1}	V_{SB2}	---	---	---	---	*Parallel* SB6	$V_{SB1} > V_{SB2}$	$V_{output} = V_{SB2}$
5	V_{SB1}	V_{SB2}	---	---	---	---	*Parallel* SB6	$V_{SB1} < V_{SB2}$	$V_{output} = V_{SB1}$
6	V_{SB1}	V_{SB2}	---	---	---	---	*Parallel* SB6	$V_{SB1} = V_{SB2}$	$V_{output} = V_{SB1} = V_{SB2}$
7	---	---	V_{SB3}	V_{SB5}	---	---	*Series* SB7	$V_{SB3} > V_{SB5}$	$V_{output} = V_{SB3} + V_{SB5}$
8	---	---	V_{SB3}	V_{SB5}	---	---	*Series* SB7	$V_{SB3} < V_{SB5}$	$V_{output} = V_{SB3} + V_{SB5}$
9	---	---	V_{SB3}	V_{SB5}	---	---	*Series* SB7	$V_{SB3} = V_{SB5}$	$V_{output} = V_{SB3} + V_{SB5}$
10	---	---	V_{SB3}	V_{SB5}	---	---	*Parallel* SB7	$V_{SB3} > V_{SB5}$	$V_{output} = V_{SB5}$
11	---	---	V_{SB3}	V_{SB5}	---	---	*Parallel* SB7	$V_{SB3} < V_{SB5}$	$V_{output} = V_{SB3}$
12	---	---	V_{SB3}	V_{SB5}	---	---	*Parallel* SB7	$V_{SB3} = V_{SB5}$	$V_{output} = V_{SB3} = V_{SB5}$
13	---	---	---	---	V_{SB6}	V_{SB7}	*Series* SB8	$V_{SB6} > V_{SB7}$	$V_{output} = V_{SB6} + V_{SB7}$
14	---	---	---	---	V_{SB6}	V_{SB7}	*Series* SB8	$V_{SB6} < V_{SB7}$	$V_{output} = V_{SB6} + V_{SB7}$

15	---	---	---	---	V_{SB6}	V_{SB7}	$Series_{SB8}$	$V_{SB6} = V_{SB7}$	$V_{output} = V_{SB7} + V_{SB7}$
16	---	---	---	---	V_{SB6}	V_{SB7}	$Parallel_{SB8}$	$V_{SB6} > V_{SB7}$	$V_{output} = V_{SB7}$
17	---	---	---	---	V_{SB6}	V_{SB7}	$Parallel_{SB8}$	$V_{SB6} < V_{SB7}$	$V_{output} = V_{SB6}$
18	---	---	---	---	V_{SB6}	V_{SB7}	$Parallel_{SB8}$	$V_{SB6} = V_{SB7}$	$V_{output} = V_{SB6} = V_{SB7}$

Table B.2: Simulation Results of 3x3 PV Array under Various Irradiance Conditions with Maximum Power Point Tracking (MPPT).

PS cases	**MPPT at Irradiance 750 W/m²**				**MPPT at Irradiance 500 W/m²**				**MPPT at Irradiance 250 W/m²**			
	SP	**BL**	**TCT**	**SB**	**SP**	**BL**	**TCT**	**SB**	**SP**	**BL**	**TCT**	**SB**
1	396.5	405.7	408.6	408.6	343.3	351.7	354.4	354.5	283.5	291.2	294.6	294.7
2	396.5	403.7	408.6	408.6	343.3	349.2	354.4	354.5	283.5	287.3	294.6	294.6
3	396.5	405.7	408.6	408.6	343.3	351.7	354.4	354.5	283.5	291.2	294.6	294.7
4	349.3	351.8	354.6	396.8	233	234.4	239.1	353.8	226.4	220.7	213.4	297.3
5	349.3	254.4	254.6	396.8	233	238.9	239.1	353.8	226.4	220.7	213.4	297.3
6	394	396.9	398.6	400.6	341.4	344.1	346.7	361.3	282	285.1	285.7	302
7	349.3	354.4	398.6	400.6	233	238.9	346.7	361.3	226.4	213.4	285.7	302
8	394	396.9	398.6	400.6	341.4	344.1	346.7	361.3	282	285.1	285.7	302
9	346.8	351	390.7	393.2	230.1	234	339.8	351.6	210.3	208.1	281.4	295.5
10	344.6	348.5	352.2	393.2	229.1	231.3	237.4	351.6	210.1	199.4	191.7	296.5
11	346.8	351.8	353.4	370.1	230.1	236.2	238.2	251	210.3	201.2	201.6	205.1
12	346.8	350.1	353.4	370.1	230.1	233.6	238.2	251	210.3	204.8	201.6	205.1
13	295	295	295	393.1	213.4	213.4	213.4	351.5	213.4	213.4	213.4	296.5
14	344.6	349.9	352.2	368.1	229.1	233.5	237.4	250.2	210.1	198.1	191.7	198.8
15	292.1	294.3	294.4	357.4	207.4	207.2	207.1	242.4	195.1	201.6	201.6	204.9
16	292.1	294.4	294.4	357.4	207.4	206.6	207.1	242.4	195.1	199.7	201.6	204.9

17	344.6	350.6	352.2	368.1	229.1	235.5	237.4	250.2	210.1	193.5	191.7	210.7
18	344.4	344.3	346.9	361.7	227.2	227.4	228.9	242.5	129.9	130.1	132	140
19	342.2	343.8	345.7	359.4	226.2	227.2	228.5	242	129.3	130	131.8	139.8
20	289.1	289.1	293.4	355	191.3	197.6	193.1	239.7	126.6	129.2	128.2	137.3
21	342.2	344.4	345.7	359.4	226.2	227.9	228.5	242	129.3	131.4	131.8	139.8
22	289.1	291.6	293.9	309.3	191.3	198.4	201.3	217.8	126.6	130.7	191.7	206.2
23	289.1	293.8	293.9	309.3	191.3	201.3	201.3	217.8	126.6	191.7	191.7	206.2
24	286.1	286.1	286.1	352.1	132.2	132.2	132.2	238.6	46.28	46.28	46.28	136.7
25	340.2	340.2	340.2	352.2	225.2	225.2	225.2	238.7	128.8	128.8	128.8	136.8
No shading	427.1	427.1	427.1	427.2								

Table B.3 : Efficiency Improvement for 3 × 3 PV Array.

Efficiency Improvement 750			**avr**	**Efficiency Improvement 500**			**avr**	**Efficiency Improvement 250**			**avr**
SP	**BL**	**TCT**		**SP**	**BL**	**TCT**		**SP**	**BL**	**TCT**	
3.05	0.71	0	1.26	3.26	0.8	0.03	1.36	3.95	1.2	0.03	1.73
3.05	1.21	0	1.42	3.26	1.52	0.03	1.6	3.92	2.54	0	2.15
3.05	0.71	0	1.26	3.26	0.8	0.03	1.36	3.95	1.2	0.03	1.73
13.6	12.79	11.9	12.76	51.85	50.94	47.97	50.25	31.32	34.71	39.32	35.11
13.6	55.97	55.85	41.81	51.85	48.1	47.97	49.3	31.32	34.71	39.32	35.11
1.68	0.93	0.5	1.04	5.83	5	4.21	5.01	7.09	5.93	5.71	6.24
14.69	13.04	0.5	9.41	55.06	51.23	4.21	36.84	33.39	41.52	5.71	26.9
1.68	0.93	0.5	1.04	5.83	5	4.21	5.01	7.09	5.93	5.71	6.2
13.38	12.02	0.64	8.68	52.8	50.26	3.47	35.51	40.51	42	5.01	29.2
14.1	12.83	11.64	12.86	53.47	52.01	48.1	51.19	41.12	48.7	54.67	48.2
6.72	5.2	4.73	5.55	9.08	6.27	5.37	6.91	-2.47	1.94	1.74	0.4
6.72	5.71	4.73	5.72	9.08	7.45	5.37	7.3	-2.47	0.15	1.74	-0.2
33.25	33.25	33.25	33.25	64.71	64.71	64.71	64.71	38.94	38.94	38.94	38.9
6.82	5.2	4.51	5.51	9.21	7.15	5.39	7.25	-5.38	0.35	3.7	-0.44
22.36	21.44	21.4	21.73	16.88	16.99	17.04	16.97	5.02	1.64	1.64	2.77

22.36	21.4	21.4	21.72	16.88	17.33	17.04	17.08	5.02	2.6	1.64	3.09
6.82	4.99	4.51	5.44	9.21	6.24	5.39	6.95	0.29	8.89	9.91	6.36
5.02	5.05	4.27	4.78	6.73	6.64	5.94	6.44	7.78	7.61	6.06	7.15
5.03	4.54	3.96	4.51	6.98	6.51	5.91	6.47	8.12	7.54	6.07	7.24
22.79	22.79	21	22.19	25.3	21.31	24.13	23.58	8.45	6.27	7.1	7.27
5.03	4.36	3.96	4.45	6.98	6.19	5.91	6.36	8.12	6.39	6.07	6.86
6.99	6.07	5.24	6.1	13.85	9.78	8.2	10.61	62.88	57.77	7.56	42.73
6.99	5.28	5.24	5.83	13.85	8.2	8.2	10.08	62.88	7.56	7.56	26
23.07	23.07	23.07	23.07	80.48	80.48	80.48	80.48	195.38	195.38	195.38	195.3
3.53	3.53	3.53	3.53	5.99	5.99	5.99	5.99	6.21	6.21	6.21	6.21
Average efficiency improvements = 10.6				Average efficiency improvements = 20.59				Average efficiency improvements = 21.69			

Table B.4: Efficiency Improvement for 4 × 4 PV Array.

Efficiency Improvement 700			**avr**	**Efficiency Improvement 500**			**avr**	**Efficiency Improvement 200**			**avr**
SP	**BL**	**TCT**		**SP**	**BL**	**TCT**		**SP**	**BL**	**TCT**	
5.15	2.86	1.32	3.11	9.62	7.05	5.03	7.23	8.02	8.60	5.47	7.36
16.68	4.44	2.74	7.95	33.60	7.42	4.66	15.23	15.46	8.40	5.89	9.91
4.90	4.39	2.67	3.99	7.60	7.03	4.66	6.43	8.41	7.94	5.89	7.41
24.20	22.49	5.34	17.34	11.61	15.03	5.55	10.73	-6.40	-3.53	0.94	-3.00
32.44	13.09	2.82	16.12	37.80	31.92	3.99	24.57	19.77	30.73	5.81	18.77
24.84	23.17	5.29	17.77	14.55	15.82	5.56	11.98	-0.15	-2.33	1.28	-0.40
8.40	6.62	5.29	6.77	6.77	8.13	5.56	6.82	-5.59	-2.14	1.28	-2.15
49.66	2.91	2.91	18.49	40.16	4.10	4.10	16.12	22.20	5.53	5.53	11.09
39.83	22.09	5.27	22.40	15.91	22.87	5.99	14.93	-18.65	11.67	6.20	-0.26
8.54	6.27	5.51	6.77	3.75	0.06	0.75	1.52	41.34	1.51	1.26	14.70
Average efficiency improvements = 12.1				Average efficiency improvements = 11.55				Average efficiency improvements = 6.34			

Table B.5: Efficiency Improvement for 3 × 4 PV Array.

Efficiency Improvement 700			**avr**	**Efficiency Improvement 500**			**avr**	**Efficiency Improvement 200**			**avr**
SP	**BL**	**TCT**		**SP**	**BL**	**TCT**		**SP**	**BL**	**TCT**	
4.63	3.88	1.78	3.43	6.57	5.88	-1.64	3.6	9.04	8.44	-3.29	4.73

16.79	14.37	3.2	11.46	34.34	30.91	2.34	22.53	27.04	36.09	-4.25	19.63
16.79	14.99	14.25	15.35	34.34	32.03	30.7	32.36	27.04	33.27	40.81	33.71
-4.48	-5.48	-5.55	-5.17	19.37	21.06	24.38	21.6	19.33	24.35	24.35	22.68
3.32	3.32	3.32	3.32	2.41	2.41	2.41	2.41	-4.1	-4.08	-4.08	-4.09
1.31	1.31	1.31	1.31	11.36	11.36	11.36	11.36	12.54	12.54	12.54	12.54
14.03	12.08	11.22	12.44	30.15	27.76	26.3	28.07	29.09	43.82	48.48	40.46
3.14	2.1	0.6	1.95	-1.39	-2.2	-4.31	-2.63	6.22	31.63	22.17	20.01
18.14	17.46	15.8	17.13	16.84	18.14	22.13	19.04	35.72	30.23	33.09	33.01
18.67	16.77	15.68	17.04	28.43	24.19	22.14	24.92	57.1	-20.66	-24.36	4.03
Average efficiency improvements = 7.83				Average efficiency improvements = 16.33				Average efficiency improvements = 18.67			

Table B.6: Power Output Comparison (W) for Different Shading Cases at 680 W/m², 425 W/m², and 255 W/m².

Shading Cases	**Shading Patterns**	**Irradiance 20, 50, 70 %**	**Simulation**				**Experimental**			
			SP	**BL**	**TCT**	**DPRA**	**SP**	**BL**	**TCT**	**DPRA**
Case 0 No Shading	1 2 3 4 5 6 7 8 9	850 W/m^2	341	341	341	332	328	328	328	313
Case 1	▨1 2 3 4 5 6 7 8 9	680 W/m^2	298.2	303.4	313.2	303.7	291.5	291.4	292	295.4
		425 W/m^2	253.1	260.8	259.1	271.6	250.3	249.7	255	255.4
		255 W/m^2	218.8	225	223.2	244.9	210	221.9	220.3	231.6
Case 2	1 2 3 4 ▨5 6 7 8 9	680 W/m^2	298.2	302.2	313.2	314.6	290.7	292.8	292	298.2
		425 W/m^2	253.1	259	259.1	263.7	248	254.4	255	255.6
		255 W/m^2	218.8	222.6	223.2	239.2	210.7	218.2	219.1	233.7
Case 3	1 2 3 4 5 6 7 8 ▨9	680 W/m^2	298.2	303.4	313.2	314.6	287.5	292.5	293.4	295.8
		425 W/m^2	253.1	260.8	259.1	261.7	245	251.2	248.6	256.3
		255 W/m^2	218.8	225	223.2	239.9	209	217.5	219.3	232.4
Case 4	▨1 ▨2 3 4 5 6 7 8 9	680 W/m^2	275.3	278	277.7	291.2	267.5	269.5	271.6	285
		425 W/m^2	172.5	173.6	184.2	261.2	168.8	167	173.4	243.5
		255 W/m^2	167.2	162.4	184.2	226	152.7	148.8	168.3	207.6
Case 5	▨1 2 3 ▨4 5 6 7 8 9	680 W/m^2	295.5	295.4	306.5	305.7	284	284.1	290.3	303.5
		425 W/m^2	251.7	251.6	253.1	259.2	233.9	233.7	237.6	244.2
		255 W/m^2	217.7	217.7	216.9	222.1	192	193.6	193.5	208.8
Case 6	1 2 3 4 ▨5 ▨6 7 8 9	680 W/m^2	275.3	277.8	277.7	291.4	259.3	261	260.7	286.2
		425 W/m^2	172.5	173.5	184.2	268.4	163.6	165.6	170.4	246.5
		255 W/m^2	167.2	162.1	184.2	233.3	153	149.9	168.3	209.4
Case 7	1 2 3 4 5 ▨6 7 ▨8 9	680 W/m^2	275.3	295.4	306.5	312.3	267.5	269.5	281.6	285
		425 W/m^2	172.5	251.6	253.1	262.5	160.8	234.2	238.6	243.5
		255 W/m^2	167.2	217.7	216.4	227.8	154.2	193.9	192.3	207.6
Case 8	▨1 ▨2 ▨3 4 5 6 7 8 9	680 W/m^2	245.3	245.3	241.1	286.4	233.2	234.4	232	269.2
		425 W/m^2	156.2	156.2	184.2	221	139.5	139.8	168.5	196.4
		255 W/m^2	156.2	156.2	184.2	210.3	138.8	139.4	165.7	187.2
Case 9		680 W/m^2	292.5	292.5	301.1	295.3	271.4	274	283.4	284.2

	1 **2** **3**	425 W/m^2	250.1	250.1	249.1	267.1	233.6	232.8	231.3	250
	4 **5** **6** 7 **8** **9**	255 W/m^2	216.9	216.9	213.2	228.2	195.6	196.7	194.3	218.1
Case 10	**1** **2** 3	680 W/m^2	245.3	245.3	276.7	288.4	232.4	232	254	267
	4 5 **6**	425 W/m^2	156.2	156.2	176.7	221	137.4	138.9	159.3	191
	7 **8** **9**	255 W/m^2	156.2	156.2	171.2	190.2	139.6	137.8	154.2	187.1
Case 11	1 2 **3**	680 W/m^2	243.3	267	272	287	224.2	243.3	252.8	255.2
	4 **5** **6**	425 W/m^2	151.5	166.9	165.8	220.5	135.4	145.7	144.2	202.2
	7 8 9	255 W/m^2	143.7	129.2	107.8	177.3	126.1	114.4	96.1	174.5
Case 12	1 2 **3**	680 W/m^2	270.8	272.7	272	274.2	255.9	257.8	252.5	257.5
	4 5 **6**	425 W/m^2	168.8	170	165.8	205	146.8	154.1	145.6	196.4
	7 **8** **9**	255 W/m^2	109.4	110.6	107.8	130	91.77	91.9	89.6	122.6
Case 13	**1** **2** **3**	680 W/m^2	270.8	272.7	272	283	257.6	259.8	259.4	257.4
	4 5 6	425 W/m^2	168.8	170	165.8	224.7	147	153.8	143.8	204.3
	7 8 9	255 W/m^2	109.4	110.6	107.8	140.6	93.8	94.5	91.9	134.5
Case 14	1 **2** **3**	680 W/m^2	270.8	270.6	275.8	280.7	255.4	255	256.6	258.6
	4 **5** 6	425 W/m^2	168.8	169	172.1	234.2	149.7	150.4	155.4	219.4
	7 **8** 9	255 W/m^2	109.4	109.6	161.5	197.2	94.7	95	145.1	188.3
Case15	1 **2** 3	680 W/m^2	270.8	270.6	271.9	291.9	255.7	254.8	257.8	261.6
	4 **5** **6**	425 W/m^2	168.8	169	165.8	227.6	149.5	151	144.6	220
	7 **8** 9	255 W/m^2	109.4	109.6	107.8	213.8	92.9	94.8	90.6	176.8
Case 16	1 2 **3**	680 W/m^2	241.4	241.4	239.8	252.3	231.5	230.7	230.5	242
	4 5 6	425 W/m^2	139.3	144.1	154.8	161.2	118.8	125.6	142.2	151.6
	7 **8** **9**	255 W/m^2	104	108.1	105.6	117.3	93.7	97.6	95.8	102.7
Case 17	**1** 2 **3**	680 W/m^2	241.3	244.2	240.1	254.5	236.6	239.1	235.3	244.4
	4 5 6	425 W/m^2	151.3	146.7	170.2	188	143.3	138.7	154.1	161.3
	7 8 **9**	255 W/m^2	143.6	140.4	161.5	167.8	133.2	129.8	142.4	145.3
Case 18	**1** 2 3	680 W/m^2	241.4	242.7	271	278.8	234	235.9	248.9	255.5
	4 5 6	425 W/m^2	139.3	142.1	165.5	188	122.2	135.2	152.6	178.3
	7 **8** **9**	255 W/m^2	104	107.7	107.7	146.2	92.2	96.4	94.5	134.2
Case 19	1 2 3	680 W/m^2	235.8	237	233.9	244.7	226	229	221	239.5
	4 5 6	425 W/m^2	96.47	97.13	95.03	141.5	89.2	88.1	86.5	137.6
	7 8 **9**	255 W/m^2	35.46	36	40.16	75.8	27	29	32	65.4
Case 20	1 2 3	680 W/m^2	234.2	234.2	231.2	253.8	228	227.8	225	240
	4 5 6	425 W/m^2	95.77	95.77	93.1	141	87.4	86.6	85	135
	7 8 9	255 W/m^2	35	35	34	53.4	26	27.3	26.5	45.3
Case 21	1 2 **3**	680 W/m^2	265.7	265.7	267.1	271.5	241.3	242.6	245.3	247.6
	4 5 **6**	425 W/m^2	167.3	167.3	163.1	194	159	155.5	152.7	172.4
	7 8 **9**	255 W/m^2	108.5	108.5	105.5	130.1	92.4	93.1	90.4	123.5
Case 22	**1** **2** **3**	680 W/m^2	239.4	239.4	234.7	243.1	225	227.2	220.8	235.6
	4 5 6	425 W/m^2	97.85	97.85	95.3	176.8	80	79	80	161.4
	7 8 9	255 W/m^2	36.17	36.17	46.36	117	29	29.6	38.8	115
Case 23	1 2 **3**	680 W/m^2	239.4	239.4	267.1	271.5	228.5	229.7	246.8	250.4
	4 **5** 6	425 W/m^2	97.85	97.85	163.1	194	81	83	154.3	178.2
	7 8 9	255 W/m^2	36.17	36.17	105.5	128.4	28.2	27.3	97	120.6
Case 24	1 2 **3**	680 W/m^2	237.6	237.5	238.5	249.3	227.1	226.2	228.6	235.6
	4 5 6	425 W/m^2	97.16	97.41	143.5	162.5	85.7	88.1	135.5	148.4
	7 8 9	255 W/m^2	35.81	40.86	102.1	116.3	30	34	90	114.6
Case 25	1 2 3	680 W/m^2	237.7	238.9	238.5	247.7	225	229.1	227	238.9
	4 5 **6**	425 W/m^2	138.6	135.9	143.5	153.6	129.4	131.2	138.6	145.5
	7 8 **9**	255 W/m^2	103.3	102.1	102.1	126.8	92	91	92.7	122

Table B.7 : Comparative Energy Improvement and Efficiency Analysis of DPRA Over Conventional PV Reconfiguration Methods.

Shading Cases	**Irradiance 20, 50, 70 %**	**Simulation Efficiency**				**Experimental Efficiency**			
		SP	**BL**	**TCT**	**DPRA**	**SP**	**BL**	**TCT**	**DPRA**
Case 1	680 W/m^2	87.45	88.97	91.85	91.48	88.87	88.84	89.02	94.38
	425 W/m^2	74.22	76.48	75.98	81.81	76.31	76.13	77.74	81.60
	255 W/m^2	64.16	65.98	65.45	73.77	64.02	67.65	67.16	73.99
Case 2	680 W/m^2	87.45	88.62	91.85	94.76	88.63	89.27	89.02	95.27
	425 W/m^2	74.22	75.95	75.98	79.43	75.61	77.56	77.74	81.66
	255 W/m^2	64.16	65.28	65.45	72.05	64.24	66.52	66.80	74.66
Case 3	680 W/m^2	87.45	88.97	91.85	94.76	87.65	89.18	89.45	94.50
	425 W/m^2	74.22	76.48	75.98	78.83	74.70	76.59	75.79	81.88
	255 W/m^2	64.16	65.98	65.45	72.26	63.72	66.31	66.86	74.25
Case 4	680 W/m^2	80.73	81.52	81.44	87.71	81.55	82.16	82.80	91.05
	425 W/m^2	50.59	50.91	54.02	78.67	51.46	50.91	52.87	77.80
	255 W/m^2	49.03	47.62	54.02	68.07	46.55	45.37	51.31	66.33
Case 5	680 W/m^2	86.66	86.63	89.88	92.08	86.59	86.62	88.51	96.96
	425 W/m^2	73.81	73.78	74.22	78.07	71.31	71.25	72.44	78.02
	255 W/m^2	63.84	63.84	63.61	66.90	58.54	59.02	58.99	66.71
Case 6	680 W/m^2	80.73	81.47	81.44	87.77	79.05	79.57	79.48	91.44
	425 W/m^2	50.59	50.88	54.02	80.84	49.88	50.49	51.95	78.75
	255 W/m^2	49.03	47.54	54.02	70.27	46.65	45.70	51.31	66.90
Case 7	680 W/m^2	80.73	86.63	89.88	94.07	81.55	82.16	85.85	91.05
	425 W/m^2	50.59	73.78	74.22	79.07	49.02	71.40	72.74	77.80
	255 W/m^2	49.03	63.84	63.46	68.61	47.01	59.12	58.63	66.33
Case 8	680 W/m^2	71.94	71.94	70.70	86.27	71.10	71.46	70.73	86.01
	425 W/m^2	45.81	45.81	54.02	66.57	42.53	42.62	51.37	62.75
	255 W/m^2	45.81	45.81	54.02	63.34	42.32	42.50	50.52	59.81
Case 9	680 W/m^2	85.78	85.78	88.30	88.95	82.74	83.54	86.40	90.80
	425 W/m^2	73.34	73.34	73.05	80.45	71.22	70.98	70.52	79.87
	255 W/m^2	63.61	63.61	62.52	68.73	59.63	59.97	59.24	69.68
Case 10	680 W/m^2	71.94	71.94	81.14	86.87	70.85	70.73	77.44	85.30
	425 W/m^2	45.81	45.81	51.82	66.57	41.89	42.35	48.57	61.02
	255 W/m^2	45.81	45.81	50.21	57.29	42.56	42.01	47.01	59.78
Case 11	680 W/m^2	71.35	78.30	79.77	86.45	68.35	74.18	77.07	81.53
	425 W/m^2	44.43	48.94	48.62	66.42	41.28	44.42	43.96	64.60
	255 W/m^2	42.14	37.89	31.61	53.40	38.45	34.88	29.30	55.75
Case 12	680 W/m^2	79.41	79.97	79.77	82.59	78.02	78.60	76.98	82.27
	425 W/m^2	49.50	49.85	48.62	61.75	44.76	46.98	44.39	62.75
	255 W/m^2	32.08	32.43	31.61	39.16	27.98	28.02	27.32	39.17

Case 13	680 W/m^2	79.41	79.97	79.77	85.24	78.54	79.21	79.09	82.24
	425 W/m^2	49.50	49.85	48.62	67.68	44.82	46.89	43.84	65.27
	255 W/m^2	32.08	32.43	31.61	42.35	28.60	28.81	28.02	42.97
Case 14	680 W/m^2	79.41	79.35	80.88	84.55	77.87	77.74	78.23	82.62
	425 W/m^2	49.50	49.56	50.47	70.54	45.64	45.85	47.38	70.10
	255 W/m^2	32.08	32.14	47.36	59.40	28.87	28.96	44.24	60.16
Case15	680 W/m^2	79.41	79.35	79.74	87.92	77.96	77.68	78.60	83.58
	425 W/m^2	49.50	49.56	48.62	68.55	45.58	46.04	44.09	70.29
	255 W/m^2	32.08	32.14	31.61	64.40	28.32	28.90	27.62	56.49
Case 16	680 W/m^2	70.79	70.79	70.32	75.99	70.58	70.34	70.27	77.32
	425 W/m^2	40.85	42.26	45.40	48.55	36.22	38.29	43.35	48.43
	255 W/m^2	30.50	31.70	30.97	35.33	28.57	29.76	29.21	32.81
Case 17	680 W/m^2	70.76	71.61	70.41	76.66	72.13	72.90	71.74	78.08
	425 W/m^2	44.37	43.02	49.91	56.63	43.69	42.29	46.98	51.53
	255 W/m^2	42.11	41.17	47.36	50.54	40.61	39.57	43.41	46.42
Case 18	680 W/m^2	70.79	71.17	79.47	83.98	71.34	71.92	75.88	81.63
	425 W/m^2	40.85	41.67	48.53	56.63	37.26	41.22	46.52	56.96
	255 W/m^2	30.50	31.58	31.58	44.04	28.11	29.39	28.81	42.88
Case 19	680 W/m^2	69.15	69.50	68.59	73.70	68.90	69.82	67.38	76.52
	425 W/m^2	28.29	28.48	27.87	42.62	27.20	26.86	26.37	43.96
	255 W/m^2	10.40	10.56	11.78	22.83	8.23	8.84	9.76	20.89
Case 20	680 W/m^2	68.68	68.68	67.80	76.45	69.51	69.45	68.60	76.68
	425 W/m^2	28.09	28.09	27.30	42.47	26.65	26.40	25.91	43.13
	255 W/m^2	10.26	10.26	9.97	16.08	7.93	8.32	8.08	14.47
Case 21	680 W/m^2	77.92	77.92	78.33	81.78	73.57	73.96	74.79	79.11
	425 W/m^2	49.06	49.06	47.83	58.43	48.48	47.41	46.55	55.08
	255 W/m^2	31.82	31.82	30.94	39.19	28.17	28.38	27.56	39.46
Case 22	680 W/m^2	70.21	70.21	68.83	73.22	68.60	69.27	67.32	75.27
	425 W/m^2	28.70	28.70	27.95	53.25	24.39	24.09	24.39	51.57
	255 W/m^2	10.61	10.61	13.60	35.24	8.84	9.02	11.83	36.74
Case 23	680 W/m^2	70.21	70.21	78.33	81.78	69.66	70.03	75.24	80.00
	425 W/m^2	28.70	28.70	47.83	58.43	24.70	25.30	47.04	56.93
	255 W/m^2	10.61	10.61	30.94	38.67	8.60	8.32	29.57	38.53
Case 24	680 W/m^2	69.68	69.65	69.94	75.09	69.24	68.96	69.70	75.27
	425 W/m^2	28.49	28.57	42.08	48.95	26.13	26.86	41.31	47.41
	255 W/m^2	10.50	11.98	29.94	35.03	9.15	10.37	27.44	36.61
Case 25	680 W/m^2	69.71	70.06	69.94	74.61	68.60	69.85	69.21	76.33
	425 W/m^2	40.65	39.85	42.08	46.27	39.45	40.00	42.26	46.49
	255 W/m^2	30.29	29.94	29.94	38.19	28.05	27.74	28.26	38.98
Averag Efficiency for all cases	680 W/m^2	76.71	77.57	79.21	84.19	76.06	76.70	77.55	84.21
	425 W/m^2	48.55	49.98	52.60	64.70	46.41	47.97	50.64	63.83
	255 W/m^2	37.87	38.50	41.56	51.81	35.35	36.14	39.13	51.23

		SP	**BL**	**TCT**	**Energy Average %**	**SP**	**BL**	**TCT**	**Energy Average %**
DPRA Energy Improvement %	680 W/m^2	9.75	8.53	6.29	**8.19**	10.72	9.79	8.58	**9.70**
	425 W/m^2	33.27	29.46	23.00	**28.58**	37.54	33.06	26.03	**32.21**
	255 W/m^2	36.80	34.55	24.65	**32.00**	44.93	41.76	30.92	**39.20**

Appendix C: Author's Publications

Publications Related to the Dissertation

[1]. Ameen, F., Siddiq, A., Trohák, A., & Benotsmane, R. (2023). A Scalable Hierarchical Dynamic PV Array Reconfiguration under Partial Shading. Energies, 17(1), 181.

[2]. Ameen, F., Trohák, A., Siddiq, A., & Benotsmane, R. (2024, May). Enhancing Photovoltaic Array Performance under Partial Shading through Dynamic Reconfiguration and Layer Equalization Algorithm. In 2024 25th International Carpathian Control Conference (ICCC) (pp. 1-6). IEEE.

[3]. The paper titled "Scalable Dynamic Photovoltaic Array Reconfiguration Scheme for Mitigating Partial Shading" has been accepted for publication in the Tikrit Journal of Engineering Sciences (TJES), a Q3-ranked journal.

[4]. The paper titled "Dynamic Probabilistic Reconfiguration for Optimized Photovoltaic Performance under Shading and Temperature Variations" has been accepted for publication in the International Journal of Intelligent Engineering and Systems (IJIES), a Q2-ranked journal.

[5]. Ameen, F. N., Trohák, A., & Siddiq, A. (2023, November 23). Dynamic PV Array Reconfiguration for Maximized Power Generation under Partial Shading. Doktoranduszok Fóruma, University of Miskolc, Hungary.

[6]. The paper titled "Review of Photovoltaic Array Reconfiguration Techniques for Mitigating the Effects of Partial Shading" has been submitted to Multidiszciplináris Tudományok. The submission is currently under review.

Other Publications

[7]. Ameen, F., & Varadine, A. (2021). Cough sound recognition based on mobile phone (MP) and machine learning (ML). In P. Ványi (Ed.), Abstract book for the 17th Miklós Iványi International PhD & DLA Symposium (Paper No. 90). University of Pécs. ISBN 978-963-429-811-3.

[8]. Ameen, N., Fatimah, & Váradiné Szarka, A. (2022). The effect of using artificial intelligence models in improving human health: A review. In G. Vadászné Bognár & I. Piller (Eds.), Doktoranduszok fóruma: Miskolc, 2021. november 18., 26.: Gépészmérnöki- és Informatikai Kar szekciókiadványa (pp. 21-29). ME Gépészmérnöki és Informatikai Kar.

[9]. Ameen, N., Fatimah, & Váradiné Szarka, A. (2021). COUGH SOUND RECOGNITION BASED ON MOBILE PHONE AND MACHINE LEARNING . XXIV. Tavaszi Szél Konferencia 2021 Absztraktkötet (p. 402). Doktoranduszok Országos Szövetsége. ISBN 978-615-5586-99-6.

[10]. Al Qaradagi, M., Ameen, F., Benotsmane, R., & Miatliuk, K. (2024, May). Application of Teleoperation Control for a Robotic Hand using a Glove. In 2024 25th International Carpathian Control Conference (ICCC) (pp. 1-6). IEEE.

[11]. Ismail, R. D., Hameed, Q. A., Habeeb, M. A., Khaleel, Y. L., & Ameen, F. N. (2024). Deep Learning Model for Hand Movement Rehabilitation. Mesopotamian Journal of Computer Science, 2024, 134-149.

Reference

[1] Kabeyi, M.J.B.; Olanrewaju, O.A. Sustainable Energy Transition for Renewable and Low Carbon Grid Electricity Generation and Supply. Front. Energy Res. 2022, 9, 1–45.

[2] K. Sundareswaran, V. Vigneshkumar, P. Sankar, S. P. Simon, P. S. R. Nayak, and S. Palani, "Development of an Improved P&O Algorithm Assisted Through a Colony of Foraging Ants for MPPT in PV System," IEEE Transactions on Industrial Informatics, vol. 12, no. 1, pp. 187-200, 2016.

[3] Fraas, L.M. (2014). History of Solar Cell Development. In: Low-Cost Solar Electric Power. Springer, Cham.

[4] Green, M.A.; Hishikawa, Y.; Dunlop, E.D.; Levi, D.H.; Hohl-Ebinger, J.; Yoshita, M.; Ho-Baillie, A.W.Y. Solar Cell Efficiency Tables (Version 53). Progress in Photovoltaics: Research and Applications 2019, 27, 3–12.

[5] Nsengiyumva W, Chen SG, Hu L, Chen X (2018) Recent advancements and challenges in solar tracking systems (STS): a review. Renew Sustain Energy Rev 81:250–279

[6] Jamroen C, Komkum P, Kohsri S, Himananto W, Panupintu S, Unkat S (2020) A low-cost dual-axis solar tracking system based on digital logic design: Design and implementation. Sustain Energy Technol Assessm 37:100618

[7] Costals ER, Masmitjà G, Almache E, Pusay B, Tiwari K, Saucedo E, Raj CJ, Kim BC, Puigdollers J, Martin I, Voz C (2022) Atomic layer deposition of vanadium oxide flms for crystalline silicon solar cells. Mater Adv 3(1):337–345

[8] Han C, Yang G, Procel P, O'Connor D, Zhao Y, Gopalakrishnan A, Zhang X, Zeman M, Mazzarella L, Isabella O (2022) Controllable simultaneous bifacial Cu-plating for high-efciency crystalline silicon solar cells. Solar RRL 6(6):2100810

[9] Chong KK, Wong CW (2009) General formula for on-axis sun-tracking system and its application in improving tracking accuracy of solar collector. Sol Energy 83(3):298–305

[10] Nadia AR, Isa NAM, Desa MKM (2018) Advances in solar photovoltaic tracking systems: a review. Renew Sustain Energy Rev 82:2548–2569

[11] Hightower M, Pierce SA (2008) The energy challenge. Nature 452(7185):285–286.

[12] PVEducation. Mismatch effects

[13] Petrone, G. ; Ramos-Paja, C. A. ; Spagnuolo, G. ; Press, IEEE (Ed.): Photo-

[14] voltaic sources modeling. 1st. Wiley, 2017.

[15] Askari Mohammad Bagher, Mirzaei Mahmoud Abadi Vahid, Mirhabibi Mohsen. Types of Solar Cells and Application. American Journal of Optics and Photonics. Vol. 3, No. 5, 2015, pp. 94-113. doi: 10.11648/j.ajop.20150305.17

[16] Handbook of Photovoltaic Science and Engineering Editor(s): Antonio Luque, Steven Hegedus First published:21 December 2010.

[17] UK Department of Energy & Climate Change. n.d. UK solar PV power generation from 2004 to 2015 (in gigawatt hours). Statista. Accessed 12 July 2017.

[18] 18 S. A. Kalogirou, "Solar Energy Engineering: Processes and Systems: Second Edition," Sol. Energy Eng. Process. Syst. Second Ed., pp. 1–819, 2014.

[19] Bagher, A.M., Vahid, M.M.A. and Mohsen, M. (2015) Types of Solar Cells and Application. American Journal of Optics and Photonics, 3, 94-113.

[20] Allam, D., Yousri, D. A., & Eteiba, M. B. (2016). Parameters extraction of the three diode model for the multi-crystalline solar cell/module using Moth-Flame Optimization Algorithm. Energy Conversion and Management, 123, 535-548.

[21] Khyani H. K. (2013). Modeling and simulation of solar photovoltaic systems. ME thesis. Electrical Engineering Department, Faculty of Engineering (MBM Engineering College) JNV University, Jodhpur, 27-75.

[22] Rahman, T.; Mansur, A.A.; Hossain Lipu, M.S.; Rahman, M.S.; Ashique, R.H.; Houran, M.A.; Elavarasan, R.M.; Hossain, E. Investigation of Degradation of Solar Photovoltaics: A Review of Aging Factors, Impacts, and Future Directions toward Sustainable Energy Management. *Energies (Basel)* 2023, *16*, 3706.

[23] Balato, M.; Costanzo, L.; Vitelli, M. Reconfiguration of PV Modules: A Tool to Get the Best Compromise between Maximi-zation of the Extracted Power and Minimization of Localized Heating Phenomena. Solar Energy 2016, 138, 105–118.

[24] K. A. Kim and P. T. Krein, “Hot spotting and second breakdown effects on reverse I-V characteristics for mono-crystalline Si Photovoltaics,” in 2013 IEEE Energy Conversion Congress and Exposition, Sep. 2013, pp. 1007–1014.

[25] Niazi, K. A. K., Yang, Y., & Sera, D. (2019). Review of mismatch mitigation techniques for PV modules. IET Renewable Power Generation, 13(12), 2035-2050.

[26] Ziar, H., S. Mansourpour, E. Afjei, M. Kazemi. "Bypass Diode Characteristic Effect on the Behavior of Solar PV Array at Shadow Condition." In 2012 3rd Power Electronics and Drive Systems Technology (PEDSTC), 2012, 229–233.

[27] G. S. Krishna and T. Moger, ``Improved SuDoKu reconfiguration technique for total-cross-tied PV array to enhance maximum power under partial shading conditions," Renew. Sustain. Energy Rev., vol. 109, pp. 333_348, Jul. 2019.

[28] P. R. Satpathy, S. Jena, and R. Sharma, ``Power enhancement from partially shaded modules of solar PV arrays through various interconnections among modules," Energy, vol. 144, pp. 839_850, Feb. 2018.

[29] M. Jazayeri, S. Uysal, and K. Jazayeri, “A comparative study on different photovoltaic array topologies under partial shading conditions,” in IEEE PES T D Conf. and Exposition, pp. 1–5 (2014).

[30] A. M. Eltamaly and A. Y. Abdelaziz, Modern Maximum Power Point Tracking Techniques for Photovoltaic Energy Systems, Springer International Publishing, Cham, Switzerland (2019).

[31] R. Ramaprabha and B. L. Mathur, “A comprehensive review and analysis of solar photovoltaic array configurations under partial shaded conditions,” Int. J. Photoenergy 2012, 1–16 (2012).

[32] O. Bingöl and B. Özkaya, “Analysis and comparison of different PV array configurations under partial shading conditions," Sol. Energy, vol.160, pp. 336_343, Jan. 2018.

[33] P. R. Satpathy and R. Sharma, ``Power and mismatch losses mitigation by a fixed electrical reconfiguration technique for partially shaded photovoltaic arrays," Energy Convers. Manage., vol. 192, pp. 52_70, Jul. 2019.

[34] Z. Zhu, M. Hou, L. Ding, G. Zhu and Z. Jin, "Optimal Photovoltaic Array Dynamic Reconfiguration Strategy Based on Direct Power Evaluation," in IEEE Access, vol. 8, pp. 210267 210276, 2020.

[35] G. Sai Krishna and T. Moger, ``Reconfiguration strategies for reducing partial shading effects in photovoltaic arrays: State of the art," Sol.Energy, vol. 182, pp. 429_452, Apr. 2019.

[36] Sun, L., Li, H., Jia, Q., & Zhang, G. (2024). Optimization method of dynamic reconfiguration in virtual power plants. *Renewable Energy*, *228*, 120667.

[37] La Manna, D., Vigni, V. L., Sanseverino, E. R., Di Dio, V., & Romano, P. (2014). Reconfigurable electrical interconnection strategies for photovoltaic arrays: A review. *Renewable and Sustainable Energy Reviews*, *33*, 412-426.

[38] Caruso, M., Di Noia, L. P., Romano, P., Schettino, G., Spataro, C., & Viola, F. (2017). PV reconfiguration systems: A technical and economic study. *Journal of Electrical Systems*, *13*(1), 55-73.

[39] Vicente, P. S., Vicente, E. M., & Ribeiro, E. R. (2015, June). A review of solar photovoltaic array reconfiguration methods. In *2015 IEEE 24th International Symposium on Industrial Electronics (ISIE)* (pp. 208-213). IEEE.

[40] C. V. Chandrakant and S. Mikkili, "A Typical Review on Static Reconfiguration Strategies in Photovoltaic Array Under Non-Uniform Shading Conditions," in CSEE Journal of Power and Energy Systems, vol. 9, no. 6, pp. 2018-2039, November 2023.

[41] Rajasekar N., Vysakh M., Harshal V. T., Mohammed A. S., Muralidhar K., Don P.., Basil J., Karthik B., & Sudhakar B. T. (2014). Application of Modified Particle Swarm Optimization for Maximum Power Point Tracking under Partial Shading Condition, In Energy Procedia, 61, pp.2633 – 2639.

[42] Nazer, M. N. R., Noorwali, A., Tajuddin, M. F. N., Khan, M. Z., Tazally, M. A. I. A., Ahmed, J., ... & Kumar, N. M. (2021). Scenario-based investigation on the effect of partial shading condition patterns for different static solar photovoltaic array configurations. IEEE Access, 9, 116050-116072.

[43] Malathy, S., & Ramaprabha, R. (2018). Reconfiguration strategies to extract maximum power from photovoltaic array under partially shaded conditions. Renewable and Sustainable Energy Reviews, 81, 2922-2934.

[44] Krishna, S. G., & Moger, T. (2019). Optimal SuDoKu reconfiguration technique for total-cross-tied PV array to increase power output under non-uniform irradiance. IEEE Transactions on Energy Conversion, 34(4), 1973-1984.

[45] Sai K.G., & Tukaram M. (2018). SuDoKu and Optimal SuDoKu Reconfiguration for TCT PV array Under Non-uniform Irradiance Condition. In Proceedings of the 8th Power India International Conference (PIICON), IEEE, pp.101–110.

[46] Cherukuri, S. K., Kumar, B. P., Kaniganti, K. R., Muthubalaji, S., Devadasu, G., Babu, T. S., & Alhelou, H. H. (2022). A novel array configuration technique for improving the power output of the partial shaded photovoltaic system. IEEE Access, 10, 15056-15067.

[47] Pachauri, R. K., Kansal, I., Babu, T. S., & Alhelou, H. H. (2021). Power losses reduction of solar PV systems under partial shading conditions using re-allocation of PV module-fixed electrical connections. IEEE Access, 9, 94789-94812.

[48] El Iysaouy, L., Lahbabi, M., & Oumnad, A. (2019). A novel magic square view topology of a PV system under partial shading condition. Energy Procedia, 157, 1182-1190.

[49] Etarhouni, M., Chong, B., & Zhang, L. (2019, March). A PV array reconfiguration algorithm for minimising partial shading effects. In 2019 10th International Renewable Energy Congress (IREC) (pp. 1-6). IEEE.

[50] Vijayalekshmy, S., Bindu, G. R., & Iyer, S. R. (2016). A novel Zig-Zag scheme for power enhancement of partially shaded solar arrays. Solar Energy, 135, 92-102.

[51] Krishna, G. S., & Moger, T. (2019). Enhancement of maximum power output through reconfiguration techniques under non-uniform irradiance conditions. Energy, 187, 115917.

[52] Murugesan P., David P. W., Balachandran P. K., Cherukuri S. K., Thanikanti S. B.,& Hassan H. A. (2021). A new Ken-Ken puzzle pattern based reconfiguration technique for maximum power extraction in partial shaded solar PV array. IEEE Access, 9, 65824 – 65837.

[53] G. Sai Krishna and T. Moger, "Static reconfiguration approach for photovoltaic array to improve maximum power," in 2020 International Conference on Electrical and Electronics Engineering (ICE3), 2020.

[54] Rezazadeh, S., Moradzadeh, A., Pourhossein, K., Mohammadi-Ivatloo, B., & Garcia Marquez, F. P. (2023). Photovoltaic array reconfiguration under partial shading conditions for maximum power extraction via knight's tour technique. Journal of Ambient Intelligence and Humanized Computing, 14(9), 11545-11567.

[55] Sahu, H. S., Nayak, S. K., & Mishra, S. (2015). Maximizing the power generation of a partially shaded PV array. *IEEE journal of emerging and selected topics in power electronics*, *4*(2), 626-637.

[56] Tianliang H., Meiyi H., Lei D., Guofang Z., Zhen Z., & Hao G. (2021). Dynamic Photovoltaic Array Reconfiguration for Standalone PV Water Pumping System. In proceeding of the 6th Asia Conference on Power and Electrical Engineering (ACPEE), IEEE.

[57] Namuq, K. A., Siddiq, A. I., & Abdulkader, H. (2023). Dynamic reconfiguration of PV array under partial shading condition by using automatic switching. International Journal of Electrical and Electronic Engineering and Telecommunications,12(4), 272-278.

[58] Srinivasan, A., Devakirubakaran, S., Sundaram, B. M., Balachandran, P. K., Cherukuri, S. K., Winston, D. P., ... & Alhelou, H. H. (2021). L-shape propagated array configuration with dynamic reconfiguration algorithm for enhancing energy conversion rate of partial shaded photovoltaic systems. IEEE Access, 9, 97661-97674.

[59] Bulárka, S., & Gontean, A. (2017, October). Dynamic PV array reconfiguration under suboptimal conditions in hybrid solar energy harvesting systems. In 2017 IEEE 23rd International Symposium for Design and Technology in Electronic Packaging (SIITME) (pp. 419-422). IEEE.

[60] Siddiq, A. I., Fadhel, H., & Anwar, M. O. (2023). Automatic PV array reconfiguration under partial shading conditions. NTU Journal of Renewable Energy, 4(1), 36-46.

[61] Huyan, T., Hou, M., Ding, L., Zhu, G., Zhu, Z., & Gao, H. (2021, April). Research on Optimal Control of Switch Array State Switching in Photovoltaic Reconfiguration. In 2021 6th Asia Conference on Power and Electrical Engineering (ACPEE) (pp. 1328-1332). IEEE.

[62] Gadiraju, H. K. V., Barry, V. R., & Jain, R. K. (2022). Improved performance of PV water pumping system using dynamic reconfiguration algorithm under partial shading conditions. CPSS Transactions on Power Electronics and Applications, 7(2), 206-215.

[63] Deshkar, S. N., Dhale, S. B., Mukherjee, J. S., Babu, T. S., & Rajasekar, N. (2015). Solar PV array reconfiguration under partial shading conditions for maximum power extraction using genetic algorithm. Renewable and Sustainable Energy Reviews, 43, 102-110.

[64] Mostafaee, G., & Ghandehari, R. (2020). Power enhancement of photovoltaic arrays under partial shading conditions by a new dynamic reconfiguration method. Journal of energy management and technology, 4(1), 46-51

[65] Jamaludin, M. N. I., Tajuddin, M. F. N., Ahmed, J., Azmi, A., Azmi, S. A., Ghazali, N. H., ... & Alhelou, H. H. (2021). An effective salp swarm based MPPT for photovoltaic systems under dynamic and partial shading conditions. Ieee Access, 9, 34570-34589.

[66] Abdalla, O., Rezk, H., & Ahmed, E. M. (2019). Wind driven optimization algorithm based global MPPT for PV system under non-uniform solar irradiance. Solar Energy, 180, 429-444.

[67] Yousri, D., Thanikanti, S. B., Balasubramanian, K., Osama, A., & Fathy, A. (2020). Multi-objective grey wolf optimizer for optimal design of switching matrix for shaded PV array dynamic reconfiguration. IEEE Access, 8, 159931-159946.

[68] Elahi M, Ashraf HM, Kim C-H. Improved partial shading detection strategy based on chimp optimisation algorithm to determine the global maximum power point of the solar array system. Energies. 2022; 15(4):1549.

[69] Babu, T. S., Yousri, D., & Balasubramanian, K. (2020). Photovoltaic array reconfiguration system for maximizing the harvested power using population-based algorithms. IEEE Access, 8, 109608-109624.

[70] Hussein, H. A., Mahdi, A. J., & Abdul-Wahhab, T. M. (2021). Design of a boost converter with mppt algorithm for a pv generator under extreme operating conditions. Eng. Technol. J, 39(10), 1473-1480.

[71] Mahmoud, A., Shamseldein, M., Hasanien, H., & Abdelaziz, A. (2019, October). Photovoltaic array reconfiguration to reduce partial shading losses using water cycle algorithm. In 2019 IEEE Electrical Power and Energy Conference (EPEC) (pp. 1-6). IEEE.

[72] Zhu, Z., Hou, M., Ding, L., Zhu, G., & Jin, Z. (2020). Optimal photovoltaic array dynamic reconfiguration strategy based on direct power evaluation. IEEE Access, 8, 210267-210276.

[73] Gadiraju, H. K. V., Barry, V. R., & Maraka, I. (2019, December). Dynamic photovoltaic array reconfiguration for standalone PV water pumping system. In 2019 8th International Conference on Power Systems (ICPS) (pp. 1-4). IEEE.

[74] Karmakar, B. K., & Karmakar, G. (2021). A current supported PV array reconfiguration technique to mitigate partial shading. IEEE Transactions on Sustainable Energy, 12(2), 1449-1460.

[75] Varma, G. H. K., Barry, V. R., Jain, R. K., & Kumar, D. (2021). An MMTES algorithm for dynamic photovoltaic array reconfiguration to enhance power output under partial shading conditions. IET Renewable Power Generation, 15(4), 809-820.

[76] Hariharasudhan, T., Suriyakala, S., Prince, W. D., & Sathya, P. (2022). Dynamic and static reconfiguration analysis of solar PV array. Ymer J, 21, 204-208.

[77] Murtaza, A. F., & Sher, H. A. (2023). A reconfiguration circuit to boost the output power of a partially shaded PV string. Energies, 16(2), 622.

[78] Li, S., Zhang, T., & Yu, J. (2023). Photovoltaic array dynamic reconfiguration based on an improved pelican optimization algorithm. Electronics, 12(15), 3317.

[79] Baka, M., Manganiello, P., Soudris, D., & Catthoor, F. (2019). A cost-benefit analysis for reconfigurable PV modules under shading. Solar Energy, 178, 69-78.

[80] Ajmal, A. M., Ramachandaramurthy, V. K., Naderipour, A., & Ekanayake, J. B. (2021). Comparative analysis of two-step GA-based PV array reconfiguration technique and other reconfiguration techniques. Energy Conversion and Management, 230, 113806.

[81] Zhou, J., Liu, C., & Li, K. (2022). PV array reconfiguration with electrical energy storage system for power system frequency regulation. Frontiers in Energy Research, 10, 971628.

[82] Fang, X., Yang, Q., & Yan, W. (2021). Switching matrix enabled optimal topology reconfiguration for maximizing power generation in series–parallel organized photovoltaic systems. IEEE Systems Journal, 16(2), 2765-2775.

[83] Bouselham, L., Rabhi, A., Hajji, B., Mellit, A., & El Fouas, C. (2019, November). An intelligent irradiance equalization approach based on fuzzy logic for small reconfigurable PV architecture. In 2019 7th International Renewable and Sustainable Energy Conference (IRSEC) (pp. 1-6). IEEE.

[84] Satpathy, P. R., Babu, T. S., Mahmoud, A. H., Sharma, R., & Nastasi, B. (2021). A TCT-SC hybridized voltage equalizer for partial shading mitigation in PV arrays. IEEE Transactions on Sustainable Energy, 12(4), 2268-2281.

[85] Noman, A. M., Sheikh, H. S., Murtaza, A. F., Almutairi, S. Z., Alqahtani, M. H., & Aljumah, A. S. (2023). Maximum Power Point Tracking Algorithm of Photo-Voltaic Array through Determination of Boost Converter Conduction Mode. Applied Sciences, 13(14), 8033.

[86] Murtaza, A. F., Sher, H. A., Al-Haddad, K., & Spertino, F. (2020). Module level electronic circuit based PV array for identification and reconfiguration of bypass modules. IEEE Transactions on Energy Conversion, 36(1), 380-389.

[87] Narayanaswamy V , Ayyanar R , Tepedelenlioglu C , et al. Optimizing solar power using array topology reconfiguration with regularized deep neural networks. IEEE Access , 2023 ,11 :7461 –7470 .

[88] Kamal, S., Ramapraba, P. S., Kumar, A., Saha, B. C., Lakshminarayana, M., Sanal Kumar, S., ... & Erko, K. G. (2022). Optimization of solar panel deployment using machine learning. International Journal of Photoenergy, 2022(1), 7249109.

[89] Rao, P. S., Ilango, G. S., & Nagamani, C. (2014). Maximum power from PV arrays using a fixed configuration under different shading conditions. IEEE journal of Photovoltaics, 4(2), 679-686.

[90] Sanseverino, E. R., Ngoc, T. N., Cardinale, M., Vigni, V. L., Musso, D., Romano, P., & Viola, F. (2015). Dynamic programming and Munkres algorithm for optimal photovoltaic arrays reconfiguration. Solar Energy, 122, 347-358.

[91] Rezk, H., Fathy, A., & Aly, M. (2021). A robust photovoltaic array reconfiguration strategy based on coyote optimization algorithm for enhancing the extracted power under partial shadow condition. Energy reports, 7, 109-124.

[92] Harrag, A., & Messalti, S. (2018). Adaptive GA-based reconfiguration of photovoltaic array combating partial shading conditions. Neural Computing and Applications, 30, 1145-1170.

[93] Yousri, D., Babu, T. S., Beshr, E., Eteiba, M. B., & Allam, D. (2020). A robust strategy based on marine predators algorithm for large scale photovoltaic array reconfiguration to mitigate the partial shading effect on the performance of PV system. IEEE Access, 8, 112407-112426.

[94] Gadiraju, H. K. V., Barry, V. R., & Maraka, I. (2019, December). Dynamic photovoltaic array reconfiguration for standalone PV water pumping system. In 2019 8th International Conference on Power Systems (ICPS) (pp. 1-4). IEEE.

[95] Verma, P., Garg, R., & Mahajan, P. (2020). Asymmetrical interval type-2 fuzzy logic control based MPPT tuning for PV system under partial shading condition. ISA transactions, 100, 251-263.

[96] Ibrahim, S. A., Nasr, A., & Enany, M. A. (2021). Maximum power point tracking using ANFIS for a reconfigurable PV-based battery charger under non-uniform operating conditions. IEEE Access, 9, 114457-114467.

[97] Wang, Y., Lin, X., Kim, Y., Chang, N., & Pedram, M. (2012, March). Enhancing efficiency and robustness of a photovoltaic power system under partial shading. In Thirteenth International Symposium on Quality Electronic Design (ISQED) (pp. 592-600). IEEE.

[98] Vadivel, S., Boopthi, C. S., Ramasamy, S., Ahsan, M., Haider, J., & Rodrigues, E. M. (2021). Performance Enhancement of a Partially Shaded Photovoltaic Array by Optimal Reconfiguration and Current Injection Schemes. Energies, 14(19), 6332.

[99] Jazayeri, M., Jazayeri, K., & Uysal, S. (2017). Adaptive photovoltaic array reconfiguration based on real cloud patterns to mitigate effects of non-uniform spatial irradiance profiles. Solar Energy, 155, 506-516.

[100] Liu, X., & Wang, Y. (2019). Reconfiguration method to extract more power from partially shaded photovoltaic arrays with series-parallel topology. Energies, 12(8), 1439.

[101] Pagliari, D. J., Vinco, S., Macii, E., & Poncino, M. (2019, March). Irradiance-driven partial reconfiguration of PV panels. In 2019 Design, Automation & Test in Europe Conference & Exhibition (DATE) (pp. 884-889). IEEE.

[102] Narayanaswamy, V. S., Ayyanar, R., Spanias, A., Tepedelenlioglu, C., & Srinivasan, D. (2019, May). Connection topology optimization in photovoltaic arrays using neural networks. In 2019 IEEE International Conference on Industrial Cyber Physical Systems (ICPS) (pp. 167-172). IEEE.

[103] Peng, Y., Zheng, S., & Sun, W. (2019, July). Solar PV array reconfiguration under partial shading conditions using optimal control. In 2019 Chinese Control Conference (CCC) (pp. 7442-7447). IEEE.

[104] Ul-Haq, A., Alammari, R., Iqbal, A., Jalal, M., & Gul, S. (2020). Computation of power extraction from photovoltaic arrays under various fault conditions. IEEE Access, 8, 47619-47639.

[105] Madhanmohan, V. P., Saleem, A., & Nandakumar, M. (2020). An algorithm for enhanced performance of photovoltaic array under partial shading condition. IEEE Access, 8, 176947-176959

[106] Polo, J., Fernandez-Neira, W. G., & Alonso-García, M. C. (2017). On the use of reference modules as irradiance sensor for monitoring and modelling rooftop PV systems. Renewable energy, 106, 186-191.

[107] Sugianto, S. (2020). Comparative analysis of solar cell efficiency between monocrystalline and polycrystalline. *INTEK: Jurnal Penelitian*, *7*(2), 92-100.

[108] R. K. Pachauri et al., "Impact of Partial Shading on Various PV Array Configurations and Different Modeling Approaches: A Comprehensive Review," in IEEE Access, vol. 8, pp. 181375-181403, 2020

[109] Rakesh, N.; Malavya, U. Maximizing the Power Output of Partially Shaded Solar PV Array using Novel Interconnection Method. In Proceedings of the International Conference on Innovative Mechanisms for Industry Applications (ICIMIA 2017), Bengaluru, India, 21–23 February 2017.

[110] Hou S, Zhu W. Dynamic Reconfiguration Method of Photovoltaic Array Based on Improved HPSO Combined with Coefficient of Variation. Electronics 2023 ;12(12):2744.

[111] Huang YP, Chen X, Ye CE. Implementation of a modified circuit reconfiguration strategy in high concentration photovoltaic modules under partial shading conditions. Solar Energy 2019; 194:628-48.

[112] Shaik, F., Lingala, S. S., & Veeraboina, P. (2023). Effect of various parameters on the performance of solar PV power plant: a review and the experimental study. Sustainable Energy Research, 10(1), 6.

[113] Gunther G. and Bettina W., "Introduction to Microcontrollers", Vienna University of Technology, ISBN N/A, 2007.

[114] Massimo B., "Getting Started with Arduino", Second Edition, O'Reilly Media, ISBN: 978-1-449-309879, 2011.

[115] Dale W., "Arduino Internals", A press, ISBN:1430238836, 9781430238836, 2012.

[116] www.arduino.cc/en/Guide/ArduinoMega2560.

[117] Introduction to ZigBee Technology - Aya Alaa - Academia.edu. https://www.academia.edu/100751839/Introduction_to_ZigBee_Technology.

[118] Solahuddin Yusuf bin Fadhlullah.(2016) Xbee Pocket ManualXbee Pocket Manual,.DOI:10.13140/RG.2.1.1540.0089.

[119] Interfacing a Voltage Sensor with Arduino," Arduino Project Hub, Arduino Project Hub, accessed April 6, 2024

[120] Current Sensor Module Pinout, Features, Specifications & Arduino Circuit." [Online]. Available: ACS712 Current Sensor And Arduino (makerguides.com). Maxim Integrated. (n.d.). DS18B20 Programmable Resolution

[121] Book (Electric Relays: Principles and Applications) April 2016, DOI: 10.1201/9781315221168, ISBN: 9781315221168.

[122] Handson Technology user guide Retrieved from https://handsontec.com/dataspecs/relay/1Ch-relay.pdf.

[123] Handson Technology user guide Retrieved from https://www.handsontec.com/dataspecs/module/30A-RelayMod.pdf.

[124] Wire Digital Thermometer. Datasheet. Retrieved from https://datasheets.maximintegrated.com/en/ds/DS18B20.pdf.

[125] Ambient Light Sensor IC Series, Digital 16bit Serial Output Type Ambient Light Sensor IC, BH1750FVI. No.11046EDT01.

[126] Amazon.com: 100 Amp Shunt. https://www.amazon.com/100-amp-shunt/s?k=100+amp+shunt.

[127] UT89X Series Digital Multimeters - UNI-T Meters - Uni-Trend. https://meters.uni-trend.com/product/ut89x-series/.

[128] Gilat, A. (2011). MATLAB: An Introduction with Applications (4th ed.). John Wiley & Sons, Inc. ISBN: 9780470873731.

[129] XCTU Configuration & Test Utility Software User Guide - Digi International. https://hub.digi.com/support/products/xctu/?path=/support/digi-xbee-cellular-modems/xctu-configuration-test-utility-software-user-guide/.